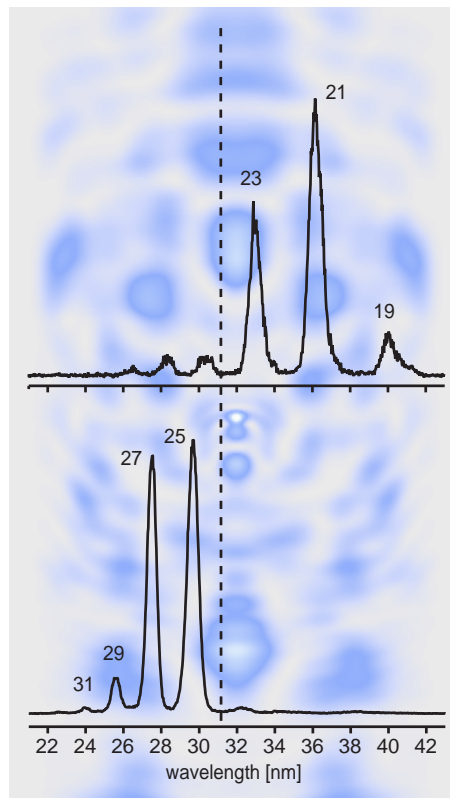


# Adaptive Control of Coherent Soft X-Rays



**Dissertation zur Erlangung des  
naturwissenschaftlichen Doktorgrades  
der Bayerischen Julius-Maximilians-Universität  
Würzburg**

vorgelegt von  
**Thomas Pfeifer**  
aus Miltenberg

Würzburg 2004

Eingereicht am: 4. Juni 2004  
bei der Fakultät für Physik und Astronomie

Gutachter der Dissertation:

1. Gutachter: Prof. Dr. G. Gerber
2. Gutachter: Prof. Dr. C. Spielmann
3. Gutachter: Prof. Dr. T. Baumert

Prüfer im Promotionskolloquium:

Prof. Dr. T. Baumert  
Prof. Dr. G. Gerber  
Prof. Dr. W. Kinzel  
Prof. Dr. C. Spielmann

Tag der mündlichen Prüfung (Promotionskolloquium): 28. Juni 2004

# List of Publications

Parts of this work have been published in the following references:

A. Flettner, J. König, M. B. Mason, T. Pfeifer, U. Weichmann, R. Düren, and G. Gerber.  
*Ellipticity dependence of atomic and molecular high harmonic generation.*  
Europ. Phys. J. D **21**, 115–119 (2002).

T. Pfeifer, U. Weichmann, S. Zipfel, and G. Gerber.  
*Compression and shaping of a self-phase-modulated laser pulse with a deformable mirror device.*  
J. Mod. Opt. **50**, 705–710 (2003).

A. Flettner, J. König, M. B. Mason, T. Pfeifer, U. Weichmann, and G. Gerber.  
*Atomic and molecular high-harmonic generation: A comparison of ellipticity dependence based on the three-step model.*  
J. Mod. Opt. **50**, 529–537 (2003).

M. Y. Emelin, M. Y. Ryabikin, A. M. Sergeev, M. D. Chernobrovtsseva, T. Pfeifer, D. Walter, and G. Gerber.  
*Attosecond Burst and High-Harmonic Generation in Molecular Ionization by Ultrashort Laser Pulses.*  
JETP Lett. **77**, 212–216 (2003).

A. Flettner, T. Pfeifer, D. Walter, C. Winterfeldt, C. Spielmann, and G. Gerber.  
*High-harmonic generation and plasma radiation from water microdroplets.*  
Appl. Phys. B **77**, 747–751 (2003).

T. Pfeifer, D. Walter, G. Gerber, M. Y. Emelin, M. Y. Ryabikin, M. D. Chernobrovtsseva, and A. M. Sergeev.  
*Transient Enhancement of High-Harmonic Generation in Expanding Molecules.*  
Phys. Rev. A, **70**, 013805 (2004).

T. Brixner, C. Dietl, G. Krampert, P. Niklaus, E. Papastathopoulos, T. Pfeifer, R. Selle, G. Vogt, D. Walter, C. Winterfeldt, and G. Gerber  
*Adaptive femtosecond quantum control,*  
In F. Krausz, G. Korn, P. Corkum, and I. A. Walmsley (Eds.), *Ultrafast Optics IV*,  
Volume 95 of *Springer Series in Optical Sciences*, pp. 117-126, Springer, Berlin (2004).

T. Brixner, T. Pfeifer, G. Gerber, M. Wollenhaupt, and T. Baumert  
*Optimal control of atomic, molecular and electron dynamics with tailored femtosecond laser pulses,*

In P. Hannaford (Ed.), *Volume on Femtosecond Laser Spectroscopy of Kluwer Series on Progress in Lasers*, Chapter 9, pp. 229–271, Kluwer Academic Publishers, Dordrecht (2004).

T. Pfeifer, D. Walter, C. Winterfeldt, C. Spielmann, and G. Gerber.  
*Adaptive engineering of coherent soft x-rays.*

In *Ultrafast Phenomena XIV, Springer Series in Chemical Physics*, accepted for publication, Springer, Berlin (2004).

T. Pfeifer, D. Walter, C. Winterfeldt, C. Spielmann, and G. Gerber.  
*Controlling the spectral shape of coherent soft x-rays.*  
submitted.

T. Pfeifer and G. Gerber.  
*Atomic and molecular high-harmonic generation in the quasistatic limit using elliptically polarized light.*  
in preparation.

T. Pfeifer, D. Walter, C. Winterfeldt, C. Spielmann, and G. Gerber.  
*Adaptive control in the soft x-ray region.*  
in preparation.

Further publications beyond the scope of this work:

T. Brixner, G. Krampert, T. Pfeifer, R. Selle, G. Gerber, M. Wollenhaupt, O. Graefe, C. Horn, D. Liese, and T. Baumert.  
*Quantum control by ultrafast polarization shaping.*  
*Phys. Rev. Lett.* **92**, 208301 (2004).

T. Brixner, G. Krampert, T. Pfeifer, R. Selle, G. Gerber, M. Wollenhaupt, O. Graefe, C. Horn, D. Liese, and T. Baumert.  
*Adaptive polarization control of molecular dynamics.*  
In *Ultrafast Phenomena XIV, Springer Series in Chemical Physics*, accepted for publication, Springer, Berlin (2004).

M. Yu. Emelin, M. Yu. Ryabikin, M. D. Chernobrovtsseva, A. M. Sergeev, T. Pfeifer, D. Walter, and G. Gerber.  
*High-efficiency generation of attosecond pulses during atomic ionization from excited electronic states.*  
submitted.

# Contents

<b>List of Publications</b>	<b>iii</b>
<b>I Introduction</b>	<b>1</b>
<b>1 Basics</b>	<b>5</b>
1.1 Ultrashort Laser Pulses . . . . .	5
1.1.1 Generation of Ultrashort Laser Pulses: The Laser System . . . . .	6
1.1.2 Mathematics of Ultrashort Laser Pulses . . . . .	9
1.1.3 Laser Pulse Dispersion . . . . .	14
1.1.4 Laser Pulse Shaping . . . . .	15
1.1.5 Laser Pulse Measurement . . . . .	20
1.2 Fundamentals of Nonlinear Optics . . . . .	27
1.2.1 Polarizability — Microscopic Source . . . . .	28
1.2.2 Phase matching — Macroscopic build-up . . . . .	35
1.2.3 Application Examples . . . . .	40
<b>2 High-Harmonic Generation</b>	<b>49</b>
2.1 Single Particle Response . . . . .	50
2.1.1 Ionization — Step I . . . . .	51
2.1.2 Propagation — Step II . . . . .	52
2.1.3 Recombination — Step III . . . . .	54
2.1.4 Quantum-Mechanical Description . . . . .	57
2.1.5 Numerical Calculation . . . . .	60
2.2 Propagation Effects . . . . .	62
2.2.1 Neutral Dispersion . . . . .	63
2.2.2 Plasma Dispersion . . . . .	63
2.2.3 Geometric Dispersion . . . . .	64
2.2.4 Absorption . . . . .	69
2.3 Attosecond Pulses . . . . .	71
2.3.1 Existence . . . . .	72
2.3.2 Measurement . . . . .	75
2.4 Applications of Ultrafast X-Rays . . . . .	78
2.4.1 Applications of High-Harmonic Generation . . . . .	78

2.4.2	Applications of Synchrotron and Free-Electron-Laser Sources . . .	79
2.4.3	Applications of Laser-induced-Plasma X-Ray Sources . . . . .	81
<b>II</b>	<b>Optimization of Harmonics by Medium Engineering</b>	<b>83</b>
<b>3</b>	<b>Molecular Media</b>	<b>87</b>
3.1	Molecular Symmetry Considerations . . . . .	87
3.2	Ellipticity Dependence . . . . .	90
3.2.1	Experimental Setup . . . . .	90
3.2.2	Experimental Results . . . . .	91
3.2.3	Simulation . . . . .	92
3.3	Electron-Wavepacket Engineering . . . . .	96
3.3.1	The Model . . . . .	97
3.3.2	Internuclear-Distance Dependence . . . . .	98
3.4	Pump–Drive Schemes . . . . .	101
3.5	Conclusion . . . . .	104
<b>4</b>	<b>Condensed Media</b>	<b>107</b>
4.1	Experimental Setup . . . . .	108
4.1.1	Microdroplet-Jet Characterization . . . . .	108
4.1.2	Vacuum and Detection Apparatus . . . . .	108
4.2	Frequency Conversion in Water Microdroplets . . . . .	110
4.2.1	Laser-induced Plasma Radiation . . . . .	110
4.2.2	High-Harmonic Radiation . . . . .	112
4.2.3	Plasma–Harmonic Transition . . . . .	114
4.3	Conclusion . . . . .	115
<b>III</b>	<b>Control of Harmonics by Laser-Pulse Shaping</b>	<b>117</b>
<b>5</b>	<b>Coherent Soft X-Ray Spectral Shaping</b>	<b>119</b>
5.1	Quantum Control . . . . .	120
5.1.1	Control Methods . . . . .	121
5.1.2	Closed-Loop Learning Control . . . . .	122
5.1.3	History of Control of High-Harmonic Generation . . . . .	125
5.1.4	Evolutionary Algorithm . . . . .	127
5.2	Closed-Loop Experimental Setup . . . . .	130
5.2.1	Laser-Pulse Compression and Shaping . . . . .	130
5.2.2	Second-harmonic Maximization . . . . .	131
5.3	Controlled Harmonic Generation in the Gas Jet . . . . .	133
5.3.1	Cut-off Extension . . . . .	137
5.3.2	Harmonic Selectivity? . . . . .	138

---

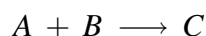
5.4	Controlled Harmonic Generation in the Waveguide . . . . .	139
5.4.1	Single-Harmonic Generation . . . . .	141
5.4.2	Selective High-Harmonic Generation . . . . .	142
5.4.3	Suppression of Single Plateau Harmonics . . . . .	143
5.4.4	Simulation and Discussion . . . . .	146
5.5	Conclusion . . . . .	146
<b>IV</b>	<b>Adaptive Control in the Soft X-Ray Region</b>	<b>149</b>
<b>6</b>	<b>Selective Photochemistry with Shaped Soft X-Rays</b>	<b>151</b>
6.1	Experimental Setup . . . . .	151
6.2	Optimal Control of Soft X-Ray Photofragmentation in SF <sub>6</sub> . . . . .	153
6.3	Conclusion . . . . .	157
<b>7</b>	<b>Attosecond Pulse Shaping</b>	<b>159</b>
7.1	Experimental Indications . . . . .	159
7.2	Numerical Modeling . . . . .	160
7.3	Conclusion . . . . .	162
<b>V</b>	<b>Summary and Outlook</b>	<b>165</b>
<b>VI</b>	<b>Appendix</b>	<b>169</b>
<b>A</b>	<b>Adaptive Femtosecond Polarization Control</b>	<b>171</b>
<b>B</b>	<b>SPIDER Details</b>	<b>177</b>
B.1	Spectral Interferometry . . . . .	177
B.2	Self-Referencing . . . . .	179
B.3	Phase-Function Retrieval . . . . .	180
B.3.1	Concatenation . . . . .	180
B.3.2	Integration Method . . . . .	181
<b>C</b>	<b>Numerical Solution of the Schrödinger-Equation</b>	<b>183</b>
C.1	Laser–Atom-Interaction Hamiltonian Operator . . . . .	183
C.2	Split-Step-Operator Method . . . . .	184
	<b>Bibliography</b>	<b>185</b>
	<b>Acknowledgments</b>	<b>215</b>
	<b>Curriculum Vitae</b>	<b>217</b>





# Part I

## Introduction



This simple general reaction formula plays a fundamental role in chemistry. Two reagent particles *A* and *B* interact with each other in some way and form a new and different particle *C*. For the chemist the particles typically can be either atoms, molecules or clusters. From a physicist's point of view, any elementary particle or conglomerate of particles existent in nature—such as quarks, leptons but certainly also photons—can take part in such a reaction. Indeed—if conditions are well-prepared—two and even much more photons “react” with each other to form one new photon. Since energy conservation must be fulfilled, the one new photon carries all the energy of the educt photons. It is easy to imagine that these kinds of “photonic reactions” can generate very high photon energies—up into the soft x-ray spectral region—by having more and more photons react with each other. In chemistry it is well-known that the reagents must be carefully prepared and catalysts must be used and optimized in order to create a maximum of the desired substance, avoiding undesired by-products.

This work presents the optical analog: For photonic reactions, we have to carefully prepare the state of the reacting light and to use a particular reaction environment as a catalyst in order to enhance the reaction efficiency and to control the high-energy photonic product state. Moreover, newly synthesized photons are directly applied in a prototype experiment, opening the door to fascinating scientific perspectives.

Due to the linearity of the classical Maxwell equations photons cannot interact with each other in vacuum. The superposition principle states that one propagating electromagnetic wave is not affected by another one—the two electric fields simply add. The situation changes when light propagates in a medium. Here, the electric field of light interacts with the electrons in the material, causing them to oscillate around their equilibrium positions. It is the acceleration of charged particles—the electrons in this case—that creates electromagnetic radiation. For small electric fields, this oscillatory motion can be approximated to be linearly dependent on the electric field strength of the light wave. For higher and higher fields, this linear dependence breaks down—we enter the field of nonlinear optics. From here on, photonic reactions are possible.

We can thus identify two vital environmental conditions that need to be set to enable photon conversion reactions: the availability of a suitable medium acting as the catalyst and high laser field strengths that call for high intensity. The latter can be accomplished by the use of ultrashort laser pulses that are focused down to very small spot sizes. Intensities on the order of  $10^{14}$  W/cm<sup>2</sup> can easily be obtained in the region where interaction with the medium takes place. In other words, in the interaction region the photon density is high

enough such that photons can talk to each other via the medium which they polarize. By a mechanism called high-harmonic generation, typically odd numbers of laser photons join to produce photons of energies far into the soft-x-ray spectral range.

This light conversion mechanism would merely be of academic interest if the high-energy light produced had the same properties as emission of thermal sources or x-ray tubes. However, by contrast, the light created in the high-harmonic generation process exhibits a number of interesting qualities. Spatial and temporal coherence properties of the generating laser light are transferred to the soft x-ray photons. This enables us to create laser-like emission at soft-x-ray frequencies. The photon conversion reaction can only occur as long as there is light provided by the laser pulse. Thus, the duration of the soft x-ray pulse that travels along with the laser pulse is shorter than or equal to the one of the laser pulse. It can really be *much shorter* than the laser pulse, down to durations of a few hundred attoseconds ( $\text{as}=10^{-18}$  s), far shorter than the optical period ( $2.67 \text{ fs} = 2670$  as for 800 nm wavelength) of the few-cycle femtosecond-duration laser pulse that generates it. These attosecond light pulses are of fundamental interest for the dawning field of attophysics, devoted to the exploration of electronic motion in atoms on the natural time-scale of the quickly moving tightly bound electrons. There is one severe drawback of this fascinating perspective: The photonic reaction efficiency, i.e. the efficiency of conversion from laser light into soft-x-ray light is very small. At the moment typically 10 laser photons per million (10 ppm) are converted. The low total soft-x-ray photon flux achievable therefore is a severe limitation for future applications of the high-harmonic radiation.

To perform light conversion by high-harmonic generation we need to provide two ingredients, the *driving laser light* and the *medium* it interacts with. In this work both of these ingredients are optimized and controlled in experiment as well as in theory. Modifying the temporal characteristics of laser pulses with pulse shaping techniques and design and preparation of the medium are shown to lead to significant enhancements of the conversion efficiency of the process. This represents a comprehensive approach to overcome the problem of limited coherent soft x-ray flux.

It turns out that the enhancement of the conversion efficiency is not the only benefit obtained from shaping the generating laser pulse. In fact, the well-known typical shape of the soft x-ray spectrum produced in the conversion process changes when the laser pulse shapes are modified. This fact has even more important consequences than increased conversion efficiency: It means that the shape of the attosecond pulses produced in the process can be controlled. In the field of quantum control, the femtosecond time-scale motion of molecular or lattice vibrations and also is nowadays routinely controlled by the shape of available femtosecond laser pulses. Similarly, in the future, the dynamics of electronic wavepackets can be controlled by the shape of the newly synthesized attosecond pulses. This finding lines out the relevance of this work: the field of coherent control has been transferred into the emerging field of attophysics in the soft x-ray spectral range. An experiment on the control of a gas-phase molecular reaction described at the end of this work demonstrates the versatility of the developed flexible coherent light source in the soft x-ray domain. Many more applications of the presented technique can be expected to follow up through the now open door.

This thesis is structured as follows:

Part I serves as a general introduction. It describes the fundamental theoretical concepts and experimental techniques needed to understand the main part of this work. The introduction covers both the preparation and manipulation of the ultrashort high-intensity laser pulses and the nonlinear response of the medium when it is irradiated by these intense light fields. The process of high-harmonic generation—being the nonlinear response of particular relevance for this work—is then discussed in detail.

Part II is devoted to the experimental and theoretical results on the optimization of high-harmonic coherent soft-x-ray generation by designing and preparing the conversion medium. Both the gas and the condensed liquid phase will be studied in order to find optimum conditions for efficient high-harmonic generation. Molecules are shown to be excellent conversion media if they are suitably prepared. The concept of ‘pump–drive’ harmonic generation is introduced to efficiently exploit the molecular inner degrees of freedom. This concept is then employed at high particle densities in the liquid phase. High-order harmonic generation observed from water microdroplets for the first time reveals new results guiding the way towards efficient coherent soft x-ray production.

The control of the high-harmonic process by shaped laser pulses is the subject of Part III. Not only an increase in conversion efficiency is achieved but the qualitative shape of the high-harmonic spectral response can be altered to produce unprecedented high-harmonic spectra. The flexibility of this variable soft x-ray emission allows for application in an adaptive control experiment in the soft x-ray region, described in Part IV. This part also discusses the effects of the spectral shaping results for the temporal shape of the sub-femtosecond pulses produced in high-harmonic generation. It represents the first description of a simple attosecond pulse shaper.

The thesis is concluded with a summary in Part V also containing an outlook to upcoming experiments based on these newly developed techniques and results.

The appendix in Part VI describes the first application of the recently developed technique of adaptive femtosecond polarization shaping in the field of quantum control and also some more specific technical issues.



# Chapter 1

## Basics

In this chapter, the fundamental aspects of the theory and techniques needed to understand the main part of this work are introduced and discussed. A large amount of the results described below focuses on the interaction of highly intense laser radiation with matter in a process called high-harmonic generation. This process can be exploited to produce light in the soft x-ray spectral region. Although one might assume that higher and higher intensity of the laser leads to more and more complex physical phenomena, we will see that much can be understood by retreating to classical Newtonian motion of a single particle—the electron—in the laser field. It is one of the intriguing aspects of nature that islands of simplicity sometimes arise in a sea of complexity. For this particular subject that means: A quantum mechanical system interacting with a strong laser field can be described using classical mechanics. From a different point of view we can state: Nonlinear optics in the complex nonperturbative regime recovers linearity.

This chapter is structured to lead from the general properties of ultrashort laser pulses to the particular application, which is high-harmonic generation. The first section is devoted to ultrashort laser pulses: How are they mathematically described and how are they affected by propagation in media exhibiting dispersion. The next section serves as an introduction to nonlinear optics, discussing the microscopic origin of frequency conversion and the macroscopic requirements that the conversion medium needs to fulfill to produce observable amounts of converted light. Finally the last section reviews the field of high-harmonic generation, where the beforehand described fundamental principles of nonlinear optics will be applied to this special case.

### 1.1 Ultrashort Laser Pulses

The field of nonlinear optics arises from the availability of highly intense laser radiation. Nowadays, the simplest way to provide these laser intensities are ultrashort pulse sources with their most common representative, the Ti:sapphire laser. This class of lasers is now able to supply pulses of duration down to 3-5 fs [1–3]. For longer pulse durations, pulse energies of several hundred Joules can be obtained, providing intensities around  $10^{21}$  W/cm<sup>2</sup> and Petawatt peak power [4]. On the other hand, Terawatt pulse energies are

available at high (1 kHz) repetition rates [5]. Amplification schemes have been proposed in theory allowing for the generation of intensities of  $10^{29}$  W/cm<sup>2</sup> [6] with present day laser systems. At these intensities (corresponding to the quantum-electrodynamic critical field strength, called the Schwinger limit), electron–positron pairs can be spontaneously created by the light, giving rise to a multitude of new effects.

The working principles of modern Ti:sapphire laser systems, in particular the ones used for the experiments in the main part of this work, will shortly be outlined at the beginning. In order to work with ultrashort laser pulses both experimentally and theoretically some further basic knowledge about their properties is helpful. How do we mathematically describe the ultrashort laser pulses, what are ways to modify their temporal shape, and how does a dielectric medium affect the pulses which travel through it? It will also become obvious that the time-frequency dualism in the description of wave phenomena is very helpful with the Fourier transformation playing a fundamental role.

### 1.1.1 Generation of Ultrashort Laser Pulses: The Laser System

The desire to create shorter and shorter laser pulses accompanied the development of the laser [7, 8] ever since its first realization. One decisive step was the discovery of the technique now known as Kerr-lens modelocking [9, 10]. As the name implies, multiple longitudinal cavity modes within the gain bandwidth of the laser become phase-locked, giving rise to a stable laser pulse train in the output of the laser. As was mentioned at the beginning, the typical ultrashort pulse laser systems today are based on the lasing medium of titanium doped sapphire (Ti:sapphire), which is a solid. Usually, a free-running solid state laser tends to produce a narrow-band continuous-wave (cw) output at a given wavelength corresponding to the maximum of the gain curve of the laser. How is it possible that multiple modes are excited and even phase-locked? We need a mechanism that is able to convert a narrow frequency spectrum into a broader range of frequencies. As will be discussed in Section 1.2, nonlinear optics allows for exactly this frequency conversion. It will be shown that the refractive index of dielectric material depends not only on the frequency but also on the intensity of the light. In most materials, the index of refraction increases with intensity. A laser beam is most intense in its center, which then gives rise to an effective positive focal-length lens, the so-called Kerr lens. This phenomenon is employed in mode-locked Ti:sapphire lasers [11]: It is done by setting up the cavity in such a way that single-mode operation is slightly disfavored when the Kerr-lens is not active. A small perturbation of a free running cw-laser will then lead to the buildup of a ultrashort laser pulse which concentrates the power of the laser into a short moment of time, thus increasing the intensity and efficiently generating the Kerr lens that corrects for the disfavored setup of the laser. Due to mode competition in a laser, the operation mode that experiences the least losses is always favored. Since the laser cavity is set up such that the least losses are encountered for a strong Kerr lens, the laser pulse duration will naturally decrease down to a very small value.

The limit is finally given by dispersion, the frequency dependence of the refractive index. Shorter and shorter laser pulses have a broader and broader spectral distribution (see below). The initially short pulse will thus suffer an increase in its duration as it trav-

els through the laser material (blue and red frequencies travel at different speeds), which decreases the intensity. The shorter the initial laser pulse, the more severe the spreading, thus the decrease in intensity. Therefore, in order to maintain the short pulses, this dispersion has to be compensated. In a Ti:sapphire laser oscillator this can be done by geometrically separating blue and red frequencies with a pair of prisms and having them travel differently long paths, counterbalancing the dispersion of the laser [11].

Since the prism compressor allows only for a limited compensation of the material dispersion, chirped mirrors have been developed [12–14] that allow to generate the shortest possible pulses. These mirrors are based on multilayer reflection, where the layer spacing is chosen such that different frequencies reflect at different depths, thereby reversing the effect of pulse dispersion in the laser crystal and cavity optics.

The typical output of a Ti:sapphire laser oscillator is a pulse train of 10-100 fs-duration pulses with a repetition rate on the order of 100 MHz. The average power is usually on the order of several 100 mW, giving rise to pulse energies of several nJ. These pulses can be focused to yield intensities on the order of  $10^{12}$  W/cm<sup>2</sup>. For the experiments discussed in the main part of this work, however, this is not sufficient. Intensities of at least  $10^{14}$  W/cm<sup>2</sup> are required. Amplification of the oscillator output pulses is thus mandatory.

The regenerative amplifier laser system that was used for the experiments discussed in this work delivers pulses of 80 fs duration centered around 800 nm wavelength at a repetition rate of 1 kHz. The amplified pulse energy is 1 mJ, corresponding to an amplification of  $10^6$  with respect to the oscillator pulses. This cannot be done by simply coupling the femtosecond oscillator pulse into the amplifier since the increase in pulse energy would result in an increase of the intensity beyond the damage threshold of the laser material. For that reason, the technique of ‘chirped-pulse amplification’ (CPA) [15] is employed (see Fig. 1.1). Prior to amplification, the oscillator pulses are sent through a ‘stretcher’, again geometrically delaying blue and red frequency parts of the pulse with respect to each other. Typically gratings are used for low-bandwidth amplifiers [16–18]. If the bandwidth to be amplified is sufficiently large, material dispersion (passing through long glass rods) can also be used instead. This results in a temporally varying instantaneous frequency of the pulse (see below) that is called a ‘chirp’, explaining the name of the technique. Importantly, the intensity of the longer pulse is now much lower than the one of the input. This low-intense long pulse can now safely be amplified in the Ti:sapphire crystal of the amplifier. This crystal has to be pumped by a pulsed laser, since we need to provide a high gain for the few round-trips performed by a single pulse. The repetition rate of the amplifier is thus always limited by the repetition rate of the (Q-switched) pump laser, which is a Nd:YLF laser in this case. It delivers 10 mJ pulses at a wavelength of 527 nm. After amplification, a ‘compressor’ is used, which is based on the same principle as the stretcher except for reversing the frequency-dependent path length differences generated in the stretcher. After compression we obtain a pulse train of high energy laser pulses which we can use in experiments. In Fig. 1.2a the spectra of the oscillator and amplifier output are presented. An autocorrelation measurement (see Section 1.1.5), which is used to determine the pulse duration, is shown for the amplified laser pulse (Fig. 1.2b). The amplified spectrum is shifted slightly into the red, due to the Ti:sapphire gain curve with a maximum around 800 nm. The FWHM (full width at half maximum) spectral bandwidth is 21 nm, the FWHM pulse duration extracted from the autocorrelation is 88 fs, assuming

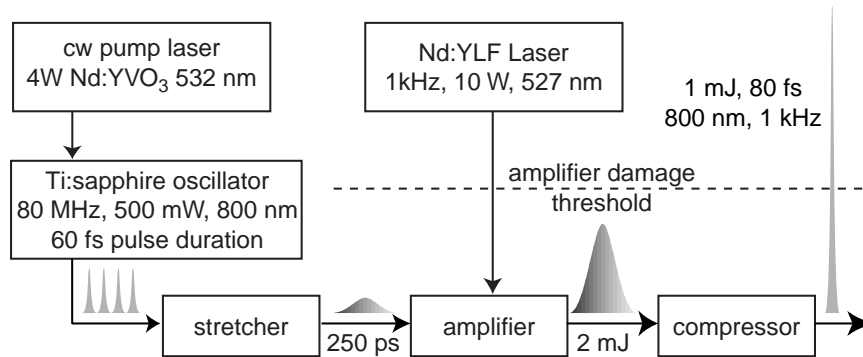


**Figure 1.1:** Schematic setup of the chirped-pulse-amplification laser system used for the experiments. A train of femtosecond laser pulses is produced in the Kerr-lens modelocked Ti:sapphire oscillator, which is pumped by a cw-laser. The pulse duration of each of these pulses is increased in the stretcher by geometrically realizing different optical path lengths for the different frequency components of the pulse. These long ‘chirped’ pulses can then be amplified at low peak intensity to avoid damaging the Ti:sapphire laser medium. After amplification, the spectral path length differences are reversed in the compressor. The pulse is thus recompressed close to its original duration and a highly intense laser pulse is now available for experiments.

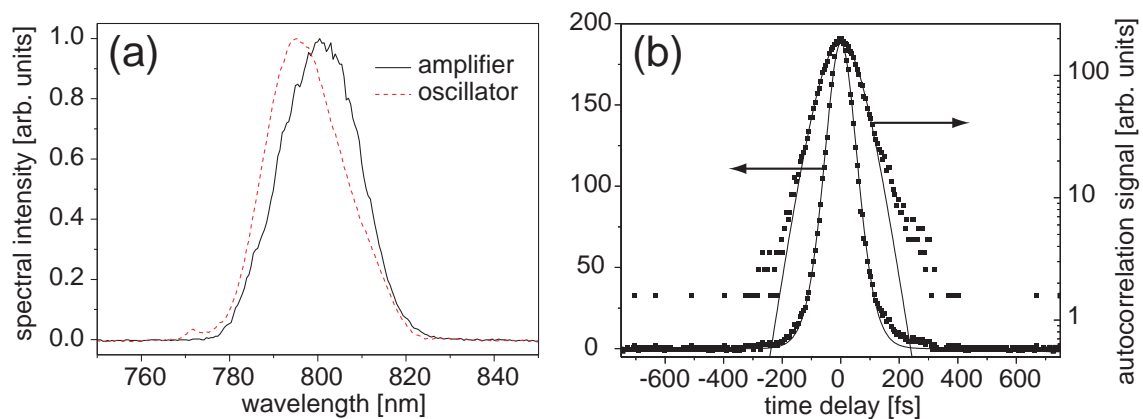


**Figure 1.2:** Spectra of oscillator (dashed line) and amplified (solid line) laser output (a) and autocorrelation measurement (b) of the amplified laser pulse (dots) along with a fit corresponding to a sech<sup>2</sup> intensity profile of the laser pulse. The spectral bandwidth is 21 nm, the autocorrelation indicates a pulse duration of 88 fs.



a  $\text{sech}^2$  intensity profile.

### 1.1.2 Mathematics of Ultrashort Laser Pulses

A suitable way of describing an ultrashort laser pulse is by its time dependent electric field  $E(t)$  at a given point in space (that is, we are not interested in propagation at the moment). We will first of all treat the electric field as a scalar quantity, which means the polarization state of the field is assumed not to change throughout the pulse. Since the electric field is a measurable quantity,  $E(t)$  is a real function. By help of the Fourier transformation, we can obtain an equivalent description of the pulse in the (angular) frequency domain (in the following, the expression ‘frequency’ will be used for ‘angular frequency’)

$$\tilde{E}(\omega) = \frac{1}{\sqrt{2\pi}} \int_{-\infty}^{\infty} E(t) e^{-i\omega t} dt \quad (1.1)$$

and recover the temporal electric field by the inverse transformation

$$E(t) = \frac{1}{\sqrt{2\pi}} \int_{-\infty}^{\infty} \tilde{E}(\omega) e^{i\omega t} d\omega. \quad (1.2)$$

The spectral distribution of the laser pulse, as experimentally measured by a spectrometer is given by

$$\tilde{I}(\omega) \propto |\tilde{E}(\omega)|^2. \quad (1.3)$$

In general,  $\tilde{E}(\omega)$  is a complex function. However due to  $E(t)$  being real, it exhibits a symmetry

$$\tilde{E}(\omega) = \tilde{E}^*(-\omega), \quad (1.4)$$

where the asterisk stands for complex conjugation. Due to this property the full information of the pulse is already contained along the positive frequency axis. We can thus define the function

$$\tilde{E}^+(\omega) = \begin{cases} \tilde{E}(\omega) & \text{if } \omega \geq 0, \\ 0 & \text{if } \omega < 0 \end{cases} \quad (1.5)$$

to fully characterize the pulse shape. We can now again use the Fourier transformation to transform back into the time domain, where we arrive at

$$E^+(t) = \frac{1}{\sqrt{2\pi}} \int_{-\infty}^{\infty} \tilde{E}^+(\omega) e^{i\omega t} d\omega. \quad (1.6)$$

The inverse transformation returns

$$\tilde{E}^+(\omega) = \frac{1}{\sqrt{2\pi}} \int_{-\infty}^{\infty} E^+(t) e^{-i\omega t} dt. \quad (1.7)$$

$E^+(t)$  is now a complex-valued function. For both functions, we can therefore write

$$E^+(t) = A(t) e^{i\phi(t)} \quad (1.8)$$

$$\tilde{E}^+(\omega) = \tilde{A}(\omega) e^{i\tilde{\phi}(\omega)}, \quad (1.9)$$

expanding the complex functions into their amplitudes and phases. The real valued temporal electric field can be reconstructed from  $E^+(t)$  as follows:

$$E(t) = 2\text{Re}(E^+(t)) \quad (1.10)$$

$$= 2A(t) \cos(\phi(t)), \quad (1.11)$$

where  $\text{Re}(z)$  denotes the real part of the complex number  $z$ . This way we can identify the temporal phase function  $\phi(t)$  in Eq. (1.8) as the quickly oscillating carrier wave under the enveloping temporal amplitude function  $2A(t)$  (see also Fig. 1.3).

The phase functions—in particular the spectral phase  $\tilde{\phi}(\omega)$ —will play a major role in this work, since we will later use spectral phase shaping to change the temporal shape of the laser pulses. We therefore analyze these phases by performing a Taylor series expansion:

$$\phi(t) = \sum_{j=0}^{\infty} \frac{a_j}{j!} t^j, \quad (1.12)$$

$$\tilde{\phi}(\omega) = \sum_{j=0}^{\infty} \frac{\tilde{a}_j}{j!} \omega^j. \quad (1.13)$$

The coefficient of zeroth order in each representation ( $a_0, \tilde{a}_0$ ) is a constant phase, which shifts the carrier wave within the fixed envelope in Eq. (1.11). This phase shift of the carrier with respect to the envelope—in the literature called ‘carrier-envelope phase’ (CEP)—is usually not important for 800 nm wavelength laser pulses longer than 10 fs, since the difference in electric fields from cycle to cycle at the maximum of the pulse is very small. For shorter and shorter pulses at the same center wavelength, the effect of the CEP becomes more pronounced (see Fig. 1.3). In particular, if highly nonlinear processes are considered that depend on the electric field  $E^n$  at high powers  $n$ , there is a significant difference in how the process evolves for different CEPs of the driving laser pulse. We will discuss these effects in more detail below (Chapter 2 on high-harmonic generation). The absolute value of the phase can be measured by various methods [19, 20]. In general, the CEP phase varies from shot to shot of the laser due to differences in group and phase velocity. Very recently, stabilizing the CEP phase of the laser oscillator [21] and amplifier output [22] has been achieved. By inserting Eqs. (1.12) and (1.13) into the expression for  $E^+(t)$  in Eq. (1.8) and  $\tilde{E}^+(\omega)$  in Eq. (1.9), respectively and performing a Fourier transformation on each, we notice that the first order coefficients  $\tilde{a}_1$  in the spectral phase or  $a_1$  in the temporal phase correspond to shifts in time or frequency, respectively. In particular, we can use this property to shift the spectral distribution (spectrum) of  $\tilde{E}^+(\omega)$  from its central frequency  $\omega_0$  to be centered around frequency  $\omega = 0$ . We can thus define the residual temporal phase

$$\varphi(t) = \Phi(t) - \omega_0 t. \quad (1.14)$$

Using this expression, the time-dependent instantaneous frequency of the laser pulse can be defined as

$$\omega(t) = \frac{d\Phi(t)}{dt} = \omega_0 + \frac{d\varphi(t)}{dt}, \quad (1.15)$$

where we can again separate off the quickly oscillating component of the central frequency  $\omega_0$  and only look at the frequency difference  $\delta\omega(t) = d\varphi(t)/dt$ . If the instantaneous frequency does not vary much throughout the pulse compared to its spectral width

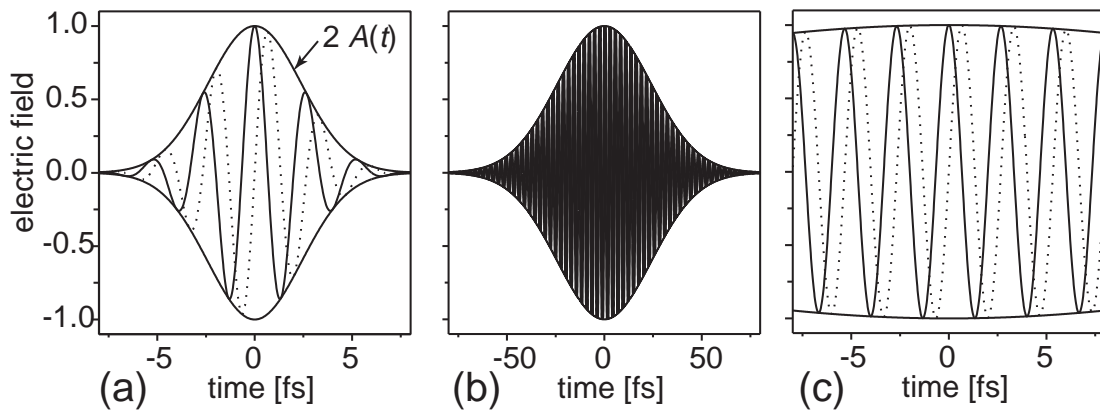


**Figure 1.3:** Ultrashort laser pulses with envelope function and carrier wave. Shown is a 4 fs pulse (left) and a 40 fs pulse (center and right). Two different carrier phase (absolute phase) situations are shown, a so-called cosine pulse—where the peak of the envelope function is reached by the carrier wave—and a sine pulse, the phase of which is shifted by  $\pi/2$ . Whereas this phase shift causes a major change in the maximum electric field attained in the 4 fs case, the difference in the 40 fs case is negligible. For pulses longer than 10 fs, the absolute phase is in general not important.

in frequency space, the pulse is close to its transform or bandwidth limit, which defines the shortest pulse achievable with a given spectrum. However, the time-dependent frequency of the laser pulse can, for example, monotonously increase—the pulse sets in with its carrier at red frequencies and sweeps into the blue—which we call an up-chirped pulse (chirp from its analog in acoustics). This pulse is now longer than the transform limited pulse. Analogously, if the frequency decreases monotonously in time, we call the pulse down-chirped. Chirp-dependence is very often used in control experiments [23–28], since it can be easily introduced and varied in practice. For example, the chirp of an initially short laser pulse can be controlled by delaying its high-frequency components (blue) with respect to the low-frequency (red) ones. This can be done by dispersive media, where optical path lengths vary due to a frequency dependent index of refraction (see Section 1.1.3 on pulse dispersion). Another way to vary the chirp is to geometrically induce a path-length difference between red and blue frequencies by spatial separation of the spectral components (e.g. prism or grating) and having them run along differently long ways with path lengths increasing or decreasing from blue to red. By introducing arbitrary path lengths for the spectral components, we can shape the laser pulse in a much more comprehensive manner, which shall be discussed in Section 1.1.4 below.

In contrast to the zeroth and first order coefficients in Eqs. (1.12) and (1.13), which do not change the amplitudes  $\tilde{A}(\omega)$  and  $A(t)$ , the higher order coefficients cause modifications of these functions. For example, if the instantaneous frequency  $\omega(t)$  of a chirped laser pulse increases linearly with time, the temporal phase—the derivative of which gives the instantaneous frequency defined in Eq. (1.15)—is quadratic versus time (see Fig. 1.4). It can be shown that also the spectral phase function  $\tilde{\phi}(\omega)$  in this case (after performing the Fourier transformation) depends quadratically on  $\omega$ . We can introduce another helpful relation, which is analogous to the definition of the instantaneous frequency in the time

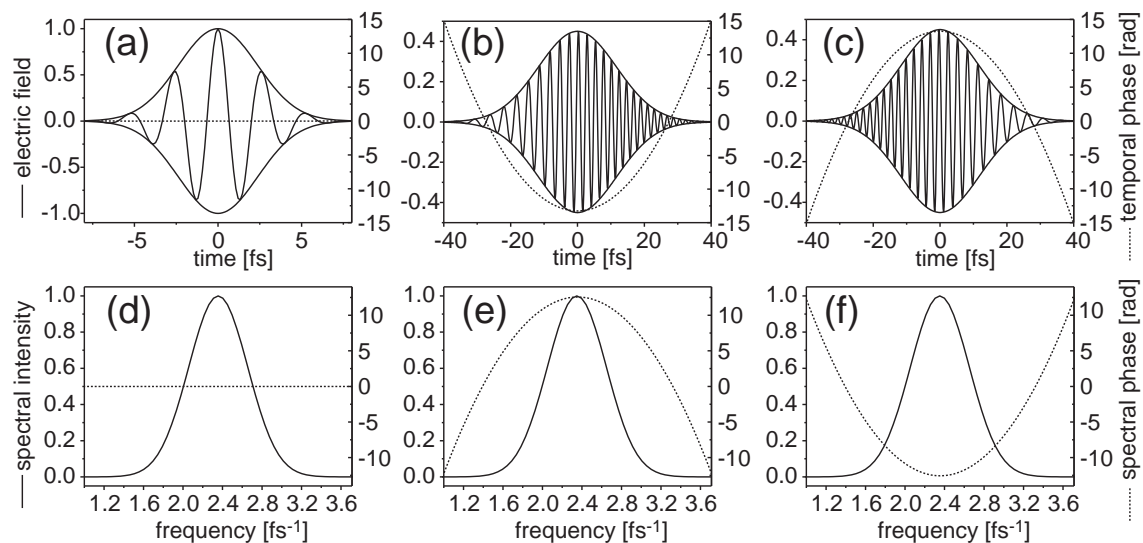


**Figure 1.4:** Chirped laser pulses. Shown is the temporal pulse shape (upper graphs) and the spectra (lower graphs). The amplitudes  $A(t)$  and  $\tilde{A}(\omega)$  are shown as solid lines whereas the phase functions  $\Phi(t)$  and  $\tilde{\Phi}(\omega)$  are shown as dotted lines. In (a) the 4 fs FWHM gaussian cosine pulse of Fig. 1.3 is again shown. Since the pulse is bandwidth limited, the temporal (a) and spectral (d) phases are flat. The corresponding spectrum is a gaussian distribution (d)-(f). A quadratic phase in either domain creates a chirped pulse. The sign of the phase determines whether the frequency is (b) temporally increasing (up-chirp) or (c) decreasing (down-chirp).

domain. The first derivative of the spectral phase

$$\frac{d\tilde{\phi}(\omega)}{d\omega} = \tau_0 + \delta\tau(\omega) \quad (1.16)$$

can be interpreted as a temporal shift (as was stated above). If the dependence of the phase on frequency is quadratic,  $\tau(\omega)$  is linearly increasing with  $\omega$ . Different frequency components thus arrive at different times, giving rise to a longer and chirped pulse. To obtain the shortest pulse, again, all frequencies should arrive at the same time at the same phase, implying a close to flat spectral phase function  $\tilde{\phi}(\omega)$ .

The intensity of the ultrashort laser pulses (measured in  $\text{W}/\text{cm}^2$ ) can be calculated by averaging over one optical cycle of the laser field

$$I(t) = \epsilon_0 cn \frac{1}{T} \int_{t-T/2}^{t+T/2} E^2(t') dt' \quad (1.17)$$

$$\cong 2\epsilon_0 cn A^2(t), \quad (1.18)$$

in which  $\epsilon_0$ ,  $c$  and  $n$  represent the dielectric constant, the vacuum speed of light, and the refractive index of the material, respectively. The intensity is only given correctly by Eq. (1.18) if the temporal variation of the amplitude  $A(t)$  is slow compared to the instantaneous carrier frequency  $\omega(t)$

$$\left| \frac{d}{dt} A(t) \right| \ll |\omega(t) A(t)|, \quad (1.19)$$

which is often referred to as slowly-varying-envelope approximation [9]. We can also define the spectral intensity (measured with a spectrometer) in an analogous fashion

$$\tilde{I}(\omega) = 2\varepsilon_0 c n \tilde{A}^2(\omega). \quad (1.20)$$

By integration over all time or frequency, respectively, we arrive at the fluence of the laser pulses, which is typically given in  $\text{J}/\text{cm}^2$

$$F = \int_{-\infty}^{\infty} I(t) dt \quad (1.21)$$

$$= \int_{-\infty}^{\infty} \tilde{I}(\omega) d\omega. \quad (1.22)$$

The identity can be understood by applying Parseval's theorem. The instantaneous total power of the laser pulse  $P$  (measured in W or J/s) on the other hand is given by integrating the temporal intensity over space instead of time:

$$P(t) = \int_{-\infty}^{\infty} dx \int_{-\infty}^{\infty} dy I(t) \quad (1.23)$$

where the  $x$ - and  $y$ -axis are perpendicular to the propagation direction  $z$  of the laser. The pulse energy (measured in J) is obtained if we integrate the intensity over spatial and temporal coordinates, i.e.

$$W = \int_{-\infty}^{\infty} dx \int_{-\infty}^{\infty} dy \int_{-\infty}^{\infty} dt I(t) \quad (1.24)$$

$$= \int_{-\infty}^{\infty} dx \int_{-\infty}^{\infty} dy F \quad (1.25)$$

$$= \int_{-\infty}^{\infty} dt P(t) \quad (1.26)$$

The duration  $\tau_p$  or spectral width  $\Delta\omega_p$  of ultrashort pulses is routinely derived from the temporal or spectral intensity, respectively. It is called the 'full width at half maximum' (FWHM) measure. It is defined as the full temporal or spectral extent of the distribution which only contains the maximum value of  $I(t)$  or  $\tilde{I}(\omega)$  and its neighborhood until it reaches half of the maximum value on either side. Due to the inverse scaling property of the Fourier transformation— $T = 2\pi/\omega$ , where  $T$  is the temporal period associated with the frequency  $\omega$ —for a given spectral intensity shape we can define the constant

$$\tau_p \Delta\omega_p \geq c_B, \quad (1.27)$$

in which  $c_B$  only depends on the spectral shape and is of the order of 1. For example, for a gaussian pulse (both spectral and temporal amplitude are gaussian),  $c_B = 4 \ln 2$ . The equality is obtained for the bandwidth-limited pulse, i.e. the shortest pulse that can be created with a given spectral width  $\Delta\omega_p$ . To arrive at the bandwidth-limit for a given spectral intensity shape—what is usually desirable to obtain the shortest possible pulse in order to get highest temporal resolution in the experiment—we need to optimize the spectral phase. In general, a flat spectral phase function, i.e. containing no Taylor coefficients higher than first order of Eq. (1.13), is required. This is also why spectral phase shaping discussed in Section 1.1.4 provides a powerful tool to shorten the duration of laser pulses [29, 30], namely by compensating any higher order spectral phase contributions to arrive at the bandwidth limit.

### 1.1.3 Laser Pulse Dispersion

Let us now examine how propagation of the laser pulse in a nonabsorbing dispersive material affects its temporal and spectral properties. The quantity of interest will thus be the frequency dependent refractive index of the material  $n(\omega)$ . A plane-wave pulse propagating along the  $z$ -axis in the medium can be written as:

$$\tilde{E}^+(\omega, z) = \tilde{A}(\omega, z) e^{i\tilde{\phi}(\omega)} e^{-ik(\omega)z} \quad (1.28)$$

where

$$k(\omega) = n(\omega)k_{\text{vac}} \quad (1.29)$$

$$= n(\omega) \frac{\omega}{c}, \quad (1.30)$$

in which  $c$  is the vacuum speed of light and  $k$  represents the wavevector. By inserting into Eq. (1.28),

$$\tilde{E}^+(\omega, z) = \tilde{A}(\omega, z) e^{i(\tilde{\phi}(\omega) - n(\omega)\frac{\omega}{c}z)}, \quad (1.31)$$

we already notice that any possible modification to the pulse brought about by its propagation in the transparent medium will only be an addition of  $\Delta\tilde{\phi} = n(\omega)\omega/c$  to the spectral phase function. If we again use the Taylor series decomposition to analyze this additional phase

$$\Delta\tilde{\phi}(\omega) = \sum_{j=0}^{\infty} \frac{\tilde{b}_j}{j!} \omega^j \quad (1.32)$$

with

$$\tilde{b}_j = \frac{d^j}{d\omega^j} k(\omega) = \frac{d^j}{d\omega^j} \Delta\tilde{\phi}(\omega), \quad (1.33)$$

the result for the coefficients  $\tilde{b}_j$  up to third order  $j = 3$  reads

$$\tilde{b}_0 = -\frac{z}{c} \omega n(\omega) \quad (1.34)$$

$$\tilde{b}_1 = -\frac{z}{c} \left( \omega \frac{d}{d\omega} n(\omega) + n(\omega) \right) \quad (1.35)$$

$$\tilde{b}_2 = -\frac{z}{c} \left( \omega \frac{d^2}{d\omega^2} n(\omega) + 2 \frac{d^2}{d\omega^2} n(\omega) \right) \quad (1.36)$$

$$\tilde{b}_3 = -\frac{z}{c} \left( \omega \frac{d^3}{d\omega^3} n(\omega) + 3 \frac{d^2}{d\omega^2} n(\omega) \right) \quad (1.37)$$

The zeroth order  $\tilde{b}_0$  coefficient is the change in absolute phase. The coefficient of first order  $\tilde{b}_1$  denotes the additional delay of the pulse caused by the time  $\Delta t$  it took to travel the distance  $z$  in the medium. This can be readily understood by recalling the definition of the group velocity

$$v_g(\omega) = \left. \frac{d\omega(k)}{dk} \right|_{k=k(\omega)} = \left( \frac{dk(\omega)}{d\omega} \right)^{-1} \quad (1.38)$$

We can thus write

$$b_1 = -\frac{z}{v_g(\omega)} = -\Delta t \quad (1.39)$$

The amplitude pulse shape in time is thus not affected by those two coefficients. However, as mentioned above, the higher orders of  $b_i$  introduce changes in the temporal amplitude  $A(t)$ . In the literature,  $\tilde{b}_2$  is often referred to as ‘group-delay dispersion (GDD)’ as it denotes the first derivative of the (possibly) frequency dependent delay  $-\Delta t$ . The higher order coefficients are simply called ‘third-order dispersion (TOD)’, ‘fourth-order dispersion (FOD)’ and so on.

### 1.1.4 Laser Pulse Shaping

As was discussed in the previous Sections, we can mathematically represent laser pulses with differently shaped temporal or spectral intensity or phase profiles. In fact, these shaped light fields can be a very valuable tool in the study or control of physical systems (see Section 5.1). This is because the nonlinear response functions (defined in Section 1.2 in Eq. (1.59)) of some system under study depend on its temporal evolution. This in turn means that we can learn about the system by analyzing its response to shaped light fields.

It is experimentally impossible to directly tune the wavelength of a laser on a femtosecond time scale. Even worse, there is no electronic or mechanical shutter available that could at least generate a shaped intensity profile that varies on the order of femtoseconds. However, we know from the equivalence of the temporal and spectral representation of the laser pulse (Eqs. (1.6) and (1.7)) that pulse shaping in the temporal domain can be done by shaping the spectral properties of the pulse. Thus, all we have to do is to modify the spectral amplitude  $\tilde{A}(\omega)$  and phase  $\tilde{\phi}(\omega)$  profiles. In particular, since we would often like to create pulses with complex temporal phase and intensity profiles, we have to ensure that higher order phase coefficients  $\tilde{a}_j$  can be produced and varied.

The question is now: How can we experimentally realize a pulse shaping apparatus? In the 1970s, the technical approach was initially introduced for picosecond pulses [31, 32]. Later, in the 80s, it has been transferred to the femtosecond regime [33, 34]. The experimental setup is easily described. A grating or a prism is used to spatially separate the different frequency components of an optical laser pulse. The spatially dispersed spectrum can then be manipulated by using spatial light modulators (SLMs). Those devices are able to modify the optical path length, attenuation and/or polarization state of light transmitted through or reflected off different points of their active area (Fig. 1.5). By recombining the separate spectral components, a modified laser pulse is created.

Basically, SLMs act as spatial filters. The easiest conceivable SLM is a fixed mask e.g. an array of apertures that transmit light in some defined regions and absorb light at other regions. Today, more sophisticated devices are available, where the optical properties of the active area can be controlled electronically. This allows the experimenter to use a computer to control the device and thus the pulse shape.

In mathematical terms, the pulse shaper creates a shaped output pulse  $\tilde{E}_{out}(\omega)$  from any

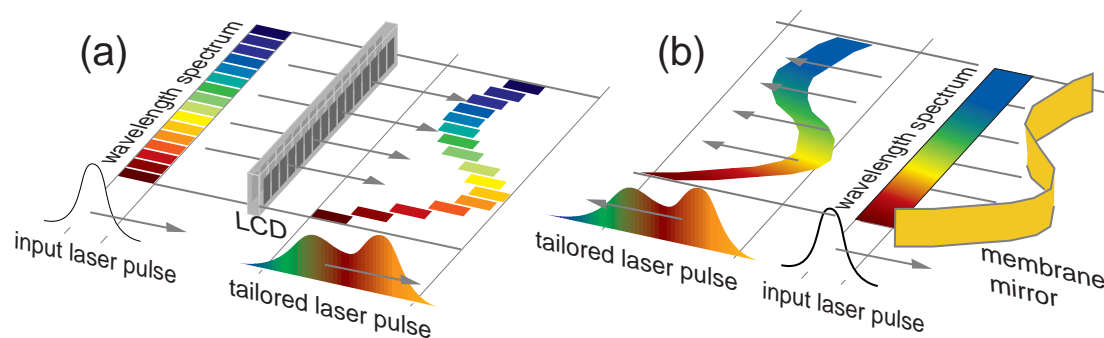


**Figure 1.5:** Working principle of a spatial light modulator for phase-only pulse shaping. Due to a modification of the active area of the device, different optical path lengths  $l(\omega)$  are created for different frequencies. The difference in path length carries over to additional phases  $\tilde{\phi}_S(\omega) = l(\omega)\omega/c$ . This additional phase is added to the spectral phase  $\tilde{\Phi}(\omega)$  of the laser pulse, thus modifying its shape.

given input pulse  $\tilde{E}_{\text{in}}(\omega)$  that enters the device by a transformation  $\tilde{S}(\omega)$ ,

$$\tilde{E}_{\text{out}}(\omega) = \tilde{S}(\omega)\tilde{E}_{\text{in}}(\omega), \quad (1.40)$$

$$\tilde{S}(\omega) = \tilde{A}_S(\omega)e^{i\tilde{\phi}_S(\omega)}. \quad (1.41)$$

If  $\tilde{A}_S(\omega) = 1$  for all  $\omega$  and only  $\tilde{\phi}_S(\omega)$  is changed, this is referred to as ‘phase-only shaping’ in the literature. Since also the polarization state can be altered by certain SLMs, we can define a  $2 \times 2$  transformation matrix  $\tilde{S}_{jl}(\omega)$  to change also the spectral polarization properties of the incoming pulse:

$$\tilde{E}_{\text{out},j}(\omega) = \tilde{S}_{jl}(\omega)\tilde{E}_{\text{in},l}(\omega), \quad (1.42)$$

$$\tilde{S}(\omega) = \begin{pmatrix} \tilde{A}_{Sxx}(\omega)e^{i\tilde{\phi}_{Sxx}(\omega)} & \tilde{A}_{Sxy}(\omega)e^{i\tilde{\phi}_{Sxy}(\omega)} \\ \tilde{A}_{Syx}(\omega)e^{i\tilde{\phi}_{Syx}(\omega)} & \tilde{A}_{Syy}(\omega)e^{i\tilde{\phi}_{Syy}(\omega)} \end{pmatrix}. \quad (1.43)$$

In practice, polarization shaping is done by manipulating the spectral phase for two perpendicular linear polarization components [35–38]. However, since any pulse-shaping apparatus consists of different optical elements like for example gratings, prisms, mirrors or lenses, we have to take into account their additional spectral phase and absorption. Polarization shaping requires particular care of operation, since any optical element not used in perfect  $p$ - or  $s$ -reflection geometry modifies the polarization state of the light. By use of Jones matrices these effects can be taken into account and the matrix  $\tilde{S}_{jl}(\omega)$  and its dependence on the SLM settings can be determined [36].

The most commonly used electronically addressable SLMs today are liquid-crystal arrays/displays (LCDs) [39], deformable mirrors (DM) [40] and acousto-optic modulators (AOMs) [41].

In Fig. 1.6 the optical setup of an LCD-based pulse shaper is shown in more detail. The laser pulse is spectrally separated by a grating, a cylindrical lens is used to enhance the spectral resolution in the Fourier-plane, where the LCD is placed. It modifies the spectral



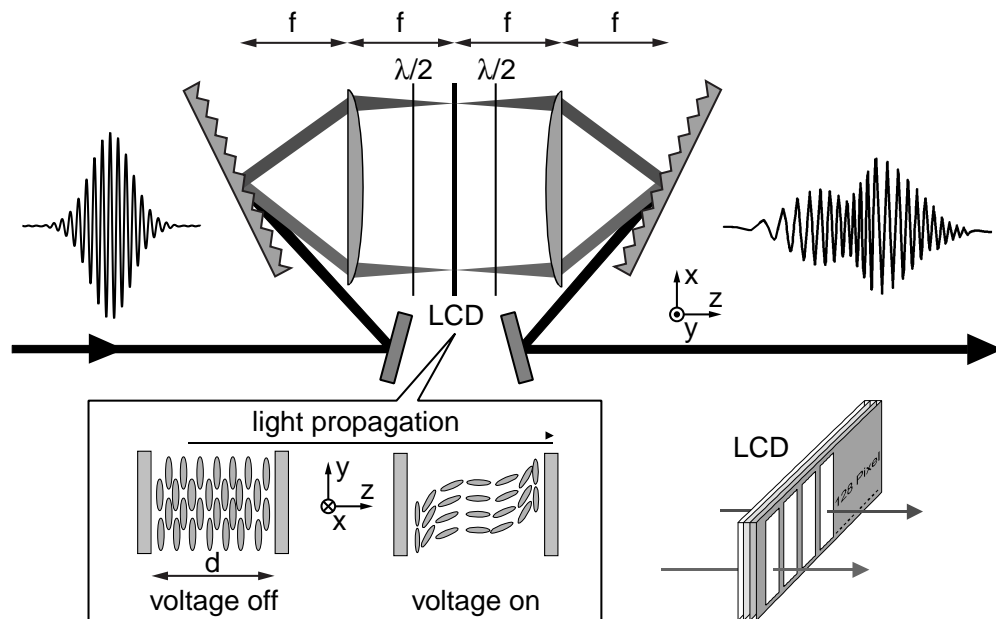


**Figure 1.6:** Liquid crystal display (LCD) used for pulse shaping. The laser pulse is spectrally dispersed by a grating. The LCD is placed into the common Fourier plane of two cylindrical lenses in order to achieve spectral resolution. The setup is symmetric with respect to the Fourier plane, thus constituting a zero-dispersion compressor, introducing only the additional spectral phase produced by the LCD. The optical path length is controlled by the refractive index of the liquid crystal material that depends on the orientation of the polarizable molecules. Applying different electric fields to the 128 pixels allows to generate well-defined modifications to the spectral phase, thus shaping the temporal amplitude profile of the laser pulses.

phase by introducing defined additional phase advances or retardations to the different spectral components (see again Fig. 1.5) passing through different pixels of the device. After passage through the LCD, the laser pulse spectrum is recombined using a cylindrical lens and grating that are identical to those on the input side (symmetric setup).

The variable additional spectral phase contributions introduced by the LCD result from different orientations of the liquid-crystal molecules in the different pixels, which change the refractive index of the material. The orientation is controlled by applying an external AC electric field. Since liquid-crystal molecules align along a particular direction parallel to the surface in their inactive (no external electric field applied) position, LCDs allow to selectively control a given polarization state of the laser pulse. If two separately addressable LCDs are used in which the molecules are aligned orthogonal to each other, the polarization state of each spectral component of the laser pulse can be controlled. This leads to temporally shaped pulses where now the polarization state of the light can be manipulated on a femtosecond time scale [35, 36]. Applications of variable polarization-shaped laser pulses are the suppression of the nonresonant background in coherent anti-Stokes Raman spectroscopy (CARS) [42] and optimal control of molecular multiphoton ionization via parallel and perpendicular molecular transitions [43].

On the other hand, if we like to conserve linear polarization by inserting a polarization filter, we are now able to control the spectral amplitude. A robust layout of an LCD-based pulse shaper has recently been published [44].

Shaping laser pulses in both time and space is possible by the application of LCDs exhibiting two-dimensional pixel masks [45]. In this case, not only the electric field in time  $E(t)$  but really  $E(t, \vec{r})$  can be shaped and used for applications [46].

Another technical realization of a programmable SLM is the deformable membrane mirror. In contrast to the LCD, the mirror works in reflection, the phase advances and retardations being introduced by a curved mirror surface (Fig. 1.5). The curvature is often introduced electrostatically. The membrane is coated with a reflective, metallic conducting material that is electrically grounded. A number of  $n$  actuator electrodes placed behind the membrane provide  $n$  degrees of freedom to control the surface shape of the device by the same number of control voltages. The metallic deformable mirror has no amplitude or polarization shaping capability, since the reflection is not dependent on polarization. As the active area of the mirror is smooth and not broken into pixels—which cause phase jumps at the boundaries and interpixel gaps—the produced temporal pulse shapes do not suffer from discretization artifacts. Another advantage is its low cost (factor 5 compared to LCD) and small response time, which is the time it takes the device to respond to a change in control parameters (voltages). Furthermore, deformable mirrors are capable of shaping deep ultraviolet laser pulses [47].

The experimental implementation of the deformable mirror for pulse shaping applications is shown in Fig. 1.7. Here we perform the spectral separation with a prism pair, the deformable mirror is mounted such that it retroreflects the spectrally separated pulse, directing it slightly upward. The shaped laser pulse will become spectrally collimated at the output, where it can be picked up by a mirror, due to the slight upward tilt of the deformable mirror. Before the laser pulse enters the first prism, it passes a lens with a long focal length to create a focus of the laser pulse at the surface of the deformable mirror. The single-frequency beam size in the direction of spectral separation must be small compared with the spectral extend on the mirror in order to ensure sufficient spectral resolution of the pulse shaper. In addition, focusing onto the mirror surface was necessary to allow coupling of the shaped pulses into a capillary, which was used in the experiments described below. A focal spot on the mirror surface will always be imaged into a second one by a suitable lens system (for paraxial rays). Therefore, the slight deformation of the mirror surface—which occurs not only in the direction of spectral dispersion but also the orthogonal one—does not adversely affect the coupling into the capillary.

The technical specifications of the pulse shaping apparatus are summarized in Table 1.1. For the experiments on pulse shaping discussed in Part III, we employed the deformable mirror setup described here. Laser pulse compression with a deformable mirror pulse shaper (Section 5.2) has been performed with the herein described setup [48], and employing a grating setup in the past [40]. Pulse compression by implementation of a deformable mirror directly into the stretcher of a CPA laser system has also been accomplished earlier [49].

The third class of systems—acousto-optic modulators (AOMs)—are based on the interaction of light with lattice vibrations in crystals excited by high-frequency sound waves.

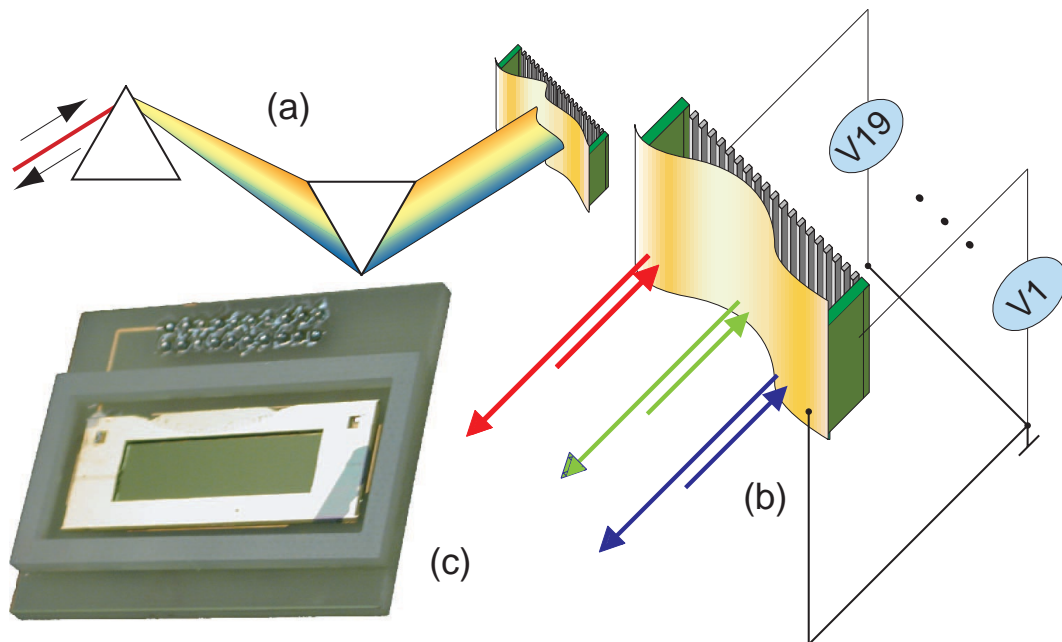


**Figure 1.7:** Deformable membrane mirror used for pulse shaping. The laser pulse is spectrally dispersed by a pair of prisms in a prism-compressor configuration (a). The collimated spectral distribution is reflected off the mirror membrane and travels back along its initial incoming path. In order to separate the outgoing laser pulse from the incoming, the deformable mirror is slightly tilted such that the output pulse is vertically displaced with respect to the input pulse. The mirror surface shape is controlled by 19 electrodes, to which voltages are applied (b). The spectral phase function is modified by different geometrical path lengths experienced by different frequencies. (c) photographic picture of the deformable membrane mirror.

parameter	value
Number of actuators	19
Maximal deflection	$7 \mu\text{m}$
Response time	2 ms
membrane height	8 mm
membrane length	30 mm
voltage range	0-300 V
focal spot width	1.2 mm
membrane coating	Gold
prism material	fused silica
prism separation	1.3 m

**Table 1.1:** Technical specifications of the deformable mirror pulse shaper

Acoustic signals coupled into a transparent crystal create periodic compressed and expanded regions, which move through the crystal at the speed of sound. A transient spatial change of refractive index of the material is thus induced due to its dependence on material density. In particular, due to the plane wave nature of the sound waves, the refractive index is periodically modulated with a period of  $\lambda_s$ , the wavelength of the sound wave. For the case of a constant frequency sound wave, the incident light can scatter off this periodically modulated index of refraction, which is analogous to Bragg scattering of x-rays off the lattice planes in a single crystal. Applying amplitude- and phase-shaped sound waves from an electrical signal generator that are then coupled into the active medium with a piezo-electric transducer, allows to create different diffraction efficiencies at different points in space. From those points the spectrally dispersed light can scatter into the Bragg angle. The phase of the scattered light is controlled by the phase of the acoustic carrier wave. Therefore, a single AOM is able to do both, spectral amplitude and phase shaping at the same time. However, the principal drawback of this device is its lower diffraction efficiency for the Bragg-scattered shaped laser pulse ( $\approx 50\%$ ) as compared to LCDs and DMs, which have efficiencies close to 100%.

## 1.1.5 Laser Pulse Measurement

To measure and characterize a short phenomenon in time, we always need a shorter one to which we can refer. For the special case of measuring an ultrashort laser pulse, we need to measure the electric field at time steps which are smaller than the duration of the pulse. In the macroscopic world we can imagine a 100 m sprint race. Since the duration of the race in this case is on the order of ten seconds, in order to evaluate a sprinters performance (to measure it), we need a stop watch resolving seconds, tenths or better hundredths of seconds. A watch that merely counts minutes would not be sufficient to tell the difference between a very fast athlete and a very slow one. Analogously, coming back to ultrashort laser pulses, in order to tell the difference between very short and longer laser pulses we need to provide a temporal resolution which is on the order of or smaller than the typical pulse duration. Since the laser pulses are in fact the shortest events available, we have to measure the pulses by using the pulses themselves as a clock. This technique is often described as self-referencing. At the moment, there are three main methods available, which are briefly lined out.

### 1.1.5.1 Autocorrelation and Crosscorrelation Techniques

The easiest way to measure the duration of laser pulses is to employ a copy of the pulse to scan the pulse itself. In practice, this is accomplished by setting up a Michelson- or a Mach-Zehnder-type interferometer, splitting the laser pulse into two replica by a beam splitter, having them travel spatially separated paths and to recombine them again on a beam splitter (Fig. 1.8). One of the paths can be varied in length which can be used to delay or advance one pulse with respect to the other. In mathematical terms, the recombined electric field  $E_{\text{res}}(t, \tau)$  can be written as

$$E_{\text{res}}(t, \tau) = E(t) + E(t - \tau) \quad (1.44)$$

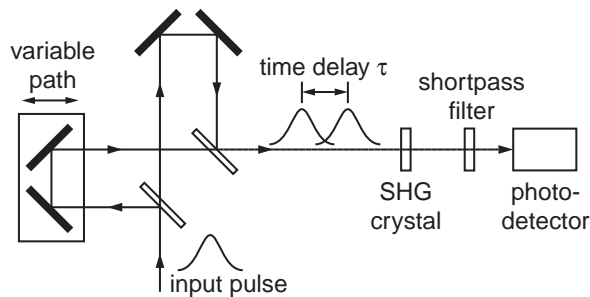


**Figure 1.8:** Autocorrelation setup used to determine the pulse duration. An interferometer is used to generate two identical replica of the laser pulse. Second-harmonic generation in a crystal is used to carry out the correlation of the pulse with a delayed replica. The dependence of the second-harmonic light (detected with a photodiode) on the delay between the two pulses provides information about the pulse shape and duration.

where  $E(t)$  is the time dependent field of the laser pulse and  $\tau$  is the time delay introduced by the length difference of the two optical paths. To perform an auto-correlation we need to generate a term containing the product  $E(t) \times E(t - \tau)$  which can be done by raising  $E_{\text{res}}$  to a power higher than one. This can easily be obtained by employing a second order nonlinear process, which produces a signal  $\propto E(t)^2$  when an incoming field  $E(t)$  is applied (see Section 1.2). The produced electric field then reads

$$E_2(t, \tau) \propto E_{\text{res}}(t, \tau)^2 = E(t)^2 + E(t - \tau)^2 + 2E(t)E(t - \tau). \quad (1.45)$$

This light signal can be detected with a photodiode, which produces an average photocurrent  $J(\tau)$  proportional to the integral over the temporal intensity:

$$J(\tau) \propto \int_{-\infty}^{\infty} I(t, \tau) \propto \int_{-\infty}^{\infty} |E_2(t, \tau)|^2 dt = \int_{-\infty}^{\infty} E_2(t, \tau) E_2^*(t, \tau) dt. \quad (1.46)$$

Inserting Eq. (1.45) yields the so-called ‘interferometric autocorrelation’ (see Fig. 1.9). We now consider a slightly modified setup where we do not recombine the two interferometer beams on the second beamsplitter but rather make them overlap in the nonlinear optical crystal at some angle (non-collinear geometry in contrast to the just described collinear geometry). By virtue of momentum conservation in nonlinear frequency mixing discussed in more detail in Section 1.2, second-harmonic light stemming from the interaction of two photons coming in at different angles will leave the interaction region at an angle half-way in between the angles of the original propagation directions. This modified setup helps us to remove the contribution of the second-harmonic signal produced by each of the pulse replica themselves, which does of course not depend on the time delay  $\tau$  and thus contains no information about the duration or shape of the pulse. We now only pick up and analyze the signal that leaves the crystal at the half-angle between the two outgoing pulses. The electric field of this signal can now be written as

$$E_{2,nc}(t, \tau) \propto 2E(t)E(t - \tau) \quad (1.47)$$

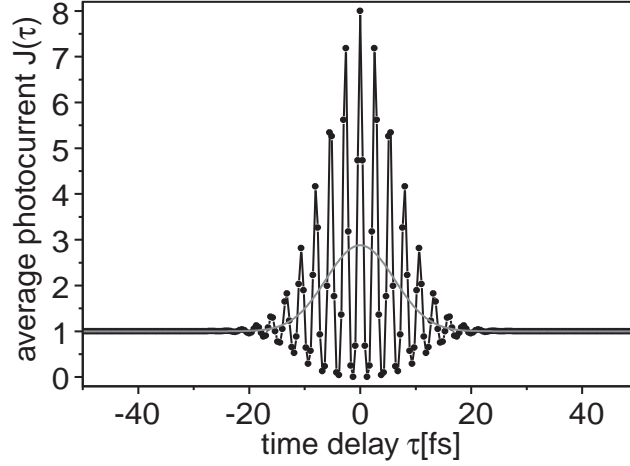


**Figure 1.9:** Autocorrelation signal for a 10 fs FWHM bandwidth-limited laser pulse simulated with [50]. The dots are samples of the interferometric autocorrelation, where the straight connecting lines are a guide to the eye. The oscillation period is about the optical cycle duration of the pulse. Averaging over the oscillatory signal results in the intensity autocorrelation, shown as a gray line.

i.e. the third summand of Eq. (1.45). It is the only one that contains both pulse replica. The experimental photocurrent, depending on  $\tau$  is (compare Eq. (1.46))

$$J_{\text{nc}}(\tau) \propto \int_{-\infty}^{+\infty} E_{2,\text{nc}}(t)E_{2,\text{nc}}(t-\tau)E_{2,\text{nc}}^*(t)E_{2,\text{nc}}^*(t-\tau)dt \quad (1.48)$$

$$\propto \int_{-\infty}^{+\infty} I(t)I(t-\tau)dt \quad (1.49)$$

The photocurrent thus depends on the correlation of the intensities of the two pulse replica. For that reason, this measurement technique is known as ‘intensity autocorrelation’. It is often also referred to as offset- or background-free autocorrelation. It can be shown that the interferometric autocorrelation signal (Eq. 1.45 used in Eq. 1.46) reproduces the intensity autocorrelation if averaging over the temporal delay is carried out.

A problem associated with the autocorrelation technique is the fact that the signal depends on the square of the pulse’s intensity. Therefore, it is hard to measure low-intensity laser pulses by autocorrelation. In the case of low light intensity, we can use a strong reference laser pulse and use it to temporally scan over the low intensity one again by second order frequency mixing, which we now call sum-frequency generation instead of second-harmonic generation. This is because the center frequency of the strong laser pulse does not necessarily have to be the same as the one of the weak pulse. We can however still use the setup in the non-collinear geometry, enabling us to perform background-free detection. The first beam splitter in the interferometer is not used since now we need two different laser pulses. The photocurrent detected in this case now reads

$$J_{\text{nc}}(\tau) \propto \int_{-\infty}^{+\infty} I(t)I_s(t-\tau)dt, \quad (1.50)$$

where  $I_s$  denotes the temporal intensity of the strong reference pulse. In order to extract information about the weak laser pulse from the variation of the temporal delay between

the two pulses, we need to have some knowledge about the strong laser pulse. This pulse needs to be intense enough such that we can perform a characterization measurement (e.g. autocorrelation, ...) on it.

However, both autocorrelation and crosscorrelation methods introduced so far do not allow for the retrieval of the complex functions  $E(t)$  or  $\tilde{E}(\omega)$ . Not even the temporal intensity  $I(t)$  can be extracted. We only get some information about the temporal localization of energy. The FWHM pulse duration can only be determined if we have knowledge about the temporal pulse shape. For a gaussian laser pulse, the ratio between the FWHM  $\tau_{AC}$  of the autocorrelation signal  $J(\tau)$  and the FWHM  $\tau_p$  of  $I(t)$  is

$$\frac{\tau_{AC}}{\tau_p} = \sqrt{2}. \quad (1.51)$$

This ratio however depends on the temporal laser pulse shape [9] and has therefore to be used with care.

We will now discuss two further techniques, which are capable of retrieving the complete information about the laser pulse, i.e. to find the spectral amplitude  $\tilde{A}(\omega)$  and phase  $\tilde{\phi}(\omega)$ . Since we can readily use a spectrometer to measure the spectral amplitude, the key to the pulse shape is only the retrieval of the spectral phase. Today, two methods have found widespread use, frequency-resolved optical gating (FROG) [51] and spectral-phase interferometry for direct electric-field reconstruction (SPIDER) [52].

### 1.1.5.2 FROG: Frequency-Resolved Optical Gating

The working principle of FROG [51, 53–55] is an extension of the intensity autocorrelation technique. When we perform an intensity-autocorrelation or crosscorrelation measurement with a photodiode, the spectral information of the up-converted (second harmonic or sum frequency) signal is lost. If we now replace the photodiode by a spectrometer (Fig. 1.10), we can resolve the spectrum of the second harmonic light produced—hence the name ‘frequency resolved’, while optical gating refers to the two identical pulses used in autocorrelation, where one pulse provides an optical ‘gate’ for the other. This can be done for any time delay  $\tau$ , which leaves us with a two-dimensional array of data (spectrum versus  $\tau$ ), which is called the FROG trace (Fig. 1.11). The FROG trace is thus given in mathematical terms by

$$I_{\text{FROG}}(\tau, \omega) = \left| \int_{-\infty}^{+\infty} E_{2,\text{nc}}(t, \tau) e^{-i\omega t} dt \right|^2, \quad (1.52)$$

i.e. the squared modulus of the Fourier transform of Eq. (1.47). We now perform an iterative search procedure, where we start with a first guess of the electric field  $E_0^+(t) = A_0(t)e^{i\phi_0(t)}$ . The resulting FROG trace is calculated from the formula above and compared to the experimental measurement data. Successive iteration steps of the temporal electric field  $E_j^+(t)$  are performed unless the mean-squared error between reconstructed and experimental FROG trace is minimized. This procedure finally leads to a good agreement between reconstructed and experimental result at iteration step  $n$ . The measured electric field is then given by  $E_n^+(t)$ .

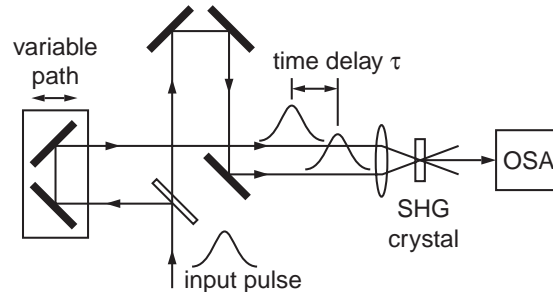


**Figure 1.10:** FROG setup used for the full characterization of laser pulse shapes. A spectrometer replaces the photodiode in an intensity autocorrelation setup. The measurement produces a two-dimensional array of data (the FROG trace) from which we can reconstruct the spectral amplitude and phase by an iterative algorithm.

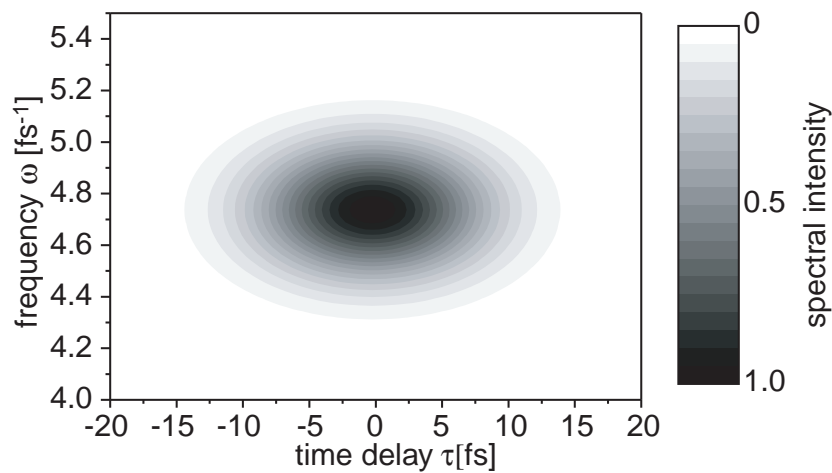


**Figure 1.11:** Second harmonic generation FROG trace measurement for a 10 fs FWHM bandwidth-limited laser pulse simulated with [50]. A two-dimensional set of data is obtained by spectrally resolving the intensity autocorrelation signal shown in Fig. 1.9. By the use of an iterative algorithm, the temporal amplitude and phase shape of the laser pulse can be extracted from this measurement.



There is one essential drawback of the FROG method described here. The direction of the temporal axis cannot be extracted from a single measurement. This comes from the time-reversal symmetry of Eq. (1.52), which stems from the time-reversal symmetry of the autocorrelation signal  $E_{2,nc}(t, \tau)$ . This problem can be overcome by simply performing a separate measurement of the pulse slightly changed in phase by some known amount. This can be realized by propagating it through a piece of glass or introducing a phase modulation in a pulse shaper and comparing to the previous measurement.

Another disadvantage of FROG is the iterative search procedure, which makes the pulse shape retrieval rather slow. However, by use of optimally designed search routines [56] and fast computers, it is nowadays possible to do pulse shape measurements on a 20-Hz real-time basis [57]. FROG provides a way to determine experimental error for the determination of laser pulse shapes [58]. Pulses of durations down to 4.5 fs have been characterized using the FROG method [59]. On the other hand, also complicated pulse shapes of supercontinuum generated from microstructured fibers can be analyzed [60].

It should be noted that the FROG technique does not rely on a second harmonic autocorrelation signal, but can be performed also using a different nonlinear process, like transient grating, third harmonic generation, polarization gating or others. FROG can also be combined with crosscorrelation (X-FROG) [61], which is again helpful for low pulse energies, down to the attojoule region [62]. FROG was applied to measure pulses in the mid-infrared [63]. In the high-frequency spectral region, laser pulses can be measured with FROG by performing nonlinear frequency downconversion [64].

In addition, FROG can be experimentally implemented in a way to characterize the spatio-temporal properties of laser pulses. If the temporal pulse shape of the laser pulse varies for different positions  $(x, y)$  along the transverse beam profile of the laser this is often called ‘spatial chirp’. The task is then to characterize not only  $E(t)$  but  $E(t, \vec{r})$ , which can be done for simple spatial chirps [65].

### 1.1.5.3 SPIDER: Spectral-Phase Interferometry for Direct Electric-field Reconstruction

The second well-known method of pulse shape retrieval is called spectral-interferometry for direct electric-field reconstruction (acronym: SPIDER). It has been introduced by Iaconis and Walmsley [52] in 1998. It is an extension of the linear spectral interferometry analysis, which is described in more detail in Appendix B.

The basic idea is to measure the pulse spectrum  $\tilde{A}(\omega)$  with a spectrometer and to find the phase  $\tilde{\phi}(\omega)$  by a separate measurement. Having both spectral amplitude and phase at hand, we can fully determine the spectral electric field  $\tilde{E}^+(\omega)$  and thus of course also the time dependent electric field  $E(t)$  by means of the Fourier transformation Eq. (1.6). As the name of the technique implies, the phase is measured with an interferometric technique. It is basically the temporal analog of diffraction of light by a double slit in space. Real space and wavevector space are related by a Fourier transformation for diffraction, as are time and frequency. Therefore, if we create two identical pulses with a temporal separation  $\tau$  and analyze them with a spectrometer, a fringe pattern will be visible. This can be understood by considering the constructive interference—similar as in a Michelson

interferometer—that is created for some wavelengths at a particular time delay while for different wavelengths the same time delay corresponds to destructive interference. If we now change the spectral phase  $\tilde{\phi}_2(\omega)$  of the second pulse by some amount  $\Delta\tilde{\phi}_2(\omega)$  but leave the phase  $\tilde{\phi}_1(\omega)$  of the first one unchanged, the signal at the spectrometer will change according to this additional phase  $\Delta\tilde{\phi}_2(\omega)$ . For example, let one frequency  $\omega_c$  be destructively interfering at the beginning. If we now add the phase  $\pi$  at this frequency ( $\Delta\tilde{\phi}_2(\omega_c) = \pi$ ), the destructive interference will turn into a constructive one.

Mathematically, the spectrometer signal can be given in frequency space by Eq. (B.3)

$$\tilde{S}(\omega) = \tilde{I}_1(\omega) + \tilde{I}_2(\omega) + 2\sqrt{\tilde{I}_1(\omega)\tilde{I}_2(\omega)} \cos(\tilde{\phi}_1(\omega) - \tilde{\phi}_2(\omega) - \omega\tau) \quad (1.53)$$

where  $\tilde{I}_j(\omega)$  is the spectrum of pulse  $j$ . Hence, for equal pulses, we obtain fringes which are equidistantly spaced in frequency. If the pulses are not equal, we can determine the phase difference by analyzing the fringe spacing in the spectrum. However, this method does not help us to find the phase of an unknown pulse. We would need a way to measure the difference between *different* frequencies, whereas here we can only measure phase differences between *the same* frequencies. The solution is to shift one pulse in frequency with respect to the other. The spectral interference signal can then be written as

$$\tilde{S}_{\text{SPIDER}}(\omega) = \tilde{I}(\omega) + \tilde{I}(\omega + \Omega) + 2\sqrt{\tilde{I}(\omega)\tilde{I}(\omega + \Omega)} \cos(\tilde{\phi}(\omega) - \tilde{\phi}(\omega + \Omega) - \omega\tau) \quad (1.54)$$

Now, we can extract information about the phase difference between the phase of frequency  $\omega$  and the one of frequency  $\omega + \Omega$ . If we choose  $\Omega$  sufficiently small and do the analysis for the complete spectrum, we can reconstruct the phase (except the constant phase  $\tilde{a}_0$ ) from this measurement by adding up the phase differences (see Appendix B).

Since we can only shift the frequency by some nonlinear process (as will become more clear in Section 1.2), most experimental implementations of SPIDER use sum-frequency generation. However, also different frequency mixing schemes can be employed. Down-conversion by difference frequency mixing was demonstrated for the characterization of high-frequency laser pulses [66]. A typical experimental SPIDER setup is schematically shown in Fig. 1.12. The pulse to be measured is split into two identical replicas by a thin glass-plate (etalon). While about 4% of the pulse's energy is contained in each replica, most of the pulse is transmitted. It is then stretched to a long pulse duration by delaying the blue frequency parts with respect to the red ones by dispersion in a long piece of glass. An up-chirped pulse is produced. This pulse can be overlapped noncollinearly with the two collinearly propagating replicas in a crystal, producing the second harmonic as in intensity cross- and autocorrelation measurements. Again, as in the case of FROG, the second harmonic signal produced from the interaction of the pair of identical pulses with the chirped one is sent into a spectrometer and spectrally analyzed. The first laser pulse interacts with the lower-frequency part of the chirped pulse ( $\omega_0 - \Omega$ ) while the second one meets higher frequencies ( $\omega_0$ ) at later times in the chirped pulse. For SPIDER, we need to ensure that the chirped pulse is sufficiently long compared to the two equally short pulses with which it is mixed. The instantaneous frequency of the chirped laser pulse interacting with the short pulses has to be roughly constant (compared to the frequency difference  $\Omega$ ). In this case, the spectral properties of the two laser pulses are up-converted to higher

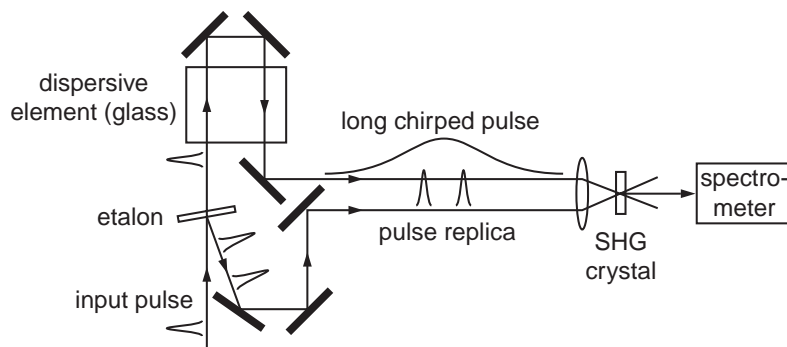


**Figure 1.12:** SPIDER setup used for full characterization of laser pulse shapes. Two replica of the pulse to be characterized are produced by front- and back-side reflection off a thin glass plate (etalon). The transmitted pulse is temporally stretched (chirped). After interaction of the long pulse with the two replica in a nonlinear crystal, one ultrashort pulse is spectrally shifted with respect to the other replica. This spectral shear allows for an interferometric detection of the spectral phase.

frequencies (sum-frequency mixing) and the spectrometer signal can be written as

$$\begin{aligned} \tilde{S}_{\text{SFM-SPIDER}}(\omega) &= \tilde{I}(\omega - \omega_0) + \tilde{I}(\omega - \omega_0 + \Omega) \\ &+ 2\sqrt{\tilde{I}(\omega - \omega_0)\tilde{I}(\omega - \omega_0 + \Omega)} \cos(\tilde{\phi}(\omega - \omega_0) - \tilde{\phi}(\omega - \omega_0 + \Omega) - \omega\tau), \end{aligned} \quad (1.55)$$

which closely resembles Eq. (1.54), except that we have an additional constant frequency upshift of  $\omega_0$ , i.e. a frequency within the bandwidth of the pulse. As stated above, from the phase difference between adjacent frequencies we can now analytically reconstruct the phase function (see Appendix B.3 for details) except for a constant offset, which cannot be measured with any of the techniques discussed until now. In Fig. 1.13, an example SPIDER spectrum is shown.

Since SPIDER does not rely on an iterative search procedure to find the pulse shape but instead only uses a series of mathematical operations, pulse reconstruction generally works faster than in FROG. It has been proven to operate at a 20 Hz repetition rate in practice [67] employing moderate computation power. Spatial characterization of laser pulses is also possible with SPIDER [68]. The shortest pulses characterized with the SPIDER technique are on the order of 5 fs [69, 70]. For characterization of low-energy pulses, the sensitivity of the SPIDER measurement technique can be improved by deriving the chirped pulse from a strong external laser pulse [71].

A comparison of the FROG with the SPIDER technique for the reconstruction of very short pulses is also available in the literature [72].

## 1.2 Fundamentals of Nonlinear Optics

As long as we deal with small perturbations, we can describe physical systems in a linear approximation. For the interaction of light with matter that means: As long as the intensity

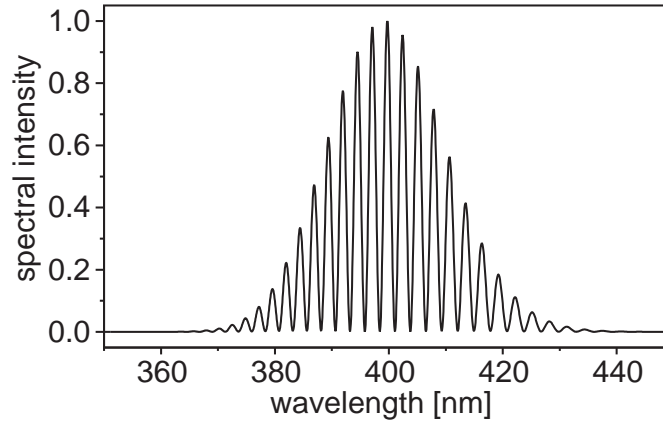


**Figure 1.13:** SPIDER spectrum obtained for a 10 fs FWHM bandwidth-limited laser pulse. The fringes in the measured spectrum arise from the interference of two frequency shifted but otherwise identical pulses. The spectral phase can be retrieved from the fringe spacing of the spectral distribution. Together with the easily accessible spectral amplitude (from the laser pulse spectrum), the pulse shape can be calculated in an analytical fashion.

of the light is sufficiently low, we can describe the induced polarization of the medium as being directly proportional to the electric field. However, when the electric field strength of an electromagnetic wave comes close to intra-atomic field strengths experienced by the valence (optically active) electrons, this approximation breaks down and we enter the regime of nonlinear optics [73–76]. With increasing field strength, higher and higher order coefficients of the Taylor series for the polarization contribute significantly. These higher-order terms are responsible for the creation of new frequencies at multiples of the driving frequency (harmonic generation) or sidebands (raman-scattering, self-phase modulation, parametric conversion). Nonlinear polarizability, however, is only one side of the coin of electromagnetic frequency conversion. To generate macroscopic amounts of converted radiation, we cannot work with a single nonlinear emitter particle in the light field alone; we need many of them to achieve significant conversion efficiencies. Additionally, in-phase superposition of all nonlinear emitters is required. This is the other side of the coin, which is termed phase-matching. Both, the microscopic source and the macroscopic propagation properties will now be discussed, as they constitute the fundamentals of nonlinear optical frequency conversion.

## 1.2.1 Polarizability — Microscopic Source

### 1.2.1.1 Polarization

The wave equation for light propagation in a medium is derived from Maxwell’s equations [77]:

$$\left(\Delta - \frac{1}{c^2} \frac{\partial^2}{\partial t^2}\right) \vec{E}(\vec{r}, t) = \mu_0 \frac{\partial^2}{\partial t^2} \vec{P}(\vec{r}, t) + \mu_0 \frac{\partial}{\partial t} \vec{j}(\vec{r}, t) + 1/\epsilon_0 \vec{\nabla} \rho(\vec{r}, t), \quad (1.56)$$

where  $\vec{P}(\vec{r}, t)$ ,  $\vec{j}(\vec{r}, t)$ , and  $\rho(\vec{r}, t)$  are polarization, current density and space charge density of the medium, respectively. The vacuum magnetic susceptibility and dielectric constant are represented by  $\mu_0$  and  $\epsilon_0$ , respectively. The frequency conversion processes of interest in this work are performed in non-conducting (insulator) materials only. Thus, the latter two terms on the right-hand side of Eq. (1.56) do not contribute. In this case, the only remaining source term is the second derivative of the polarization  $\vec{P}(\vec{r}, t)$ . It can be interpreted as the bremsstrahlung emitted by a charged particle, which is the electron. The electronic motion relative to the fixed ions gives rise to an electric dipole moment  $\vec{d}_e$  and thus creates the polarization  $\vec{P} = N\vec{d}_e$ , where  $N$  is the density of equal dipoles in the medium. Bremsstrahlung is only emitted if a charged particle is accelerated, explaining the second derivative in the source term.

In the following we will drop the position dependence of the polarization, since in this work the polarization can always be considered local, which means that the polarization at  $\vec{r}$  only depends on the electric field at the same point. However, nonlocal polarization does come into play if we, for instance, consider polaron motion in crystals [46]. In this case, the polarization is mediated not only by the propagation of light—which is included in Maxwell's equations—but also by lattice vibrations (phonons).

Since an incoming electric field (called the ‘pump’) is interacting with the electrons in the medium, dipole moments are induced and change, depending on the time-dependent electric field. Thus, the polarization can be written as a functional of the electric field:

$$\vec{P}(t) = \vec{P}[\vec{E}(t)]. \quad (1.57)$$

We can now decompose the time-dependent polarization of the medium  $\vec{P}(t)$  in a Taylor series:

$$\vec{P}(t) = \sum_{n=0}^{\infty} \vec{P}^{(n)}(t), \quad (1.58)$$

where the  $\vec{P}^{(n)}(t)$  are of order  $n$  in the electric field  $E(t)$ . In most general terms, we can write [78]

$$\vec{P}^{(n)}(t) = \epsilon_0 \int_{-\infty}^{+\infty} d\tau_1 \cdots \int_{-\infty}^{+\infty} d\tau_n \hat{R}^{(n)}(\tau_1, \dots, \tau_n) |\vec{E}(t - \tau_1) \cdots \vec{E}(t - \tau_n), \quad (1.59)$$

where we introduced the nonlinear response functions of the medium  $\hat{R}^{(n)}$ , which are tensors of  $n$ th-rank. The vertical line stands for a contraction of the tensor with the  $n$  electric field functions. We can rewrite the latter formula in index notation to yield

$$P_{\mu}^{(n)}(t) = \sum_{\alpha_1=x,y,z} \cdots \sum_{\alpha_n=x,y,z} \epsilon_0 \int_{-\infty}^{\infty} d\tau_1 \cdots \int_{-\infty}^{\infty} d\tau_n \times R_{\mu\alpha_1 \dots \alpha_n}(\tau_1, \dots, \tau_n) E_{\alpha_1}(t - \tau_1) \cdots E_{\alpha_n}(t - \tau_n). \quad (1.60)$$

$R^{(n)}$  is a real quantity, since both,  $\vec{E}(t)$  and  $\vec{P}(t)$  are real (physically measurable). Since only the electric field at an earlier time  $t - \tau < t$  can influence the polarization at time  $t$ ,  $R^{(n)}$  vanishes for at least one negative  $\tau_i$ .

Since the wave equation (1.56) is more easily tractable in the frequency domain, let us now find the expression for the  $n$ th order nonlinear polarization as a function of frequency. By

inserting the Fourier relation Eq. (1.2) for  $\vec{E}(t)$  into the temporal expression Eq. (1.59) we arrive at

$$\vec{P}^{(n)}(t) = \frac{\epsilon_0}{\sqrt{2\pi}} \int_{-\infty}^{\infty} d\omega_1 \cdots \int_{-\infty}^{\infty} d\omega_n \chi^{(n)}(-\omega_s; \omega_1, \dots, \omega_n) |\vec{E}(\omega_1) \cdots \vec{E}(\omega_n) e^{i\omega_s t}, \quad (1.61)$$

in which the  $n$ th order electric susceptibility tensor can be written as

$$\chi^{(n)}(-\omega_s; \omega_1, \dots, \omega_n) = \frac{1}{(\sqrt{2\pi})^{n-1}} \int_{-\infty}^{\infty} d\tau_1 \cdots \int_{-\infty}^{\infty} d\tau_n \hat{K}^{(n)}(\tau_1, \dots, \tau_n) e^{-i\sum_{j=1}^n \omega_j \tau_j}. \quad (1.62)$$

The sum frequency  $\omega_s$  is introduced:

$$\omega_s = \omega_1 + \omega_2 + \cdots + \omega_n. \quad (1.63)$$

The Fourier transformation

$$\vec{P}^{(n)}(\omega) = \frac{1}{\sqrt{2\pi}} \int_{-\infty}^{\infty} \vec{P}^{(n)}(t) e^{-i\omega t} dt \quad (1.64)$$

is now applied to arrive at the  $n$ th order nonlinear polarization as a function of frequency:

$$\vec{P}^{(n)}(\omega) = \epsilon_0 \int_{-\infty}^{\infty} d\omega_1 \cdots \int_{-\infty}^{\infty} d\omega_n \chi^{(n)}(-\omega_s; \omega_1, \dots, \omega_n) |\vec{E}(\omega_1) \cdots \vec{E}(\omega_n) \delta(\omega - \omega_s). \quad (1.65)$$

The Dirac delta function in Eq. (1.65) can be interpreted as energy conservation law. It is now obvious that frequencies can be generated that were not initially present in the electric fields. This is due to the fact that the polarization now has a nonzero contribution at the sum-frequency  $\omega_s$ , which can be a new frequency that was initially not present. As stated above, the second order time derivative of the polarization enters the wave equation as a source term, which leads to the generation of frequency  $\omega_s$ . This can be understood as the key to frequency conversion. In other words, photons of some frequencies can interact with each other to produce different frequencies as soon as the wave equation (1.56) becomes nonlinear. In this case, the superposition principle of linear physics has become invalid.

Some examples for nonlinear ‘‘photon reactions’’ are the following:

$$\begin{array}{llll} \text{second-harmonic generation:} & \hbar(\omega) + \hbar(\omega) & \rightarrow & \hbar(2\omega) \\ \text{sum-frequency mixing:} & \hbar(\omega_1) + \hbar(\omega_2) & \rightarrow & \hbar(\omega_1 + \omega_2) \\ \text{difference-frequency mixing:} & \hbar(\omega_1) - \hbar(\omega_2) & \rightarrow & \hbar(\omega_1 - \omega_2) \\ \text{self-phase modulation:} & \hbar(\omega_1) \pm (\hbar(\omega_2) - \hbar(\omega_3)) & \rightarrow & \hbar(\omega_1 \pm (\omega_2 - \omega_3)) \\ \text{high-harmonic generation:} & m \times \hbar(\omega) & \rightarrow & \hbar(m\omega) \end{array} \quad (1.66)$$

A minus sign in front of a photon on the left hand side means that instead of destroying this photon in the course of the reaction (as is the case for a plus sign), it is created in the light field. In Section 1.2.3 and Chapter 2 these examples are addressed in more detail.

### 1.2.1.2 Time-dependent Dipole Moments

The polarization treated so far is a mesoscopic quantity which can be used to characterize some unit volume of the medium which is larger than the atomic volume but still much

smaller than the wavelength of the light. Its microscopic origin is the electric-field induced time-dependent dipole moment of the atoms that constitute the medium as has already been mentioned above. The polarization is connected to the single dipole moments in the following way

$$\vec{P}(t, \vec{r}) = \frac{1}{V(\vec{r})} \sum_{r_i \in V(\vec{r})} \vec{d}_i(t), \quad (1.67)$$

where  $V(\vec{r})$  denotes a compact space volume around  $\vec{r}$  which contains many dipoles and is still small compared to the wavelength of the light under consideration.  $\vec{r}_i$  is the position of dipole  $\vec{d}_i(t)$ . The polarization can thus be considered to be an average dipole moment.

We can thus write the analogous equations (1.57)–(1.65) also for the dipole moments instead of the polarization, arriving at the time-dependent and frequency dependent expressions for the  $n$ th order nonlinear dipole moments

$$\vec{d}^{(n)}(t) = \int_{-\infty}^{+\infty} d\tau_1 \cdots \int_{-\infty}^{+\infty} d\tau_n \hat{R}'^{(n)}(\tau_1, \dots, \tau_n) |\vec{E}(t - \tau_1) \cdots \vec{E}(t - \tau_n) \quad (1.68)$$

$$\vec{d}^{(n)}(\omega) = \epsilon_0 \int_{-\infty}^{\infty} d\omega_1 \cdots \int_{-\infty}^{\infty} d\omega_n \alpha^{(n)}(-\omega_s; \omega_1, \dots, \omega_n) |\vec{E}(\omega_1) \cdots \vec{E}(\omega_n) \delta(\omega - \omega_s) \quad (1.69)$$

with the microscopic  $n$ th order response function  $\hat{R}'^{(n)}$  and the  $n$ th order nonlinear polarizability tensor  $\alpha^{(n)}$ , which is given by

$$\alpha^{(n)}(-\omega_s; \omega_1, \dots, \omega_n) = \frac{1}{(\sqrt{2\pi})^{n-1}} \int_{-\infty}^{\infty} d\tau_1 \cdots \int_{-\infty}^{\infty} d\tau_n \hat{R}'^{(n)}(\tau_1, \dots, \tau_n) e^{-i\sum_{j=1}^n \omega_j \tau_j} \quad (1.70)$$

The calculation of the dipole moment allows us to include the particular properties of the atoms in the medium via their collective polarization into the wave equation (1.56). The latter has then to be self-consistently solved. This will be treated in more detail in Section 1.2.2.

We now reexamine the formula for the frequency dependent nonlinear polarization Eq. (1.65). Let us take the squared modulus on both sides to study the intensity dependence. In general, if we look at the scaling of the nonlinear polarization only with intensity of the different pump components (without changing the shape of the pump fields), we may write

$$I_s^{(n)} \propto \prod_{j=1}^n I_j, \quad (1.71)$$

where  $I_s^{(n)}$  is the intensity of the converted light emitted by the induced  $n$ th order nonlinear polarization  $\vec{P}(\omega)$  and the  $I_j$  represent the intensities of the pump fields at different frequencies. In particular, if we only assume one fundamental excitation frequency  $\omega_f$

$$I_s^{(n)} \propto I_f^n. \quad (1.72)$$

These intensity dependencies have an interesting statistical interpretation. In an  $n$ th order nonresonant nonlinear process, the atom needs to absorb  $n$  photons of frequency  $\omega$  at the same time to release for instance a photon of  $n$  times the fundamental frequency.

The probability to absorb one photon scales linearly with intensity, since the intensity is linearly proportional to the probability to find one photon in some neighborhood of the atom. Thus, the probability to find and absorb  $n$  photons in this neighborhood scales with the intensity to the  $n$ th power in the case of only one pump frequency. If different frequencies contribute, then of course all partial probabilities (intensities) have to be multiplied to give the scaling for the intensity of the converted light. However, the validity of this scaling law is limited, as will be discussed in more detail below.

### 1.2.1.3 Example: Adiabatic Approximation

Let us now consider a simple example, which allows us to obtain an instructive and qualitative view of the nonlinear response of an atom exposed to a strong laser field. Imagine a classically bound electron in an atom. To first order, we can describe the binding potential as a parabola ( $V(r) \propto er^2$ ). The force acting on the electron is then given by  $F(r) \propto -er$ . If we slowly (adiabatically) apply a static electric field, the electron is displaced by  $r \propto -E$  since the two forces on the electron have to balance. This displacement gives a dipole moment  $d = -r$ . If the electric field is now slowly changing with a frequency much lower than the resonance frequency of the electron in the potential, the electron and thus the dipole moment will follow the field  $E(t)$  with  $d(t) \propto E(t)$  instantaneously. Let us consider the electric field to be given by

$$E(t) = A \cos \omega t = \frac{A}{2} e^{i\omega t} + c.c., \quad (1.73)$$

i.e. a single-frequency ac-field, where *c.c.* stands for the complex conjugate. Due to the linear dependence of the dipole moment on the electric field, it will contain the same harmonic oscillatory time dependence with frequency  $\omega$ . As a consequence (wave equation (1.56), dipole moment  $\rightarrow$  polarization is a source), no additional frequencies are produced in the interaction.

However, if we now increase the intensity of the light interacting with the electron in the atom, the quadratic approximation of the electron binding potential breaks down at high values of the field. For that reason, we decompose the effective binding potential in a Taylor series:

$$V(r) = \sum_{j=0}^{\infty} \frac{V_j}{j!} r^j. \quad (1.74)$$

Again, we calculate the force by taking the derivative

$$F(r) = - \sum_{j=1}^{\infty} \frac{V_j}{(j-1)!} r^{j-1}. \quad (1.75)$$

If this force is generated by the slowly oscillating (far below resonance) external electric field, the electron is displaced by an amount  $r(-eE)$ , leading to a dipole moment of

$$\hat{d}(E) = -r(-eE) = -F^{-1}(-eE), \quad (1.76)$$

where  $F^{-1}(F)$  is the inverse function of  $F(r)$ . This function can again be expanded in a Taylor series

$$\hat{d}(E) = \sum_{j=0}^{\infty} \hat{\alpha}^{(j)} E^j. \quad (1.77)$$



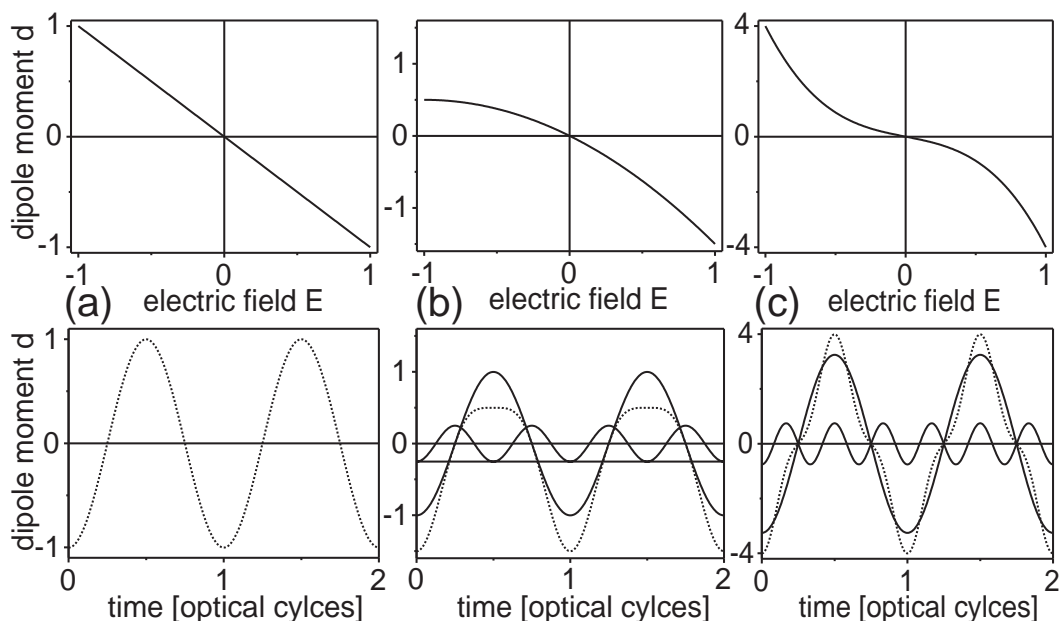


**Figure 1.14:** Linear (a) and nonlinear (b,c) dependence of the dipole moment on the applied electric field (upper graphs). The lower graphs show the dipole moment (dotted line) as it depends on an AC-electric laser field (compare dotted line in (a)). The solid line shows contributions at different frequencies. In the linear case, the only frequency contributing to the dipole oscillation is the frequency of the driving laser. For the case of a quadratic nonlinearity (b), the second harmonic (twice the laser frequency) and a constant offset are produced. The third order nonlinearity produces the third harmonic.

In the case of a linear  $F(r)$ , the summation stops at  $j = 1$  since all higher  $\hat{\alpha}^{(j)}$  are zero. However, for any higher order dependence of  $F(r)$  on  $r$ , higher order coefficients are nonzero. These nonzero coefficients are responsible for frequency conversion. By inserting the electric field Eq. (1.73) into the last equation, different powers of  $e^{i\omega t}$  are produced, i.e.

$$\hat{d}(E) = d(t) \propto \sum_{j=0}^{\infty} a_j (e^{i\omega t})^j + c.c. = \sum_{j=0}^{\infty} a_j e^{ij\omega t} + c.c., \quad (1.78)$$

with some weighting coefficients  $a_j$ . It is thus the nonlinearity of the effective binding potential  $V(r)$  of the electron which produces additional harmonic ( $j\omega$ ,  $j \in \mathbb{N}$ ) frequencies via a nonlinear  $\hat{d}(E)$  curve. In Fig. 1.14, this relationship is graphically illustrated. It is important to notice at this point, that symmetry properties of the potential are transported to the  $\hat{d}(E)$  relation and have an interesting interpretation (see also Section 3.1): For example, if the potential is symmetric with respect to inversion  $r \rightarrow -r$ , we obtain an odd function  $F(r) = -F(-r)$ . As a consequence, the inverse function  $r = F^{-1}(F)$  and thus also  $\hat{d}(E)$  are odd functions. Their Taylor series thus only contain odd orders of  $F$  and  $E$ . This allows for the generation of odd harmonic frequencies  $(2n+1)\omega$  only. In order to generate also even orders, the inversion symmetry has to be broken.

In fact, it can be generally proven that the nonlinear susceptibilities and polarizabilities of even order vanish for the case of material with inversion symmetry.

In order to show the connection to the general quantities introduced above, the  $\hat{\alpha}^{(n)}$  in Eq. (1.77) can be directly compared to the response function  $\hat{R}^{(n)}(\tau_1, \dots, \tau_n)$  in Eq. (1.68). Since we assume an instantaneous response of the atomic system to the electric field (far below resonance), we can write

$$\hat{R}^{(n)}(\tau_1, \dots, \tau_n) = \hat{c} \delta(\tau_1) \cdots \delta(\tau_n), \quad (1.79)$$

with  $\hat{c}$  being a constant which does not depend on any  $\tau_j$ . If we now perform the integration given in Eq. (1.68) we are left with one summand of formula Eq. (1.77).

If the response of the medium is instantaneous, this has an important implication for the nonlinear susceptibility  $\chi^{(n)}(-\omega_s; \omega_1, \dots, \omega_n)$ . After having performed the  $n$  integrations in defining formula Eq. (1.62) over the instantaneous response defined above in Eq. (1.79), we obtain a constant  $\hat{\chi}^{(n)}$ . Thus, in the case of an instantaneous medium response, the susceptibility does not depend on the frequency of the light.

#### 1.2.1.4 Nonlinear Polarization in Quantum Mechanics

In quantum mechanics, the state of a microscopic system can be described by means of a time-dependent wave-function  $|\psi(\vec{r}, t)\rangle$ . It is a solution to the time-dependent Schrödinger equation [79, 80]

$$i\hbar \frac{\partial}{\partial t} |\psi(\vec{r}, t)\rangle = \hat{H} |\psi(\vec{r}, t)\rangle, \quad (1.80)$$

where  $\hat{H}$  is the Hamiltonian operator, describing the microscopic system and the laser field. It can be broken up into two parts:

$$\hat{H} = \hat{H}_0 + \hat{V}(t), \quad (1.81)$$

where  $\hat{H}_0$  describes the atomic system when it is not interacting with an electric field, and  $\hat{V}(t)$  describes the interaction with the electric field as the additionally imposed potential

$$\hat{V}(t) = -\vec{\hat{\mu}} \vec{E}(t), \quad (1.82)$$

where we call  $\vec{\hat{\mu}}$  the electric dipole moment operator. It can be written as

$$\vec{\hat{\mu}} = -e\vec{r}, \quad (1.83)$$

with  $-e$  being the charge of the electron.

In order to determine the nonlinear polarizability tensors, we need to calculate the dipole moment as a function of time. It is given by the time-dependent expectation value of the dipole moment operator:

$$\vec{\mu}(t) = \langle \psi(\vec{r}, t) | \vec{\hat{\mu}} | \psi(\vec{r}, t) \rangle. \quad (1.84)$$

By applying perturbation theory, we can expand this expression in a Taylor series in powers of  $E(t)$ . This leads us to the nonlinear response functions defined in Eq. (1.68) from which we can calculate the polarizability tensors.

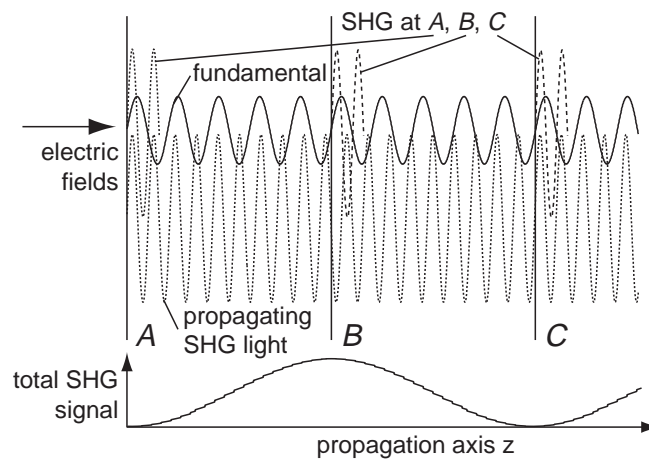


**Figure 1.15:** Illustration of the phase-matching problem for second-harmonic generation (SHG), where fundamental light enters from the left (arrow). If the phase velocities of fundamental and signal (SHG) light are different, the wavelength of the second harmonic inside the crystal will not be equal to half the wavelength of the fundamental light. As newly generated SHG light is always produced with a constant phase relationship to the fundamental radiation, it will interfere with the earlier generated SHG light that propagates through the crystal. Light generated at *B* or *C* interferes destructively or constructively, respectively, with light generated at *A*. The total amount of SHG light will thus show a periodic modulation in intensity along the propagation axis.

In computer simulations, we can solve the Schrödinger equation numerically by defining and evolving the wavefunction  $\psi(\vec{r}, t)$  on a grid. The time-dependent dipole moment can then straightforwardly be analyzed. This will be addressed in more detail in Chapter 2 with particular emphasis on high-harmonic generation. In the main part of this work, a numerical approach is used to study high-harmonic generation in molecules.

### 1.2.2 Phase matching — Macroscopic build-up

For nonlinear frequency conversion, we would like to extract macroscopic amounts of radiation (called ‘signal’) from the conversion medium as it interacts with intense light referred to as ‘fundamental’ or ‘pump’ radiation. Of course a single particle (atom, molecule, cluster, ...) is not able to convert large amounts of fundamental light, due to its small size. We therefore need to consider an extended conversion medium. The nonlinear optical signal can then build up to larger and larger intensity along the optical path, given all contributions of the single particles to the signal light field add up constructively.

To get a first idea, we consider the process of second-harmonic generation (SHG), where we convert fundamental light into signal light at twice the fundamental frequency. Let us imagine the fundamental wave, as it propagates through the (transparent) medium (Fig. 1.15). It excites nonlinear dipole motion all the way along its propagation path. Any of those nonlinear dipole moments will emit signal light at some frequency which is different from the fundamental but always with a fixed phase relation to the fundamental. In general, any material exhibits dispersion, thus the phase velocities of the fundamental and the signal radiation are not equal. Let us consider a plane wave incident on the

conversion medium which starts at the surface plane  $A$ . After some propagation distance from plane  $A$  to plane  $B$  inside the medium, this difference in phase velocities leads to a phase shift of  $\pi$  between signal generated at  $A$  that traveled through the medium and signal generated directly at  $B$ . After this distance, we will no longer increase the amount of signal, since destructive interference of newly produced second harmonic with the one produced at  $A$  occurs. The signal will thus disappear, feeding back into the fundamental field, which is also called ‘back conversion’. This will continue until we reach another plane  $C$  after the same propagation distance as from  $A$  to  $B$ , where all signal light will have disappeared. Signal build-up will start again at  $C$  as initially from  $A$ .

To generate maximum amount of signal, it would of course be optimal to have a continuous growth over the propagation distance. In practice, there are two solutions to this problem.

The first one is to find a way that both phase velocities are the same. This results in the phase of newly produced signal radiation always to match the phase of the propagating signal (thus the term ‘phase matching’ or more precisely ‘perfect phase matching’). If this is the case, each plane of atoms along the propagation direction will contribute the same amount of electric field to the signal field. It will thus grow linearly with propagation distance in the medium, which results in a quadratic increase of the intensity.

The second solution to provide steady growth along the interaction path is to use a medium which is “switched off” or “turned around” in the very regions where destructive interference would occur. The phase slippage is thus not avoided (perfect phase matching is not accomplished) but by manipulation of the medium we do not allow destructive interference. Switching off can mean simply to remove the medium from these regions [81], but also to modulate the intensity [82–85], since we know from Section 1.2.1 that any nonlinear process depends strongly on intensity. “Turned around” refers to the material structure, which in the case of second-harmonic generation has to break inversion symmetry (see Section 1.2.1). By mechanically inverting the medium in the otherwise destructively contributing regions [86], we regain constructive interference. This idea of manipulating the medium at appropriate distance in order to ‘almost match the phase’ everywhere (nowadays referred to by the name ‘quasi-phase matching’) has been introduced in the early days of nonlinear optics (1962) by Armstrong *et al.* [87].

After this conceptual overview of phase matching let us now discuss the mathematical description in more detail. We know that the source of nonlinear emission at some signal wavelength is governed by the polarizability. By inserting  $n$  plane fundamental waves (often also called ‘pump’) at frequencies  $\omega_j$

$$\vec{E}_j(\vec{r}, \omega_j) = \vec{E}_{j0} e^{i(\omega_j t - \vec{k}_j \vec{r})} \quad (1.85)$$

into the expression for the frequency dependent polarization Eq. (1.65), we obtain

$$\vec{P}^{(n)}(\vec{r}, \omega) \propto e^{i((\sum_{j=1}^n \omega_j) t - (\sum_{j=1}^n \vec{k}_j) \vec{r})}. \quad (1.86)$$

The assumption of plane waves is only justified when the intensity of the corresponding waves in the medium does not change due to either absorption or depletion by conversion. This scenario is referred to as the ‘non-depleted-pump approximation’ [73, 74]. Recalling

the wave equation (1.56), the second order derivative of the polarization acts as a source. With Eq. (1.86) this results in the creation of a new wave with frequency  $\omega_s = \sum_{j=1}^n \omega_j$  and  $\vec{k}_{\text{eff}} = \sum_{j=1}^n \vec{k}_j$ , which can be regarded as an effective wavevector of the source. Once some amount of this light field is created it is also propagated by the wave equation with a refractive wavevector of  $k_s = n(\omega_s)\omega_s/c$  where  $c$  and  $n(\omega_s)$  denote the vacuum speed of light and the refractive index of the medium, respectively. It is clear that if both effective wavevector  $\vec{k}_{\text{eff}}$  and refractive wavevector  $\vec{k}_s$  would agree, we would “match the phase” (perfect phase matching) between generation and propagation. This would lead to continuous growth of the signal along its propagation path. The condition for phase matching can now be formulated as follows:

$$\vec{k}_s = \sum_{j=1}^n \vec{k}_j \quad (1.87)$$

Since the photon momentum  $\vec{p}_{\text{ph}}$  can be written as  $\hbar\vec{k}_{\text{ph}}$ , and due to the additional constraint of generating the angular frequency  $\omega_s$  we may write

$$\begin{aligned} E_s &= \sum_{j=1}^n E_j \quad (\text{energy conservation}) \\ \vec{p}_s &= \sum_{j=1}^n \vec{p}_j \quad (\text{momentum conservation}), \end{aligned} \quad (1.88)$$

where  $E_j = \hbar\omega_j$  are the photon energies. The energy conservation is actually already derived from Eq. (1.65). It is therefore a microscopic single-atom effect. The momentum conservation principle on the other hand follows from achieving phase matching between the propagating generating and signal fields and is thus a macroscopic effect. To summarize:

$$\begin{aligned} \text{single-atom response} &\rightarrow \text{photon energy conservation} \\ \text{propagation} &\rightarrow \text{photon momentum conservation} \end{aligned} \quad (1.89)$$

These results can be considered to be some of the most fundamental ones in nonlinear optics. It should be noted that of course momentum conservation has also to be fulfilled on the single particle level. However, only if it is fulfilled over a macroscopic region within the conversion medium the different single atom responses can coherently add up constructively.

When perfect phase matching is not fulfilled, we obtain

$$\sum_{j=1}^n \vec{k}_j - \vec{k}_s = \vec{k}_{\text{eff}} - \vec{k}_s = \Delta\vec{k} \neq 0 \quad (1.90)$$

In this case a phase slippage between generating and signal radiation will occur. Since the signal  $\vec{k}_s$  usually points into the same direction as  $\vec{k}_{\text{eff}}$ , there will be a phase lag of  $\pi$  at some propagation distance  $L_c$ . It can be calculated by

$$L_c(k_{\text{eff}} - k_s) = \pi \Rightarrow L_c = \frac{\pi}{k_{\text{eff}} - k_s} = \frac{\pi}{\Delta k} \quad (1.91)$$

This length  $L$  corresponds to the separation of the two planes  $A$  and  $B$  described at the beginning of this section. It is called the ‘coherence length’ and corresponds to the optimal length of the conversion medium in the case of non-perfect phase matching. When starting

from zero signal intensity, at the input of the medium, it will continuously grow inside the crystal until it saturates after a distance of  $L$ . At that point, the nonlinear process will generate wavelets interfering destructively with the ones earlier produced and convert signal light back into the pump.

We can also quantify those considerations by assuming another plane wave for the signal, the amplitude of which is dependent on position along the propagation direction  $z$ :

$$\vec{E}_s(z, t) = \vec{E}_{s0}(z) e^{i(\omega_s t - \vec{k}_s \vec{r})}. \quad (1.92)$$

We now insert this expression into the wave equation Eq. (1.56) on the left-hand side and use the polarization Eq. (1.86) on the right-hand side. We also apply the slowly varying envelope approximation [74, 78]

$$\left| \frac{\partial^2}{\partial z^2} \vec{E}_{s0}(z) \right| \ll \left| k_s \frac{\partial}{\partial z} \vec{E}_{s0}(z) \right|, \quad (1.93)$$

which is fulfilled when the growth rate of the signal light does not change significantly over one wavelength, which is almost always granted. We then obtain

$$\frac{\partial}{\partial z} \vec{E}_{s0}(z) = c_0 e^{i\Delta k z}. \quad (1.94)$$

Here,  $c_0$  is a proportionality factor which will be addressed below for the sake of clarity.  $\vec{E}_{s0}(z)$  can now easily be found by integration from 0 (where the medium begins) to some propagation length  $L$  to yield

$$\vec{E}_{s0}(L) = c_0 \frac{e^{i\Delta k L} - 1}{i\Delta k}. \quad (1.95)$$

The intensity of the signal can then be calculated (see Eq. (1.18)) to be

$$\begin{aligned} I_s(L) &= \frac{\epsilon_0 c n(\omega_s)}{2} |E_{s0}(L)|^2 \\ &= |c_1|^2 \left| \frac{e^{i\Delta k L} - 1}{i\Delta k} \right|^2 \\ &= |c_1|^2 L^2 \text{sinc}^2 \left( \frac{\Delta k L}{2} \right) \end{aligned} \quad (1.96)$$

with the sinc function  $\text{sinc}(x) = \sin(x)/x$  and  $c_1 = c_0 \epsilon_0 c n(\omega_s)/2$ . Fig. 1.16 depicts the intensity versus the two quantities of interest here, the phase mismatch  $\Delta k$  and the propagation length  $L$ . Again, the coherence length  $L_c$  defined above can be calculated and observed from Fig. 1.16 as the length  $L$  over which the signal steadily increases. We can also insert  $L_c$  into Eq. (1.96):

$$I_s = |c_1|^2 L^2 \text{sinc}^2 \left( \frac{\pi L}{2 L_c} \right). \quad (1.97)$$

The proportionality constants  $c_1$  and  $c_0$ , which were introduced to reduce complexity in writing, contain the nonlinear polarizability of the microscopic particle  $\alpha^{(n)}$ , the particle density  $N$  (if all particles are equal, otherwise we have to employ the summation

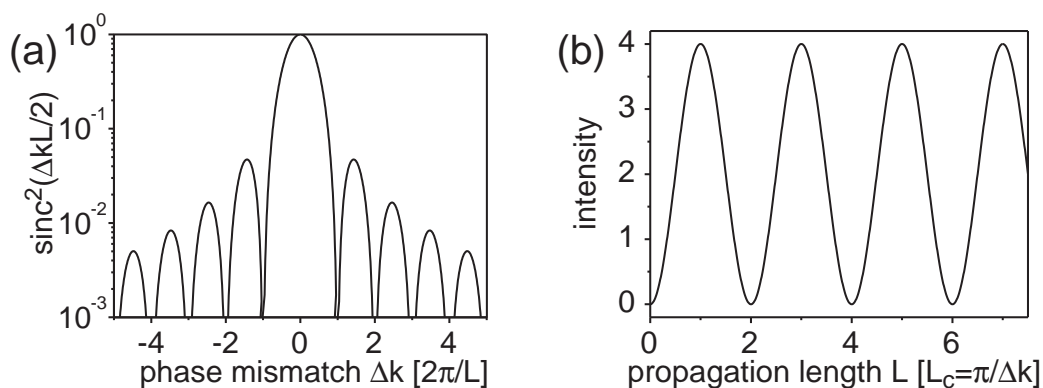


**Figure 1.16:** Phase matching in a frequency conversion process. The wavevector mismatch has to be zero (perfect phase matching) in order to generate a maximum of converted light (a). For a given wavevector mismatch, the amount of converted light is oscillating sinusoidally with the length of the conversion medium (b).

Eq. (1.67)) and the electric field amplitudes  $E_{j0}$  of the pump light from Eq. (1.85) in the following manner:

$$c_0 \propto c_1 \propto N \alpha^{(n)} \prod_{j=1}^n E_j. \quad (1.98)$$

Taking all of this into account, we finally arrive at [88–90]

$$E_{s0} \propto \underbrace{\alpha^{(n)} \prod_{j=1}^n E_{j0}}_{\text{single-particle response}} \underbrace{NL \frac{e^{i\Delta k L} - 1}{i\Delta k L}}_{\text{collective response}} \quad (1.99)$$

for the electric field amplitudes of the signal wave and

$$I_s \propto \underbrace{|\alpha^{(n)}| \prod_{j=1}^n I_j}_{\text{single-particle response}} \underbrace{N^2 L^2 \text{sinc}^2 \left( \frac{\Delta k L}{2} \right)}_{\text{collective response}} \quad (1.100)$$

for its intensity, where the  $I_j$  stand for the intensities of the pump waves. This expression tells us which parameters have to be manipulated in order to modify and to control a certain frequency conversion process. Since high-harmonic generation at present works only at a very low conversion efficiency, we are of course interested in an enhancement. This can be done by optimizing single atom parameters like the nonlinear dipole moments or the field strength of the driving laser. For simplicity in this fundamental section, we did not include the time dependent pump-light amplitudes, which of course also modify both the single-atom response and phase-matching. The latter can be controlled particularly well in quasi-phase matching schemes. As another collective parameter, the density of the generation medium can be increased in particular for high-harmonic generation, where mainly all work today is done in low-density gases. Finally, we can increase the interaction length, which for high-harmonic generation means to work in hollow fibers

Radiation	Wavelength	Frequency	photon energy	conversion method
Terahertz	200-20 $\mu\text{m}$	1-15 THz	6-60 meV	DFM
FIR-MIR	20-1 $\mu\text{m}$	15-300 THz	0.06-1 eV	OPG-DFM,DFM
NIR-VIS	0.4-1.0 $\mu\text{m}$	0.3-0.8 PHz	1-3 eV	OPG,SPM
UV-VUV	400-40 nm	0.8-8 PHz	3-30 eV	SFM,OPG-SFM,HHG
soft x-ray	40-2 nm	8-150 PHz	30-600 eV	HHG

**Table 1.2:** Ranges of the electromagnetic spectrum that are accessible by nonlinear optical frequency conversion of Ti:sapphire 800 nm fundamental radiation. The most important conversion processes are indicated. FIR: far infrared, MIR: mid infrared, NIR: near infrared, VIS: visible, UV: ultraviolet, VUV: vacuum ultraviolet, SFM: sum-frequency mixing, DFM: difference-frequency mixing, OPG: optical parametric generation, SPM: self-phase modulation, HHG: high-harmonic generation.

instead of only focusing into a gas jet or cell. Any of these approaches now discussed is subject of this thesis and will be discussed in detail in the main part of this work.

It should however be noted here that the converted fields  $E_{s,0}$  and intensity  $I_s$  do not always follow the simple scaling law shown above. In particular, if higher-order susceptibilities become of comparable order (which is often the case, in particular for the process of high-harmonic generation described in Chapter 2) the scaling behaviour with the product of the applied light fields and intensities breaks down. Additionally, resonances and saturation effects play an important role in the scaling behavior and need to be treated with particular care.

### 1.2.3 Application Examples

Now that the fundamentals of nonlinear optics have been laid out, it is reasonable to present some technical implementations. Of course there is a wide range of different possible applications, since nonlinear optics provides the unique possibility to switch and to control the color of light. A modern research laboratory needs to operate in principle only one primary laser system (which is usually the widespread Ti:sapphire laser) and convert light into wavelength regions around and far away from its fundamental 800 nm radiation. The accessible wavelength region extends from the Terahertz frequency range via the far- and mid-infrared (FIR and MIR) over into the visible, ultraviolet (UV) and beyond into the soft and hard x-ray spectral region. In all these parts of the electromagnetic spectrum except the x-ray region spatially and temporally coherent light is generated. This is because instantaneous nonlinear optical conversion in general conserves coherence and thus transfers the coherence properties of the laser over to the converted radiation. However, the conversion of frequencies into a totally different part of the electromagnetic spectrum is only one application of nonlinear optics. As was already discussed in Section 1.1.5, we can employ nonlinear optics for pulse measurement and characterization. When our electronic detectors (photodiodes, ...) are too slow to resolve the optical laser pulse shape in time, we are always bound to use some sort of nonlinear process to observe phase differences between different spectral components (frequencies) of one pulse and to reconstruct the temporal pulse shape by Fourier transformation Eq. (1.2). For these pulse characterization methods, the second-harmonic generation process is the one that found most



widespread use, which is due to its simplicity of implementation. It is a very recent effort in ultrafast physics to measure the pulse duration and shapes of the attosecond pulses which are produced in the high-harmonic generation process. This represents a challenge due to the fact that nonlinear susceptibilities and polarizabilities drop off rapidly for higher and higher frequencies of light. Another important application of nonlinear optics is the spectral broadening of ultrashort pulses and the corresponding pulse compression capability. This is achieved by generating new frequencies which are only slightly different from the ones available in the fundamental spectrum. The most popular nonlinear process used to accomplish this is termed self-phase modulation.

In the following, we shall discuss these most common (low-order) nonlinear processes used in practice. High-order harmonic generation will be subject of the following Chapter, since it is the central process under investigation in this work.

### 1.2.3.1 Second-Harmonic Generation (SHG), Sum- and Difference-Frequency Mixing (SFM and DFM)

The most commonly used processes in nonlinear optics are sum- and difference frequency mixing:

$$\begin{aligned} \text{sum-frequency mixing: } \hbar(\omega_1) + \hbar(\omega_2) &\rightarrow \hbar(\omega_1 + \omega_2) \\ \text{difference-frequency mixing: } \hbar(\omega_1) - \hbar(\omega_2) &\rightarrow \hbar(\omega_1 - \omega_2) \end{aligned} \quad (1.101)$$

Second-harmonic generation can be considered as a special case of sum-frequency mixing.

$$\text{second-harmonic generation: } \hbar(\omega) + \hbar(\omega) \rightarrow \hbar(2\omega) \quad (1.102)$$

Since any of these processes is a two photon interaction, the lowest order nonlinear susceptibility of interest is the second order  $\chi^{(2)}(\omega_s; \omega_1, \omega_2)$  Eq. (1.62). Therefore, we can write the nonlinear polarization Eq. (1.65), i.e. the source of the converted light, as follows:

$$\vec{P}^{(2)}(\omega) = \epsilon_0 \int_{-\infty}^{+\infty} \chi^{(2)}(-\omega; \Omega, \omega - \Omega) \vec{E}(\Omega) \vec{E}(\omega - \Omega) d\Omega \quad (1.103)$$

Note, that difference-frequency mixing is obtained when  $\Omega$  or  $\omega - \Omega$  are negative ( $\vec{E}(\omega)$  contains nonzero frequency components for  $\omega > 0$  and  $\omega < 0$  in Eqs. (1.1) and (1.4)). In the following we will only address the case of an instantaneous response of the medium (see Section 1.2.1), where the nonlinear susceptibility tensor  $\chi^{(2)}(-\omega; \Omega, \omega - \Omega) = \hat{\chi}^{(2)}$  is constant, i.e. not dependent on frequency. We will also assume linearly polarized pump and signal electric fields. The polarization state of each of the pump or signal waves, however, can be different. This is important in order to achieve phase matching.

As has been discussed above, even-order susceptibilities are only nonzero in materials that are non-symmetric with respect to inversion. Therefore, we have to choose an appropriate medium which has this property. In practice, a very common conversion medium is  $\beta$ -barium-borate (BBO) [91–93]. It exhibits large  $\chi^{(2)}$  tensor elements and a high damage threshold.

We need to accomplish phase matching in order to extract macroscopic amounts of converted radiation. If we consider only one pump laser pulse, the refractive index at the

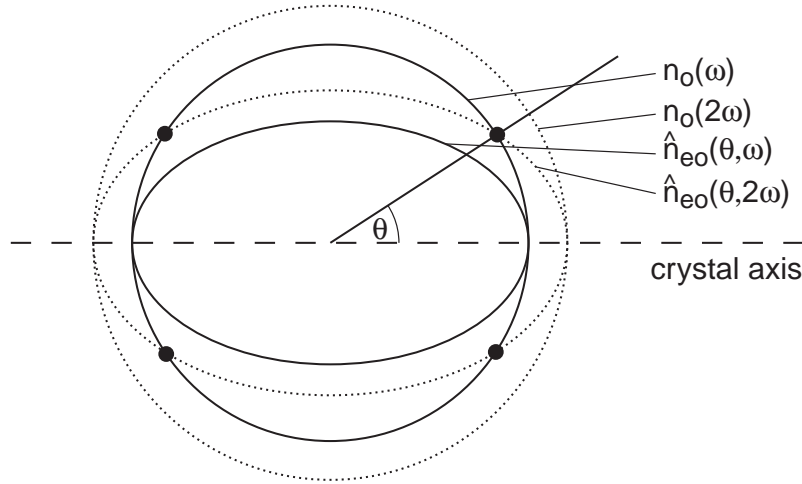


**Figure 1.17:** Phase matching in an anisotropic birefringent crystal. The dependence of the refractive index on the polarization of light relative to the crystal axis can be used to realize perfect phase matching. Ordinary light (polarized perpendicular to the optical axis) experiences the refractive index  $n_o(\omega)$ , otherwise the light is called extraordinary and the refractive index  $\hat{n}_{eo}(\theta, \omega)$  depends on both the angle  $\theta$  of its wavevector with respect to the optical axis and the frequency  $\omega$ . For phase-matching in second harmonic generation, the refractive indices at the fundamental and second harmonic frequency have to be equal (dots).

signal sum or difference frequency  $n(\omega_s)$  will not be the same as the one at the pump frequency  $n(\omega_p)$ . In a collinear conversion geometry, this necessarily leads to a wave-vector mismatch

$$\Delta k = 2k_f - k_s = (n(\omega_p) - n(\omega_s)) \frac{2\omega_p}{c}. \quad (1.104)$$

with the energy conservation implicitly given in Eq. (1.103)  $2\omega_p = \omega_s$ . How can we realize the same refractive index for both frequencies? The answer is to use an anisotropic birefringent crystal. BBO is a representative of this class of crystals. Due to their structure, they exhibit different indices of refraction  $n_o(\omega)$  and  $n_{eo}(\omega)$  depending on the polarization plane of the propagating light. Light that is polarized perpendicular to the crystal axis is called ordinary light. If there is a different angle between polarization and crystal axis, it is called extraordinary light. The refractive index  $n_{eo}$  is experienced by extraordinary light that is polarized along the crystal axis. For any arbitrary angle  $\theta$  between the wavevector of extraordinary light with respect to the crystal axis, the refractive index is given by

$$\frac{1}{\hat{n}_{eo}(\theta, \omega)} = \frac{\cos^2(\theta)}{n_o^2(\omega)} + \frac{\sin^2(\theta)}{n_{eo}^2(\omega)} \quad (1.105)$$

which defines an ellipse (see Fig. 1.17), the principal axes of which are given by the ordinary and extraordinary refractive index.

This property can be exploited to obtain phase matching in sum- and difference-frequency generation. By choosing the pump to be ordinarily polarized and the signal to be extraordinary, both refractive indices can be made equal under a certain angle with respect to the optical axis (Fig. 1.17).

In general, phase matching in any  $\chi^{(2)}$  process can be achieved by having one or two of the contributing light waves (two pump waves that can be identical, one signal wave) be polarized extraordinarily while the remaining two or one, respectively, are polarized ordinarily. For one ordinary wave the term ‘Type I’ phase matching has been introduced, while for two ordinary waves the term ‘Type II’ phase matching is used.

### 1.2.3.2 Optical Parametric Generation (OPG)

For many applications we would like to have a laser light source which is tunable throughout a certain region of the frequency domain. Starting out with an ultrashort pulse laser operating at a certain central frequency dictated by the laser medium, we cannot easily generate *arbitrary* frequencies only by application of sum- and difference-frequency mixing using laser light as a pump with a certain bandwidth. However, even in a vacuum, quantum fluctuations are existent. Single pairs of quanta are continuously generated and destroyed. In optical parametric generation we use nonlinear optics to amplify a signal initially generated from a quantum fluctuation (also called ‘superfluorescence’). This is very similar to the working principle of the laser. There, the lasing operation also starts from the spontaneous emission of light into the stable resonator mode. The spontaneous emission is in turn governed and triggered by a quantum fluctuation. The difference: the laser medium can only amplify light in a given frequency range as the gain curve is only larger than unity in a finite range of frequencies. If we work with an instantaneously responding nonlinear medium, the whole transparency range of the medium can be employed in principle, since  $\hat{\chi}^{(2)}$  does not depend on frequency.

Optical parametric generation is again based on difference frequency mixing with only one pump wave at frequency  $\omega_p$ . The second pump wave at frequency  $\omega_i$  which is “subtracted” from the first one  $\omega_p$  is not present at the beginning. It is generated by the mentioned quantum fluctuation, which provides virtual photons at  $\omega_i$ . One virtual photon acts as the second pump and produces light at the difference frequency. In terms of quantum-electrodynamics, it will create one real photon at the difference frequency  $\omega_s = \omega_p - \omega_i$  out of one real photon of the incoming pump wave at the frequency  $\omega_p$ . To retain the energy conservation, another real photon at  $\omega_i$  is generated, which from now on can take the role of the second pump. From here on, the process does not rely on quantum fluctuations but on the steady amplification of real photons. Two usually separate frequencies are generated, namely  $\omega_s$  (‘signal’) and  $\omega_i$  (‘idler’). In the literature, idler is most commonly used for the smaller frequency of the two. They are continuously amplified since more and more signal photons generate more and more idler and signal photons due to energy conservation. On the other hand, also the increasing amount of idler light will drive the difference-frequency mixing process to produce both, more idler and signal light from the pump wave. We can reformulate the “photon reaction” for difference-frequency mixing from above with the frequencies used here

$$\begin{array}{l} \text{difference-frequency mixing : } \hbar(\omega_p) - \hbar(\omega_i) \rightarrow \hbar(\omega_s) \\ \text{optical-parametric generation : } \hbar(\omega_p) \rightarrow \hbar(\omega_s) + \hbar(\omega_i). \end{array} \quad (1.106)$$

The decision of which frequencies are generated in the process is made by the choice of the phase-matching conditions. Again, an anisotropic non-centrosymmetric crystal like

e.g. BBO has to be used at the correct angle  $\theta$  with respect to the crystal axis.

It is possible to provide a seed pulse in OPG, which eliminates the need for a quantum fluctuation to start the conversion process. In addition, the spectral phase of the seed pulse is conserved in the conversion process. Therefore, we are able to achieve amplification of the seed pulse without changing its shape the same way as in a conventional laser medium. This technique is called ‘optical parametric amplification (OPA)’. In difference to the case of a conventional laser medium, the optical parametric case is not limited by the natural gain curve of the medium since  $\chi^{(2)}$  is not depending on frequency for a typically-employed instantaneous nonlinear response.

If we use the collinear geometry discussed so far where all waves propagate along the same direction, the wavevector mismatch  $\Delta k$  can become zero for one particular set of frequencies  $\omega_s$  and  $\omega_i$ . But as mentioned, the bandwidth of the instantaneous nonlinear process is almost arbitrarily large, which is why we would like to have the phase-matching condition met for a large range of frequencies in a seed pulse at once to yield very short pulses of tunable frequency (see Eq. 1.27). We will now see that by sacrificing the collinear geometry and thus having different waves propagate into different directions, we can achieve broad-bandwidth phase matching. To show this, the vectorial wavevector mismatch (compare Eq. (1.90))

$$\Delta \vec{k} = \vec{k}_p - \vec{k}_s - \vec{k}_i \quad (1.107)$$

is expanded as a Taylor series in  $\Delta \omega_s$  around the central frequency of the signal  $\omega_{s0}$

$$\Delta \vec{k}(\omega_s) = \Delta \vec{k}(\omega_{s0}) + \left. \frac{\partial \Delta \vec{k}(\omega_s)}{\partial \omega_s} \right|_{\omega_s = \omega_{s0}} \Delta \omega_s + \dots \quad (1.108)$$

Clearly, if we manage to not only make  $\Delta \vec{k}(\omega_{s0})$  equal to zero (which is done in any phase matching approach considered so far) but additionally succeed in cancelling the second coefficient in the Taylor expansion, phase matching is fulfilled in a certain range of frequencies around the center frequency  $\omega_{s0}$ . If we allow noncollinear orientation of the wavevectors, we basically gain the angle between signal and idler wavevector  $\Omega$  (Fig. 1.18) as an additional degree of freedom to achieve the broadband-phase-matching condition:

$$\left. \frac{\partial \Delta \vec{k}(\omega_s)}{\partial \omega_s} \right|_{\omega = \omega_{s0}} = \Delta \vec{k}(\omega_{s0}) = 0 \quad (1.109)$$

By splitting  $\Delta \vec{k}(\omega_s)$  into its components parallel and perpendicular to  $k_s$  (see Fig. 1.18)

$$\Delta k_{\parallel} = k_p \cos(\Psi) - k_s - k_i \cos(\Omega) \quad (1.110)$$

$$\Delta k_{\perp} = k_p \sin(\Psi) - k_i \sin(\Omega), \quad (1.111)$$

we can calculate the derivative of each with respect to  $\omega_s$  ( $k_p$  does not depend on  $\omega_s$ ), which has to be zero:

$$0 = \frac{\partial \Delta k_{\parallel}}{\partial \omega_s} = -\frac{\partial k_s}{\partial \omega_s} - \frac{\partial k_i}{\partial \omega_s} \cos \Omega + k_i \sin(\Omega) \frac{\partial \Omega}{\partial \omega_s}, \quad (1.112)$$

$$0 = \frac{\partial \Delta k_{\perp}}{\partial \omega_s} = -\frac{\partial k_i}{\partial \omega_s} \sin(\Omega) - k_i \cos(\Omega) \frac{\partial \Omega}{\partial \omega_s}. \quad (1.113)$$

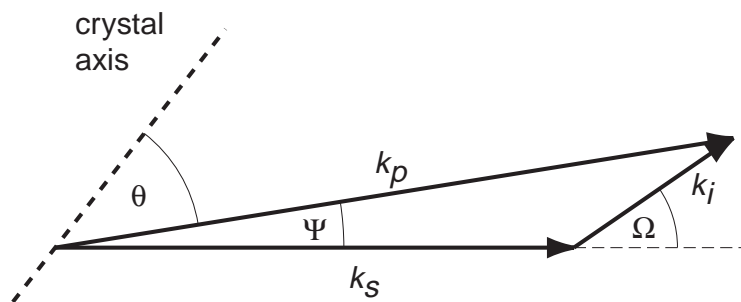


**Figure 1.18:** Vectorial phase matching used in broad-band noncollinear optical parametric amplification (NOPA). The pump photons are converted to signal and idler photons, for which a phase-matched geometry has to be realized. By sacrificing the constraint of collinearity we can achieve phase matching not only for a particular set of three frequencies but for a range of frequencies around a given central one. This allows for the amplification of very broad spectra, leading to very short tunable pulses.

Multiplication of Eq. (1.112) with  $\cos(\Omega)$ , Eq. (1.113) with  $\sin(\Omega)$  and addition of both equations leads us to

$$\frac{\partial k_s}{\partial \omega_s} \cos(\Omega) + \frac{\partial k_i}{\partial \omega_s} = 0. \quad (1.114)$$

This equation can be rewritten in terms of the group velocities (having in mind the photon energy conservation law,  $\omega_p = \omega_s + \omega_i$ )

$$v_{g,s} = \frac{1}{\frac{\partial k_s}{\partial \omega_s}}, \quad (1.115)$$

$$v_{g,i} = \frac{1}{\frac{\partial k_i}{\partial \omega_i}} = -\frac{1}{\frac{\partial k_i}{\partial \omega_s}} \quad (1.116)$$

as

$$v_{g,s} = v_{g,i} \cos(\Omega). \quad (1.117)$$

This relation can be interpreted in the following way. As the signal pulse propagates through the crystal with group velocity  $v_{g,s}$ , the group velocity of the idler pulse  $v_{g,i}$  projected onto the propagation direction of the signal is the same in the case of broad-band phase matching (Fig. 1.19b). This allows amplification of very short pulses down to 4 fs [94] in the visible by the use of noncollinear optical parametric amplification (NOPA) [95]. Details about the operation of a NOPA can be found in [96, 97].

### 1.2.3.3 Self-Phase Modulation (SPM)

In the linear regime of optics, the index of refraction does not depend on the intensity of the light. This is due to the linear response of the electrons, leading to a dipole moment that is directly proportional to the electric field applied. For higher and higher intensities, however, this is no longer true. For high electric fields, the induced dipole moment will not be linearly proportional to the applied electric field anymore, which therefore leads to

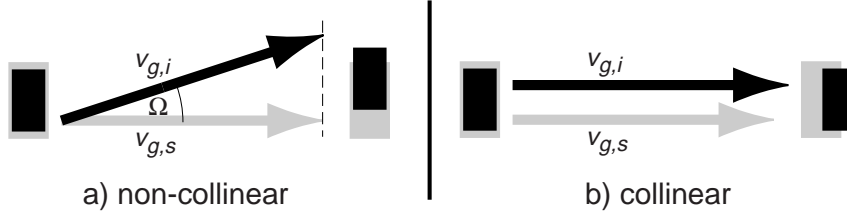


**Figure 1.19:** The condition of broad-band phase matching can be understood in terms of the group velocities of signal and idler. For the noncollinear case (a) the pulse fronts of signal and idler pulses copropagate along a given direction. Very short pulses can therefore be amplified. In the collinear geometry (b), the pulse fronts advance at different velocities, smearing out the generated pulses. The minimum achievable pulse duration in this case is longer than in the noncollinear case.

a different refractive index, now depending on the intensity. We can expand the intensity dependent refractive index in a Taylor series

$$n(I) = n_0 + n_2 I(t) + \dots, \quad (1.118)$$

where  $n_2$  is called nonlinear index coefficient. Its origin lies in the  $\chi^{(3)}$  nonlinear susceptibility tensor. Writing the third order nonlinear polarization Eq. (1.59) for monochromatic pump light using Eq. (1.73), we obtain

$$P^{(3)}(t) = \epsilon_0 \chi^{(3)} E(t)^3 = \epsilon_0 \chi^{(3)} \left( \frac{3}{8} |A|^2 A e^{i\omega t} + \frac{1}{8} A^3 e^{i3\omega t} \right) \quad (1.119)$$

The first summand is responsible for the intensity dependent index of refraction, as can be seen by inserting it as a source into the wave equation (1.56). The second summand produces the third harmonic, which we will not discuss here. Since the intensity of the laser pulse is a function of time, the laser pulse will be subject to a changing index of refraction at any point in space. Let us first of all assume an initially monochromatic electric field subject to a time-dependent refractive index

$$E^+(z, t) = A e^{i(\omega t - kz)} = A e^{i(\omega t - n(t) \frac{\omega}{c} z)} = A e^{i\phi(t)}. \quad (1.120)$$

We know from Eq. (1.15) that the instantaneous frequency of the light is given by

$$\omega = \frac{d\phi(t)}{dt} = \omega - \frac{dn(t)}{dt} \frac{\omega}{c} z \quad (1.121)$$

The time-dependent refractive index thus causes a frequency shift of the light. The effect increases with propagation length  $z$ . Since  $n_2$  is positive in most materials, a compact laser pulse (the intensity is monotonously increasing up to a maximum and monotonously decreasing afterwards) will experience a rising refractive index on the leading edge and a decreasing one at the trailing edge. This leads to the generation of additional red frequencies at the leading and blue frequencies at the trailing edge. However, the temporal amplitude of the laser pulse is not affected, i.e. only the phase is modified, hence the name ‘self-phase modulation’. The laser pulse modifies its own temporal phase by its intensity

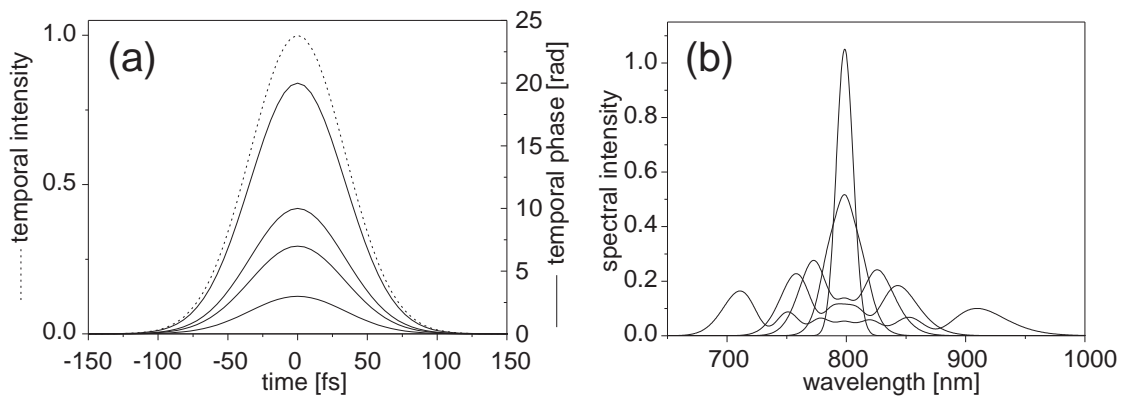


**Figure 1.20:** The effect of self-phase modulation on bandwidth-limited ultrashort laser pulses. An intensity dependent index of refraction generates a temporal phase profile (a) (solid line) that mimics the temporal intensity of the laser pulse (dotted line). For increasing interaction length or nonlinear refractive index  $n_2$ , the maximum temporal phase is steadily increased. Likewise, the spectral width (b) is increasing. This effect can be used in order to compress ultrashort laser pulses to even shorter durations, since a larger spectral extent results in a smaller bandwidth limited pulse duration.

profile. In Fig. 1.20 the effect of an increasing propagation length is shown as the pulse travels through medium exhibiting an intensity-dependent nonlinear refractive index.

By deriving  $P^{(3)}$  in Eq. (1.119) for the case of an ultrashort laser pulse (which contains more than one frequency) it can be seen that  $P^{(3)}$  contains frequencies composed of the sum of two frequencies contained in the pulse's spectrum minus a third one, which also belongs to the spectrum. Therefore, we can summarize the self-phase modulation process:

$$\text{self-phase modulation : } \hbar(\omega_1) \pm (\hbar(\omega_2) - \hbar(\omega_3)) \rightarrow \hbar(\omega_1 \pm (\omega_2 - \omega_3)) \quad (1.122)$$

We see that the spectrum becomes broadened to either side by creating new frequencies as a combination of available ones.

Self-phase modulation finds a number of applications in nonlinear optics. For example, it can be used to broaden the spectrum of ultrashort pulses in order to compress them to even shorter time durations. Typically, amplified laser pulses are sent through gas-filled hollow fibers [98, 99]. This is a technique also used for the experiments conducted in this work and will be addressed in more detail below. It is even possible to use a cascade of hollow fibers to generate more and more bandwidth [100]. Another application is the generation of spectral continua of white-light in order to seed NOPAs [95]. In this case, the signal in the NOPA is not generated from a quantum fluctuation but the seed is provided by real photons in the coherent white light. Spectral white-light continua also serve as invaluable tools in time-resolved spectroscopy for example in chirped supercontinuum probing [101]. A detailed review of self-phase modulation for supercontinuum generation can be found in [102].





## Chapter 2

# High-Harmonic Generation

The main topic of this work is the optimization and engineering of coherent light in the soft x-ray region. It is therefore necessary to describe the particular nonlinear process employed, which is high-harmonic generation (HHG). First studies were performed in the late 1980s [103, 104]. A plateau of equally intense harmonics of high order was observed, which was not immediately understood. Applying perturbation theory one would expect a rapid decrease in efficiency with increasing harmonic order: in the framework of  $n$ -photon excitation, the excitation probability decreases exponentially with  $n$  as explained in Section 1.2. However, since there was a large number of equally strong harmonic peaks, another mechanism had to be found to explain the results. In 1993 Corkum [105] and Kulander *et al.* [106] published a quasiclassical theory, which reproduced the plateau behavior of harmonic emission found in the experiments. According to these works, the electron can not be treated as a bound particle in the high electric fields at work in the experiments, which had so far been assumed. In fact, the electron is ionized (freed from the binding force of the nucleus) when the absolute electric field of the laser is close to its peak during an optical cycle and is driven away from the parent ion. Since the laser electric field changes its sign about a quarter of a period later, the electron will slow down, stop at a position far from the ion and start to reaccelerate towards it. When it returns to the ion, it can possess a significant amount of kinetic energy, much larger than the photon energy. This energy plus the ionization potential will be transferred into photon energy as soon as the electron recombines with its parent ion, which gives rise to the very high harmonic orders observed in the experiment. It is thus three steps which make up the model: Ionization, propagation in the laser field, and recombination. The model has therefore been named ‘three-step model’ or also ‘simple-man’s model’, due to its striking simplicity. As this three-step process—and therefore also high-energy photon emission—usually occurs every half-cycle of the laser field it is immediately clear that the spectrum of the produced radiation has to consist of peaks at odd integer multiples of the laser frequency. Inspired by Kulander’s and Corkum’s idea, a fully quantum-mechanical treatment of the three-step model has also been found shortly after its introduction [107, 108] which confirmed the validity of the classical approximation. It is a very intriguing aspect of nonlinear physics that highly nonlinear effects (as the process of high-harmonic generation indeed is) can be treated with high accuracy by considering simple models.

Typical high-harmonic spectra are shown in Fig. 2.1. As was mentioned, the harmonic in-

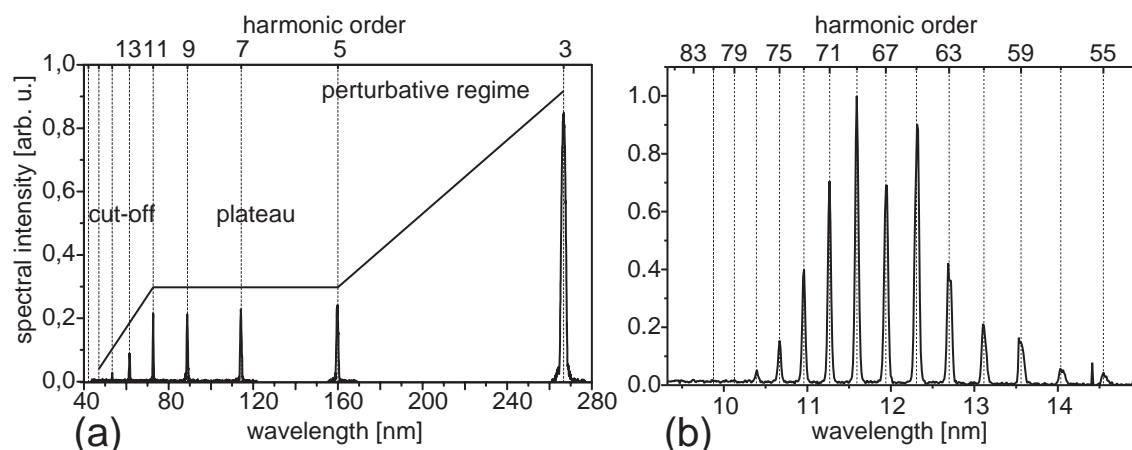


**Figure 2.1:** Typical spectra produced in high harmonic generation. (a) A full harmonic spectrum generated in xenon gas shows the characteristic spectral shape (from [109]). For low orders, the harmonic intensity is rapidly decreasing. A plateau is visible for the higher orders which is terminated at the cut-off, the highest harmonics that are generated. The spectral position of the plateau depends on both, the gas species used and the intensity of the driving light. Another measurement in neon reveals very high harmonic orders (b). Lower orders are less intense due to the zirconium filter used to separate fundamental and harmonic light.

tensity decreases rapidly for low harmonic orders (the so-called perturbative region). For higher orders, a plateau of equally intense harmonics is found, which extends up to the cut-off harmonic order. In the following, the mechanism of high-harmonic generation will be discussed in more detail (reviews can also be found in [89, 110]). First of all the single particle response is considered in Section 2.1, since it is this microscopic process outlined above which generates the harmonic frequencies in the first place. High-harmonic generation is not a process involving only one single atom but many of them which are coherently stimulated by the laser. For that reason, the importance of propagation effects, including phase-matching schemes and distortions, are addressed in Section 2.2. High-harmonic generation can be employed to produce the shortest pulses of light ever created in the laboratory. The duration of these pulses is on the order of hundreds of attoseconds, far shorter than the optical cycle of the laser light. Attosecond-pulse generation will be discussed in Section 2.3. Finally, this chapter concludes with the potential applications of ultrafast x-rays in Section 2.4.

## 2.1 Single Particle Response

As has just been mentioned, the process of high-harmonic generation can be broken up into three steps: ionization, propagation and recombination. Each of these fundamental processes will now be discussed separately.

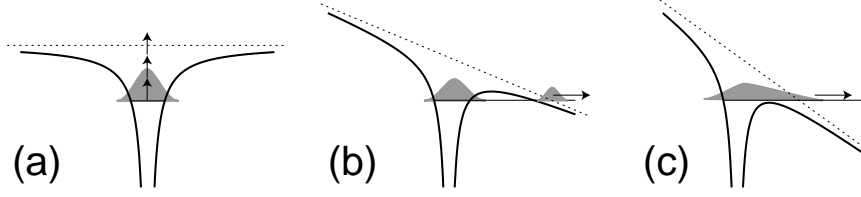


**Figure 2.2:** Different ionization scenarios. If the ionization potential is low compared to the frequency of the light and large compared to the electric field of the laser the absorption of multiple photons is the dominant ionization mechanism (multiphoton ionization (a)). If the electric field strength is increased, the coulomb potential is significantly modified. If the frequency of light is low enough such that the electron can respond to this changing potential, ionization can be understood as the tunneling of the electron through a static potential wall (tunnel ionization (b)). If the electric field is yet higher, the barrier is completely suppressed and the electron will be classically “ripped off” the ion (barrier-suppressed ionization (c)).

### 2.1.1 Ionization — Step I

If the intensity of light interacting with matter is steadily increased, the electric field of the electromagnetic wave  $E(t) = E_0 \cos(\omega t)$  at some point outgrows the intratomic field strength (i.e. the average field strength sensed by the electron). At this intensity, the laser electric field (at its maximum) is strong enough to literally ‘rip off’ the electron from the ion. However, already at lower values of the electric field, the electron can escape the binding potential of the atom through tunneling. The electric field of the laser will produce a potential  $e\vec{E}(t)\vec{r}$  in addition to the Coulomb potential of the ion:

$$V(\vec{r}, t) = -\frac{e^2}{4\pi\epsilon_0 r} + e\vec{E}(t)\vec{r} \quad (2.1)$$

As a result, the Coulomb potential is significantly distorted (Fig. 2.2b). A barrier is created for the bound electronic state, which can be overcome by tunneling, upon which the electron can be considered to be free, only affected by the electric field of the laser (note the proximity of the asymptote to the real potential at the appearance position of the electron in Fig. 2.2b). This process of tunnel ionization has been treated in detail in the literature. The first notion by Keldysh [111] dates back to 1965. He calculated an analytical formula for the ionization rate  $w$  of the Hydrogen atom exposed to a strong electric field  $E$  in the quasi-static limit:

$$w_K = \frac{\sqrt{6\pi}I_p}{4\hbar} \left( \frac{eE\hbar}{m^{1/2}I_p^{3/2}} \right)^{1/2} \exp \left( -\frac{4\sqrt{2m}I_p^{3/2}}{e\hbar E} \left( 1 - \frac{m\omega^2 I_p}{5e^2 E^2} \right) \right), \quad (2.2)$$

where  $e$  and  $m$  are unit charge and electron mass, respectively, and  $I_p$  denotes the ionization potential.

Much later, in 1986, Ammosov, Delone, and Krainov published a generalized analytical theory [112] extending Keldysh’s approach to arbitrary atoms and initial electronic states.

Their calculated ionization rate, which agreed very well with experimental findings, is now known as the ADK ionization rate. It reads (atomic units  $\hbar = m = e = 1$  are used here)

$$w_{\text{ADK}} = \sqrt{\frac{3E}{\pi(2I_p)^{\frac{3}{2}}}} |C_{n^*l^*}|^2 f(l, m) I_p \left( \frac{2(2I_p)^{\frac{3}{2}}}{E} \right)^{\left( \frac{2Z}{\sqrt{2I_p}} - |m| - 1 \right)} \exp\left( -\frac{2(2I_p)^{\frac{3}{2}}}{3E} \right), \quad (2.3)$$

with the (time dependent) electric field strength  $E$ , the ionization potential  $I_p$ , the ion charge  $Z$  (once the electron is detached),  $l$  and  $m$  represent the angular momentum and magnetic quantum number, respectively. Further, the factor  $f(l, m)$  is given by

$$f(l, m) = \frac{(2l+1)(l+|m|)!}{2^{|m|}(|m|)!(l-|m|)!},$$

and the constant  $C_{n^*l^*}$  is on the order of 2, but more precisely

$$|C_{n^*l^*}|^2 = \frac{2^{2n^*}}{n^* \Gamma(n^* + l^* + 1) \Gamma(n^* - l^*)}.$$

The effective principal and angular momentum quantum number are given by  $n^* = Z(2I_p)^{-1/2}$  and  $l^* = n^* - 1$ , respectively.

The work of Keldysh contained another important finding. He determined for which range of laser field strengths  $E_0$  and angular frequency  $\omega$ —together defining the so-called ponderomotive potential  $U_p = E_0^2/(4m\omega^2)$  in atomic units—in combination with a particular ionization potential  $I_p$  the tunneling description is valid. He introduced a parameter

$$\gamma = \sqrt{\frac{I_p}{2U_p}}, \quad (2.4)$$

which is now called ‘Keldysh parameter’. By use of this quantity we are able to determine whether the atom is ionized in the tunnel ( $\gamma \ll 1$ ) or the multiphoton regime ( $\gamma \gg 1$ ). To understand this in a qualitative way we can imagine the laser-distorted Coulomb potential to oscillate with the laser frequency. For higher and higher frequency (larger and larger  $\gamma$ ), the quasi-static approximation breaks down and the electron does not have enough time to accommodate to the fast changes in the potential. Its motion will be governed by an average over many cycles of the laser field rather than tunneling in a single cycle, since the tunneling time—depending on  $E_0$  and  $I_p$ —is larger than the optical period. The steady nonlinear interaction with the laser field (absorption of many photons) will finally lead to an electronic state with an energy larger than zero, thus a free electron (Fig. 2.2a). In the opposite limiting case, the field of the laser can get high enough to fully suppress the barrier (Fig. 2.2c). The electron is then classically ‘ripped off’ the atom. This ionization scenario is called the ‘barrier-suppressed ionization’ [113]. It will now be discussed why the tunnel-ionization regime is best suited for high-harmonic generation.

## 2.1.2 Propagation — Step II

After the electron is ionized, it can approximately be treated to be interacting with the linearly polarized laser field only. To understand the motion of the electron, we first

regard an initially free classical electron interacting with a laser field  $E(t) = E_0 \cos(\omega t)$  and calculate its velocity

$$v(t) = \int_0^t -\frac{e}{m} E(t') dt' + v_0 = -\frac{E_0 e}{m\omega} \sin(\omega t) + v_0, \quad (2.5)$$

where vector arrows are omitted due to the one-dimensional motion of the electron. If we consider only electrons possessing a zero drift velocity  $v_0 = 0$ , their average kinetic energy  $\bar{E}_{\text{kin}}$  defines the ponderomotive potential  $U_p$  mentioned above, now in SI units:

$$U_p = \bar{E}_{\text{kin}} = \frac{e^2 E_0^2}{4m\omega^2}. \quad (2.6)$$

Note that  $U_p$  is proportional to  $E_0^2$ , which makes the average kinetic energy of the electrons grow linearly with laser intensity. The ponderomotive potential can be regarded as a unit measure for energy in the high-harmonic generation process.

Let us now consider an electron which is initially bound to an atom at  $x = 0$  to appear in the continuum (i.e. to be ionized) at time zero with initial velocity  $v_0 = 0$ . It is ionized at an arbitrary phase  $\varphi$  of the electric field  $E(t) = E_0 \cos(\omega t + \varphi)$ . Velocity  $v(t)$  and position  $x(t)$  can then be calculated to be:

$$v(t) = \int_0^t -\frac{e}{m} E(t') dt' = -\frac{E_0 e}{m\omega} (\sin(\omega t + \varphi) - \sin(\varphi)) \quad (2.7)$$

$$x(t) = \int_0^t v(t') dt' = \frac{E_0 e}{m\omega^2} (\cos(\omega t + \varphi) - \cos(\varphi)) + \sin(\varphi)t \quad (2.8)$$

The constant expression in the velocity can be understood as a drift velocity. If this term is zero, the electron will oscillate around a fixed reference position. If it is nonzero, the reference position will be moving in time. These electrons also have a higher average kinetic energy (larger than  $U_p$ ). The maximum kinetic energy of an electron can also be extracted from Eq. (2.7) to be  $8U_p$ . The amplitude  $E_0 e / m\omega^2 = a_0$  of the oscillatory position is sometimes referred to as the ponderomotive radius  $a_0$ . Typical values (at laser intensities  $\approx 10^{14} \text{ W/cm}^2$ ) are on the order of some nanometers, thus much larger than the atomic radius, demonstrating the validity to treat the electron as a freely moving particle in the laser field. Note that the ponderomotive radius is limited to a quarter of the wavelength for electrons moving close to the speed of light. These relativistically moving electrons of course need to be treated differently from above and are not within the scope of this work. The laser intensities needed to accelerate electrons to relativistic intensities are beyond  $10^{16} \text{ W/cm}^2$ , whereas the laser intensities used in this work are on the order of some  $10^{14} \text{ W/cm}^2$ . If we plot the electron trajectory versus time, we observe different paths for electrons that become ionized at different phases of the AC electric field (Fig. 2.3). In particular, only some electron trajectories return to the origin at  $x = 0$ , where the electron can recombine with the parent ion. In addition, only the first two encounters of the electron with the ion lead to significant photon emission. The reason for that is the quantum-mechanical nature of the electron, which suffers from dispersion (spreading of the wavefunction, thus the overlap with the atom becomes smaller) as soon as it is not bound to a potential. This will be treated in more detail below.

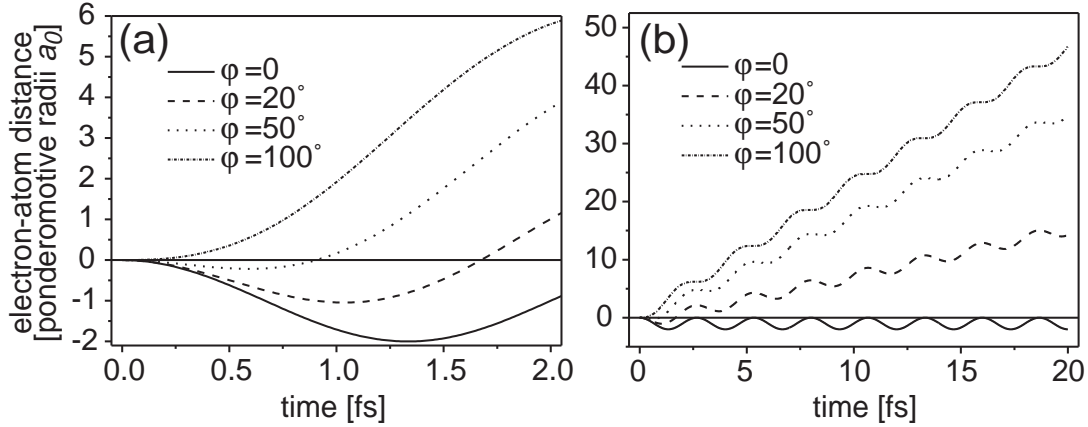


**Figure 2.3:** Electron trajectories in a laser electric field. Plotted is the distance to the atom versus time for a unidirectional motion in a linearly polarized laser field. (a) is an enlarged view of (b) for early times. Electrons that ionize at different phases of the AC-field travel different paths. Only some of them reencounter the atom, leading to possible recombination. The absolute value of the slope of the electron trajectory at the zero crossings is the velocity and thus a measure for the kinetic energy of the electron. Its highest value is reached at an ionizing phase of the laser close to  $20^\circ$ .

### 2.1.3 Recombination — Step III

When an electron recombines with an ion, typically a photon is emitted carrying away the excess energy of the electron. In particular, the electrons accelerated in the laser field emit a high harmonic photon with energy

$$\hbar\omega_n = E_{\text{kin}} + I_p \quad (2.9)$$

where  $E_{\text{kin}}$  is the kinetic energy of the electron acquired in the laser field and  $I_p$  is the ionization potential. As can be seen in Fig. 2.3, the slope of the trajectory at the intersection with  $x = 0$  assumes different values, corresponding to different velocities and thus different kinetic energies. In particular, there exists a maximum kinetic energy that the electron can have when it reencounters its parent ion. This maximum kinetic energy therefore corresponds to the maximum photon energy which can be generated in the process. By solving the equation  $x(t) = 0$  numerically and calculating the kinetic energy for various phases  $\phi$ , we can calculate this maximum kinetic energy to be  $\sim 3.17U_p$  (Fig. 2.4). It occurs at a phase of  $18^\circ$ . Electrons that are ionized at this moment of time produce harmonic photons of the highest energy. We expect the high-harmonic soft x-ray spectrum to vanish (to be cut off) at photon energies higher than

$$\hbar\omega_c = 3.17U_p + I_p, \quad (2.10)$$

which indeed is the case in experiments. This formula is commonly called the ‘cut-off’ law for high-harmonic generation. It is another example for the remarkable agreement of the three-step model [105] with experimental data. Before the idea of the semi-classical

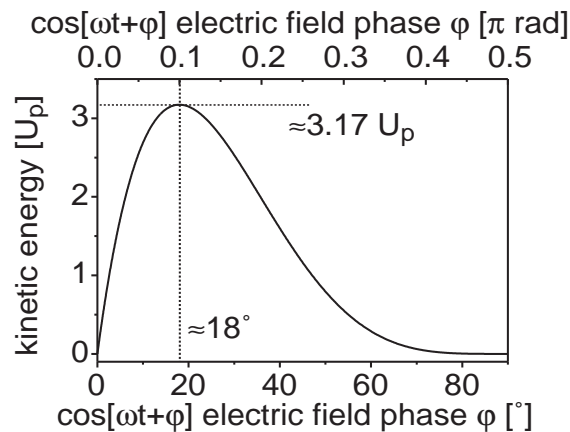


**Figure 2.4:** Kinetic energy of the electrons at the moment of reencounter for various phases  $\varphi$  of the driving laser field. A maximum exists at a phase of  $18^\circ$ .

three-step model was published, Kulander and coworkers empirically introduced this cut-off law formula [114].

It can now also be understood why the tunneling regime supports the generation of high-harmonic radiation. The highest photon energies are produced when electrons ionize at a phase of  $18^\circ$ , which is close to the peak of the electric field in the optical wave. In the tunnel-ionization regime, the ionization rate given by Eqs. (2.2) and (2.3) is increasing with the electric field. Therefore, the many ionized electrons will contribute to high-harmonic generation. On the other hand, in the multiphoton-ionization regime electrons are continuously produced, only depending on the intensity of the field not on the phase of the carrier. This leads to a “wasting” of electronic trajectories for harmonic generation, namely of those that are ionized in the regions far away from the optimum phases around  $18^\circ$ . It is also clear from considering the cut-off formula Eq. (2.10) that in order to generate the highest harmonic orders, we need to provide a large ponderomotive potential  $U_p$ . This is also fulfilled in the tunneling regime of ionization, where the Keldysh parameter  $\gamma$  defined in Eq. (2.4) has to be much smaller than unity.

In Fig. 2.5 the three-step model is summarized. What has not been discussed so far is the fact that harmonic *peaks* exist at *odd integer* multiples of the fundamental frequency  $f$ . We can understand this by considering the temporal structure of the high-harmonic emission. The three-step process repeats every half-cycle  $T/2$  of the laser field. The Fourier transform will thus be discrete, with a separation corresponding to  $1/T/2 = 2f$ , which is what we observe in the spectrum. If the conversion medium exhibits a broken inversion symmetry (as will be shown in Chapter 3), harmonic emission will not occur the same way every half-cycle but every full cycle of the laser field. In the harmonic spectrum this gives rise to an harmonic peak spacing of one times the laser frequency, thus odd and even harmonic orders are produced. Another way to break inversion symmetry is to drive a plasma at very high intensities, where the magnetic field of the laser becomes high enough to break the inversion symmetry. This occurs in the process of nonlinear Thompson scattering [115]. In this case the laser intensities are on the order of more than  $10^{18}\text{W/cm}^2$  and the free-electron motion is not harmonic anymore as described by

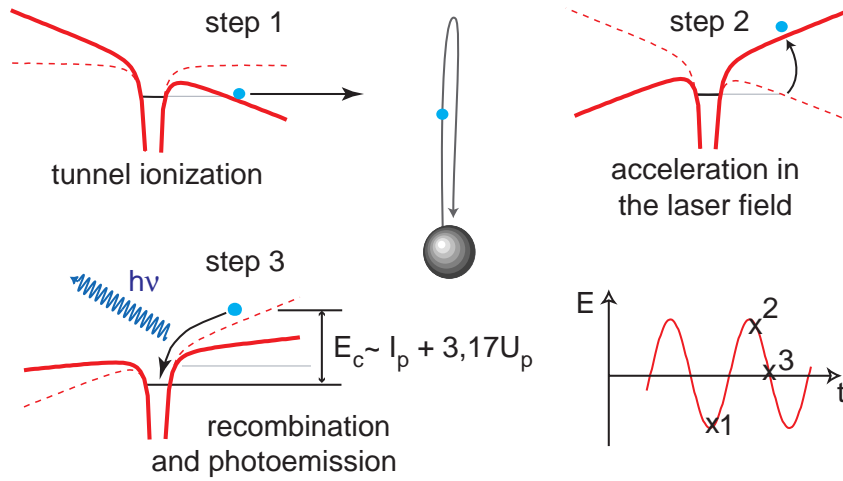


**Figure 2.5:** Summary of the three-step model. The electron is ionized in step 1 at some particular phase of the electric field. It is then driven away from the parent ion in the laser field (step 2). After sign reversal of the AC-field, the electron stops far from the atom, possibly returns and recombines to emit a photon carrying the kinetic energy of the electron plus its ionization potential (step 3). The kinetic energy of the returning electron can be as high as  $3.17 U_p$ , defining the so-called cut-off photon energy in the harmonic spectrum.

the classical propagation equation (2.8). It is strongly influenced by the relativistic mass increase of the electron and the high magnetic fields. This leads to the well-known non-linear ‘figure of eight’-motion of the electron, which again radiates harmonics at even and odd frequencies. Yet another possibility to generate even harmonics is the use of few-optical-cycle duration laser pulses. In this regime, where the absolute phase of the laser pulse becomes important (Section 1.1.2), the situation for the atom is also different for successive half-cycles and even harmonic orders and coherent continuum radiation can be generated.

It should be stated here that high-harmonic generation represents only one class of strong-field nonlinear processes. The two most important processes other than high-harmonic generation are called non-sequential double ionization and above-threshold ionization (ATI). Any of these processes can be understood in the framework of the three-step model that was introduced above.

In non-sequential double ionization [116, 117], a characteristic intensity dependence of doubly ionized atomic ions was reported that followed the intensity dependence of single ionization. A “knee” was obtained in the intensity dependence exactly at the point where single ionization saturated, indicating that both processes are coupled. The coupling can again be understood in terms of the three-step model [105]. The first electron is tunnel ionized and accelerated in the laser field. When it returns to the ion, the high kinetic energy can be sufficient to “knock out” a second electron.

In above-threshold ionization [118, 119] high-energy photo electrons are detected at inte-



ger multiples of the photon energy. Again, the photo-electron spectra show a characteristic plateau structure, reminiscent of the plateau of photon energies obtained in high-harmonic generation. The high kinetic energy and the peaked structure of the electrons can again be explained by the three-step model [105]: The tunnel-ionized electron that is accelerated to high kinetic energies by the laser field can scatter off its parent-ion. This scattering event changes the motion of the electron in such a way that it can reach very high energies after further acceleration by the laser field.

The common aspect in all these effects is the interaction of a tunnel-ionized free electron, accelerated in the laser field, with its ion core. Only the particular kind of interaction with the core differentiates between these processes. Elastic or inelastic scattering of the electron with the ion core leads to above-threshold ionization or non-sequential double ionization, respectively. Recombination of the electron with the core produces high-harmonic radiation.

Strong-field process	$\Leftrightarrow$	electron-core interaction
High-harmonic generation	$\Leftrightarrow$	recombination
Non-sequential double ionization	$\Leftrightarrow$	inelastic scattering
Above-threshold ionization	$\Leftrightarrow$	elastic scattering

The electron always has to revisit the core in order for any of these processes to occur. Therefore the term ‘rescattering’ scenario is nowadays frequently used to describe these strong-field effects.

### 2.1.4 Quantum-Mechanical Description

We now turn towards the quantum-mechanical formulation of the three-step model, which has been found by Lewenstein *et al.* [107, 108]. As has been pointed out in Section 1.2, the source of additional frequencies to be generated besides the fundamental incoming laser frequency is the nonlinear dipole oscillation of the medium. We thus have to calculate the dipole response for the special case of high-harmonic generation. The Schrödinger equation in this case is given by (in atomic units)

$$i \frac{\partial}{\partial t} |\psi(\vec{r}, t)\rangle = \left( -\frac{1}{2} \nabla^2 + V(\vec{r}) + \vec{r} \vec{E} \cos(\omega t) \right) |\psi(\vec{r}, t)\rangle. \quad (2.11)$$

We need to calculate the time-dependent dipole moment,

$$\vec{\mu}(t) = \langle \psi(\vec{r}, t) | -\vec{r} | \psi(\vec{r}, t) \rangle, \quad (2.12)$$

from which we can then extract the harmonic spectrum by Fourier transformation. The calculation presented in [107] expands the time-dependent electron wavefunction (where only one electron is considered to be responsible for harmonic generation, which is often referred to as ‘single-active electron approximation’ (SAE) in the literature [106, 120]) in terms of the bound electron ground state of the atom and the continuum states  $|\vec{v}\rangle$  where  $v$  stands for the kinetic momentum

$$|\psi(\vec{r}, t)\rangle = e^{i\mu t} \left( a(t) |0\rangle + \int b(\vec{v}, t) |\vec{v}\rangle d^3\vec{v} \right), \quad (2.13)$$

with time-dependent ground-state  $a(t)$  and continuum-state amplitudes  $b(\vec{v}, t)$ . By doing so, we do not take into account excited bound states of the electron. Since the continuum states are defined to be solutions to the free electron Schrödinger equation,

$$E_{\text{kin}} |\vec{v}\rangle = -\frac{1}{2} \nabla^2 |\vec{v}\rangle, \quad (2.14)$$

the potential of the nucleus is neglected as soon as the electron is ionized. Using the definition of the time-dependent electron wavefunction in Eq. (2.13), the time-dependent dipole moment can be calculated to be

$$\begin{aligned} \vec{\mu}(t) = & i \int_0^t dt' \int d^3\vec{p} E \cos(\omega t') \times \\ & \underbrace{\left( \vec{d}(\vec{p} - \vec{A}(t')) \right)}_{\text{'a'}} \times \underbrace{\exp(-iS(\vec{p}, t, t'))}_{\text{'b'}} \times \underbrace{\vec{d}^*(\vec{p} - \vec{A}(t'))}_{\text{'c'}} + c.c. \end{aligned} \quad (2.15)$$

$\vec{A}(t)$  is the vector potential of the laser field. The canonical momentum  $\vec{p}$  is given by

$$\vec{p} = \vec{v} + \vec{A}(t). \quad (2.16)$$

$S$  denotes the so-called quasi-classical action and is written as

$$S(\vec{p}, t, t') = \int_{t'}^t dt'' \left( \frac{(\vec{p} - \vec{A}(t''))^2}{2} + I_p \right) \quad (2.17)$$

It contains the phase advance of the electron during the time it spends in the continuum. The atomic potential only enters as a constant ionization potential  $I_p$ . The expression  $\vec{d}(\vec{v})$  in Eq. (2.15) stands for the transition probability from the bound electronic state  $|0\rangle$  to a continuum state  $|\vec{v}\rangle$  (describing ionization), where the complex conjugate describes the inverse process, i.e. recombination of the free electron to the ground state

$$\vec{d}(\vec{v}) = \langle \vec{v} | \vec{r} | 0 \rangle \quad (2.18)$$

$$\vec{d}^*(\vec{v}) = \langle 0 | \vec{r} | \vec{v} \rangle. \quad (2.19)$$

This helps us to find a very intuitive interpretation of the formula of the time-dependent dipole moment  $\vec{\mu}(t)$  in Eq. (2.15). We can now straightforwardly identify the different parts of the formula

- 'a' : ionization of the ground state at time  $t'$ ,
- 'b' : propagation in the continuum in the time interval  $t - t'$ ,
- 'c' : recombination to the ground state at time  $t$ .

Thus, the classical three-step model discussed before is contained in the quantum-mechanical description as well. It also resembles Feynman's path integral description of quantum mechanical processes [121]. To calculate  $\mu(t)$ , we do not need to calculate

the integral over all  $\vec{p}$ . We only need to consider the  $\vec{p}$  for which the action becomes stationary

$$\vec{\nabla}_p S(\vec{p}, t, t') = 0 \quad (2.20)$$

This relation can again be interpreted in terms of the classical three-step model. Since

$$\vec{\nabla}_p S(\vec{p}, t, t') = \vec{x}(t) - \vec{x}(t'), \quad (2.21)$$

the stationary phase condition Eq. (2.20) yields the information that we only need to account for those electron trajectories that return at time  $t$  to the same point they left at time  $t'$  where they were ionized. Most importantly, the quantum-mechanical treatment also yields the classical cut-off law Eq. (2.10) up to a small correction. By Fourier transforming the time-dependent dipole moment, the harmonic spectra can be calculated and analyzed, the cut-off photon energy can now be found to be

$$\hbar\hat{\omega}_c = 3.17U_p + f\left(\frac{I_p}{U_p}\right)I_p, \quad (2.22)$$

where  $f(x)$  is a slowly varying function on the order of 1, which assumes the values  $f(0) \approx 1.32$  at  $x = 0$  ( $U_p \gg I_p$ ) and  $f(3) \approx 1.25$ . The physical origin of this correction lies in purely quantum-mechanical effects like tunneling and the spreading of the electron wavepacket in the continuum that have not been included in the purely classical treatment. These effects enable the electron to collect more energy on its trajectory than the amount predicted by the classical equations of motion.

According to the formula for the dipole moment Eq. (2.15), different electron trajectories contained in the integral acquire different phases  $\varphi_{\text{at}} = S(p, t, t')$  (called the atomic dipole phases) during their propagation in the continuum. The shape of the electronic wavepacket at the moment of recombination will be governed by interference between these separate quantum paths. In particular, different trajectories leading to the same photon energy (having the same kinetic energy at the time of recombination) will interfere with each other. Reexamination of the classically calculated kinetic energy of the electron (which agrees very well with the quantum-mechanical result) at the moment of return to the nucleus reveals that each kinetic energy in the plateau region of an electron can be produced by two distinct particular phases of the electric field at the moment of ionization (see Fig. 2.6). Therefore, there are two electron trajectories which are most important for the generation of a particular photon energy. Since one of them spends a longer time in the continuum, we call it the ‘long trajectory’ (the one ionizing at a smaller phase of the electric field), the other one is called ‘short trajectory’. These trajectories will interfere constructively or destructively, depending on their relative dipole phase. Since the electric field enters the dipole phase, it can be used to modify this interference. Hence, one possibility to control the harmonic generation process is to manipulate the atomic dipole phase with a shaped laser field [122, 123].

It can be shown by careful analysis that only one of the two trajectories mentioned (the long trajectory) exhibits a phase that is linearly proportional to the laser intensity  $I$ , while the phase of the other (short) one is almost constant [124, 125]:

$$\frac{d\varphi_{\text{at},l}}{dI} = a, \quad \frac{d\varphi_{\text{at},s}}{dI} \approx 0, \quad (2.23)$$

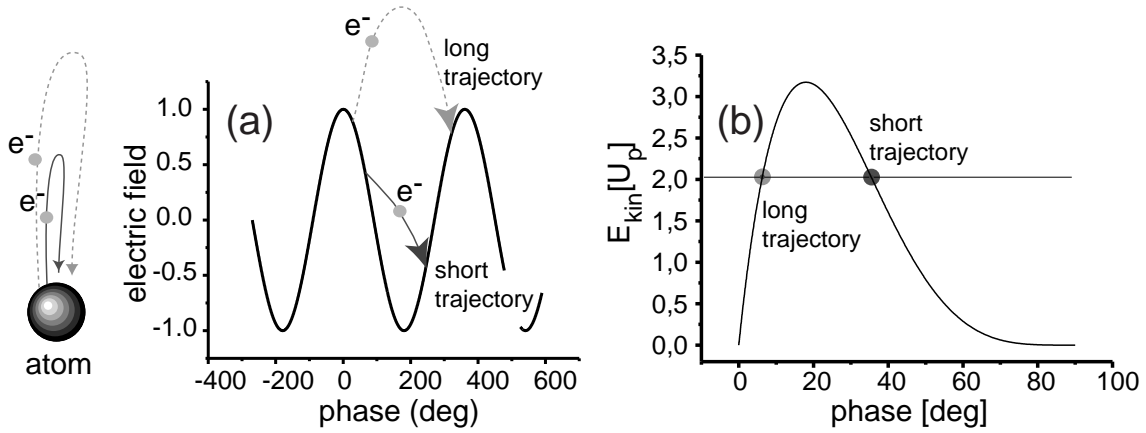


**Figure 2.6:** Atomic dipole phase. For the generation of a particular photon energy in high-harmonic generation, two electron trajectories (a) contribute that ionize at different phases of the electric field (b). They spend different times in the continuum, giving rise to different phases of their nonlinear atomic dipole contribution. One of these phases is linearly proportional to the intensity of the laser field, while the intensity dependence of the other one can be neglected. Interference between these trajectories is one way to control the high-harmonic-generation process.

where  $\varphi_{\text{at,l}}$  and  $\varphi_{\text{at,s}}$  denote the atomic dipole phases of the long and the short trajectory, respectively and  $a$  is some constant on the order of  $26 \times 10^{14} \text{ cm}^2/\text{W}$ .

The effect of this intensity-dependent nonlinear dipole phase becomes evident in modifications of the spectral line shape of high-harmonics [121]. In addition, the spatial properties of harmonic generation in the near-field region [126] and the beam profile [127] are altered as a consequence of the intensity dependence.

This dependence is also responsible for the linear chirp (quadratic phase) imposed on the high harmonics. Since the laser pulse intensity at the peak of the laser pulse can be approximated to vary quadratically with respect to time, the same temporal dependence will be imparted on the temporal high-harmonic phase [128, 129].

In conclusion, high-harmonic generation is an example of how the coherence properties of the laser can be transferred to the electronic wavefunction. Another recent demonstration of coherence transfer from laser light to electrons concentrated on the direct measurement of the momentum wavefunction of free electrons [130]. It was shown that the free electrons created by phase-coherent double pulse excitation exhibit a clear signature of wavepacket interference in the continuum.

### 2.1.5 Numerical Calculation

Another approach to model the single particle response in high-harmonic generation is to directly solve the time dependent Schrödinger equation Eq. (2.11) numerically on a computer (see Appendix C for details). The space in which the atom and the electron are contained is discretized into boxes. An initial state is specified which is iteratively propagated in time by performing successive time steps  $\Delta t$ . The time-dependent dipole acceleration that enters the wave equation as the second derivative of polarization with

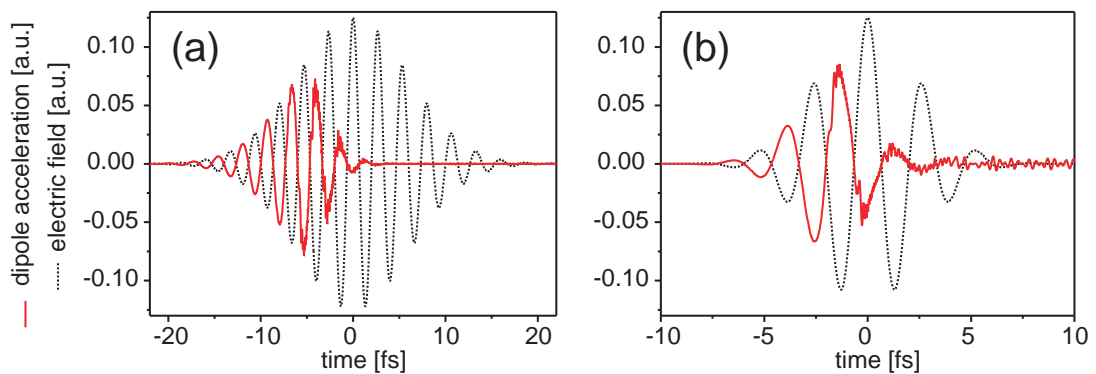


**Figure 2.7:** Time-dependent dipole acceleration value (solid line) and electric field of the driving pulse (dotted line). Shown is the interaction of a 4 fs (a) and a 10 fs (b) laser pulse with a hydrogen atom. The peak intensity in both cases corresponds to  $5.5 \times 10^{14}$  W/cm<sup>2</sup>.

respect to time is evaluated and Fourier analyzed to calculate the nonlinear frequencies (high harmonics) generated. This is done by applying the Ehrenfest theorem:

$$\frac{d^2}{dt^2} \vec{d}(t) = \frac{d^2}{dt^2} \langle \vec{r}(t) \rangle = \langle \vec{\nabla} V \rangle. \quad (2.24)$$

It has been found [131] that direct evaluation of the dipole acceleration has advantages over initial calculation of the time-dependent dipole and then calculating its second derivative with respect to time. Although in mathematical terms there should be no difference, numerical noise in simulations makes the direct calculation via Eq. (2.24) more reliable. Fig. 2.7 shows the time-dependent dipole acceleration for an atom. Although an arbitrary degree of precision can be reached in principle, limits arise by computation speed. To understand the basic features of the process, however, we can retreat to lower-dimensional models and carry out the simulation in two- or one-dimensional space.

Since we directly evolve the wavefunction in space and time, the numerical approach allows for a straightforward monitoring of the microscopic electronic motion in the process. Snapshots at different times can be used to generate movies of the time-dependent electronic wavefunction (see Fig. 2.8). The numerical simulation is helpful for the study of more complex systems like molecules (see Chapter 3) for which it is hard to find accurate analytical expressions. Any analytical theory and simulation discussed in here, however, has been and will be restricted to the single-active-electron approximation, which means that only one electron contributes to the process of high-harmonic generation. This is of course not valid in any physical medium and some studies in the literature concentrate on the subject of more electrons acting as high-harmonic emitters [132, 133]. In particular in molecular systems it can become important to consider the rearrangement of the bound electron's wavefunction during the time another ionized electron is accelerated in the laser field until it comes back to recombine.

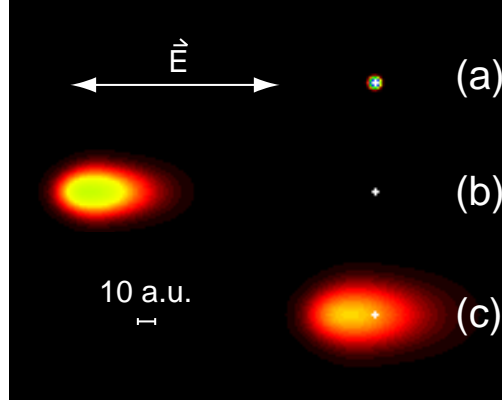


**Figure 2.8:** Snapshots of the time-dependent electronic wavefunction at different times for high-harmonic generation in atoms (a) at the time of ionization, (b) close to the turning point (velocity equal zero in the continuum), (c) at the time of recollision with the ion core. The electron can be seen to undergo quantum-mechanical spreading in the continuum. The size of the wavepacket in (b) appears larger due to saturation of the scaling. a.u. stands for atomic length units (bohr radii).

## 2.2 Propagation Effects

We will now turn towards discussing phase-matching issues in the special case of high-harmonic generation. The equation for the wavevector mismatch Eq. (1.90) for production of the  $m$ th harmonic order Eq. (1.100) can then be written as:

$$\Delta k = mk(\omega_f) - k(m\omega_f), \quad (2.25)$$

with  $\omega_f$  denoting the fundamental laser frequency. Since we will only consider the collinear harmonic generation geometry throughout this work, we wrote the formula in the scalar form. The wavevector dependence on  $\omega$  is governed by a variety of physical effects. First of all, since the generation medium used for high-harmonic generation is usually a gas which exhibits dispersion, the refractive index depends on  $\omega$ . This modifies the wavevector by the amount  $\Delta k_{disp.}$ . Second, very high intensities are employed to drive the harmonic-generation process. This inevitably leads to the generation of free electrons—the majority of electrons are not recombining in the third step of the three-step model—producing a collective plasma resonance that modifies the refractive index and creates another contribution  $\Delta k_{plasma}$  to the wavevector. In addition to these contributions, the focusing and propagation of the laser beam itself gives rise to a geometrical modification  $\Delta k_{geom.}$  of the wavevector. In mathematical terms, we can write

$$k(\omega) = k_{vac.}(\omega) + k_{disp.}(\omega) + k_{plasma}(\omega) + k_{geom.}(\omega), \quad (2.26)$$

where  $k_{vac.} = 2\pi\omega/c$  is the wavevector in free space. If we consider the wavevector mismatch, which is the quantity of interest in terms of the harmonic intensity Eq. (1.100) we may write

$$\Delta k = \Delta k_{disp.} + \Delta k_{plasma} + \Delta k_{geom.}, \quad (2.27)$$

with any of the  $\Delta k$  given by  $mk(\omega_f) - k(m\omega_f)$ . The vacuum contribution  $\Delta k_{vac}$  vanishes due to

$$\Delta k_{vac} = m \frac{\omega_f}{c} - \frac{m\omega_f}{c} = 0, \quad (2.28)$$

thus phase matching is always accomplished in vacuum.

Let us now discuss each of the other contributions in more detail.

### 2.2.1 Neutral Dispersion

Any conversion medium used for high-harmonic generation exhibits dispersion, which is a refractive index  $n(\omega)$  that depends on the frequency  $\omega$  (or wavelength  $\lambda$ ) of the light. Since the wavevector in turn depends on the refractive index

$$k_{disp.}(\omega) = (n(\omega) - 1) \frac{\omega}{c}, \quad (2.29)$$

the wavevector mismatch

$$\Delta k_{disp.}(\omega) = mk_{disp.}(\omega_f) - k_{disp.}(m\omega_f) = (n(\omega_f) - n(m\omega_f)) \frac{m\omega_f}{c} \quad (2.30)$$

thus depends solely on the difference of the refractive indices  $n(\omega)$  at  $\omega = \omega_f$  and  $\omega = m\omega_f$ . Dispersion is caused by resonances of the medium. Therefore, the refractive index depends on the spectral position of absorption lines or bands in the medium. If we are not too close to a resonance, the wavelength dependence of the refractive index can in general be approximated by the Sellmeier equations which take a form similar to:

$$\hat{n}(\lambda) = \hat{n}_0 + \frac{\hat{n}_1^2}{\lambda^2 - \hat{n}_2^2} - \hat{n}_3^2 \lambda^2, \quad (2.31)$$

where  $n_j$  are constants (Sellmeier coefficients) which are specific for a particular medium. For a certain medium, a particular set of constants is only valid over a limited spectral range. The applicability of the Sellmeier equation is usually limited to sub-UV photon energies and can thus only be used for the fundamental laser pulse. In general, the refractive index is higher in the visible or the near-infrared (where the fundamental laser light is located) than in the XUV, where the harmonics are generated. Therefore, we obtain

$$\Delta k_{disp} > 0. \quad (2.32)$$

There are however ways to manipulate and control the refractive index of the medium by mixing of different gases or the application of controlling light fields [134], which is a common technique closely related to electromagnetically induced transparency (EIT) [135].

### 2.2.2 Plasma Dispersion

High-harmonics are generated when the laser electric field is high enough to generate free electrons that are accelerated in the field and recombine. As we discussed in Section 2.1, only a very small part of electrons really recombine or interact with the core to

emit a harmonic photon. The vast majority of electrons misses the core and become free for a long time compared to the duration of the laser pulse (several ns $\gg$ fs). If electrons are ionized by the leading edge of the pulse, they will create an additional plasma resonance in addition to the neutral medium resonances. The plasma resonance is a collective phenomenon, where the whole cloud of free electrons is oscillating with respect to the embedded ionic centers. The plasma frequency  $\omega_p$ , which is the resonance frequency of the collective oscillation, can be calculated to be

$$\omega_p = \frac{e^2 N_e}{\epsilon_0 m_e}, \quad (2.33)$$

where  $e$  is the unit charge,  $N_e$  the free-electron density,  $\epsilon_0$  is the dielectric constant, and  $m_e$  is the electron mass. This resonance leads to a polarizability of the plasma that in turn causes a refractive index of the form

$$n_{plasma}(\omega) = \sqrt{1 - \left(\frac{\omega_p}{\omega}\right)^2} = \sqrt{1 - \left(\frac{N_e}{N_c(\omega)}\right)^2}, \quad (2.34)$$

where

$$N_c = \frac{\epsilon_0 m_e \omega^2}{e^2} \quad (2.35)$$

is the critical plasma density. It is the free-electron density at which the plasma becomes completely absorbing for electromagnetic radiation of frequency  $\omega$ . Typically, in high-harmonic-generation experiments the plasma densities generated are very small compared to the critical density ( $N_c = 1.75 \cdot 10^{21}/\text{cm}^3$ ) of the fundamental 800 nm laser radiation (and even more so for the high-harmonics), we can linearly approximate the refractive index, which gives

$$n_{plasma}(\omega) \simeq 1 - \frac{1}{2} \left(\frac{\omega_p}{\omega}\right)^2 \quad (2.36)$$

The plasma contribution to the wavevector then yields

$$k_{plasma}(\omega) = (n_{plasma}(\omega) - 1) \frac{\omega}{c} = \frac{\omega_p^2}{2c\omega}. \quad (2.37)$$

For the wavevector mismatch, that means

$$\Delta k_{plasma} = m k_{plasma}(\omega_f) - k_{plasma}(m\omega_f) = \frac{\omega_p^2(1 - m^2)}{2mc\omega_f}. \quad (2.38)$$

We are left with a negative contribution of the plasma to the phase mismatch,

$$\Delta k_{plasma} < 0. \quad (2.39)$$

### 2.2.3 Geometric Dispersion

Now let us discuss the geometrical contribution to the wavevector. This term is only present if the electromagnetic light wave is confined to a small region in space. For a plane wave, this contribution would be zero. Since we need to generate high light intensity in



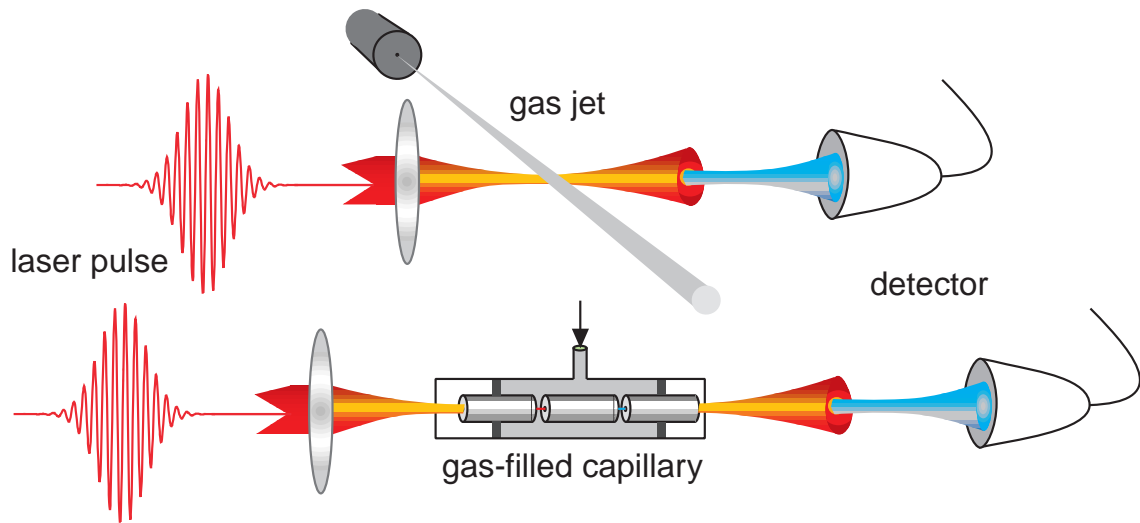


**Figure 2.9:** High-harmonic generation can be conducted in the free focusing and the waveguide geometry. A specific geometric phase is imparted onto the femtosecond laser pulse as it propagates through a focus or through a capillary.

order to drive the process of high-harmonic generation, we always have to take this term into account. There are basically two geometries that play a role in practice. The region around the waist of a focused laser beam and propagation in a waveguide. The initially collimated gaussian laser beam—meaning the radial intensity distribution is gaussian, which is also known as  $TEM_{00}$  mode—is sent through a lens, which creates a converging beam. The radius  $w$  of this beam is continuously decreasing down to the so-called waist size

$$w_0 = \frac{f}{\pi w} \lambda \quad (2.40)$$

where  $f$  is the focal length of the lens and  $w$  denotes the radius of the beam at the lens. This formula is derived from the more general formula for the propagation of a gaussian beam [7]

$$w(z) = w_0 \sqrt{1 + \left(\frac{z}{z_R}\right)^2} \quad (2.41)$$

where  $w(z)$  is the radius of the beam at some point  $z$  along the propagation direction (optical axis). The Rayleigh length is given by

$$z_R = \frac{\pi w_0^2}{\lambda}. \quad (2.42)$$

A focused beam with waist size  $w_0$  transmits the same electromagnetic power everywhere along the optical axis. Thus the intensity increases with  $1/w_0^2$ . However, due to Eq. (2.41), the focal spot size is only sustained over approximately one Rayleigh length, after which the beam size increases approximately linearly with  $z$ .

To overcome this problem, hollow waveguides (capillaries) can be used for high-harmonic generation (Fig. 2.9). When a laser pulse is focused into a capillary having about the same radius as  $w_0$ , the beam radius is bound to be constant over the length of the capillary, due to (partial) reflection of the light at the boundaries. The capillary geometry also affects the

wavevector, due to the particular boundary conditions at the capillary walls. The smaller the diameter of the waveguide compared to the wavelength of the guided light, the larger is the modification of the wavevector.

### Focused Beam

In analogy to the temporal phase  $\phi(t)$  discussed in Section 1.1, we can define the spatial phase of a laser beam  $\Phi(\vec{r})$ :

$$E(\vec{r}) \propto e^{-i\vec{k}\vec{r}} + c.c. = e^{-i\Phi(\vec{r})} + c.c. \quad (2.43)$$

Also analog to the definition of the instantaneous frequency in Eq. (1.15), we can define the local wavevector

$$k(\vec{r}) = \vec{\nabla}\Phi(\vec{r}). \quad (2.44)$$

By solving the source-free (vacuum) wave equation (Eq. (1.56) with the right-hand side equal to zero) for a focusing (converging) beam, we obtain an additional spatial phase  $\Phi_{geom.} = \Phi_{foc.}$  along the optical axis ( $z$ -direction) that is equal to

$$\Phi_{foc.}(z) = \arctan\left(\frac{\lambda z}{\pi w_0^2}\right) = \arctan\left(\frac{2z}{b}\right), \quad (2.45)$$

with the confocal parameter  $b = 2\pi w_0^2/\lambda = 2z_R$ . This is also called the Guoy phase shift [7]. It means that the beam acquires a phase of  $\pi$  (as compared to a plane wave) during its passage through the focus. For a small region around the focus ( $z \ll b$ ), we may write, using Eq. (2.44):

$$k_{foc.}(z) = \frac{d\Phi_{foc.}(z)}{dz} \simeq \frac{2}{b}. \quad (2.46)$$

Since the harmonics are generated with the same confocal parameter  $b$  of the driving beam, this leads to  $k_{foc.}(\omega_f) = k_{foc.}(m\omega_f)$  and thus

$$\Delta k_{foc.} = qk_{foc.}(\omega_f) - k_{foc.}(m\omega_f) = \frac{2(m-1)}{b}. \quad (2.47)$$

For this contribution, we can therefore write

$$\Delta k_{foc.} > 0. \quad (2.48)$$

It should be noted that  $\Delta k_{foc.}$  can be varied by placing the focus at different positions on the optical axis relative to the conversion medium.

### Guided Beam

If harmonics are generated in a guided geometry [136–139], the laser light is focused into the capillary and propagates inside. The solution to Maxwell's equations taking into account the boundary conditions of the hollow waveguide results in a system of waveguide modes that are capable of transmitting electromagnetic radiation. These modes are called

the  $EH_{nl}$  modes [140]. Each of these modes exhibits a particular dispersion relation of  $k_{geom.}(\omega) = k_{cap.}(\omega)$ :

$$k_{cap.}(\omega) = \frac{u_{nl}^2 c}{2a^2 \omega}, \quad (2.49)$$

with the capillary inner radius  $a$  and  $u_{nl}$  being the  $l$ th zero of the Bessel function  $J_{n-1}(u_{nl}) = 0$ . This is valid as long as the capillary is much larger than the wavelength. The wavevector mismatch contribution of the waveguide now becomes

$$\Delta k_{cap.} = mk_{cap.}(\omega_f) - k_{cap.}(m\omega_f) = \frac{u_{nl}^2 c(1 - m^2)}{2ma^2 \omega_f}. \quad (2.50)$$

Obviously, the capillary wavevector contribution has the same form as the one resulting from the plasma. Even the sign

$$\Delta k_{cap.} < 0 \quad (2.51)$$

is the same.

### Synthesis

To generate high-harmonic radiation at the maximum possible efficiency, we have to ensure phase-matching conditions, taking into account any given contribution to the phase mismatch. Since neutral dispersion and plasma dispersion are always present, resulting in  $\Delta k_{disp.}$  and  $\Delta k_{plasma}$ , we have to consider two separate cases for the two different geometries with their contributions  $\Delta k_{geom.}$ : focusing into a jet or cell in a free space geometry ( $\Delta k_{foc.}$ ) or propagating in a hollow capillary filled with the conversion medium as a waveguide ( $\Delta k_{cap.}$ ). For both cases, the focusing and the guiding geometry, we will now summarize the relevant issues.

The total phase mismatch for the focusing geometry can be written as

$$\begin{aligned} \Delta k &= \underbrace{\Delta k_{disp.}}_{> 0} + \underbrace{\Delta k_{plasma}}_{< 0} + \underbrace{\Delta k_{foc.}}_{> 0} \\ &= \underbrace{(n(\omega_f) - n(m\omega_f)) \frac{\omega_f}{c}}_{> 0} + \underbrace{\frac{\omega_p^2(1 - m^2)}{2qc\omega_f}}_{< 0} + \underbrace{\frac{2(m-1)}{b}}_{> 0}, \end{aligned} \quad (2.52)$$

Since we need to achieve  $\Delta k = 0$  for most efficient conversion of laser light into  $m$ th harmonic radiation, the positive contribution of neutral dispersion and the focusing geometry have to be balanced by the plasma dispersion. The above expression contains only the formula for  $k_{foc.}$  at the position of the waist. However this term in general depends on  $z$ , the distance from the focus on the optical axis, as can be seen by looking at Eqs. (2.45) and (2.44). In addition to this geometric contribution, we need to keep in mind that also the intensity changes along the propagation direction  $z$  as the beam is focused. Since the atomic dipole phase depends on intensity with Eq. (2.23) for one particular trajectory, this also affects the wavevector of the harmonic radiation [126, 141]. This behavior leads to different spatial distributions of harmonic intensity in the generated beam depending on whether the gas jet is placed before or behind the focus [121, 126]. The beam shape itself can be used in order to optimize the harmonic production process in the free focusing case [142].

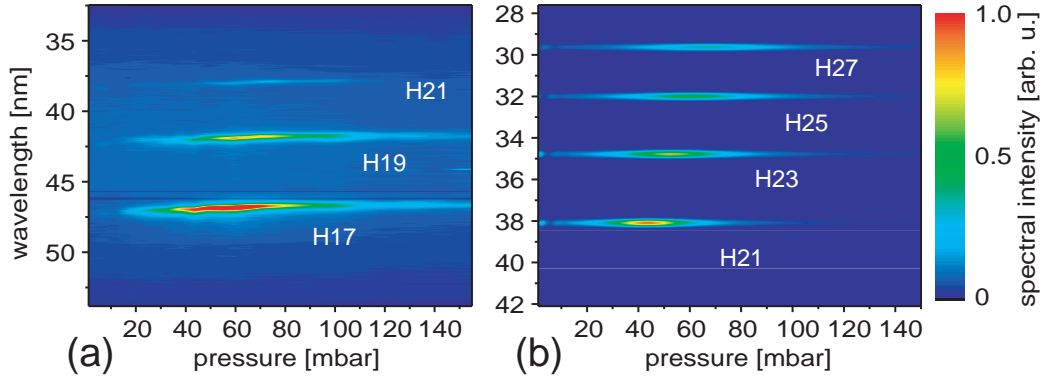


**Figure 2.10:** Phase-matched generation of high-order harmonics in a capillary. The gas pressure (krypton gas was used here) can be employed as a means to control the wavevector mismatch  $\Delta k$  in the high-harmonic generation process. At a particular pressure, perfect phase matching is realized and the harmonic conversion efficiency is maximized. The simulation (b) agrees with the experimental finding (a). In particular, the shift of the optimum pressure, which is due to the wavelength dependence of  $\Delta k$ , is reproduced in the experiment. Since refractive index values were not available for simulation in the experimental wavelength region, the simulation was carried out for higher harmonic orders.

The density of the gas can also be varied in order to arrive at perfect phase matching. This can either be done by increasing the backing pressure of the gas jet or increasing the pressure in the gas cell.

The plasma density can be controlled by means of the intensity or the duration of the laser pulse. Note, however, that a change in intensity will naturally cause a change in the maximum harmonic order (cut-off law Eqs. (2.10) and (2.22)) that can be produced.

For the case of a hollow waveguide filled with the conversion medium, the total wavevector mismatch reads

$$\begin{aligned}
 \Delta k &= \underbrace{\Delta k_{disp.}}_{> 0} + \underbrace{\Delta k_{plasma}}_{< 0} + \underbrace{\Delta k_{cap.}}_{< 0} \\
 &= \underbrace{(n(\omega_f) - n(m\omega_f)) \frac{\omega_f}{c}}_{> 0} + \underbrace{\frac{\omega_p^2(1 - m^2)}{2mc\omega_f}}_{< 0} + \underbrace{\frac{u_{nl}c(1 - m^2)}{2ma\omega_f}}_{< 0}
 \end{aligned} \tag{2.53}$$

Now, the geometric contribution  $\Delta k_{cap.}$  has the opposite sign as in the focusing geometry. This means that the neutral gas dispersion alone has to balance both the plasma and the waveguide contribution. The only free parameters in this case are plasma density (controlled by the intensity and duration of the laser pulse) and the density of the neutral medium. In practice, we are often bound to work at a given laser pulse duration and intensity to produce harmonics up to a certain harmonic photon energy. Thus varying the neutral density is the easiest way to experimentally accomplish phase matching. In Fig. 2.10 the harmonic spectrum is plotted versus pressure in the capillary. Obviously, the experimental finding matches the simulation based on the above formula quite well. In particular, note the shift of the optimum pressure to higher values with increasing harmonic order  $m$ , which is visible in both experiment and simulation results. This is due

to the inherent dependence of the wavevector mismatch Eq. (2.53) on the harmonic order  $m$ . The refractive indices of the gas in the soft x-ray region used for the simulation were taken from the literature [143].

The high-harmonic capillary output has also been shown to have extraordinary spatial coherence properties [144]. This is because the fiber acts as a spatial filter for the driving laser pulse. If high-harmonics are generated at phase-matching conditions (correct gas pressure), the good spatial properties of the driving laser are transferred to the harmonic beam. In the unguided free-space focusing case, a good spatial profile of the harmonic radiation can also be obtained, which is however strongly dependent on the position of the focus relative to the conversion medium and the fundamental pulse's spatial quality.

For both geometries, the fiber and the focus geometry, the plasma contribution represents the ultimate limit for phase-matching. This will be shown in the experiments on high-harmonic generation from water droplets in Chapter 4. As can be seen from Eq. (2.38),  $\Delta k_{plasma}$  becomes very large for increasing harmonic order  $m$ . It is therefore crucial to always keep the plasma density at low values. On the other hand, we need to apply high intensities to generate very high harmonic orders. This apparent contradiction of requirements can be resolved by using very short driving laser pulses [145–150]. Plasma generation is governed by the rate Eq. (2.3), stating that for a given electric field strength a given number of ions are created *per unit time*. Therefore, the shorter pulse can reach a higher peak intensity (compared to a longer pulse) for the same amount of plasma being created. This is particularly important for the extreme case, when the long pulse has fully ionized the medium by the time it reaches its peak intensity. This intensity cannot be used for harmonic generation since the process relies on the availability of non-ionized (bound) electrons. The shorter pulse on the other hand reaches the same intensity in a shorter time such that the medium has not enough time to become fully ionized (assuming ionization with a rate depending predominantly on instantaneous electric field or intensity). The remaining bound electronic population in the short pulse case can thus generate very high harmonics corresponding to the high peak intensity of the pulse.

For the sake of completeness, it should be mentioned at this point that guiding of laser pulses can also be achieved by the self-focusing effect [151]. If the laser is suitably focused, the intensity-dependent index of refraction of the gas and the free-electron plasma can counterbalance each other. In this case, the laser beam propagates over long distances at a confined beam diameter without an externally applied guiding structure. Thus, an effective wave-guide scenario is created and harmonic generation can take place over a long interaction length [152, 153].

## 2.2.4 Absorption

A limiting factor to phase-matched high-harmonic generation is reabsorption of the generated harmonic light in the conversion medium. The high-harmonic photon energies are typically in the soft x-ray spectral region (for 800 nm driving laser pulses), where light is extremely well absorbed by matter. This is because the outermost electrons in many materials are bound with energies corresponding to 10–100 eV. This results in large photoionization cross-sections  $\sigma$  of any system in this spectral range, explaining the strong

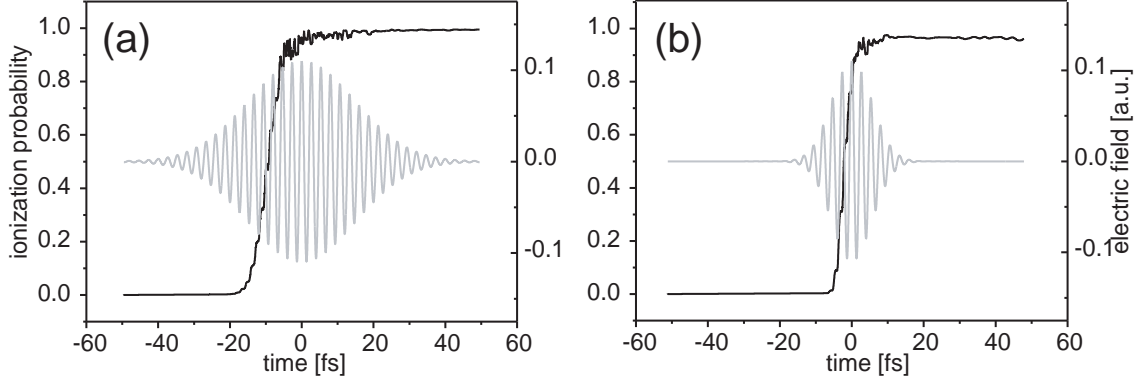


**Figure 2.11:** Plasma build-up in a long 25 fs FWHM (a) and a short 8 fs FWHM (b) laser pulse of the same peak electric field. The probability of ionization reaches 1 for the long pulse before the peak electric field is reached. Therefore, no harmonic photons corresponding to the highest intensity can be produced in this case. For the shorter pulse, the electron has about 20% probability to survive in the atom when the peak electric field is reached. This is the reason why very short pulses are beneficial for the production of highest harmonic photon energies.

absorption. The absorption length  $L_a$  (the distance after which the intensity of light propagating in an absorbing medium has dropped to  $1/e$ ) is given by

$$L_a = \rho\sigma, \quad (2.54)$$

where  $\rho$  denotes the particle density. As the driving laser pulse propagates through the conversion medium, it continuously generates new harmonic light that adds to the co-propagating harmonic radiation generated earlier. This earlier-generated light however is affected by absorption. By summing over all contributions to the  $m$ th-harmonic radiation at the point where the laser pulse leaves the conversion medium, we find for the  $m$ th-harmonic yield [154]:

$$I_m \propto \left| \int_0^L \rho A_m(z) \exp\left(-\frac{L-z}{2L_a}\right) \exp(i\phi_m(z)) dz \right|^2, \quad (2.55)$$

with the harmonic amplitude  $A_m(z)$  of the single-particle response and phase  $\phi_m(z)$  at the exit of the conversion medium of length  $L$ . If we consider  $A_m(z)$  not to depend on the position  $z$  along the optical axis—as is approximately the case in the waveguide or loose focusing geometry where the laser intensity stays roughly constant—Eq. (2.55) becomes

$$I_m \propto \rho^2 A_m^2 \frac{4L_a^2}{1 + 4\pi^2(L_a^2/L_c^2)} \left( 1 + \exp\left(-\frac{L}{L_a}\right) - 2 \cos\left(\frac{\pi L}{L_c}\right) \exp\left(-\frac{L}{2L_a}\right) \right), \quad (2.56)$$

where again  $L_c = \pi/\Delta k$  is the coherence length that can be calculated from the total wavevector mismatch  $\Delta k$  introduced above. It can be seen that unlike for perfect phase matching without absorption (where the converted signal increases with  $L^2$ ) Eq. (2.56) converges to a finite value for the case of  $L \rightarrow \infty$ . In Fig. 2.12, Eq. (2.56) is evaluated for different ratios of  $L_c/L_a$ . In order to generate about half the asymptotic high-harmonic

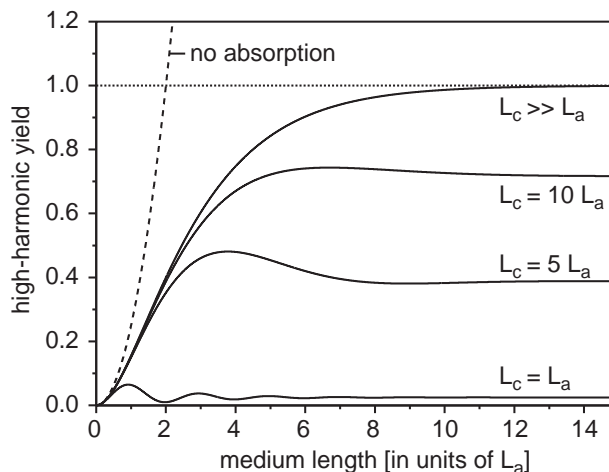


**Figure 2.12:** The effect of reabsorption in the conversion medium during high-harmonic generation. If absorption is not included in the consideration, the harmonic yield increases quadratically with the medium length (dashed line). If absorption is present (absorption length  $L_a$ ) there is a limit (dotted line) to the maximum harmonic yield even in the case of perfect phase matching  $L_c \gg L$ . For smaller coherence lengths  $L_c$  the maximum achievable harmonic yield decreases.

yield obtained for a long coherence and propagation length (indicated as dotted line in Fig. 2.12), we have to fulfill the conditions [154]:

$$L > 3L_a \quad (2.57)$$

$$L_c > 5L_a. \quad (2.58)$$

In this case, we generate close to the maximum amount of harmonic radiation that is possible given the absorption of the gas. This absorption limit has been attained in a number of experiments [154–156].

## 2.3 Attosecond Pulses

The duration of the optical cycle of visible to near infrared light is on the order of 1-3 fs. The ultimate goal in ultrashort pulse technology is to reach the ‘single-cycle limit’, a laser pulse that lasts only one cycle of the laser AC-field. A shorter time-duration is not possible, since the integral over the electric field of the laser pulse over all times must be zero in order to solve the wave equation of free space (see Eq. (1.56) with the right-hand side equal to zero). In addition to the generation of larger and larger coherent continua [98, 100] and subsequent adaptive compression [3], two methods have been proposed in the literature which principally allow for the generation of pulses on the order of a single femtosecond in the single cycle regime. They are based on ultrafast molecular phase modulation either by Raman techniques [157, 158] or by controlled rotational wavepackets [159].

If we like to break the femtosecond barrier and create flashes of light of sub-femtosecond (attosecond,  $10^{-18}$  s) duration, we will necessarily have to use carrier frequencies higher

than optical ones. Attosecond pulses thus can only exist in the VUV to soft x-ray and higher photon energy range. Since high-harmonic generation is a way to generate spectrally coherent radiation in these spectral regions, it has early been realized that this process is capable of producing attosecond pulses. As was discussed in Section 1.1.2, a close to flat spectral phase relationship is required to produce short pulses from a broad spectral distribution. In fact, this flat spectral phase behavior is typical for high-harmonic generation [136, 160] and can be understood by considering the three-step model [105] in the time domain. Due to the classical character of the electron trajectory, any returning electron of a given kinetic energy recombines with the parent ion at a particular phase of the laser electric AC-field. Thus, a given photon energy—corresponding to the electron kinetic energy—is produced only at particular short times in the laser cycle [161], giving rise to attosecond flashes of light if those photon energies are filtered out. However, since the process is repeated every optical cycle of the driving field, it is in general hard to extract a single attosecond pulse.

### 2.3.1 Existence

After the first indirect experimental indication of attosecond bunching [162], the first direct experimental measurement of these trains of attosecond pulses was carried out in 2001 [163]. The key was to measure the relative phase between harmonic peaks. An interferometric crosscorrelation of the harmonic soft x-ray beam with the driving laser pulse in helium gas was performed. This produced characteristic intensity modulations of the harmonic sidebands of the photoelectron spectra, from which the relative harmonic spectral phases could be extracted. Having those at hand along with the harmonic spectra the temporal shape of the attosecond pulse train could be reconstructed. The same technique was used afterwards to measure the timing of attosecond pulse production with respect to the driving field in a large region of harmonics [164]. But the problem was still not solved: How can we generate a *single* attosecond pulse?

One of the earliest ideas to solve the problem dates back to 1994 and was also introduced by Corkum and coworkers [165]. As will be addressed in more detail in Chapter 3, the harmonic generation process is strongly dependent on the ellipticity of the driving field [166]. Only linearly polarized laser light generates harmonics at maximum efficiencies, whereas even small degrees of driving-laser ellipticity result in decreased harmonic production. By different linear chirps in two orthogonal polarization states of the light it is possible to create laser pulses that switch their polarization state from elliptical to linear and back to elliptical on a time scale corresponding to the bandwidth limit of the ultra-short laser pulse. This ‘polarization gating’ approach has recently been experimentally applied [167] where an increase of harmonic bandwidth could be observed. However, a direct temporal measurement of the pulse duration has not been achieved yet.

Another theoretical idea for single attosecond pulse generation was the use of two-color light fields [168]. The relative phase of the two frequencies can be used to control the phase of the electron wave-packet along its path through the continuum. This allows for the control of the temporal properties of the recollision event and single attosecond pulses can be realized. This approach can also be understood as being related to the control of



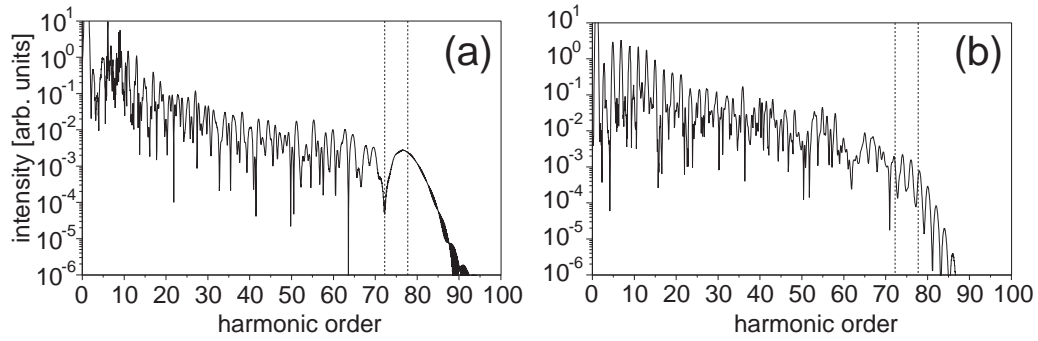


**Figure 2.13:** Harmonic spectra for the simulation of a two-dimensional H-atom in a strong laser field. (a) shows the spectrum for a 4 fs laser pulse, in (b) the laser pulse is 10 fs. The spectrum exhibits differences mainly in the cutoff region, where the shorter pulse shows a continuous spectral distribution in contrast to the longer pulse. There, the harmonic spectrum is modulated with twice the fundamental frequency. The vertical lines indicate the FWHM of a filter that is applied in order to generate a single attosecond pulse in the case of (a) and a train of attosecond pulses in the case of (b) (see Fig. 2.15).

the transient polarization state for single attosecond pulse generation.

The intuitive experimental solution to generate a single attosecond pulse was the use of very short light pulses [169, 170] of less than 10 fs which resulted in the production and measurement of 650 as pulses [171]. If only the most intense optical cycle of the laser pulse is intense enough to generate the highest energy photons, they will be emitted in a singular event, when the electrons of the corresponding trajectory recombine with the parent ion. A band-pass filter (e.g. thin material films or also multilayer optics [172, 173]) can be used in order to select the photon energy range which corresponds to the single attosecond pulse. In order to shed more light onto this process, a two-dimensional quantum-mechanical simulation of a hydrogen atom in an intense  $5.5 \times 10^{14} \text{ W/cm}^2$  800 nm laser field was performed, using the split-step-operator technique (Appendix C). The resulting single-atom high-harmonic spectra for interaction with 4 fs and 10 fs FWHM duration laser pulses are depicted in Fig. 2.13. From the harmonic spectra alone it is hard to tell which spectral region is the most suitable for the generation of single attosecond pulses after filtering. To overcome this difficulty of selection, a windowed Fourier transformation can be employed. It is a way to visualize the harmonic temporal response of the system in narrow spectral regions. In mathematical terms, the spectral harmonic distribution  $\tilde{E}_H(\omega)$  (which is obtained from the Fourier transformation of the dipole acceleration, see above) is transformed as follows:

$$\mathcal{E}_H(t, \omega) = \frac{1}{\sqrt{2\pi}} \int_{-\infty}^{+\infty} \tilde{E}_H(\omega') F_\Omega(\omega', \omega) e^{i\omega't} d\omega' \quad (2.59)$$

$$F_\Omega(\omega', \omega) = \exp\left(-2\ln 2 \left(\frac{\omega' - \omega}{\Omega}\right)^2\right). \quad (2.60)$$

In words,  $\mathcal{E}_H(t, \omega)$  is the inverse Fourier transform into the time domain of the spectral harmonic emission  $E_H(\omega)$  multiplied with a gaussian window filter  $F_\Omega(\omega', \omega)$ , centered

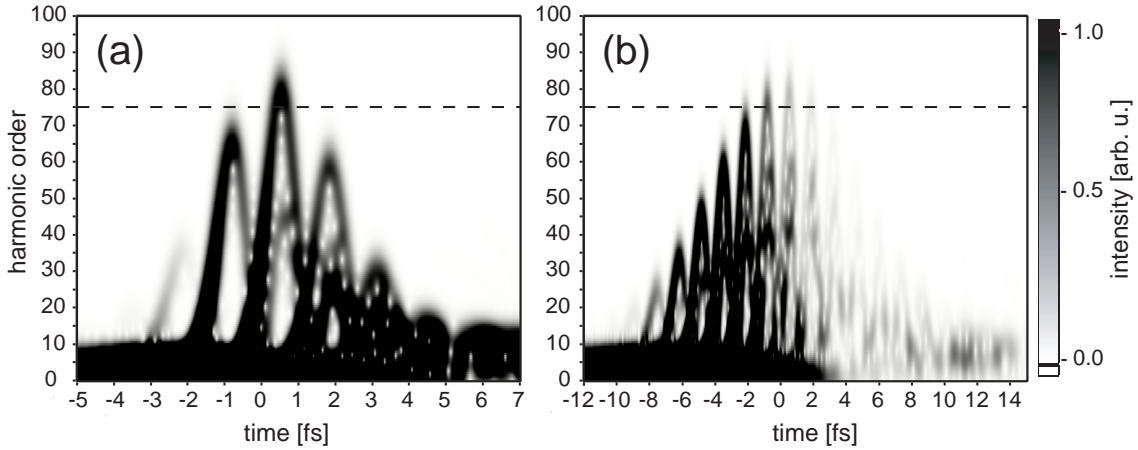


**Figure 2.14:** Windowed Fourier transform of the spectral high-harmonic response. (a) 4 fs driving laser pulse, (b) 10 fs driving laser pulse. The bow-like structures indicate different electron trajectories. At a given constant harmonic order (central position of the gaussian filter) the shorter pulse generates less harmonic emission events than the longer pulse. At highest-frequency photon energies, single attosecond-pulse generation is possible with the short laser pulse. The dashed line indicates a cut through the windowed Fourier transform depicted in Fig. 2.3.

at a frequency of  $\omega$ .  $\Omega$  stands for the intensity FWHM of the filter. The harmonic temporal intensity distribution depending on the central frequency of the filter can thus be written as

$$\mathcal{I}_H(t, \omega) = |\mathcal{E}_H(t, \omega)|^2. \quad (2.61)$$

This function of the two variables time  $t$  and frequency  $\omega$  is shown in Fig. 2.14 again for the case of the 4 fs and 10 fs driving laser pulse and a filter width  $\Omega$  of 5.5 harmonic orders. The frequency is given in multiples of the fundamental frequency. Bow-like structures are obtained, which can be understood immediately from the picture of returning electrons with different kinetic energies at different times. The effect of multiple trajectories is also visible for the most intense emission events, where a smaller bow is contained in a larger one. When a slice at a fixed harmonic order is considered, the temporal duration of the emission events is smaller than a single femtosecond. The effect of a shorter laser pulse is visible in fewer overall harmonic emission events at a given harmonic order. In particular, when the high photon energy region is considered, the short laser pulse produces only one harmonic attosecond pulse whereas the longer driver pulse shows a train of attosecond pulses. To visualize this, a cut through the windowed Fourier-transform at a harmonic order of 75 is shown in Fig. 2.15. In addition to the qualitative difference of the harmonic temporal structure, the intensity of the single attosecond pulse is higher than in the case of a pulse train. The attosecond pulse train can be understood also in the spectral domain by a second look at Fig. 2.13. In the cutoff region, where the FWHM of the applied filter is indicated, a modulated structure is visible for the longer laser pulse. For the shorter laser pulse, the spectral intensity is a smooth continuum. The spectral modulation at twice the fundamental frequency gives rise to a modulated temporal distribution. The temporal modulation period is the inverse of the spectral one, thus half an optical cycle (1.33 fs). Implications of short and long pulses for the generation of single attosecond pulses or

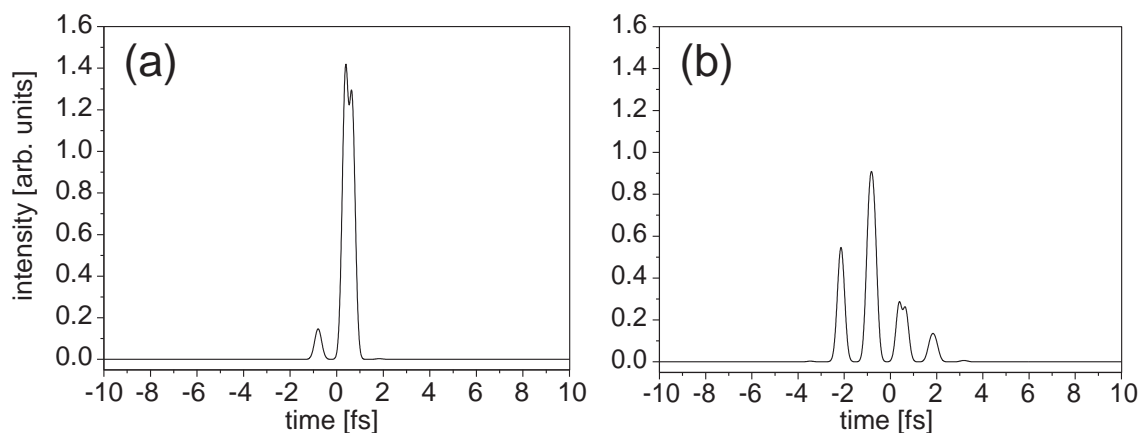


**Figure 2.15:** Single (a) and a train (b) of attosecond pulses from the interaction of short (4 fs) and longer (10 fs) pulses, respectively. The attosecond pulses are obtained if the harmonic spectrum is filtered as indicated in Fig. 2.13 and Fig. 2.14. The pulse duration of the attosecond pulses is on the order of 600 as.

trains have already been studied earlier in the literature [169, 174].

The windowed Fourier transformation has recently helped to illuminate the importance of ground-state population for the high-harmonic generation process [175]. It was shown there that the “bows” in  $\mathcal{S}_H(t, \omega)$  (Fig. 2.14) cannot be the result of bremsstrahlung emitted from an electronic wavepacket colliding with a bare ion (i.e. where no electric wavefunction is left in any bound state). In contrast, the interference with ground-state electronic population is the origin of the intense harmonic radiation. In addition, harmonic generation is dependent on the carrier-envelope phase (CEP) of the driving laser pulse [176]. The CEP of the ultrashort driver pulse can be determined by an analysis of the harmonic intensity spectrum obtained in experiments with a method closely related to the windowed Fourier transformation [177].

It should be mentioned for the sake of completeness that the windowed Fourier transform shows some similarity to the Wigner and Husimi representation [76, 178] that is often used for the analysis of quantum phenomena in phase space.

It is interesting to notice that the production of the attosecond pulses—trains or single ones—is relatively easy. We basically get them ‘for free’ in the process of high-harmonic generation without any additional effort. Much harder, however, is to measure the time duration or even to characterize the attosecond pulses in the experiment. In the following, measurement and characterization schemes for attosecond pulses shall be discussed in some more detail.

### 2.3.2 Measurement

The measurement of the temporal structure of the high-harmonic radiative response is a complicated task due to a variety of reasons. First of all, the intensity of the generated signals is very weak, making it almost impossible to apply the standard technique of autocorrelation (see Section 1.1.5). This is due to the fact that the autocorrelation is based

on a nonlinear process involving a nonlinearity of at least second order. As long as the intensity of the light to be measured is too low to induce measurable signal of a nonlinear process, autocorrelation is not possible. Unfortunately, the nonlinear interaction cross-sections decrease very rapidly with increasing photon energy, which makes experimental observation particularly challenging. It has been possible, however, to use autocorrelation to analyze harmonic pulse trains for the low-order harmonics which are sufficiently intense [179]. The nonlinear medium used was helium gas. Two-photon ionization by XUV-light was the experimentally extracted nonlinear signal.

In general, any nonlinear interaction can be used to learn about the temporal properties of an unknown ultrashort signal. The requirement of a nonlinear process arises naturally by the necessity to compare the spectral phases of different frequency components of the spectrum, which cannot interfere in linear optics if only time averaged quantities can be experimentally extracted (slow detectors).

Another nonlinear approach therefore is the crosscorrelation of the (weak) harmonic radiation with the (strong) fundamental driving field of the laser. This method has early been proposed as an analog to a ‘streak camera’ [180, 181] employed for the measurement of short electron pulses. In such a device, a short electron bunch is deflected by an electric field that is rapidly increasing or decreasing. If the trace of deflected electrons is recorded on a screen, a characteristic “streak” image is obtained from which the temporal structure of the electron pulse can be extracted. In order to measure attosecond features, the deflecting field change must be fast enough to resolve the pulse on this time scale. The field strength of an optical laser changes very rapidly on the time scale of an optical cycle. Therefore, photoelectrons that are instantaneously produced by the high-harmonic attosecond pulsed radiation can be deflected by the fundamental laser field, creating a characteristic streak on a detector. This technique was first worked out for the case of circularly polarized light in theory [182]. It was however experimentally shown that recording the kinetic energy change of the photoelectrons produced at different phases in the linearly polarized fundamental laser field is sufficient to determine the duration of the harmonic emission [170, 171, 183]. This can be understood very easily by reexamination of formula Eq. (2.7). If an electron is ionized far above threshold by a high-harmonic photon pulse of frequency  $\omega_m$ , it is produced in the continuum at nonzero kinetic energy, which is given by the excess energy  $E_{exc} = E_{kin} = \hbar\omega_m - I_p$ , where  $I_p$  is the ionization potential of the ionized state. The electron will thus have an initial velocity  $v_0$ , which will however be modified by the action of the fundamental laser field  $E(t)$ :

$$v_\varphi(t) = \int_0^t -\frac{e}{m}E(t')dt' = -\frac{E_0e}{m\omega}(\sin(\omega t + \varphi) - \sin(\varphi)) + v_0. \quad (2.62)$$

The additional drift velocity of  $-E_0e/(m\omega)\sin(\varphi)$  caused by the laser field depends on the phase of the fundamental field. If the attosecond pulse is shorter than the optical cycle, the kinetic energy of the photoelectron bunch produced varies on a sub-cycle time scale of the delay between the fundamental and the high-harmonic pulses. The depth of the modulation can be used to extract the temporal duration of the attosecond pulse. Even the chirp of the attosecond pulses can be reconstructed by this measurement technique [184]. Although the measurement process can be understood in this classical fashion, a quantum mechanical theory of this measurement method has been worked out [185].

Within the framework of crosscorrelation, also the chirp of single high-harmonic orders can be measured [186]. Pulse characterization methods like SPIDER [187] and crosscorrelation FROG (X-FROG) [188] can be transferred to the XUV for the characterization of high-harmonic (attosecond) pulses. Whereas the SPIDER method has not been experimentally accomplished yet, FROG of extreme ultraviolet wavelength harmonic orders has been carried out in experiment. FROG was already employed to measure the intensity-dependent dipole phase [189]. In an additional approach, recording the asymmetry of photoelectron production (photoelectrons that travel into opposite directions) was theoretically shown to provide a way to measure the duration of attosecond pulses [190].

Another general experimental problem in the measurement of the attosecond XUV pulses—and also in the design of attosecond time-resolved experiments—is the control of the delay between the XUV pulses (e.g. in autocorrelation [179]) or the XUV and the laser pulse (crosscorrelation). Small angles between the propagation directions of the pulses to be correlated lead to a temporal smearing out of the correlation signal. This is because one part of the beam experiences a different temporal delay than another part if the beams cross at an angle in the interaction region. The effect is proportional to  $w \sin \theta$  and thus becomes worse for larger angles  $\theta$  and larger beam sizes  $w$ . The beam size is typically on the order of  $50 \mu\text{m}$ , which requires angles of smaller than  $0.05^\circ$  in order to retain a temporal resolution on the 100 as time-scale. For that reason, the best way to perform correlation measurements is to work in a collinear geometry. However, there are no beamsplitters and recombiners easily available in the XUV spectral range. A sophisticated dispersion-balanced XUV interferometer has been introduced [191] which employs XUV transmission gratings as beamsplitters and recombiners. Another solution is the use of special mirrors. For instance the center part of a mirror can be cut out and translated with respect to the outer mirror surface [170, 171]. By using spatial filters in the beam, the harmonic radiation only hits the center part of the mirror and can thus be delayed with respect to the fundamental laser pulse, which hits the outer part of the mirror. A piezo-translator with nanometer resolution controls the delay on an attosecond time scale.

For the autocorrelation experiment reported in [179] another mirror design was employed to generate two almost identical replica of the harmonic pulses. The mirror was split along a line to cut the harmonic beam into two halves, which were delayed with respect to each other. The autocorrelation in this case is not exactly an interferometric one, since the harmonic beams are not exactly copropagating. This effect has to be taken into account in the analysis.

Another method used for controlling the time delay between fundamental and harmonic pulses is the use of annular beams for harmonic generation [163, 164]. Harmonic generation also takes place in a focused beam, from which the central part has been cut (annular profile) before focusing. Harmonic light is still generated into the forward direction and can be crosscorrelated with a femtosecond laser pulse that uses the inner part of the driving beam. Since this crosscorrelation pulse itself does not participate in the generation process, we can introduce the delay by tilting transparent apertures in the beam (see setup in [163]), a ring-shaped one for the annular driver pulse and a circular-shaped one for the inner crosscorrelation pulse.

The next Section is devoted to the multiple ways of application of ultrashort x-ray pulses.

## 2.4 Applications of Ultrafast X-Rays

A whole new area of research has started to grow in recent years, which is now most commonly known as ‘ultrafast x-ray science’. It was not only the advances in attosecond pulse production in high-harmonic generation that played a key role in the development of this field. A variety of different approaches to generate short x-ray pulses is nowadays available and is continuously extended. Besides high-harmonic generation, the most important sources of short x-rays are synchrotron and free-electron-laser facilities [192,193] on the one hand and laser-induced plasmas [194] on the other hand. These sources exhibit very different properties in terms of their spatial and temporal coherence properties making them useful for particular applications, which shall in the following be discussed in more detail.

### 2.4.1 Applications of High-Harmonic Generation

As has been mentioned above, high-harmonic generation allows for the production of the shortest pulses of light ever produced in the laboratory. In principle, it is now possible to do time-resolved spectroscopy on coherent superpositions of energetically widely spaced electronic states, as they occur close to the ground state of the electron or for core-electron excitations. For example, if a superposition state is created in a hydrogen atom with contributions of principal quantum numbers  $n = 1$  and  $n = 2$ , a quantum beat with a period of  $\simeq 400$  as is expected in a transient ionization measurement. The only direct application of attosecond pulses at the moment is the direct recording of the electric field of the laser pulse [195]. The technique is based on the crosscorrelation technique mentioned above. Another theoretical idea was published earlier [196] providing an alternative way to measure the laser electric field by asymmetric photoionization with an attosecond pulse.

It was also shown in experiment that the kinetic energy of photoelectrons could be controlled by setting particular delays between the attosecond pulse and the fundamental laser field [197]. An application to atomic physics and multielectron dynamics in the Auger decay is reported in two works [198, 199], where the dynamics of the Auger decay could be directly monitored in the time domain.

To generate single attosecond pulses a very sophisticated laser system is required. Therefore, many experiments have been performed in a regime, where only the temporal resolution of the driving femtosecond laser pulse (i.e. a single harmonic or a train of attosecond pulses with a total duration comparable to the duration of the femtosecond laser pulse) was used [200–204].

Dissociating  $\text{Br}_2$  molecules have been studied using time resolved photoelectron spectroscopy [200, 201]. Ramsey-type spectroscopy of autoionizing states in krypton was carried out by use of the ninth harmonic [202]. Lattice relaxation following inner-shell excitation in a CsCl crystal was monitored in real time [203]. Interferometry with high-harmonic radiation can also be used as a diagnostic tool to study the temporal evolution of free-electron density in plasmas [204].

All these studies made use of the short pulsed nature of high-harmonic generation in order to obtain insight into the dynamics of the process under study. Some earlier experiments

were devoted to prove the suitability of high-harmonic radiation for generating x-ray fluorescence [205], auger-free luminescence [206] or for the application of photoelectron spectroscopy on surfaces [207, 208].

Another interesting aspect of the ultrafast soft x-ray radiation is its applicability for time-resolved imaging. It was already shown that high-harmonic generation produces enough photons in order to perform zone plate microscopy [209] and interferometry [210] at 13 nm wavelength.

Temporal resolution is only one benefit of short pulses. Another one is of course the high peak intensity of the harmonic radiation, which can reach values of  $10^{14}$  W/cm<sup>2</sup> at the moment. This is only possible if the harmonic light is suitably focused to very small focal spot sizes employing zone plates, multilayer [156] or toroidal metal mirrors [211]. At these intensities, nonlinear interactions of harmonic photons are possible, for example the two-photon ionization of helium has recently been observed in experiment [212] and was used for an autocorrelation of the harmonic pulses [179] as was already mentioned above. Higher and higher harmonic pulse energies lead to higher and higher intensities, making novel nonlinear optical experiments in the XUV region possible in the future. The highest pulse energies obtained to date are in the microjoule region [213–215].

It was also recently shown that high-harmonics can be generated with high-repetition rate laser systems, e.g. at 100 kHz [216]. This is very important for pump-probe photoelectron (in particular electron-ion coincidence) studies in the soft x-ray region, where the number of counts per shot is very low.

It is furthermore possible to use an optical parametric amplifier (OPA) for harmonic generation, allowing for generation of tunable high-harmonic radiation [217]. In addition, tunability of high-harmonic radiation has recently been shown to be possible also by pulse shaping of the driver pulses. Using an evolutionary algorithm, the harmonic peaks in the plateau region could be shifted [218]. In Chapter 5 it will be shown that even isolated harmonic peaks in the plateau region at various harmonic orders can be produced, providing an invaluable tool for future soft x-ray time resolved studies.

To summarize, the advantage of high-harmonic radiation is its very short (attosecond) time duration and high peak brightness that arises also due to its complete spatial coherence. Limitations are given by the total photon flux and maximum photon energy, which has been limited to the order of 500 eV [147, 219] until today. We now address electron-beam and plasma sources that provide a way to generate much harder x-rays, however with the sacrifice of reduced temporal resolution.

## 2.4.2 Applications of Synchrotron and Free-Electron-Laser Sources

In the following, electron-beam x-ray sources will be discussed, which also feature good spatial coherence. However, the pulse length of standard synchrotron pulses is on the order of 100 ps and thus much longer than attoseconds, even in the case of the newly developed free-electron lasers, where pulse durations 10-100 fs are expected. An advantage of these sources is the high photon energy that is achievable, which can be several keV. This enables applications like time-resolved structure determination in crystals. X-ray

free-electron lasers are expected to deliver enough x-ray photons in one shot to resolve the structure even of single molecules.

Due to the high photon energy achievable, experiments carried out with synchrotrons focused on transient structure determination in recent years [220–225]. X-ray absorption spectroscopy (XAS) was performed, where the x-ray absorption fine structure (XAFS) was transiently analyzed to obtain structural information about reaction intermediate states [220]. Another experiment investigated the x-ray absorption near edge structure (XANES) of a molecule in solution in order to temporally resolve a charge-transfer process [221]. Metal-insulator transitions were followed in real time by core-level photoelectron spectroscopy [222]. Structural changes in melting silicon could be temporally resolved in another experiment [223]. Another interesting and impressive application of ultrafast x-rays has been the real-time tracking of CO motion and associated structural changes in a protein on the natural time scale of the reaction [224].

In almost any of these experiments, the authors directly mentioned the limitations of the synchrotron pulse duration, which did not allow to obtain full insight into the temporal behavior of the system under study. To overcome these limitations in the future, interesting new techniques to shorten the synchrotron x-ray pulses were developed and implemented experimentally. The so called ‘slicing scheme’ was experimentally realized by Schoenlein *et al.* [226]: Before the electron pulse passes through the undulator or bend magnet to produce x-ray radiation, it interacts with an intense femtosecond laser pulse in another undulator section. This leads to a femtosecond duration electron subpulse of lower and higher energy electrons in the main electron bunch, which can be extracted. This femtosecond subpulse of electrons will generate a femtosecond pulse of x-rays along its passage through the bend magnet or undulator. These ultrashort x-ray pulses were already used for experimental applications. Direct evidence of ultrafast disordering in laser-perturbed InSb on a sub-picosecond time scale could be observed for the first time by time resolved x-ray diffraction [225]. Another means to shorten the duration of synchrotron light pulses is to use ultrafast shutters. It could be shown that laser-induced acoustic pulses in crystals can modulate and switch the x-ray transmission properties by making use of the Borrmann effect. This could potentially be used to generate subpicosecond pulses [227].

Common to both shortening approaches just discussed is the fact that only a shorter pulse is “cut out” of the longer synchrotron pulse, leading to a decrease in the photon number per shot. For that reason, tremendous effort around the world is put into the development and construction of free-electron lasers, which would supply both ultrashort pulses of hard x-rays and large photon numbers per shot.

The free-electron laser (FEL) working principle is an extension of the undulator technique. In an undulator, the electron beam is deflected by a periodic magnetic structure along the propagation path where the modulation period is chosen such that the bremsstrahlung emitted by each electron constructively interferes with the radiation produced one modulation period further downstream. The radiation produced by different electrons, however, is not coherent and leads to a linear growth of x-ray radiation produced with electron density. In the FEL, the electron density in the beam is increased, such that the more intense radiation produced by the electrons is interacting with the elec-



tron cloud. In this case, microbunches are formed in the electron beam which now lead to a coherent addition of the radiation produced by each electron. This leads to an increase in x-ray flux proportional to the electron density squared. If the microbunches have to form spontaneously, this is called self-amplified spontaneous emission or SASE [228]. If the microbunching is created externally by interaction with a laser field for example, this is termed a seeded free electron laser [192, 193].

Recently the first experiments on nonlinear interaction of VUV light from a SASE FEL with xenon atoms and clusters were carried out [229]. The very high charge states of xenon ions detected in the experiment led to fundamentally new insights into light-matter interaction [230].

### 2.4.3 Applications of Laser-induced-Plasma X-Ray Sources

When a highly intense femtosecond laser pulse interacts with high-density material (solid-state), a hot and dense plasma is created. Electrons can be accelerated to very high kinetic energies. These high kinetic energies can be released as bremsstrahlung when the electrons scatter with the ionic cores. The time it takes the very hot plasma to cool down is typically in the sub-picosecond regime. Therefore, the emitted x-ray pulses have femtosecond time durations. The first laser-induced plasma femtosecond x-ray source was demonstrated by Murnane *et al.* [194] in 1991. The production of very hard x-ray emission on a femtosecond time-scale is possible when femtosecond-laser-accelerated highly-energetic electrons create inner-shell vacancies in atoms, leading to the emission of characteristic line radiation [231]. The duration of the x-ray pulse is dependent on the maximum depth the energetic electrons can penetrate into the material.

These sources are unique in that they can deliver very high photon energies in very short (a few hundreds of femtoseconds) pulses. A drawback is the very low number of photons that can be used for experiments. This is due to the fact that the generated plasma radiation is spatially incoherent and thus has almost no directionality (emission into  $4\pi$  solid angle). Sophisticated collection optics have to be employed to collect a large solid angle which is focused onto the sample object. High-repetition rate (multi-kHz) laser systems delivering high pulse energies (multi-mJ) have to be used [232] in order to keep integration times at acceptable levels.

Plasma-based sources allow for monitoring of structural changes on the natural time scale of nuclear vibrations. It was possible to monitor lattice vibrations in crystals (coherent acoustical phonons) induced by an incident ultrashort laser pulses [233, 234]. Another field of study with these sources is the real-time observation of non-thermal melting on the surface of germanium [235, 236] and in organic thin films [237]. In all of these cases, Bragg scattering was employed to extract structural information. Expansion or compression dynamics of the material could be inferred from the shifting of particular Bragg peaks.

Another experiment focused on temporal shifts of x-ray absorption lines during chemical reactions [238]. Time-resolved near-edge absorption spectroscopy of a shape resonance in an SF<sub>6</sub> molecule allowed to track structural changes occurring during photoinduced dissociation.

At the end of this section about applications of ultrashort x-ray pulses it should be mentioned that the application of short pulse *sources* is only one way to obtain temporal resolution of a process. Another way is to realize a fast *detector*. X-ray streak cameras have been introduced in 1971 [180, 181], allowing to resolve picosecond features. The highest temporal resolution obtained today is 600 fs [239].

The number of applications of ultrashort x-rays in recent years is accelerating at a high pace. Better and better sources of ultrafast x-rays are developed to push our understanding of quantum dynamics forward. The ultimate goal is the molecular movie, allowing us to observe the spatially resolved motion of nuclei in complex molecular or crystalline systems on their natural time scale.

## Part II

# Optimization of Harmonics by Medium Engineering

High-harmonic generation provides the possibility to convert infrared or visible laser light into the soft x-ray region. It even conserves the coherence properties of the driving laser light. There is tremendous interest in generating ultrashort pulses of light in the x-ray region [192–194, 226, 228], since they can immediately be used to perform spectroscopy on the atomic time- and length-scale. The direct observation of lattice vibrations [233, 234] or the structural dynamics of non-thermal melting [235, 236] are indications for the rising of the new field of ultrafast x-ray science. The interest in free-electron lasers (FELs) [192, 193, 228] is also spawned by the desire to create ultrashort coherent x-ray pulses. FELs are large-scale facilities since they require electron linear accelerators to produce highly energetic high density electron beams. It would clearly be more favorable to circumvent the construction of these large highly expensive facilities if there were other ways to produce this kind of radiation. However, in order for high-harmonic generation to work as a substitute for FELs, we would need to overcome two major limitations: The photon energy that is attainable in high-harmonic generation is currently limited to below 1 keV and the conversion efficiency  $\eta = E_{x\text{-ray}}/E_{\text{laser}}$  from driving laser pulse energy into one particular harmonic order is very low. This conversion efficiency is limited at the moment to  $\eta = 10^{-4}$  [214] or  $10^{-5}$  [240] at best, with the larger value corresponding to low-order harmonics. Using very intense driving lasers, only microjoule level harmonic emission could be facilitated to date [214].

A major constraint for efficient high-harmonic generation is the problem of reabsorption of the radiation in the generating medium. Since a long interaction length is needed for maximum conversion yields, it is always absorption which places the upper bound on the conversion efficiency [154, 155] in the phase-matched case. But even if absorption in the medium could be overcome by some means (e.g. using dark resonances), there would be another severe fundamental limitation: Ionization of the medium effectively extracts energy from the generating laser pulse without contributing to high-harmonic photon production. If only one out of 10 ionization acts leads to the production of a high-energy photon (which can be regarded as a typical value), we “waste” 90% of the absorbed pulse energy for additional ionization of the medium. It is within the scope of this work to introduce a new mechanism, which allows the ionized and returning accelerated electron to recombine with the parent ion with an increased probability.

Since the process of high-harmonic generation is understood very well for atomic systems, it is all the less understandable how little is known about the same process in more extended, complex systems. These latter systems provide means of optimization of

the infrared(IR)–soft-x-ray conversion process which are beyond the possibilities of their simple atomic counterparts. In particular, since high-harmonic generation is a coherent process, the conversion efficiency increases quadratically with the density of nonlinear emitters (see Eq. (1.100)). From this point of view, a solid or a liquid system, exhibiting high particle densities, could be a very favorable conversion medium.

Solid-state conversion media have been subject of a number of investigations in the past [241, 242]. Since we have not yet found a way to overcome the problems of absorption of harmonic radiation in the high-density medium, we are still restricted to work on the surface of solids [241]. The generation process in this case is different from the three-step model discussed in Section 2. Very high intense laser pulses have to be used to create relativistically moving electrons close to the surface of the material. The magnetic field in this case can no longer be neglected and leads to the well-known ‘figure-of-eight motion’ of the electrons. The nonlinear response can be understood in the picture of a ‘moving mirror’, the layer of free-electrons above the surface that oscillates up and down. The laser will scatter off this rapidly moving surface which leads to periodic Doppler shifts into the XUV, giving rise to harmonic peaks in the spectral domain. Phase matching is also difficult to achieve for harmonic generation in solids, due to high free-electron densities. However, schemes are available to overcome this substantial problem, for example employing Bragg-scattering in thin solid layers [243].

It is not only the density of a medium that is important. Any kind of inner degree of freedom of a particle can be used to control and optimize a process like high-harmonic generation. Another example is the size of the particle, which comes into play in the mesoscopic world.

Cluster targets, representing mesoscopic systems, have also been studied [244–247]. They were expected to increase the cut-off harmonic order from a simple argument given in terms of the three-step model: In a cluster, the electron does not need to recombine with its parent ion, but has different recombination centers available. Since the kinetic energy of the electron can be as high as  $8U_p$  (see Section 2.1, Eq. (2.7)) we would expect harmonic emission of orders  $n > 1/\hbar(I_p + 3.17U_p)$  to be emitted. In fact, the cutoff position was observed to shift slightly towards higher photon energies [244].

Molecular conversion media are particularly interesting most of all because of their simplicity. From an experimental point of view, they can easily replace the commonly used rare gas without having to change the apparatus. Regarding the theoretical aspects, molecules (in particular simple ones) are well understood. For example, the alignment of linear molecules [248] and its influence on the harmonic generation process has been investigated [249, 250]. It was theoretically found that the molecular alignment introduces an extra phase in addition to the atomic dipole phase  $\varphi_{at}$ . Alignment of the molecular sample led to a slight increase in the conversion efficiency, proving the importance to match the molecular phase. However, the magnitude of the observed effect could not provide sufficient proof for the theoretical considerations.

Moreover, molecular ions allow for additional quantum paths for the electronic trajectories as is the case in clusters. If the electron was ionized from one atom in the molecule, it does not need to return to the same one but could also recombine with the other atom [251]. This effect can also explain why molecules are more efficient emitters of

high-harmonic radiation relative to atoms when the driving laser is elliptically polarized, as will be detailed below. In addition, very high harmonic photon energies up to  $8U_p$  could possibly be generated [252] again for the reason that the electron does not need to return to the point where it ionized.

In Chapter 3 it will be shown how the structure of molecules can be employed to enhance the harmonic conversion efficiency to values higher than in the case of rare-gas atoms. A new method of preparing the molecular medium in a highly efficient state will be presented. A pump laser pulse can be used to create a vibrational wavepacket before the successive highly intense harmonic driver pulse interacts with the medium at a suitable time delay to generate high-harmonic radiation most efficiently.

This ‘pump–drive’ scheme is then experimentally applied in Chapter 4. As has been mentioned above, the density of the medium is a crucial parameter to optimize the conversion efficiency. Thus, water droplets are used as the providers of high-density medium. By a first laser pulse we can disperse the water droplet before it interacts with a second laser pulse that drives the high-harmonic generation process. This implementation of the pump–drive scheme allows to continuously scan the density region from solid down to gaseous in order to learn more about high-harmonic generation in condensed media. Additionally, as the water microdroplet undergoes explosion, it will fragment into clusters. Microdroplets thus provide a valuable conversion medium allowing to gain a deeper insight into almost any aspect of interest for optimal medium selection in high-harmonic generation.



# Chapter 3

## Molecular Media

Since molecules naturally exhibit more internal degrees of freedom than atoms, it was soon realized that molecular systems could be interesting emitters of harmonic radiation [253, 254]. Initial studies concentrated on extending the high-harmonic plateau to generate higher photon energies [252], followed by ideas how molecular ionization mechanisms could be exploited to enhance the conversion efficiency [255]. However, expectations to increase the harmonic efficiency above values obtained in atoms were not met in experiments to date.

This chapter is structured as follows: Section 3.1 outlines how the molecular geometry can affect the high-harmonic generation process. Symmetry properties exhibited by particular geometric shapes of the molecules modify the spectral response of the process. In Section 3.2 it is shown how the geometry of the molecule can be used to enhance the efficiency of the harmonic generation process in elliptically polarized driving fields. The design of efficient electronic ground-states for high-harmonic generation is the subject of Section 3.3. The spreading of the electronic wavepacket during ionization and recombination is a limiting factor of efficient high-harmonic generation. By the choice of carefully engineered bound electronic wavefunction—using the molecular degrees of freedom—the efficiency can be increased far above atomic levels. Finally, Section 3.4 introduces a technique how coherent control methods can be used to exploit the molecular degrees of freedom in order to enhance the conversion efficiency of the high-harmonic-generation process.

### 3.1 Molecular Symmetry Considerations

An interesting feature of molecular high-harmonic generation is the fact that due to a change in the geometry and symmetry of the microscopic system, the temporal and spectral harmonic emission properties can be affected. In theory, when a  $\text{H}_2$  molecule (aligned parallel to the polarization of the light) interacts with a laser field, the spectrum closely resembles the one observed in the atomic scenario. This is due to the fact that in this geometry, inversion symmetry is conserved. If the  $\text{H}_2$  molecule is replaced by a heteronuclear diatomic system, as for example HF, this inversion symmetry is broken and both

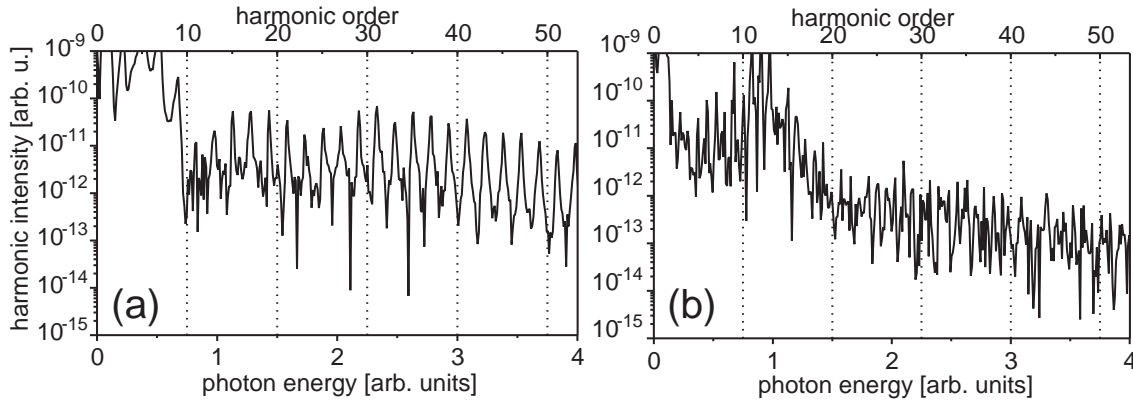


**Figure 3.1:** Molecular high-harmonic generation. In homonuclear diatomic molecules (a), only odd harmonics are visible as is also the case in atoms. If the inversion symmetry of the conversion medium is broken as is in heteronuclear diatomic molecules (b), odd and even order harmonics are produced. Results are obtained from a numerical simulation (Section 2.1.5) considering the single particle response in a laser field of 800 nm center wavelength and 0.1 a.u. peak electric field.

odd and even harmonic orders are produced (see Fig. 3.1). This can be understood since in the latter case the three-step process is not the same for electrons departing into one or the other direction. This leads to a repetition of the process only every full cycle of the laser optical period which explains the harmonic spacing of one times the fundamental laser frequency.

Typically, only the electric potential of the conversion medium needs to exhibit inversion symmetry to lead to the emission of only odd harmonic orders. However it was shown that also a deuterated hydrogen molecule (HD) which has a symmetric electronic configuration produces even order harmonics [256]. This is due to the fact that the symmetry is broken by the motion of the nuclei. The deuterium core will move smaller distances than the hydrogen core (accelerated by the laser field), creating a non-symmetric electronic potential for the dynamic system.

In fact, it is possible to extend our simple symmetry considerations to more complex molecular systems, exhibiting any discrete rotational symmetry

$$\mathcal{C}_N = \left( \varphi \rightarrow \varphi + \frac{2\pi}{N} \right). \quad (3.1)$$

For example, the benzene molecule  $C_6H_6$  has a  $\mathcal{C}_6$  symmetry, whereas the ammonium molecule  $NH_3$  is  $\mathcal{C}_3$  symmetric and all homonuclear diatomic molecules like  $H_2$ ,  $N_2$  or  $O_2$  for example exhibit  $\mathcal{C}_2$  symmetry. When these systems interact with a circularly polarized laser electric field, Alon *et al.* [257] pointed out another symmetry property  $\mathcal{D}_N$ , which is called a dynamical symmetry due to the fact that it combines space and time:

$$\mathcal{D}_N = \left( \varphi \rightarrow \varphi + \frac{2\pi}{N}, t \rightarrow t + \frac{2\pi}{N\omega} \right). \quad (3.2)$$

The Hamiltonian of the system is invariant under this transformation, in other words, rotation by an angle of  $\theta = 2\pi/N$  around the  $\mathcal{C}_N$  symmetry axis and shifting time by an



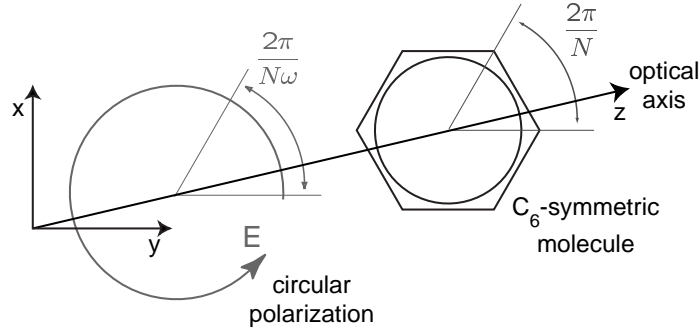


**Figure 3.2:** The effect of molecular discrete rotational  $\mathcal{C}_N$  symmetry for the interaction with circularly polarized laser light of frequency  $\omega$ . The example here shows a benzene molecule with  $N = 6$ . The identical situation is obtained when the molecule is rotated by an angle of  $2\pi/N$  and the temporal axis is shifted by  $2\pi/(N\omega)$ . This has important consequences for the molecular high-harmonic spectral response.

$N$ th of the optical period  $T = 2\pi/\omega$  (which advances the rotating electric field vector also by the angle  $\theta$ ) leads to identity (Fig. 3.2). For the emission of the  $n$ th order harmonic, we now examine the  $n$ th order nonlinear dipole moment

$$d_n = c |\langle \Phi | re^{\pm i\varphi} e^{-in\omega t} | \Phi \rangle|^2 \quad (3.3)$$

where  $re^{\pm i\varphi}$  denotes the two components of the dipole operator in cylindrical coordinates perpendicular to the laser propagation direction,  $c$  is some constant and  $\Phi$  is any eigenfunction of the Floquet-Hamiltonian. We can now apply the transformation  $\mathcal{D}_N$  on the right hand side of the last equation, which has to reproduce the same dipole moment

$$d_n = c |\langle \mathcal{D}_N \Phi | \mathcal{D}_N re^{\pm i\varphi} e^{-in\omega t} \mathcal{D}_N^{-1} | \mathcal{D}_N \Phi \rangle|^2. \quad (3.4)$$

Since  $\mathcal{D}_N$  commutes with the Hamiltonian of the system, the eigenfunctions of the Hamiltonian are also eigenfunctions of  $\mathcal{D}_N$ . The corresponding eigenvalues are  $N$ th unit roots ( $\sqrt[N]{1}$ ), since  $N$ -fold repeated application of the  $\mathcal{D}_N$  results in the identity operation. Therefore we may write, by setting the latter two equations equal to each other

$$\begin{aligned} e^{\pm i(\varphi + \frac{2\pi}{N})} e^{-n\omega(t + \frac{2\pi}{N\omega})} &= e^{\pm i\varphi} e^{-in\omega t} \\ \Leftrightarrow e^{i\frac{2\pi(n\pm 1)}{N}} &= 1 \\ \Rightarrow n = 1 \vee n = lN \pm 1; l \in \mathbb{N}. \end{aligned} \quad (3.5)$$

We obtain harmonic emission for these values of  $n$ . The same reasoning can be used in order to explain why harmonic generation with circularly polarized driving light is absent for atoms, which exhibit  $\mathcal{C}_\infty$  symmetry: only the dipole moment corresponding to  $n = 1$  is nonzero. High-harmonic generation and in particular this calculation are good examples to show that symmetries can be used to characterize the properties of a process.

## 3.2 Ellipticity Dependence

From the three-step model we know that in order to generate high harmonics, the electron has to return to the ion core it left. If an elliptically polarized driving field is employed instead of a linearly polarized one, it is easy to imagine that the electron will not directly return to its parent ion but slightly “miss it”. The electronic wavefunction will thus interact with the ion at a different impact parameter depending on the degree of ellipticity of the driving light. The ellipticity dependence of the high-harmonic generation process can thus be used as a sensitive probe to investigate the recollision dynamics in the high-harmonic generation process. In this section, the different ellipticity dependencies of an atomic system compared to a molecular system will help to increase the understanding of high-harmonic generation in molecules.

Many past experiments concentrated on the comparison of high-harmonic generation in different atomic and molecular gases [258–262]. It was noticed [258] that the static average polarizability is an important parameter for the dependence of generation efficiency on laser intensity. Overall, a very similar behavior of molecules as compared to rare gases was reported. However, these studies were performed using linearly polarized laser light.

Elliptically polarized light has earlier been used as a tool to probe our understanding of the high-harmonic generation process [166, 263–266]. Additionally, as has been noted in [267, 268], ellipticity dependence (for small ellipticity values  $\varepsilon$ ) is an efficient way to isolate the single particle response from propagation effects. The ellipticity  $\varepsilon$  is defined as the ratio of the smaller to the larger principal axis of the ellipse drawn by the electric field vector.

In a molecule, the dipole matrix element of the returning electronic wave packet with the bound-state wave function (governing recombination, thus harmonic emission) can be larger for higher values of  $\varepsilon$  than in the atomic case. In simple terms, for elliptic polarization, the classical trajectory of an electron starting with zero velocity [107] never returns to its starting point. For the case of a molecule, the electron can recombine with a second atom, which might be closer to its trajectory than the atom it left.

The gases used for this comparative study were argon and nitrogen as they are very similar in relevant characteristics: first of all, they have almost identical ionization potentials (Ar: 15.8 eV, N<sub>2</sub>: 15.6 eV). In addition, they show similar static average polarizabilities (Ar:  $1.7 \times 10^{-24}$  cm<sup>3</sup>, N<sub>2</sub>:  $1.6 \times 10^{-24}$  cm<sup>3</sup>) [258, 259, 261]. The third-order susceptibilities at  $\lambda=1055$  nm also lie close to each other ( $\chi_0^{(3)}(\text{Ar})= 23.5 \times \chi_0^{(3)}(\text{He})$ ,  $\chi_0^{(3)}(\text{N}_2)= 21.1 \times \chi_0^{(3)}(\text{He})$ ) [269]. Therefore, these gases are good candidates for this fundamental comparison. Until now, they were used to compare the polarization state of the emitted harmonics [270].

### 3.2.1 Experimental Setup

The laser system described in Section 1.1.1 was used for this experiment. A lens with a focal length of 300 mm focused the laser into a vacuum chamber. A piezoelectric pulsed valve operating at 1 kHz synchronized to the laser pulse provided the nonlinear medium,

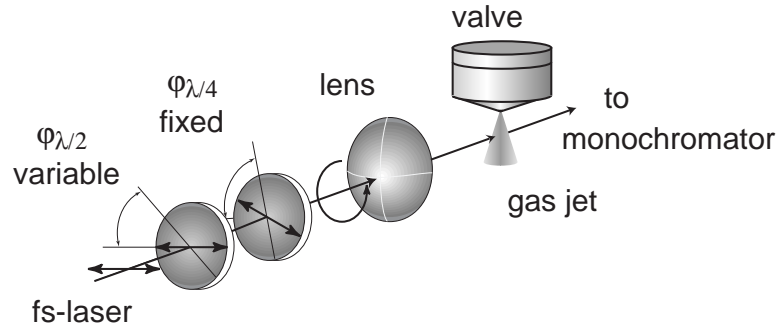


**Figure 3.3:** Experimental setup for the measurement of high-harmonic ellipticity dependence. By rotating the half-wave plate in front of the quarter-wave plate, the polarization state of the initially linear polarized laser pulses could be continuously changed from linear to circular. The lens was used to focus the laser close to the gas jet.

in this case Ar and N<sub>2</sub>. The details of the valve used are described in detail elsewhere [109, 271]. The originally linearly polarized laser light was manipulated using a combination of a half-wave plate and a quarter-wave plate as depicted in Fig. 3.3. Both were zeroth order wave plates for 800 nm. The polarization state could thus be continuously changed from linear to circular by rotating the half-wave plate in front of the fixed quarter-wave plate. A stepper motor connected to a computer was used to control the orientation of the half-wave plate.

The intensity in the focus was obtained by measuring the ion yield of different noble gases and comparing it to Ammosov-Delone-Krainov (ADK)–ionization [112] rate calculations (see Section 2.1.1). The result was  $3 \times 10^{14} \text{ W/cm}^2$  (see Fig. 3.4). The ionization yield in the simulation was obtained by assuming a gaussian transverse spatial intensity profile and a  $\text{sech}^2$  laser pulse of 80 fs time duration. The ADK ionization rate given in Eq. (2.3) was then integrated over time and space. Cylindrical symmetry around the propagation axis was assumed. A more detailed description of this intensity calibration can be found in [109]. Two different monochromators were used as detectors for the high-harmonic radiation: a home-built Seya-Namioka monochromator (from here on referred to as MC1), which allowed detection of the third harmonic (H3) down to H17, and a grazing incidence monochromator (referred to as MC2) capable of detecting harmonic orders higher than H11. The two monochromators are described in detail in [272]. Behind the exit slit of the monochromator, the vacuum-ultraviolet (VUV) radiation was converted into visible fluorescence by a Na-Salicylate scintillator and detected with a photomultiplier tube. Data was acquired with a computer by using a boxcar integrator.

### 3.2.2 Experimental Results

For the measurements of the ellipticity dependence at a given harmonic order, the monochromator was set to the corresponding wavelength and the half-wave-plate was turned at least one full rotation. The backing pressure behind the valve was chosen to be

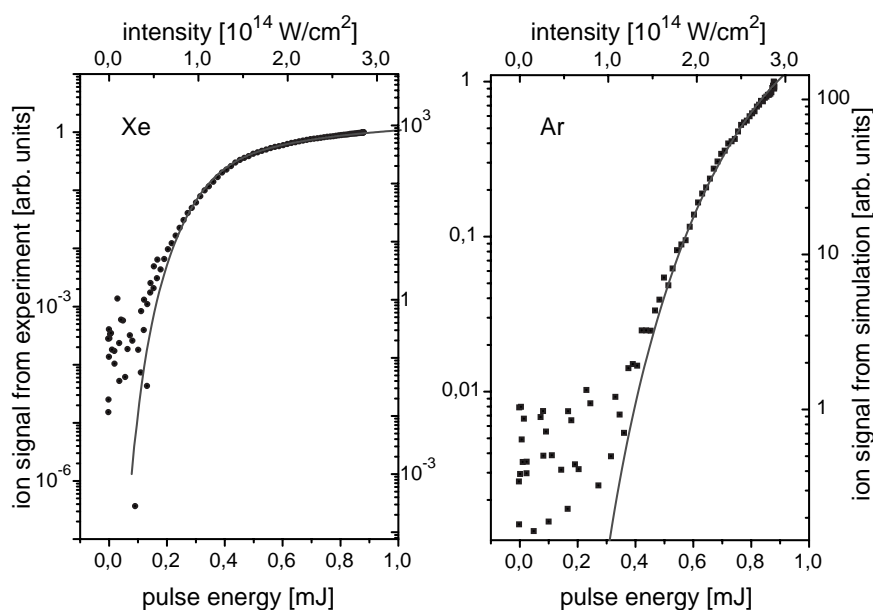


**Figure 3.4:** Experimental determination of the intensity of ultrashort laser pulses. Comparing the experimental ion yield for various pulse energies with calculations based on the ADK theory of ionization it was possible to find the focal laser intensity through fitting. The calculations have to account for the temporal and spatial properties of the laser.

2 bar for both gases, to allow most stable operation of the valve. In Fig. 3.5 experimental results are shown for different harmonic orders. Clearly, the molecular ellipticity dependence (squares) is weaker than in the atomic case (circles). To check the reproducibility, four subsequent measurements have been performed for the case of H5 (Fig. 3.5a) in the order Ar, N<sub>2</sub>, Ar, N<sub>2</sub>, where all experimental parameters were kept constant except for the medium. The difference is even more pronounced for the plateau harmonics H13 and H21, which are shown in Fig. 3.5b and c, respectively. Data in the latter two cases are shown for  $\epsilon < 0.6$  as the noise level of the detection system is reached for higher ellipticities.

### 3.2.3 Simulation

An analytical solution of the Schrödinger equation for the case of a molecule following the approach given in [108] is not yet available and seems to be a rather intricate calculation. Therefore, to evaluate the experimental results, a numerical simulation based on the model developed in [108] was performed. It shows some similarity to an earlier approach used in [268]. There, the authors report very good agreement to their experimental data.

The electric field is described as:

$$\vec{E}(t) = E_0 \sqrt{\frac{1}{1 + \epsilon^2}} (\cos(\omega t) \vec{e}_x + \epsilon \sin(\omega t) \vec{e}_y), \quad (3.6)$$

where  $E_0$  stands for the amplitude of the electric field vector,  $\omega$  is the angular frequency

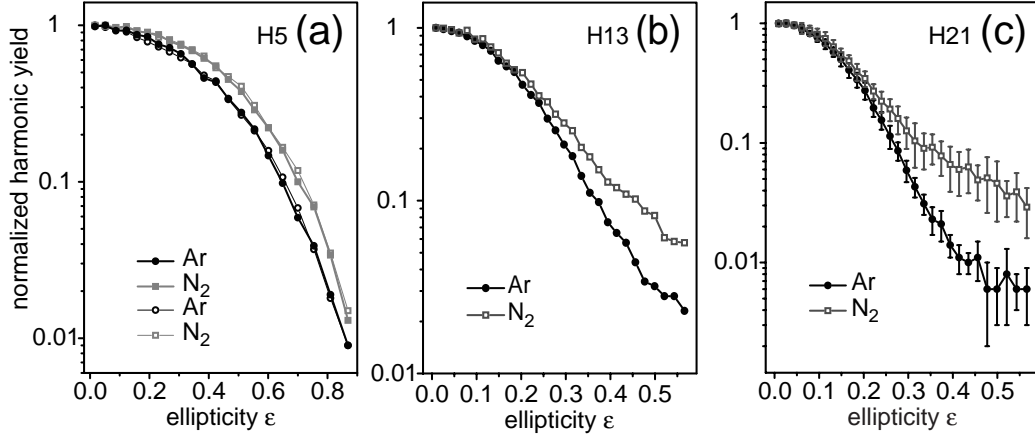


**Figure 3.5:** Ellipticity dependence of different harmonic orders in Ar compared to N<sub>2</sub>. The harmonic intensities are normalized with respect to the harmonic intensity produced with linearly polarized light. The molecule N<sub>2</sub> shows an increased efficiency at non-vanishing ellipticities  $\varepsilon$  of the driving laser pulses, which is consistent for low-order harmonic H5(a) and plateau harmonic orders H13(b) and H21(c).

of the laser field and  $\vec{e}_x$  and  $\vec{e}_y$  are unit vectors in  $x$ - and  $y$ -direction respectively. The simulation contains the following assumptions: The electron is ionized at a time  $t'$  with probability according to the ADK theory [112] Eq. (2.3) and appears in the continuum with zero velocity. It then propagates under the influence of the electric field alone. Emission of a harmonic photon of energy  $E_n$  can occur at time  $t_n$  if

$$E_n = E_{kin}(t_n, t') + I_p. \quad (3.7)$$

$E_{kin}(t, t')$  is the kinetic energy of the electron at time  $t$ . The photon is emitted when recombination takes place, which occurs with probability

$$p_n(t') \sim |\langle \psi_g(\vec{r}) | r | \psi_c(\vec{r}, t_n, t') \rangle|^2, \quad (3.8)$$

where  $\psi_g(\vec{r})$  and  $\psi_c(\vec{r}, t, t')$  are stationary ground state and continuum wave functions of the electron, respectively. In other words the emission probability is proportional to the overlap of the electron continuum wavefunction with the ground state (see Fig. 3.6). If the spatial extent of the continuum wavepacket is much larger than the one of the ground state (which is the case for plateau harmonics), we can (for the atom case) let  $\psi_g$  approach a delta function centered at the origin and thus arrive at

$$p_n(t') \sim |\psi_c(0, t_n, t')|^2. \quad (3.9)$$

The time-dependent continuum wave function was assumed to be

$$\psi_c(\vec{r}, t, t') = \left( \frac{2}{\sqrt{\pi}v(t-t')} \right)^{3/2} \exp \left( - \left( \frac{\vec{r} - \vec{r}_{cl}(t, t')}{v(t-t')} \right)^2 \right), \quad (3.10)$$

i.e., an initially localized Gaussian wave packet, spreading with a velocity of  $v$  to approximate a freely evolving massive particle wave function.  $\vec{r}_{cl}(t, t')$  stands for the classical electron trajectory (see Section 2).

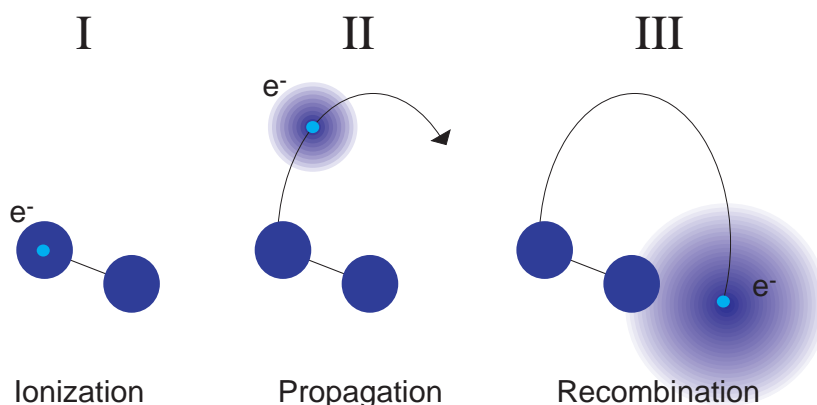


**Figure 3.6:** Illustration of the model to calculate the ellipticity-dependent high-harmonic yield in molecules and atoms. At some time  $t'$  the electron is tunnel ionized with a probability according to the ADK ionization rate. After acceleration of the electron in the laser field—following the classical Newtonian path—it can recombine with the parent ion to emit high-harmonic radiation only if the wavefunction overlaps with the molecule or atom.

The amount of harmonic emission is calculated by averaging over all ionization times  $t'$ . The only free parameter in this treatment is  $\nu$ , which can be used to fit the model to the (atomic) experimental data. The best fit is obtained for a value of  $\nu=5.3 \text{ \AA/fs}$  (see Fig. 3.7) at H21.

To get an estimate of the harmonic generation efficiency for the molecule, the squared modulus of the continuum wave function at both atomic centers was calculated. As the experiment was carried out with a statistically aligned molecular sample, an average was performed over an ensemble of molecular orientations all located in the polarization plane of the laser.

The ellipticity dependencies shown in Fig. 3.7 were calculated for a molecular atom separation of  $1.4 \text{ \AA}$ , corresponding to the equilibrium distance of the nuclei in  $\text{N}_2$  and for  $2^n$  multiples of that value. With increasing internuclear separation the ellipticity dependence becomes weaker and weaker for the range of values shown. For eight times the equilibrium distance even a non-monotonous behavior is obtained. A non-monotonous behavior of the ellipticity dependence has already been observed in experiment [267, 273] and was attributed to the role of the Coulomb potential of the parent ion [274], which is neglected in the three-step model. The quantum-mechanical formulation of the three-step model [108] only predicts monotonous dependence of the harmonic yield on ellipticity. The non-monotonicity of the high-harmonic ellipticity dependence in the above presented simulation on molecular high-harmonic generation has a different origin. For elongated internuclear separations, some electron trajectories leave the molecule from one atom and recombine with the other one. If the molecule is aligned perpendicular to the large principal axis of the polarization ellipse, there is an optimum ellipticity  $\epsilon_{opt}$  for which the electron that departs at a given atom recombines with the other atom. In addition, linearly polarized light  $\epsilon = 0$  leads to perfect return to the same atom. In between these two ellipticity values, the harmonic yield will pass through a minimum. This effect is retained even although orientational averaging was performed. Future experiments will shed more

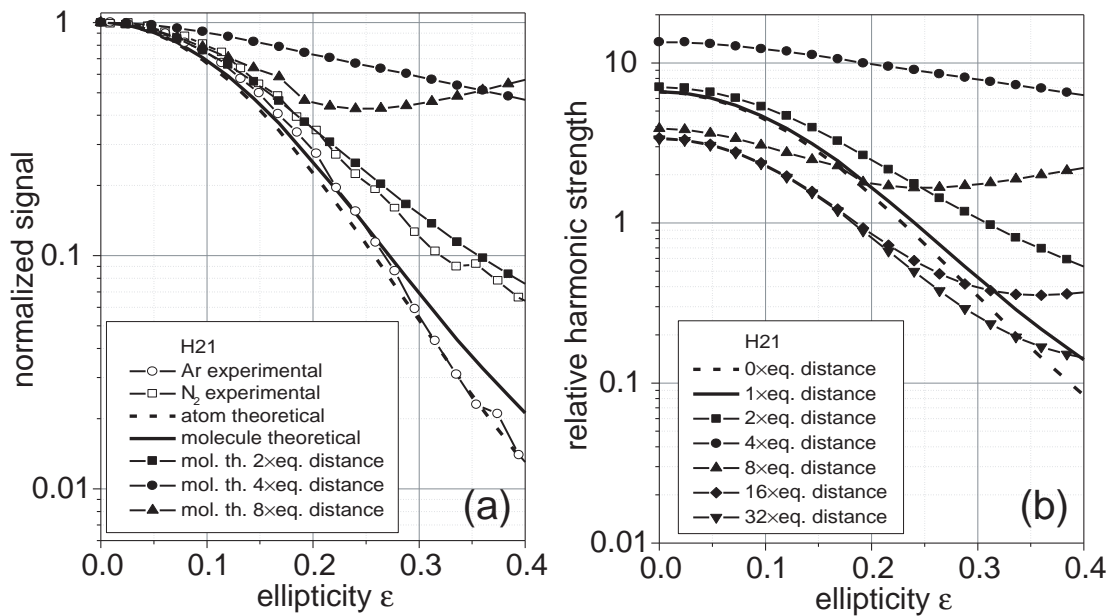


**Figure 3.7:** Comparison of theory with experiment at H21. (a) Relative results for comparison with the experiment. The data are again normalized to 1 at  $\epsilon=0$ . The results for the molecular system are shown for different inter-nuclear separations in multiples of  $2^n$  times the equilibrium distance (1.4 Å). (b) Comparison of emission strengths without normalization. Significant enhancements at small ellipticities indicate possible enhancements of harmonic generation by the use of molecular systems.

light on this particular feature of molecular high-harmonic generation.

Fig. 3.7 shows normalized harmonic emission strength (normalized to 1 at  $\epsilon = 0$ ) to compare to experimental results. Fig. 3.7b directly compares emission strengths without normalization.

All results obtained, experimental and theoretical, reveal a weaker dependence on ellipticity for the molecule than for the atom. A visible influence of the spatial extent of the generation medium can thus be reported. This is in agreement with earlier experimental results in [265], where the ellipticity dependence of organic molecules (e.g. benzene and n-hexane) was compared to xenon atoms using similar driving pulse durations of 70 fs. Another study with longer laser pulses (240 fs) [266] showed the opposite behavior between molecule and atom, i.e. the atomic ellipticity dependence being weaker than the molecular one. This was explained by fragmentation of the molecule and harmonic generation occurring from each isolated fragment instead from the whole molecule.

Regarding just the theoretical results it can be stated that the three-step model in the form employed is predicting a weaker ellipticity dependence for molecules than for atoms, which becomes even more pronounced at larger inter-nuclear separations. From Fig. 3.7b we learn, that an enhancement of harmonic efficiency would occur even for linearly polarized laser light at a separation of around four times the equilibrium distance. At an ellipticity of 0.3 the enhancement would be even larger: far more than one order of magnitude. Designated experiments will be needed to further elucidate these predictions.

The three-step model in the above approximation does not show convincing agreement with the experimental findings. This is due to the smallness of the internuclear separation as compared to the length scale of the free electron trajectory. The experimental data for the  $N_2$  molecule can be reproduced in the model by adjusting the nuclear separation. A value of about twice the equilibrium distance is obtained in this case. This could indicate the generation of harmonics from expanded molecules. As the strong laser field significantly alters the electronic ground state of the molecules, the covalent bond strength is reduced. The ground state vibrational period of the  $N_2$  molecule is 14 fs. It is therefore possible that the molecule expands within the time scale of the 80 fs laser pulse used in the experiments.

There could be explanations of the experimental results that go beyond the three-step model. In this model, contributions due to bound-bound transitions are neglected. Contributions from these transitions to the high-harmonic-generation process have been under study in [254]. The authors focus on high-harmonic generation from charge-resonant states in molecular ions, treating the molecule as a two-level system with a large dipole matrix element between the two states. However, the theory described there is only valid for larger nuclear separations and cannot directly be applied to the presented experiment.

The next section returns to the case of linearly polarized driving light and shows how not only the recombination act—as was studied in this section—but also the ionization and most importantly propagation of the electron can be optimized by exploiting molecular degrees of freedom.

### 3.3 Electron-Wavepacket Engineering

It has been demonstrated in both experiment and theory that harmonic generation in molecular media can be enhanced by the control of molecular degrees of freedom, for instance by aligning the target molecules [249, 250]. However, it remained unclear in these works whether molecular media could be any more efficient than atomic ones. As was shown above, the high-harmonic conversion efficiency of molecules drops slower compared to atoms for increasing ellipticity of the driving field. Only recently, the first experiments on high-harmonic generation in dissociating molecules were carried out [275]. Indeed an enhancement of harmonic production in stretched molecules was observed. However, the enhancement was attributed to near resonant enhancement of the dissociated atom and was not caused by molecular properties.

It is already known from theory [276] that cross-correlation of an XUV and a strong IR pulse in a molecule aligned along the electric field vector can drastically increase the high-harmonic-generation efficiency by optimizing the ionization step. The crosscorrelation method can also be used to efficiently create a large continuum near the cutoff [255], which in turn is beneficial for attosecond pulse production (see Section 2.3). This method, however, requires the availability of an attosecond pulse prior to high-harmonic generation.

A new mechanism is now pointed out which shows that high-harmonic generation can also be enhanced by modifying the propagation of the electron in the continuum. The



conversion efficiency from IR into the soft x-ray region can be increased by up to a factor of 10 by controlling the electronic ground state of the molecules through excitation of vibrational wave packets. The basic idea is to slow down the quantum-mechanical spreading of the free-electron wavepacket in the continuum. In a linearly polarized electric field, the most compact returning electron wave packet can interact most efficiently with the ionic core, giving rise to most efficient high-harmonic generation. It has been shown that for the case of relativistic electrons the velocity of spreading can be reduced [277]. However, this is of no value for the case of high-harmonic generation considered here, which only occurs at sub-relativistic laser electric fields. The new mechanism of wavepacket-engineering introduced here does not depend on the laser field strength but merely on the design of the electronic initial state. In addition, to build a bridge towards an immediate application and verification an experiment is proposed and simulated at the end of this chapter.

### 3.3.1 The Model

Similar to earlier theoretical studies [253, 254], the  $\text{H}_2^+$  molecule [278] was chosen as the model system for the reason of simplicity. As a first step, the nuclear degrees of freedom were ignored, i.e. the molecular vibrational and rotational motion was frozen. Since laser pulses of  $\sim 17$  fs duration were assumed, this approximation is not valid for the  $\text{H}_2^+$  molecule but would surely apply for heavier molecules. Consequently, the Hamiltonian in the dipole approximation and velocity gauge is written as:

$$H = \frac{\vec{p}^2}{2} + \vec{p}\vec{A}(t) + V(\vec{r}) \quad (3.11)$$

in atomic units ( $\hbar = e = m = 1$  used throughout) for an electron under the influence of a stationary molecular potential  $V(\vec{r})$  and the time-dependent vector potential  $\vec{A}(t)$ . The molecular potential was considered to be a two-center softened Coulomb potential  $V(\vec{r}) = (-1)/\sqrt{x^2 + (y - d/2)^2 + a} + (-1)/\sqrt{x^2 + (y + d/2)^2 + a}$ , where the smoothing parameter  $a$  was set to 0.5. The molecule was aligned along the  $y$ -direction with internuclear distance  $d$ .

The time-dependent Schrödinger equation was solved on a two-dimensional grid in spatial coordinates  $x$  and  $y$ . Propagation in time was accomplished by means of the split-step operator technique [279, 280] described in more detail in Appendix C. The grid comprised an area of 410 by 205 atomic units (a.u.) with absorbing boundaries. The ground state was propagated in time under the action of the ac electric laser field. The  $\sin^2$ -shaped laser pulses were linearly polarized along  $x$ , thus perpendicular to the molecular axis. Their duration (FWHM-intensity) was 722 a.u. (17 fs) with an angular frequency centered around 0.057 a.u. corresponding to 800 nm wavelength. The peak electric field was set to 0.125 a.u. yielding an intensity of  $5.5 \times 10^{14} \text{ W/cm}^2$ .

Care was taken that the relevant electronic trajectories be well contained in the box. This can be done by calculating the maximum ponderomotive radius  $a_0$  (see Section 2). Electrons returning to the ion are confined to a distance of  $2a_0$ . If the atom or molecule is located at the center of the box, the box size has to be larger than  $4a_0$ . Using the peak

electric field strength  $E$  and laser frequency  $\omega$  given above, the ponderomotive radius is  $a_0 = E/\omega^2 = 38.5$  and thus smaller than one fourth of the box size in the polarization direction of the laser field.

The nonlinear radiative response  $\vec{S}_{nl}(t)$  of the molecule was calculated via the time-dependent dipole acceleration expectation value as discussed in Section 2.1.5,

$$\vec{S}_{nl}(t) \sim \frac{d^2}{dt^2} \langle \vec{r}_{nl} \rangle = \langle \vec{\nabla} V \rangle, \quad (3.12)$$

using Ehrenfest's theorem [131]. From this quantity, the harmonic emission spectra  $|\vec{S}_{nl}(\omega)|^2$  were obtained by Fourier-transformation into the frequency domain.

### 3.3.2 Internuclear-Distance Dependence

Fig. 3.8a shows harmonic spectra for various internuclear separations and for the atom in comparison. The high-frequency cutoff positions  $n_c$  agree with the analytical result  $n_c = I_p + 3.17U_p$  [105, 107], where  $I_p$  and  $U_p$  are the ionization potential and the ponderomotive potential of the electron, respectively. Fig. 3.8a also shows that in the plateau region of the spectra there are significant differences in high-harmonic yield. The change of cutoff position on the other hand is due to different ionization potentials  $I_p$ . When the summed harmonic yield in the indicated interval is plotted versus internuclear distance, a clear enhancement appears for intermediate values of  $d$  (Fig. 3.8b). This behaviour can be explained by considering two aspects of the high-harmonic generation process, namely ionization of the active electron and propagation in the electric field. Since the ionization potential for  $\text{H}_2^+$  into  $\text{H}_2^{2+}$  rapidly decreases for increasing values of  $d < 2.5$  a.u., the harmonic yield rises from very small values as a result of increased probability for tunnel ionization with decreasing barrier height. For larger values of  $d$ , the efficiency increases further until it starts to rapidly decrease at internuclear distances greater than 11 a.u. We understand this latter feature by the following mechanism [281]: During propagation in the continuum, the electronic wave function suffers quantum mechanical dispersion (spreading). However, if the initial state of the electron at the starting point of its orbit is largely delocalized—as is the case in molecules, particularly in elongated ones (see Figs. 3.9 and 3.10)—the velocity of spreading will be reduced since the electronic wave packet has a narrower width in momentum space. Hence, a compact wave packet can finally return to the parent molecule and interact more efficiently with the molecular potential to generate bremsstrahlung. The probability for emission of a harmonic photon per ionization act can thus be effectively increased compared to the atom, where the ground state electronic wave function is more localized than in the optimal molecular case. Fig. 3.10 illustrates this behavior for the atomic and different molecular geometries. For one particular internuclear distance, the returning electronic wavepacket shows the highest probability density at the positions of the nuclei, hence conversion is maximized. These snapshots of the electronic wave-function have been calculated in the barrier-suppressed-ionization (BSI) field-strength regime [113] in order to obtain only a single ionization act and thus a single electronic wavepacket for a clear demonstration of the effect [281]. It is directly visible that an increased amount of delocalization of the real space wave-function, which is connected to a reduced width of the momentum space

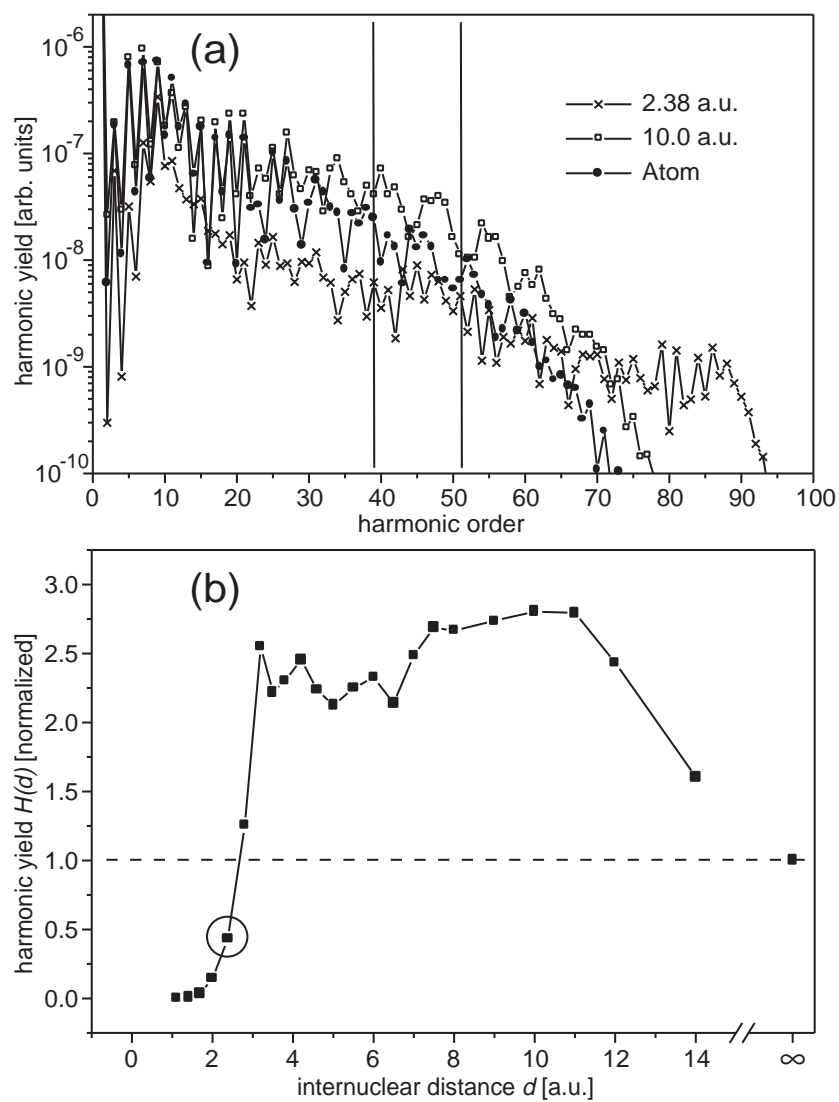


**Figure 3.8:** Harmonic spectra (a) and integrated XUV-emission (H39 to H51) versus internuclear distance  $d$  (b). In a broad range of  $d$ , high-harmonic generation is more efficient by a factor of 3 than for the atomic case ( $\infty$ ). Compared to the equilibrium bond length of the molecule (encircled data point) the enhancement is about one order of magnitude

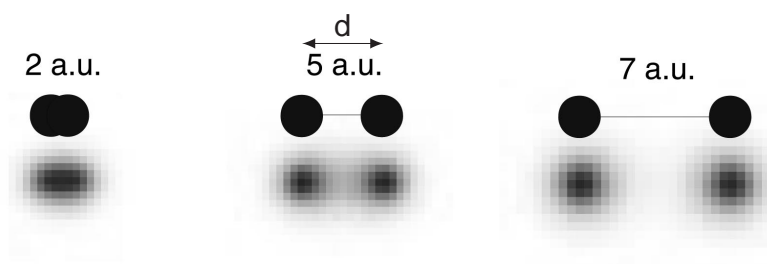


**Figure 3.9:** Effect of internuclear separation  $d$  in molecules on the delocalization of the electronic ground state. Shown is the squared modulus of the electronic wavefunction in a model  $H_2^+$  molecule. For small  $d$  a unimodal distribution is obtained and the electron is confined to a small region in space along the molecular axis. At intermediate values of  $d$ , the electronic wavefunction is distributed over a larger region i.e. delocalization is increased. At very large values of  $d$ , the electron is again confined since the wavefunction is almost zero between the nuclei.

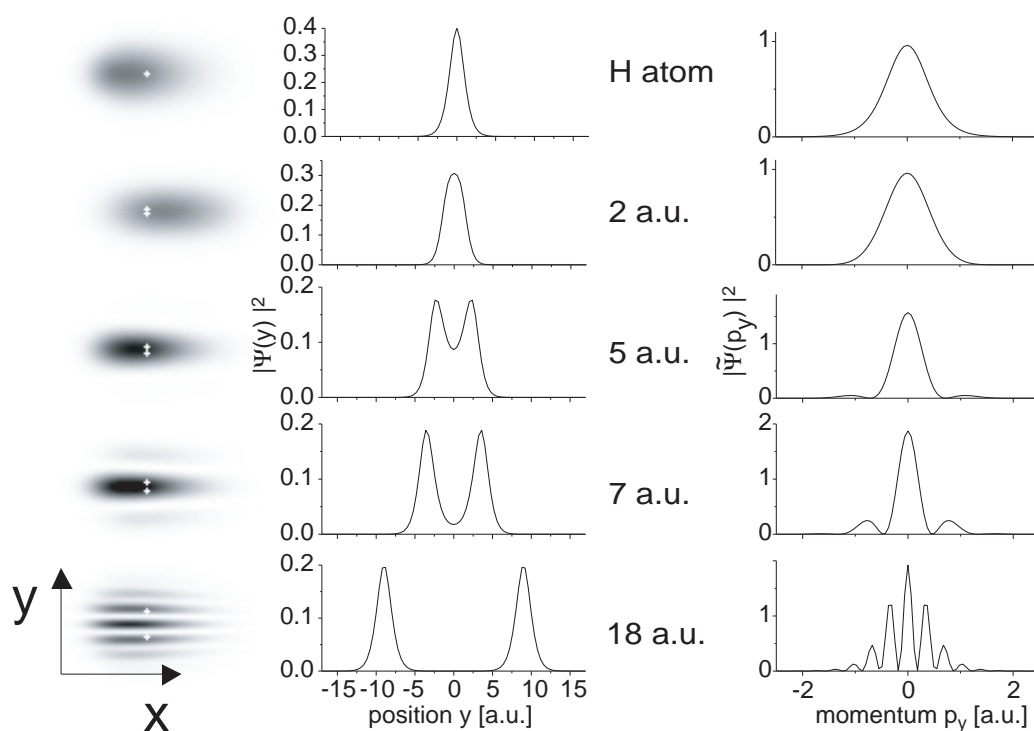


**Figure 3.10:** Snapshots of the two-dimensional wavefunction of the ionized and returning electron in a strong laser field (shown in grayscale) at the moment of interaction with the atomic/molecular parent ion. White dots represent the positions of the nuclei. For a particular interatomic separation, the wavefunction is most compact, indicating most efficient high-harmonic generation. Shown besides are the corresponding electronic wavefunctions of the field-free ground state of each system in both real space and momentum space. A high degree of delocalization of the electronic ground state leads to a small width of the momentum space distribution, i.e. small velocity of spreading of the electronic wavepacket during propagation in the continuum.

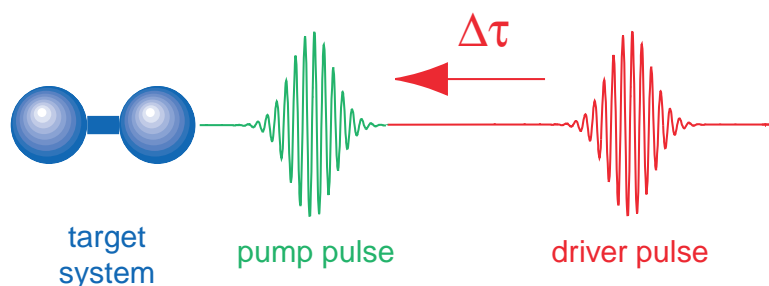


**Figure 3.11:** Illustration of the pump–drive scheme for high-harmonic generation. A first laser pulse (pump) is used to prepare the system in a suitable state. This can for instance be achieved by exciting a vibrational wavepacket in the molecules as discussed in the text. In general any method of coherent control can be applied. The second pulse is the intense driver pulse, which generates high-harmonics from the prepared quantum system.

wave-function carries over to a reduced width of the returning electron wavepacket in real space. This is understood from the fact that the electronic wave-function is subject to quantum-mechanical dispersion of a free particle while it is moving far away from the ion. This finding directly expresses the necessity of research on molecules with regard to efficient coherent XUV generation. In particular, there are many more ways of optimizing and tailoring the ground state electronic wave function in more complex molecular compounds than simple diatomic media can provide.

### 3.4 Pump–Drive Schemes

Let us now turn towards an idea to experimentally verify these stated predictions. The question is: How can we measure (and afterwards: exploit) the harmonic yield as a function of the internuclear separation of a diatomic molecule? In analogy to the work by Numico *et al.* [252] the following strategy is proposed: An initially aligned molecular sample [249] is illuminated with two ultrashort laser pulses. The first one serves as the pump pulse preparing a dissociative or vibrational molecular wavepacket whereas the second time-delayed pulse is the driver for high-harmonic generation, probing the nonlinear dipole response of the system at different times corresponding to different internuclear distance situations (see Fig. 3.11). The time-delay dependence of the high-harmonic yield can then be used to verify the dependence of high-harmonic-generation efficiency on internuclear distance. This ‘pump–drive’ scheme can be implemented in various ways, two general ones of which are (1) resonant excitation to an excited molecular state or (2) non-resonant single (XUV) photon, multi-photon, or resonance-enhanced multi-photon ionization (REMPI) to generate a time-dependent ionic molecular wavepacket. In the following, the latter case is considered in more detail.

Based on the given model Hamiltonian the potential energy curve for the model  $\text{H}_2^+$  system was calculated (see Fig. 3.12). If instantaneous ionization from the neutral  $\text{H}_2$  (with a bond length of 1.4 a.u.) to the singly ionized molecule by a broadband ultrashort XUV-

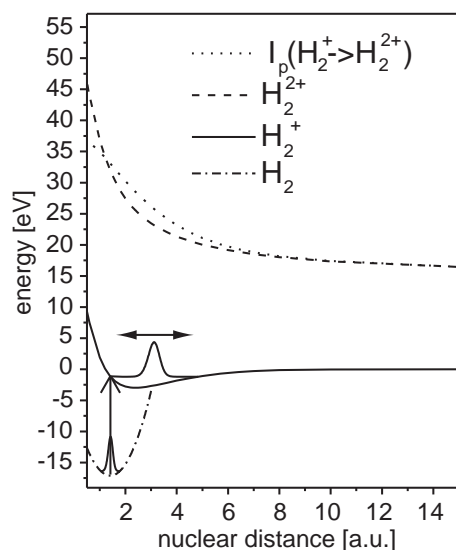


**Figure 3.12:** Potential energy curve for the model  $\text{H}_2^+$  system on which the molecular wavepacket is created by ionization of the vibrational ground state of the neutral  $\text{H}_2$  molecule (dash-dotted line). The potential energy curve of the  $\text{H}_2^+$  (dashed line) is the Coulomb repulsion between the naked nuclei. The ionization potential of  $\text{H}_2^+$  is shown as dotted line.

pulse is assumed, the nuclear wavepacket is transferred from the  $\text{H}_2$  (vibrational state  $v=0$ ) to the  $\text{H}_2^+$  potential energy curve. In this case, since the model  $\text{H}_2^+$  molecule at an internuclear distance of 1.4 a.u. is a bound system, the wavepacket motion succeeding ionization will be purely vibrational, not dissociative.

The molecular wavepacket evolution  $\Phi(d,t)$  on the  $\text{H}_2^+$  curve is shown in Fig. 3.13a. It was again calculated by application of the split-step-operator technique (see Appendix C). After ionization (defining time 0 in the wavepacket evolution), it takes about 15 fs for the wavepacket to travel from the inner turning point to the outer one. Since many vibrational modes are excited (due to the large bandwidth of the XUV pulse) close to the dissociation threshold, dephasing occurs very rapidly. Note that the ultrashort XUV pulse is only used to accommodate the very fast vibrational dynamics in the  $\text{H}_2^+$  molecule. The experiment can be performed in a heavier molecule like  $\text{Na}_2$ ,  $\text{Br}_2$  or similar with pump pulses of duration on the order of tens of femtoseconds. It is only necessary that the exciting pulse is much shorter than the vibrational period. To illustrate this, Fig. 3.13b shows the wavepacket dynamics in  $\text{Na}_2^+$ , created by the action of a 25 fs laser pulse at a wavelength of 620 nm. In this case, an almost classical oscillatory behavior is obtained due to the smaller bandwidth of the exciting laser pulse.

To calculate the transient harmonic emission of a sample of  $\text{H}_2$  molecules irradiated by the driver pulse after pre-ionization by the pump pulse, the probability distribution function  $|\Phi(d,t)|^2$  is multiplied by the harmonic yield  $H(d)$  shown in Fig. 3.8. The result is plotted as  $\tilde{H}(t)$  in Fig. 3.14. As can be seen, the integrated harmonic signal (H39-H51) shows a very rapid initial increase. This is because the molecule expands from the very inefficient interatomic distance range  $d < 2$  a.u. into the more efficient region with  $d > 3$  a.u. (Fig. 3.8 and Fig. 3.13). Afterwards, the signal oscillates as a consequence of

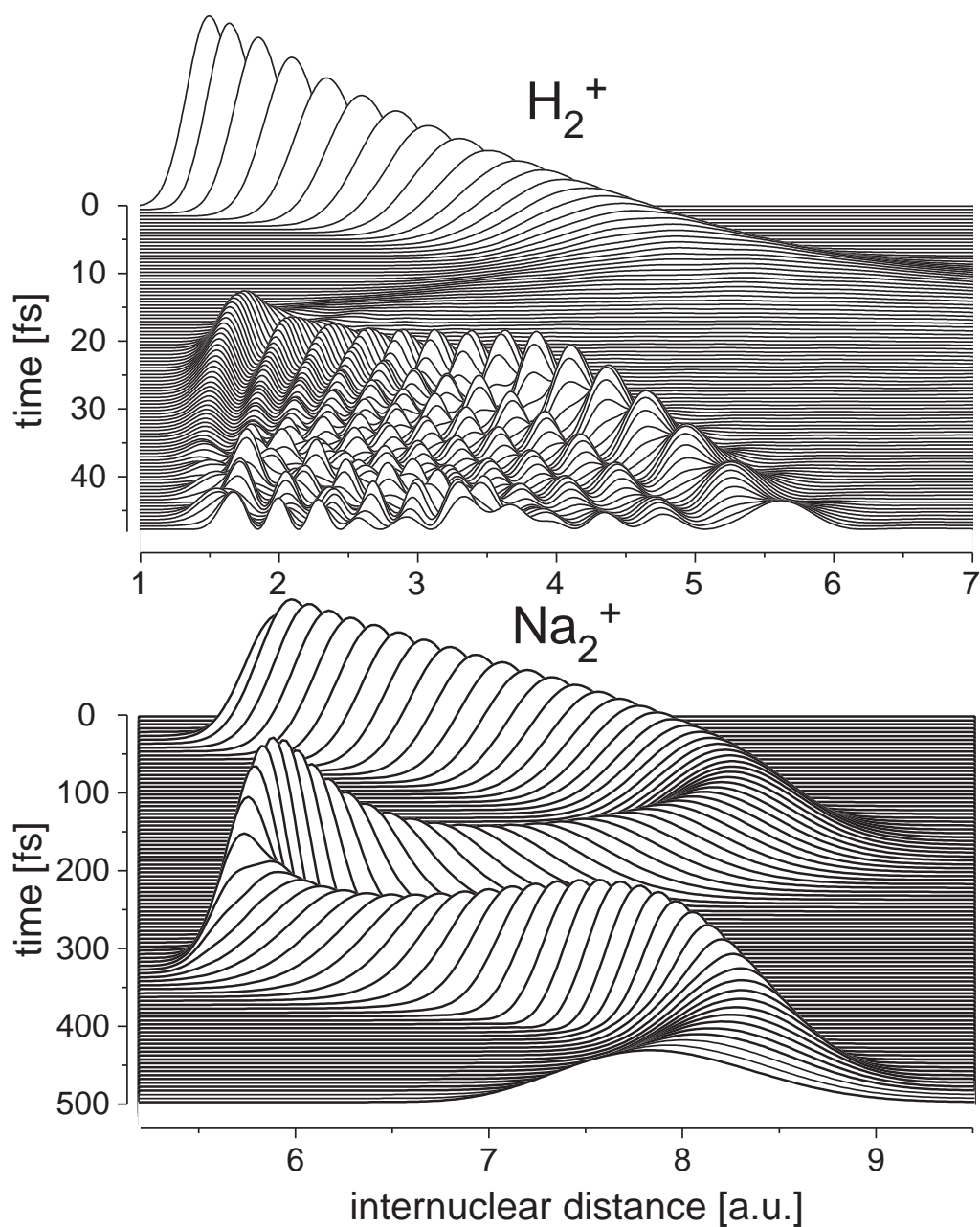


**Figure 3.13:** Vibrational molecular wavepacket evolution in the model  $H_2^+$  (a) after ultrafast ionization of the neutral  $H_2$  molecule with an XUV pulse. Since many vibrational levels are excited close to the dissociation threshold, dephasing occurs on a very short time scale. The wavepacket dynamics in  $Na_2^+$  (b) (Courtesy of M. Erdmann and V. Engel) after ionization with a laser pulse at central wavelength 620 nm is shown below for comparison.

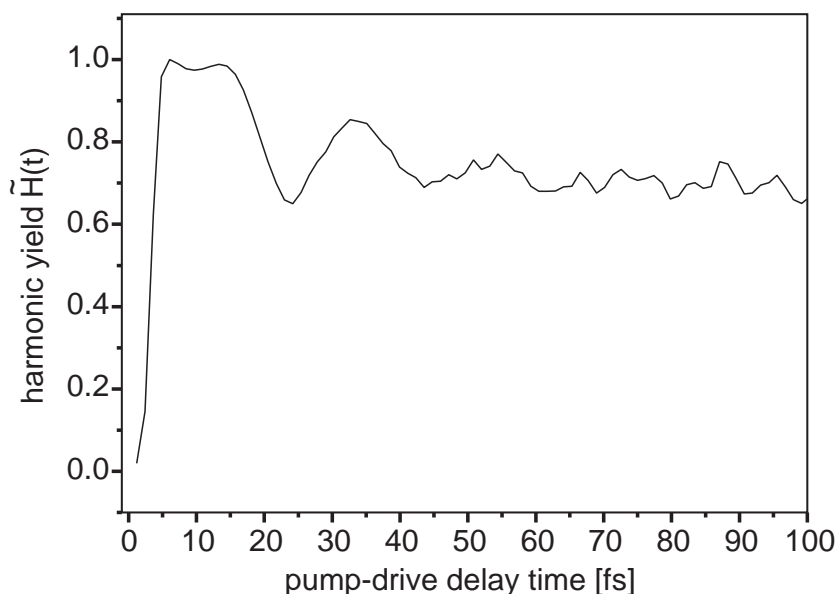


**Figure 3.14:** Integrated harmonic signal (H39-H51) in our model  $\text{H}_2^+$  generated by the second (driver) pulse in a pump-drive scheme. Oscillations are due to molecular vibration (see Fig. 3.13 top graph) after ionization by the first (pump) pulse. A very rapid initial increase of the high-harmonic yield is predicted.

the molecular vibrational wavepacket motion.

### 3.5 Conclusion

By the use of internal degrees of freedom of molecules, the process of high-harmonic generation can be controlled and optimized. Experimental results were presented to prove that molecules are superior to atoms in their efficiency behavior in elliptically polarized driving laser fields [282]. In a model approach, this could be shown to be due to the molecular geometry, providing a larger recombination cross section for the returning electronic wavepacket [283].

Given the results on the design of optimum initial electronic states it is now clear that molecular systems are media which allow more efficient high-harmonic generation than atomic targets [284]. Two promising and new ways to enhance high-harmonic generation were pointed out: First of all, controlling the ground state wave function of the electron to ensure less spreading during continuum propagation and, second, variable choice of the ionization potential to allow perfect matching to the desired soft x-ray frequency range.

Taking all these results into account, it can be stated that using molecules for high-harmonic generation is beneficial to the optimization and control of any of the steps in the three step model, i.e. ionization, propagation and recombination.



---

It should be pointed out that these calculations and experiments were restricted to simplest diatomic molecules. Employing larger scale compounds like organic strings or cyclic-shaped molecules for high-harmonic generation should result in yet higher enhancements after suitable preparation by a controlling laser pulse. Thus, both experimental and theoretical investigations into the direction of molecular high-harmonic generation seem to bear great potential for table-top high-power ultrashort coherent soft-x-ray production.



# Chapter 4

## Condensed Media

The efficiency of the high-harmonic generation in the case of perfect phase matching scales quadratically with the density of the conversion medium. On the other hand, increasing particle density—and thus also electron density—leads to the build-up of a high-density plasma which will eventually absorb any laser radiation. It is crucial to find the limitations for high-harmonic generation when pushing the density of the conversion medium to higher and higher values. Studying the high-harmonic response of water droplets as presented here can be regarded as a pioneering experiment into the direction of high-density high-harmonic generation in condensed media.

Microdroplets turned out to be very efficient media to convert visible laser radiation into the XUV and soft x-ray spectral region [285, 286]. So far, however, they have only been used as sources of incoherent soft-x-ray plasma recombination light being emitted into a solid angle of  $4\pi$ . To collect a large amount of this radiation sophisticated optics have to be employed. A much more desirable light source for many applications would feature a fully coherent directional emission, which is provided by high-order harmonic generation. It is shown here that a strong interdependence of high-harmonic generation and plasma radiation exists. Observations point to the fact that both radiation processes cannot occur simultaneously.

When highly intense laser radiation interacts with a water microdroplet, the spherically curved surface results in a focusing of the light. ‘Hot spots’ are created inside the droplet [287], where high-density plasma is generated. Afterwards, the droplet starts to expand. Within the framework of pump–drive schemes discussed in the Chapter 3, an intense pump pulse can be used to drive the droplet into expansion. This way one can directly assess different density regimes ranging continuously from liquid down to gaseous by employing a second (driver) pulse which generates the high-harmonic radiation. Using this implementation of the pump–drive scheme provides insight up to which densities high-harmonic generation is possible, which is an important issue for efficiency considerations.

Another interesting feature about microdroplets is their breaking up into nanometer-sized fragments upon irradiation by a strong pulse. Such clusters are extensively studied with respect to their unique frequency conversion properties [244, 288, 289]. In some of these studies it has been shown that clusters can be used to reach conversion efficiencies for

incoherent plasma radiation comparable to those obtained in solid state systems. On the other hand, high-harmonic generation in clustered media turned out to occur at smaller intensities, to have a higher photon energy cutoff and to saturate at higher laser intensities as compared to mono-atomic targets.

This chapter is devoted to the presentation of the first experimental results on high-order harmonic generation from water-droplets, with harmonic orders up to the 27th. This is the highest harmonic order ever observed from a water target. So far, harmonic generation from water only up to the seventh order has been reported [290].

The experimental setup is described in Section 4.1. Section 4.2 contains the experiments on laser interaction with water droplets. Both frequency conversion processes of relevance in laser-generated ultrafast x-ray production are discussed: Plasma luminescence and high-harmonic generation, where a transition between these two regimes could be observed.

## 4.1 Experimental Setup

### 4.1.1 Microdroplet-Jet Characterization

The water microdroplets are produced by a glass capillary of 10  $\mu\text{m}$  inner diameter backed with liquid water (see Fig. 4.1). With a controlled fluid pump the pressure can be kept constant in a range of 2 to 5 MPa. The capillary and the fluid pump are commercial products of 'Microjet Components' (Sweden). The capillary is mounted vertically such that the water leaves at the lowermost end. A continuous water jet streams out of the capillary. After a certain propagation distance droplets are formed due to the Rayleigh-Taylor instability. To ensure reproducible droplet sizes, the capillary is equipped with a piezo transducer to modulate the capillary diameter. Applying a high-frequency voltage of 15 V results in a fixed droplet repetition rate. The frequency has to be close to the 'natural' repetition rate given by the Rayleigh-Taylor instability. In the given case, these frequencies are between 0.9 and 1.1 MHz. In Fig. 4.2 photographs of the droplet jet are shown. A microscope objective was used for magnification and a CCD camera for image acquisition. The jet was illuminated by laser pulses incident on a screen placed behind the jet. When the backing pressure is increased, larger droplet diameters are obtained. On the other hand, increasing the piezo-frequency results in smaller droplets.

### 4.1.2 Vacuum and Detection Apparatus

For the XUV emission experiments, the capillary is mounted inside a vacuum chamber to avoid reabsorption of the generated radiation by air or the water vapor. With a 880 l/s turbo pump a background pressure of  $\sim 2 \times 10^{-3}$  mbar was achieved. Differential pumping stages along the way to the spectrometer lowered the pressure further until it reached  $\sim 10^{-5}$  mbar at the spectrometer. At a distance of  $\sim 5$  mm below the exit of the capillary, the laser beam interacts with the droplet jet (see Fig. 4.1). Further down, after  $\sim 40$  mm,

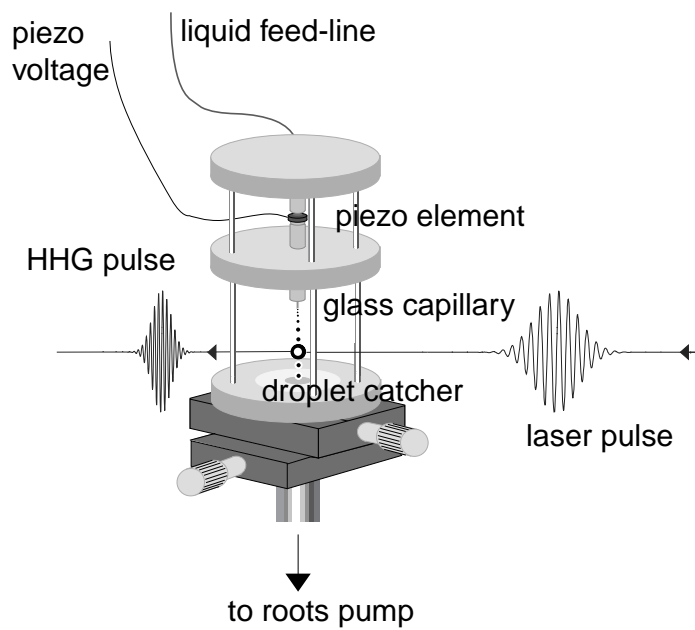


**Figure 4.1:** Schematic setup for the experiments on high-harmonic generation in water microdroplets. The glass capillary is mounted inside a vacuum chamber. The water-droplet jet is directed vertically downwards. A piezo element can be used to control the droplet repetition rate. Droplets not used in the experiment are removed by direct pumping with a roots pump. Laser pulses interact with the water droplet jet  $\sim 5$  mm below the capillary exit to induce plasma luminescence or high-harmonic generation.

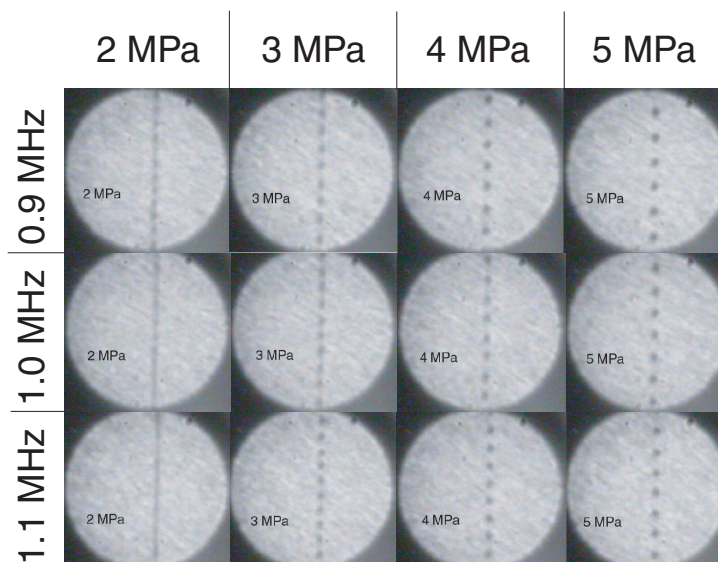


**Figure 4.2:** Droplet size characterization. Increasing the backing pressure results in larger droplets. An increase of the piezo AC frequency decreases the droplet diameter.

the jet enters through a small diameter aperture (0.5 mm) into a separate “catcher” compartment, which is kept evacuated directly by a roots pump. In order not to damage the pumps, a liquid-nitrogen cooled cold trap is installed between the chamber and the pump. As liquid water at room temperature brought into vacuum tends to freeze and grow stalagmites where it hits an obstacle, it is important to keep the catcher at an elevated temperature of about 350 K. If the temperature is too low, ice stalagmites will grow all the way up to the exit of the capillary, preventing stable operation of the jet. For more details on the droplet source see also [291].

The laser source for this experiment was the regeneratively amplified Ti:sapphire system described in Section 1.1.1. Focusing with a 20 cm focal length lens provides laser intensities on the order of  $5 \times 10^{14}$  W/cm<sup>2</sup>.

The emitted XUV radiation was detected with different monochromators for two different photon energy ranges. The low energy radiation is characterized by a home-built Seya-Namioka monochromator (MC1) with a spherical concave grating. The full scanning range provides access to harmonic orders three (H3) to nineteen (H19). A scintillator (Na-salicylate) behind the exit slit converts the XUV radiation into the visible. A photomultiplier is then used to acquire the spectrum as the grating rotates. The signal is DC-converted by a boxcar-averager which is read by a computer. The other monochromator (MC2) consists of a toroidal concave grating illuminated under grazing incidence. The accessible photon energy range extends from  $\sim 20$  eV (H13) to around 80 eV corresponding to H51. The spectrum is acquired with a back-side illuminated thinned x-ray CCD camera (‘Roper Scientific’). Using plasma emission lines, it was possible to estimate the resolution of the spectrometer to be better than 0.3 nm in a wavelength range of 17 to 25 nm. Fig. 4.1 displays a schematic view of the droplet system. The system is aligned in such a way that the laser beam propagates directly into the spectrometer. For detecting harmonic orders greater than H17, we inserted two aluminum filters (thicknesses 0.3 and 0.8  $\mu\text{m}$ ) in order to block the fundamental light (Fig. 4.3).

## 4.2 Frequency Conversion in Water Microdroplets

For the experiments, the droplet-generating system was operated at a backing pressure of 5 MPa. The piezo driver was not used, i.e. the jet was operated in the free-running Rayleigh-Taylor instability regime. Under this conditions water droplets with diameters of about 20  $\mu\text{m}$  were produced.

### 4.2.1 Laser-induced Plasma Radiation

The first results concentrate on the plasma that is created when a single intense laser pulse interacts with the water droplets. Fig. 4.4 is a photographic picture of a water droplet illuminated by different laser intensities. For the intermediate (center picture) and high intensities (lower picture) a BG40 filter was used to suppress the fundamental laser light. For very low intensity, only the unperturbed spherical droplet is visible, while at increasingly higher intensities we observe bright light from the front face (towards the

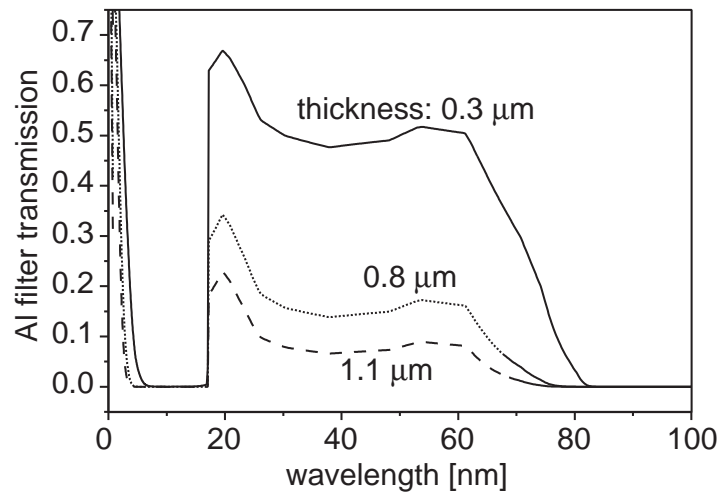


**Figure 4.3:** Transmission characteristics of the aluminum filters used to block the fundamental and lower order harmonics in order to prevent noise due to stray light in the soft x-ray spectrometer. Radiation in the wavelength range from 17 nm (Al L edge) to 70 nm is transmitted. The transmission is shown for different filter thicknesses that have been used in the experiments.

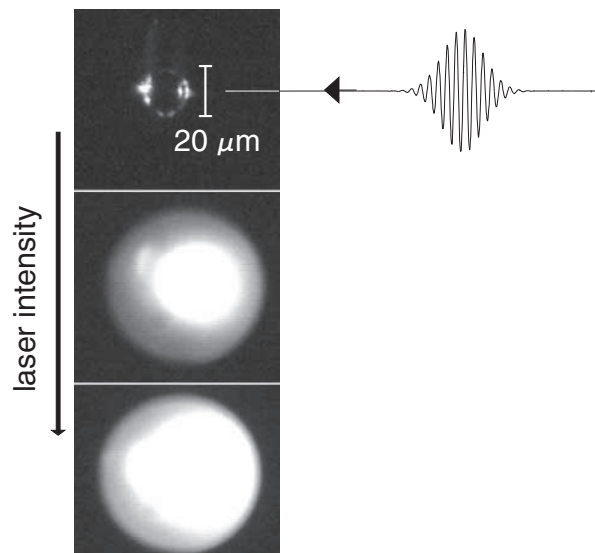


**Figure 4.4:** Photographic images of water droplets for irradiation with different laser intensities. Laser pulses arrive from the right hand side as indicated. Intensity increases from top to bottom. The top picture shows the unperturbed droplet. The center and bottom picture were taken through a BG40 filter to remove contributions of the fundamental laser radiation. An increasing amount of light is emitted from the laser input side of the droplet.

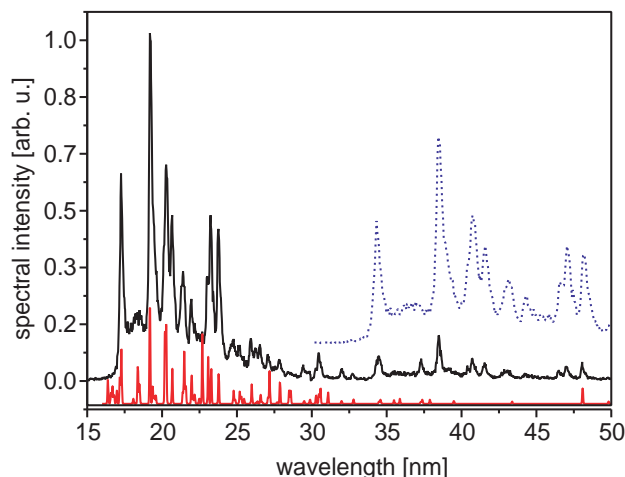


**Figure 4.5:** Typical plasma emission spectrum observed in our experiments for short pump-drive pulse delays. Literature values for emission lines of highly ionized oxygen ( $O^{4+}$ ,  $O^{5+}$ ) are plotted underneath. The cutoff for frequencies below 17 nm is due to the absorption edge of the aluminum filter. Signal at longer wavelengths is partly caused by the second diffraction order of the spectrometer grating. For better visibility, the detected first order signal has been manually converted to second order (dotted line).

laser) of the droplet. Two possible explanations for this finding are: (1) Optical breakdown and plasma mirroring of the fundamental laser radiation close to the front face of the droplet or (2) plasma emission [292] from a backward directed emission plume of the droplet similar to the one reported in [293].

Fig. 4.5 shows a measured soft x-ray spectrum for the case of a single laser pulse interacting with the microdroplets. Employing the spectrometer MC2, strong plasma recombination light emitted from the droplets can be detected. Comparison with literature values [294, 295] shows that the lines can be attributed to highly ionized oxygen (up to  $O^{5+}$ ). The spectrum can only be observed for wavelengths longer than 17 nm, which is the L edge of Al. In solid media, this plasma luminescence can generate very high photon energies up to the hard x-ray region [296].

No high-harmonic emission for orders H17 and higher could be observed using a single laser pulse. Switching to spectrometer MC1 without Al filters third harmonic emission can faintly be observed. Single photon events of the fifth harmonic were recorded on the photomultiplier about each 5000 laser shots. No harmonic signal for higher orders is detected.

#### 4.2.2 High-Harmonic Radiation

In a first approach, the Pockels cell of the regenerative amplifier was set to release two pulses spaced by the round-trip time of the laser cavity, which is 10 ns. The material dispersion corresponding to an additional round-trip of the second pulse results in an increase of its pulse duration to  $\sim 300$  fs and a frequency upchirp. The spectral emission recorded



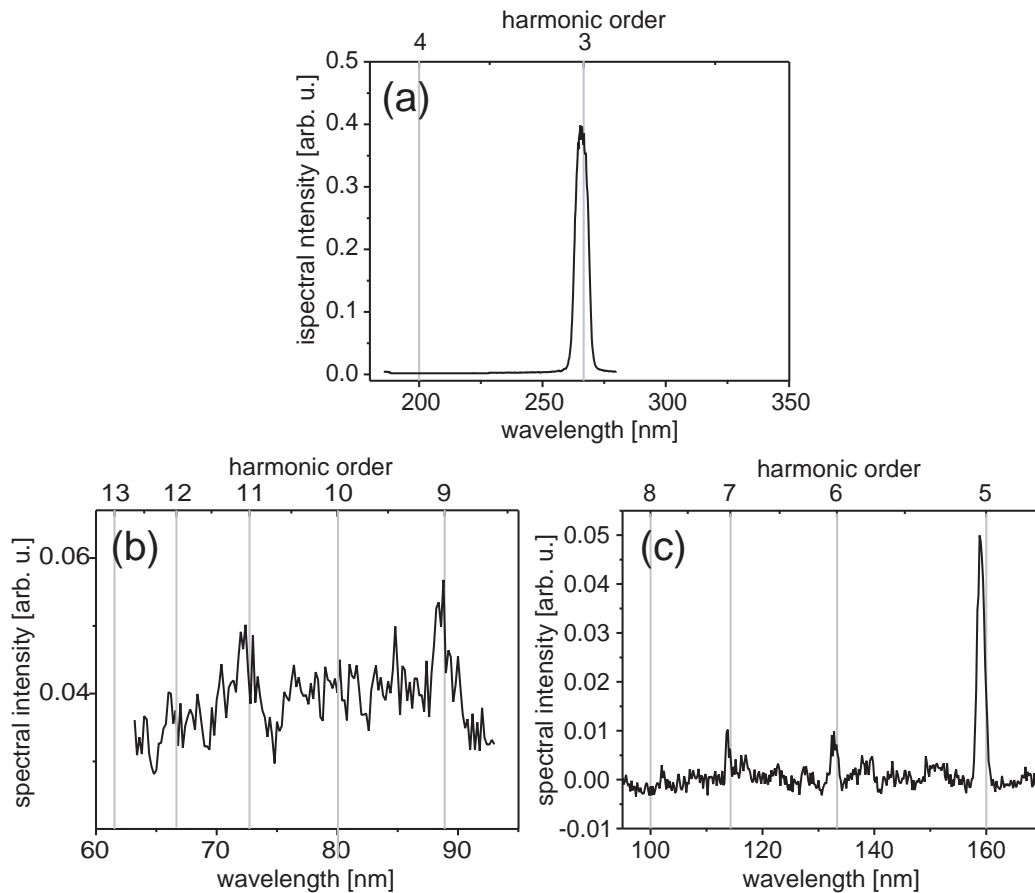


**Figure 4.6:** Lower-order harmonic emission spectra detected for droplets interacting with a double pulse (see text). Harmonics from order H3 (a) via H5 and H7 (b) up to H9 and H11 (c) can be detected with decreasing emission strengths. The signal close to the sixth harmonic can be attributed to a strong plasma line.

from the interaction of laser light with the droplets changes dramatically when the laser pulse energy is distributed between these two pulses. By switching from single pulse to this double pulse operation mode a large increase (by about three orders of magnitude) in harmonic generation efficiency could be observed for the third and the fifth harmonic. Harmonic emission spectra for lower orders (H3-H11) acquired using MC1 are shown in Fig. 4.6.

In order to obtain a deeper insight into the droplet dynamics, a delay stage was set up in order to control the time delay between pump and driver pulse. For these pump-drive experiments, a noncollinear excitation geometry is employed. The pump laser pulse does not enter the spectrometer directly, while the driver one does. XUV emission characteristics from the water droplets change qualitatively at a certain delay time ( $\sim 650$  ps), which is shown in Fig. 4.7. At early times, only plasma emission can be observed (in second diffraction order) while at later times high-harmonic generation is present almost

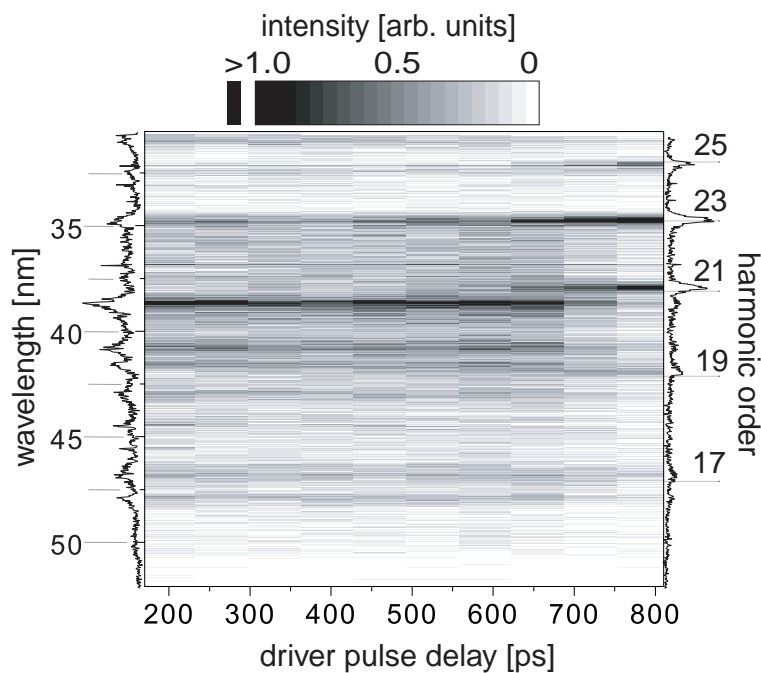


**Figure 4.7:** Transient XUV-emission spectrum acquired in the pump-drive experiment. A transition occurs at  $\sim 650$  ps from a regime where only plasma luminescence is detected (in second diffraction order) into a different one with high-harmonic generation being the dominant contribution to the spectrum.

exclusively. At a time delay of  $\sim 650$  ps, a rapid transition occurs leading to inhibition of plasma emission and promotion of high-harmonic generation.

The highest harmonic orders from water observed to date are shown in Fig. 4.8. They were recorded for a time delay of  $\sim 1$  ns with MC2 using the Al filters mentioned above. Applying the driving pulse intensities of  $\sim 2 \times 10^{14} \text{ W/cm}^2$  in the cut-off law Eq. 2.10 yields a harmonic cutoff frequency ( $I_p(\text{H}_2\text{O})=12.6$  eV) around the 33rd harmonic. This can be regarded to be in accordance with the experimental position of the cutoff ( $\sim 27$ th harmonic), in particular since the laser intensity corresponds to the value obtained when focusing into vacuum. In the actual experiment, however, defocusing of the incoming laser occurs due to plasma build-up.

### 4.2.3 Plasma–Harmonic Transition

The transition behavior observed in the pump–drive experiment can be explained as follows: I) The first pulse ionizes the water molecules creating a hot and dense plasma with nearly solid state density. Dense plasmas are well known as efficient emitters of line radiation. If the delay between the two pulses is small both pulses contribute evenly to the heating of the plasma. II) The hot and dense plasma starts to expand immediately. The second pulse interacts with a less dense plasma resulting in a reduced conversion efficiency. Similar behavior has also been observed using Ar and Kr microdroplets. McNaught *et al.* [286] have measured a decay time of the plasma emission of a few hun-

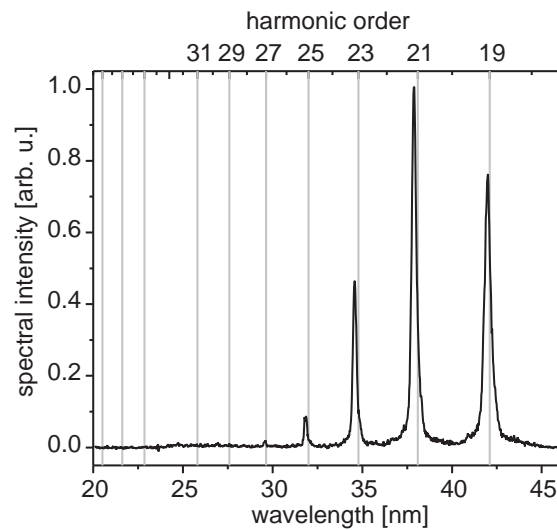


**Figure 4.8:** Highest harmonics ever observed from water microdroplets in the cutoff region of the spectrum acquired at a time delay of  $\sim 1$  ns.

dreds of ps, which is in agreement with our observations. III) After 600 ps the estimated molecular density results in an average distance between atoms that is greater than the classically calculated excursion length of the electron during high-harmonic generation. This gives the electrons the chance to return to their parent ion without colliding with other molecules which would impair the generation of spatially and temporally coherent high-harmonic radiation. Besides the single particle response propagation effects play a major role in high-harmonic generation. Therefore a significant spatial and temporal distortion by the existing and newly generated plasma has to be considered. After  $\sim 1$  ns the plasma generated by the combined action of the two pulses is subcritical. This explains why the increase in high-harmonic signal at a particular time delay coincides with the decline of plasma line emission, since effective plasma heating by the second pulse rules out its undisturbed propagation through the medium. Additionally, as long as the electron density is too high, phase-matching between the high-harmonic radiation and the fundamental is not possible over significant length scales. The explanation is summarized in Fig. 4.9.

### 4.3 Conclusion

The observation of high-harmonic radiation up to the 27th order in water microdroplets is reported for the first time [297]. This can be achieved only for slightly expanded droplets, whereas it is absent for laser interaction with unperturbed droplet targets. In the latter case, only plasma luminescence from highly charged states of oxygen (up to  $O^{5+}$ ) can be observed. These highly ionized oxygen ions have been reported in earlier studies on the explosion of water clusters in intense light fields [298].

Depending on the delay of the driver pulse (generating harmonics) with respect to a pump

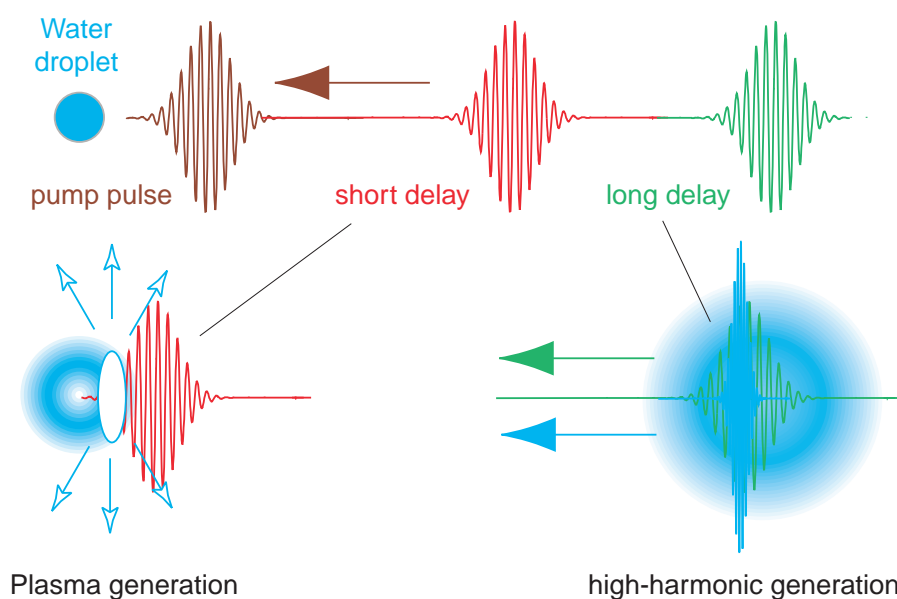


**Figure 4.9:** Frequency conversion processes in microdroplets depend on the delay between the pump and the driver pulse. The pump pulse creates a confined plasma region inside the droplet, which expands and leads to explosive fragmentation of the droplet. For small pump-drive delay times, the driver pulse thus interacts with a high-density clustered gas, which leads to effective absorption of the laser pulse since the plasma can become critically dense (plasma frequency equals laser frequency). All energy of the pulse is thus fed into the plasma, leading to effective plasma luminescence. At later times in contrast, the droplet has expanded to a larger size, the density is thus decreased and the critical plasma density cannot be reached. The laser pulse can thus propagate through the droplet, generating high harmonics along the complete interaction length.

pulse (expanding the droplet) a sharp transition can be observed from a regime (for short time delays) where only plasma recombination light is emitted into another region (at longer time delays) where high-harmonic generation takes place with negligible contribution of plasma emission.

Using the pump–drive setup it is possible to study high-harmonic generation in media of particle densities spanning the entire range from liquid state down to gaseous density. In order to push the conversion efficiency to the maximum, we must acquire knowledge about which are the maximum tolerable particle densities. On the other hand, once limitations to maximum density are encountered, the presented experimental environment will serve as a versatile tool and testbed in finding ways to overcome these problems. These studies will be the subject of future work.

This work is carried out in an effort to spur further research on the subject of high-harmonic generation in extended and condensed-matter systems i.e. other than monoatomic (rare gas) ones which are the ones currently routinely used. The latter can be regarded as very well understood and almost optimally exploited. On the other hand, large improvements in coherent soft x-ray generation efficiency are to be expected by switching to molecular [281] or even more complex media.

## Part III

# Control of Harmonics by Laser-Pulse Shaping

High-order harmonic generation, as the name implies, is a high-order nonlinear optical process. This generally means that it depends on the electric field  $E(t)$  of the laser in a highly nontrivial and complex fashion. In Section 2 we discussed the atomic dipole phase as being dependent on the intensity of the laser. However, this is not the only way the pulse shape enters the process. A plasma is generated by the action of the laser pulse, leading to sudden changes in the refractive index of the medium. Therefore, any modification of the shape of the laser pulse will naturally result in a different plasma build-up. Therefore, not only the single atom response but also propagation effects like phase matching depend on the laser pulse shape.

The first demonstration of control of high-harmonic generation by applying shaped laser pulses has been published in 2000 by Bartels *et al.* [299]. They were able to observe a significant increase of the conversion efficiency in high-harmonic generation when a tailored laser pulse was used. The best laser pulse shape was not known beforehand but had to be found experimentally. To that end, a computer algorithm had been implemented that used the high-harmonic yield as a feedback from the experiment in order to iteratively improve the shape of the driving laser pulse to most efficiently generate high harmonics. These so-called closed loop algorithms—the most widely used are genetic algorithms and evolutionary strategies—have been proposed in 1992 by Judson and Rabitz [300] as a solution to a general problem in quantum control: How can we experimentally produce the laser fields that direct a quantum system from its initial state  $|\Psi_0\rangle$  into its desired target state  $|\Psi_t\rangle$ . After its first experimental implementations [301, 302] the idea of closed-loop control rapidly spread in the field of quantum control where the first application to high-harmonic generation has been the above mentioned work.

In later studies, a theory was worked out which was able to describe some of the experimental results on controlled high-harmonic generation [123]. Any effect observed in the experiment had been attributed only to the response of the single atom, neglecting any propagation effects. The interference of different electron trajectories was found as a reason for the controllability of the process. The atomic dipole phase associated with each electronic trajectory is directly coupled to the time-dependent electric field, which explains the observed enhancement if all electronic quantum paths are made to interfere constructively. However, the theory is not able to account for the very high contrast ratio observed in the experiment. It was always argued that harmonic generation is governed not only by the single-atom response. The collective response of all emitters in the interaction region should also be considered.

Very recently (2004) Reitze *et al.* [218] presented new results on controlling high-harmonic generation with shaped laser pulses. They concentrated on the spectral position of the comb of harmonic lines in the plateau region. It was possible to shift the center wavelength of a given harmonic in a certain range. Again, a genetic algorithm was used to find the optimal laser pulse shape for a given target wavelength. An analysis of the experimental results was also performed. The simulation in this case agreed with the experiment only if propagation effects were included.

This part of the work provides additional information about the nature of harmonic control by comparing the control of high-harmonic generation in two different generation geometries: the jet and the hollow fiber. In addition, a variety of the control objectives studied and achieved here differ significantly from earlier results in a most interesting way. All of the above mentioned earlier works focused only on particular simple characteristics of the high-harmonic generation process. The basic questions asked were about enhancement, spectral line width and center wavelength. The very crucial question was never raised: Is it possible to control the *qualitative overall shape* of the high-harmonic spectral response? Can we produce any coherent soft x-ray spectral distribution? A completely new field of research could emerge from a positive answer to those questions [303]. The field of quantum control was pushed forward in experiment by the application of femtosecond pulse shaping techniques. By the use of the latter, experimentalists were able to manipulate molecular or in general vibrational dynamics, which occurs on a time scale of several femtoseconds. The pulse shaping technique is based on the manipulation of the laser pulse spectrum. If we are able to do the same to a multi-eV broadband coherent soft x-ray spectrum produced in high-harmonic generation, the emerging attosecond-duration pulses are also temporally modified. It will be shown in this part, that we are indeed able to control the spectral properties of the harmonic spectra in this qualitative sense relevant for future experiments on quantum control of electron dynamics in the attosecond soft x-ray regime.

## Chapter 5

# Coherent Soft X-Ray Spectral Shaping

Recent advances in femtosecond-laser technologies not only allow to follow atomic motion in real time but also to control molecular processes with tailored femtosecond-laser pulses. With recent experiments proving the existence of soft x-ray light pulses of durations below a single femtosecond, science is about to enter a new field of ultrafast physics devoted to the direct exploration of electronic motion. Since exploration and observation of processes in turn are accompanied with the desire and ability to control them, the search for ways to manipulate the properties of these soft x-ray pulses is about to begin.

Femtosecond-laser pulse shaping plays an important role in the field of coherent control of molecular dynamics. Likewise one can expect soft x-ray pulse shaping to be a very efficient tool in our efforts towards the control of electronic motion. However, a direct transfer of pulse shaping techniques developed in the optical wavelength range to the soft x-ray regime is not feasible. Existing devices either require spectral dispersion (e.g. liquid-crystal or acousto-optical spatial light modulators, deformable mirrors) or extensive passage through material (acousto-optic programmable dispersive filter ‘Dazzler’ [304]) which precludes their applicability in the soft x-ray spectral range due to small diffraction efficiencies for spectral dispersion and high absorption.

It would clearly be advantageous if one could circumvent the pulse shaping apparatus to act onto the soft x-ray pulse *after* its production. It appears more desirable to directly generate a shaped soft x-ray pulse for instance by shaping the fundamental laser pulse *prior to* the conversion process. In this chapter it will be demonstrated that it is possible to control high-harmonic generation in a very general sense by shaping the ultrashort driving laser pulse. The presented results demonstrate control of the overall shape of the high-harmonic soft x-ray spectrum, beyond enhancement of the total harmonic yield which has been the goal of earlier studies. It is possible to selectively generate certain extended parts of the high-harmonic spectra while keeping the remaining part at low intensity. Single harmonics at different wavelengths can be selectively generated with high contrast ratio. It is also feasible to suppress single harmonic orders while neighboring ones are generated. Due to the temporally coherent nature of the soft x-ray light produced in high-harmonic generation, spectral shaping and engineering on the other hand means the ability to shape the emerging trains of attosecond pulses, as will be shown below. These results thus suggest an open road towards coherent control in the soft x-ray spectral range.

This chapter is structured as follows: Section 5.1 gives a brief introduction into the field of quantum control, lining out the most important ideas and developments. The closed-loop concept is introduced. A description of evolutionary algorithms, in particular the one used for the experiment, is given. The same section also summarizes past achievements regarding control of high-harmonic generation. The experimental setup is then described in Section 5.2 and a test of the closed-loop approach is carried out by maximizing the amount of second-harmonic light created in a nonlinear crystal. Afterwards, Section 5.3 and Section 5.4 present and compare the results obtained for adaptive control of high-harmonic generation in the gas jet and waveguide geometry, respectively.

## 5.1 Quantum Control

The idea of controlling quantum systems with laser light has been fascinating the scientific community ever since the invention of the laser. Laser light is a unique source of powerful and coherent electromagnetic radiation. Coherence in the physical context generally means that waves—for example the electromagnetic waves that constitute light—have a fixed phase relation. A fixed phase relation at different times is called temporal coherence whereas a fixed relative phase in space is called spatial coherence. Lasers are temporally and spatially coherent, making them a perfect instrument in optics.

Coherence plays an important role in the dynamics of quantum systems. The evolution of quantum mechanical systems is described by a wavefunction, which is the solution to the time-dependent Schrödinger equation. As in the case of the laser and electromagnetic waves, these “quantum waves” can also be characterized in terms of their coherence properties. Different quantum states in an ensemble of equal quantum systems evolving together in time can be in a given fixed phase relation with each other, which defines a coherent superposition of quantum states.

Electromagnetic waves—light—are used to excite quantum systems, transferring electronic, vibrational and rotational population between different states. If the photon energy of the light matches the energy difference between two quantum states, these states become coupled through the interaction with the laser. In this interaction of light with matter, the coherence properties of the light source are directly transferred to the quantum system. It is therefore obvious that the laser is the ideal light source to create coherent states in quantum mechanics. Furthermore, due to the spatial coherence properties of the laser, the emitted light can be focused to very high intensities. This enables us to defy one counteracting mechanism: Spontaneous decay, which is a statistical process and therefore destroys existing coherence.

The following is a brief outline of the history, fundamental principles and achievements in the field of quantum control. Comprehensive reviews are available in the literature [305–310].

Early experiments on the control of quantum systems with coherent light focused on the selective cleavage of chemical bonds in molecules. Single frequency laser light tuned into resonance with the vibrational frequency of the selected bond was expected to excite the bound atoms into high-vibrational states, eventually leading to fragmentation [311–315].



These experiments turned out to be little efficient, since it was basically always not the selected bond but the weakest one that broke. This experimental evidence led to the discovery of the mechanism of intramolecular vibrational redistribution (IVR) [316–320]. In brief, upon vibrational excitation of a particular molecular bond, the vibrational energy is quickly redistributed over the whole molecule. The molecule is therefore only heated by the interaction with the laser light. This phenomenon can be illustrated in a classical picture of coupled oscillators. If one of the oscillators is excited at its resonance frequency the whole system of oscillators will start to dissipate the excitation energy and start to move. The time scale of this dynamical rearrangement in molecules in the gas-phase is on the order of tens of picoseconds. It is generally decreasing with an increase in the number of degrees of freedom of the molecular system, making this approach of bond selective photofragmentation not practicable. The laser light in this case only represents an expensive oven. For that reason, different ideas had to be worked out to control quantum dynamics with laser light.

Different general methods to exert control over quantum systems will now be addressed in the following section. Afterwards, the experimental method of quantum control employed in the experiments of this work will be explained in more detail, which is called closed-loop learning control. This technique can be reduced to a global optimum seeking problem in a high-dimensional search space, for which the practical solution is the application of evolutionary algorithms, which will be described in the final section.

### 5.1.1 Control Methods

As the application of single-frequency cw laser fields turned out to be ineffective, the natural consideration was to use multi-frequency light fields in a second approach to obtain control over quantum systems. In the mid-1980s, three theories were developed that allow for the controlled transfer of quantum mechanical population by coherent light fields, opening up the field of coherent control.

One idea was developed by Brumer and Shapiro [321, 322]. Two different phase-locked frequencies of light couple the same electronic transition if for example one is the resonant frequency whereas the other is an odd integer fraction of the resonance (multiphoton-transition). Depending on the relative phase between these frequencies, population transferred from the lower to the upper final state by each of the light fields can interfere either constructively or destructively in the final state, enabling us to control the population transfer by tuning the relative phase.

A second idea was reported by Tannor, Kosloff and Rice [323, 324], which was formulated in the time domain. In a molecular system, a molecular wavepacket can be created on an excited state by the interaction of a ground state molecule with an ultrashort laser pulse. This wavepacket will start to propagate on the excited potential energy curve or surface. A second ultrashort laser pulse can then be applied to the system at a particular time at which the wavepacket passes the Franck-Condon window to the desired target state. The “control knob” in this case is the temporal delay between the two pulses, as it was the phase difference in the Brumer-Shapiro scheme discussed before. As we know from Section 1.1, time and frequency are dual quantities, which are connected by the Fourier

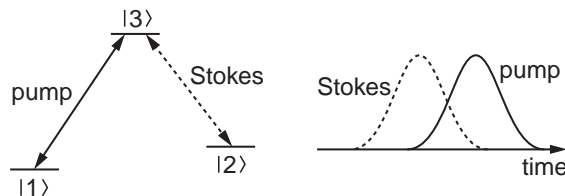


**Figure 5.1:** The technique of stimulated raman adiabatic passage (STIRAP). In a  $\Lambda$ -type level system, population can be completely transferred from state  $|\Psi_1\rangle$  to  $|\Psi_2\rangle$  by two laser pulses called pump and Stokes pulse. The pump pulse couples  $|\Psi_1\rangle$  with  $|\Psi_3\rangle$ , whereas the Stokes pulse couples  $|\Psi_2\rangle$  with  $|\Psi_3\rangle$ . In order to completely transfer the population, these pulses have to be applied in a counter-intuitive way, where the Stokes pulse is sent first, followed by the pump pulse.

transformation. It was mentioned in Section 1.1.2 that a temporal delay corresponds to the slope of a linear spectral phase. In other words both schemes presented—although they might be easier understood in different domains—are physically identical [325].

A third way of quantum control entangles the temporal and spectral aspect of the control fields. If we consider a so called  $\Lambda$ -type level system as shown in Fig. 5.1 (its name is derived from the electronic transitions that are possible resembling the greek letter  $\Lambda$ ) two laser pulses can be applied to transfer population completely from the lowest state  $|\Psi_1\rangle$  to the second lowest  $|\Psi_2\rangle$ , without populating the intermediate high lying excited state  $|\Psi_3\rangle$  at any time. The two fields coupling  $|\Psi_1\rangle$  with  $|\Psi_3\rangle$  and  $|\Psi_2\rangle$  with  $|\Psi_3\rangle$  are called the pump and the Stokes pulse, respectively. Most interestingly, the two pulses have to be switched on and off in a counter-intuitive way [326–328]: To completely transfer population from  $|\Psi_1\rangle$  to  $|\Psi_2\rangle$ , first of all the Stokes pulse has to be sent—coupling  $|\Psi_2\rangle$  with  $|\Psi_3\rangle$ —followed by the pump pulse coupling  $|\Psi_1\rangle$  with  $|\Psi_3\rangle$ . This technique is called stimulated Raman adiabatic passage (STIRAP).

It is always a single parameter in any of these three schemes which is varied in order to exert control on the system. It is either a phase between two lasers of different frequencies, a time delay of two pulses, frequency or intensity. Another experimental approach is the variation of the chirp of the controlling laser pulse [23–28].

The idea to use arbitrarily shaped laser fields in the time or frequency domain—defined by many parameters  $E(t)$  or  $\tilde{E}(\omega)$ —came up together with the just presented methods of single parameter control. As a first approach, a variational concept was used to find optimal theoretical laser pulse shapes [323]. Shortly afterwards, a more general approach was developed [329–331], where the optimal control fields could be calculated by an iterative algorithm. These works laid the groundwork for the field of optimal control theory (OCT).

### 5.1.2 Closed-Loop Learning Control

While OCT could calculate optimal control fields for a variety of quantum systems, it remained a problem for experimentalists to apply these fields in the laboratory. This

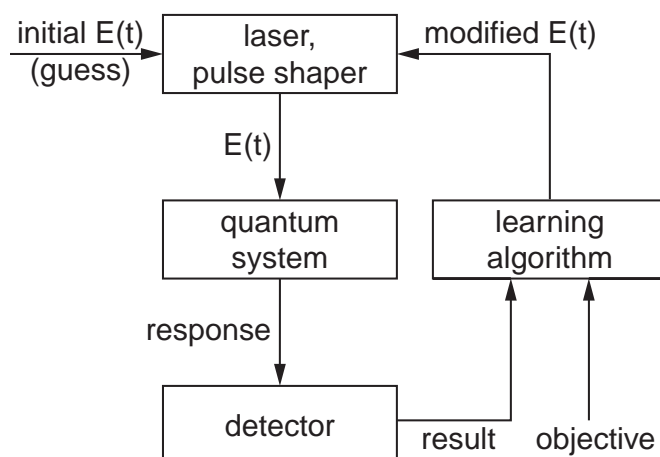


**Figure 5.2:** Illustration of closed-loop quantum control. The experiment is set up such that the learning algorithm on a computer is able to program the laser-pulse shaper and read out the detector to acquire the response of the quantum system to the particular laser pulse shape. It continuously compares the response of the quantum system with a user-defined control objective. The learning algorithm gradually adapts and modifies the laser pulse shape  $E(t)$  such that it creates the measured response in the quantum system that is closest to the objective. Typically a random pulse or a guess from theory is used as the first pulse shape. It is important that the detected result is above the noise level of detection.

can be readily understood for a couple of reasons: In general, OCT has to retreat to *model* Hamiltonians in order to describe quantum systems. Thus it cannot calculate exact control fields that account for any dynamical property of the real-world system. A second reason is the experimental problem to precisely produce an arbitrary predefined control field in the interaction region. In particular, experimental fluctuations due to instability of the laser source can never be ruled out completely.

This problem of finding the optimal control field directly in the experiment was solved by the famous idea of Judson and Rabitz of how to “Teach[ing] lasers to control molecules” [300]. Their idea is very simple. Different pulse shapes are experimentally applied to a quantum system under study and the achievement of control is derived from the measurement of an observable quantity. A search algorithm can now be used to optimize the experimental parameters defining the pulse shape (settings of the pulse shaper) where always the best performing laser pulses are stored and iteratively improved by variation of parameters (see Fig. 5.2). For example, the control goal could be the maximization of population transfer to an excited state. Fluorescence of this state would thus be an experimental observable to judge the “performance” of a certain laser pulse shape in exerting control. Throughout the course of the iterative search procedure—which can be carried out on a computer that is connected to the pulse shaper and the fluorescence detector—the fluorescence signal will continuously improve since better and better laser pulse shapes are found. As can be seen in Fig. 5.2, the working principle of the control experiment is reminiscent of a “closed loop”: The computer sets a laser pulse shape which is applied in the experiment and the control result is fed back into the computer. The terms ‘closed-

loop control' or 'feedback control' are therefore often associated with these experiments. As the computer iteratively "learns" the optimal pulse shape by adaptation to the user-defined control goal, the terms 'learning control', 'adaptive control' and 'optimal control' are also used in practice.

It should be noted here that also 'open-loop control' has made significant progress, particularly pushed forward by Silberberg and coworkers [42, 332, 333]. In an open-loop experiment, again a multiparameter control field (produced by a pulse shaper) is experimentally applied. By introducing user-defined variations to the control field and monitoring the control goal by measurement we can learn about the control mechanism. Here, the achievement of the control goal is not used as a feedback as in the closed loop approach but as a probe to evaluate our understanding of the process.

Many applications of these control techniques were reported in recent years, mainly for the closed-loop approach. The first demonstrations of experimental control of photochemistry by laser light were reported by Bardeen *et al.* [301] and Assion *et al.* [302]. The control goals achieved were the optimization of the excited state population of a dye in solution and the control of photodissociation, respectively.

After these first demonstrations of feasibility, a variety of further applications was reported. In closed-loop quantum control experiments it was now possible to realize the old dream of selective bond cleavage in molecules [334, 335] by optimally shaped femtosecond laser pulses. Control in atomic systems focused on the generation of arbitrary Rydberg wave packets [336] and optimizing two photon transitions in atoms [337].

Selective population control is also achievable in molecules in solution [338], where it has long been argued that complex solute–solvent interactions would possibly make these systems difficult to control with light. In the solid phase it has been possible to control semiconductor nonlinearities by optimizing differential transmission [339]. The energy flow pathways in a complex biological system, the light-harvesting antenna complex used in photosynthesis, could be controlled by using a closed-loop learning algorithm [340]. These latter experiments proved in particular that complexity of the quantum system does not impair controllability.

Another experiment on control of photofragmentation explicitly focused on the understanding of experimental control laser fields with theoretical *ab initio* calculations [341].

Recently, the technique of polarization shaping of femtosecond laser pulses has been developed and experimentally applied. The first closed-loop optimization experiment with polarization shaped laser pulses made particularly clear that a larger variety of quantum pathways can now be addressed by the use of shaped laser light of arbitrary temporal polarization [43]. A direct comparison to the results of an optimal linearly polarized laser pulse showed a significant difference in the degree of control obtained, which was much higher for the polarization shaped pulse (Appendix A). Polarization shaping has also been used in an open-loop experiment to suppress the non-resonant background in coherent anti-Stokes Raman spectroscopy (CARS) [42].

The control of polariton waves in crystals by using spatio-temporally shaped laser pulses showed that not only the temporal coherence of a system could be manipulated but in addition macroscopic spatial coherence can be induced [46].

Interestingly, the application of closed-loop algorithms not only paved the way to the experimental feasibility of control in quantum systems but also laser engineering benefited from closed loop techniques. By maximizing the amount of second-harmonic light produced in a nonlinear crystal, laser pulses could be compressed down to their bandwidth limit [29,30,40,49,342–345]. The shortest pulse in the visible-to-infrared region of 3.4 fs is actually produced by this method [3]. Not only the compression of laser pulses but also the generation of arbitrary pulse shapes was shown to be possible by the application of a closed-loop algorithm [346].

However, if we consider the results of closed-loop control of quantum systems, it often remains obscure what the mechanism or controlled quantum path really is. Having at hand the optimal laser pulse shape what can we really learn about the system? This is commonly called the problem of inversion [347–350]. Some new ideas were recently published how we could implement different algorithms in the experiment that would not try to improve the achievement of a particular control goal but rather “improve our understanding” of the system Hamiltonian [351,352].

There is a general benefit in closed-loop optimization experiments, even if the control mechanism cannot immediately be identified. Two cases are conceivable: a) the controlled target state (or a variety of controlled target states) can immediately be of use in successive experiments or b) the quality of control opens the way to completely new applications. In the experiments on harmonic generation reported in this work, both of these cases apply as will be shown.

### 5.1.3 History of Control of High-Harmonic Generation

The control of the enhancement and linewidth [299] in high-harmonic generation was accomplished by application of closed-loop pulse shaping control. Recently it was shown, that the spectral position of an extended comb of harmonics could be controlled in a broad range of frequencies [218].

Applying closed-loop optimization in theory helped to identify the role of the intra-atomic dipole phase in the control of the single atom response of high-harmonic generation [123,353]. Constructive and destructive interference of different quantum paths contributing to the production of certain harmonic orders was considered as the explanation to the results on control published in [299,353]. However, there has been ongoing argument about whether the single atom response could be the only origin of control. As will be shown by the results presented in this chapter and as has been observed in [218], the single-atom response alone does not satisfactorily agree with the experimental results.

In another earlier theoretical work [354], different experimental parameters like the intensity of the driving laser pulse, the gas pressure in the interaction region, the interaction length and the position of the focus relative to the gas jet were optimized for various control goals. Optimal sets of experimental parameters were obtained by a closed-loop learning algorithm and also underlined the importance of spatial effects in the control of the process.

Besides the given works using shaped laser pulses or other multi-parameter approaches,

the control of high-harmonic generation has been the subject of a multitude of single-parameter optimization studies in the past. As conversion efficiencies of infrared laser to soft-x-ray light are very low, the most important control target has been the enhancement of total harmonic flux. Besides post-production amplification schemes [355, 356], it was early noticed that laser pulse duration is an important parameter in the optimization of high-harmonic yield [357]. Short pulses are very efficient in the production of the cutoff-harmonics whereas the photon number in the plateau harmonics scales about linearly with the pulse duration.

When high harmonics are produced by the combined action of an intense infrared driver pulse and a VUV pulse it could be shown in theory [255, 358] that the intensity of high-harmonic radiation could be enhanced by several orders of magnitude for certain cases. In both theories, an enhancement of ionization is responsible for the increase in high-harmonic generation efficiency. As has been discussed in Part II, pump–drive schemes can be used to increase the high-harmonic production efficiency by controlling the shape of the electronic wavefunction in the ground state.

All these experiments and theories basically studied the single-particle response and tried to find ways to optimize the *temporal* characteristics of the driving fields. On the other hand, since propagation effects are important in high-harmonic generation, many additional studies focused on the *spatial* optimization of the process.

Counterpropagating light has been considered to control phase-matching for enhanced high-harmonic efficiencies [359]. Only very low intensities of the counterpropagating control field are needed. If truncated Bessel beams—produced by the output of hollow fibers—are employed in the generation process the brightness of the produced radiation could be optimized [142]. Careful selection of the length of the conversion medium has been shown to lead to the highest conversion efficiencies in argon gas observed to date (up to  $3 \times 10^{-5}$  for the 23rd harmonic) [240].

Besides enhancement of the total soft x-ray photon flux, some single-parameter control approaches focused on the harmonic linewidth [128, 360] and tunability [129, 360] of the high harmonic peaks. It could be shown that very narrow harmonic lines can be produced by controlling the chirp of the fundamental pulses. This is because the intrinsic harmonic chirp produced by the intensity-dependent atomic dipole phase (see Section 2.1.4) can be compensated by the chirp of the laser pulse. In [360], a spectrally narrow, long laser pulse has been employed to generate high-harmonic lines of very high spectral purity. Tuning of the harmonic frequencies can be done either by changing the center wavelength of the driving laser pulse [360] or again by varying its chirp [129].

Any of the given studies of control of high-harmonic generation only focused on specific scalar spectral properties such as enhancement, harmonic linewidth or tunability. None of the approaches so far has ever been asking the question whether it were possible to control the overall spectral shape of the coherent soft x-ray spectra. With the results presented at the end of this chapter, the positive answer to this question enables us to transfer the concepts of adaptive control and pulse shaping over into the soft x-ray spectral region and to the attosecond time scale.

Since the experiments on the control of high-harmonic generation reported here are of the closed-loop type, it is important to explain the working principle of the global search

algorithm used for the optimization experiment, which is an evolutionary algorithm.

### 5.1.4 Evolutionary Algorithm

In many problems of the mathematical sciences, the same general question appears: How can we find the global maximum of some quantity  $F$ , written as

$$F = f(x_1, \dots, x_n), \quad (5.1)$$

which depends on a total of  $n$  parameters  $x_j$ , along with the set of parameters  $\bar{x}_1, \dots, \bar{x}_n$  that produces the maximum? In general, the  $x_j$  are unbounded continuous parameters, which makes it hard to find the global optimum. In particular, the function  $f(x_1, \dots, x_n)$  often depends on the  $x_j$  in nontrivial ways. In these cases, not even local maxima can be analytically calculated by setting the partial derivatives  $\partial/\partial x_j$  of  $f$  equal to zero. It is then necessary to retreat to numeric, computer-based search algorithms, which often suffer from one problem: to be trapped in a local maximum of the search space. For example, the gradient-walk method will find a way from the starting position in the  $n$ -dimensional space  $(x_{1,0}, \dots, x_{n,0})$  to the maximum which is given by a “continuous up-hill movement” determined by the direction of the gradient vector  $(\partial f/\partial x_1, \dots, \partial f/\partial x_n)$ . This will lead us to the maximum, i.e. the point where the gradient vanishes, and stop at this point which is one local maximum in the search space. The region of the search space that is covered by the search routine is the path connecting the starting point with the point of the local maximum and is thus a one-dimensional space. Since the search space is  $n$ -dimensional, even a repeated application of the gradient walk would still not sample a significant fraction of the whole space.

Evolutionary algorithms [361–363] are particularly well-suited for global maximum search in a very high-dimensional search space. In principle, nature itself invented these algorithms. Any individual creature on earth is characterized by a very large number (which may as well be infinite) of parameters. Part of it is its genetic code and we will restrict our discussion to this for the sake of simplicity. Also disregarding the fact of a varying number of genes characterizing each creature, we just say that each individual is fully characterized by a sequence of  $n$  genes  $(x_1, \dots, x_n)$ . For a specific environment, a creature containing a particular genetic sequence is best adapted, the environment thus serves as the function  $f(x_1, \dots, x_n)$ , giving higher and higher values  $F$  for individual creatures that are increasingly well adapted to the particular environment. Evolution of life on earth is thus a constant optimization procedure in this  $n$ -dimensional search space. Nature found a way to sample this large search space by the application of a few principles, which also constitute the foundations of an evolutionary algorithm.

1. The principle of ‘survival of the fittest’. Different individual creatures have to compete for natural resources and are thus adapted differently well to the environment. The best adapted individuals will typically survive longer than others.
2. Genetic crossover. The currently best adapted individuals will produce more offspring than worse adapted ones. Since both parents could have been well adapted for complementary genetic reasons, their offspring can inherit both of these qualities.

3. Mutation of genes. Since the search space would be limited by the parameters of the initial population, statistical variation of genes allows to reach in principle any point of the  $n$ -dimensional space.

Iterative repetition of these principles leads to optimally adapted individuals in nature. The implementation of these principles in a computer algorithm also increases the value of  $F$  in any kind of optimization problem of the form of Eq. (5.1). After a number of iterations, the algorithm will have converged to some value of  $F$ , which can be considered to be the global maximum of a large subset of the search space. Of course, also in the case of evolutionary algorithms we are never sure whether we found the global maximum of the complete search space.

A similar situation of a tremendously large search space arises in experiments on quantum control with laser fields. In this case, we would like to steer the quantum system from its initial state  $|\Psi(0)\rangle$  into some defined target state  $|\Psi_t\rangle$  by applying a suitably shaped laser pulse with a temporal electric field  $E(t)$ . The population of the target state  $|\langle\Psi_t|\Psi(t)\rangle|^2$  can be regarded as the value  $F$  which we seek to maximize. The evolution of the quantum system is governed by the full Hamiltonian  $\hat{H}(E(t))$ , which depends on the laser field  $E(t)$ :

$$|\Psi(t)\rangle = e^{-\frac{i}{\hbar} \int_0^t \hat{H}(E(t)) dt} |\Psi(0)\rangle, \quad (5.2)$$

Even if the Hamiltonian is known,  $F$  typically depends on the electric field in a highly nontrivial way. Optimal control theory is devoted to calculate the optimal control fields (maximizing the population of  $|\Psi_t\rangle$ ) for given known Hamiltonians. In the experiment, we often deal with quantum systems that are rather complex and exact representations of the Hamiltonian are not available. High-harmonic generation adds the additional problem of the propagation effects in the medium, which would require us to solve the Hamiltonian of the single gas particle and the wave equation Eq. (1.56) in a self-consistent way, which exceeds current capabilities. But even if a solution could be found, we would need to experimentally generate the electric field which exactly reproduces the calculated one, which can be difficult to do because of limitations of the laser system.

In practice, we therefore map the control experiment on an optimization problem of the form given above in Eq. (5.1). Our laser pulse can approximately be described by  $(E(t_1), \dots, E(t_n))$ , the electric field at  $n$  specific times which are chosen close enough to ensure good sampling. Alternatively we can describe it by the electric field versus frequency  $(\tilde{E}(\omega_1), \dots, \tilde{E}(\omega_n))$ , which is usually the favorable representation since it is directly accessible for pulse shaping in the experiment (see Section 1.1.4). On the other hand, we can measure the population of the final state giving us access to the function  $F$ . For example, for the spectral optimization of high-harmonic generation, we are interested in the high-frequency spectral electromagnetic response of the system, in other words, the high-harmonic soft x-ray spectrum. This can simply be measured with a spectrometer. Now we are again left with the problem of how to scan a large search space for optimal solutions for the  $\tilde{E}(\omega_j)$  that produce a high value of  $F$ . The deformable-mirror pulse shaper employed in the experiments described herein can be used to control the spectral phase of the laser pulse by applying voltages to the mirror electrodes. The deflection of the mirror surface will lead to a modification of the spectral phase function and thus to a change in the laser pulse shape. To apply the evolutionary optimization strategy, we



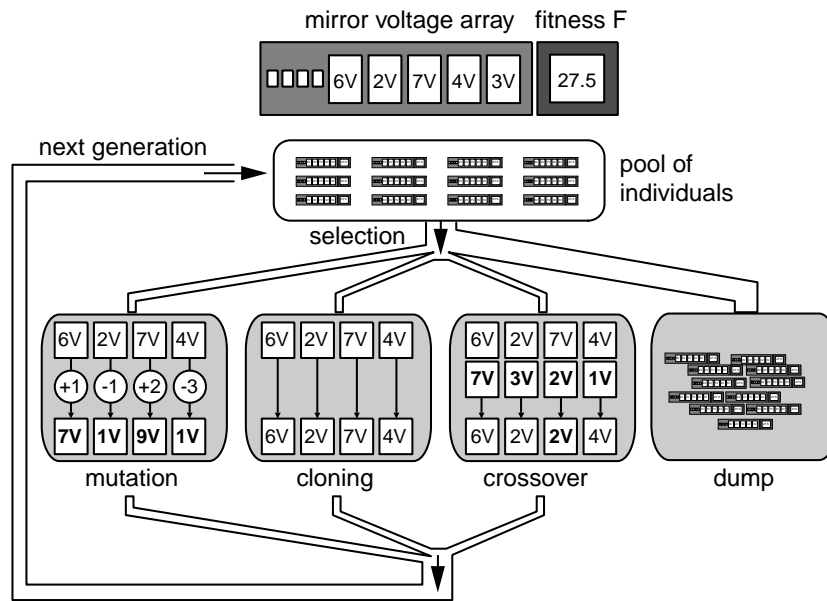


**Figure 5.3:** Basic working principle of an evolutionary algorithm as the one used in the experiment. Individuals (different laser pulse shapes) are characterized by their genetic code, i.e. the voltage array applied to the deformable mirror. One generation consists of a pool of fifty individuals. Each of these pulses is applied in the experiment and the result obtained from a measurement on the quantum system is converted into a scalar quantity called the fitness  $F$  that is now associated with each individual. The fitness is derived from the experiment in such a way that it increases the closer the response from the quantum system matches a user-defined control objective. The fittest individuals are then selected and the least fittest ones are removed from the pool. Improvement of individuals follows the natural principles of reproduction by crossover (two individuals pass complementary parts of their genes to the offspring as indicated) and mutation (genes are randomly altered). Cloning is added to store the best laser pulse shapes. From a more natural point of view, cloning can also be interpreted as surviving for a longer period. The improved individuals are members of the next generation. Iteration of this closed loop strategy results in a continuous increase of the fitness of the fittest individuals, hence, the control goal is approached.

characterize each laser pulse shape with the array of voltages  $(V_1, \dots, V_{19})$  applied to the mirror electrodes. These arrays can be considered to be the genetic code of the individual laser pulses. Our goal is to find the optimum value of  $F$ . This is done by the following strategy: An initial “population” (the first generation) of  $m$  different laser pulses is generated. These pulses are applied in the experiment and the value of  $F$  is extracted for each of the pulses. The best performing individual pulse shapes (the ones that produced the highest  $F$  values) are kept for the next generation (they survive). Also, the best performing individuals produce new members of the next generation by crossover, which means that these “offspring” individuals have a subset of genes from one parent and the complement from the other parent. The remaining part of the next generation is filled up by mutants, which are generated by random variation of one or more genes of high- $F$  individuals. In Fig. 5.3 the algorithm is shown in schematic form. Implementations of this algorithm for optimization of femtosecond pulse shapes have first been reported by the group of

Silberberg [30] and the group of Gerber in 1997 [29].

For the experiments on the control of the high-harmonic spectra, an evolutionary computer algorithm as the one described above is used. For this specific application the closed-loop optimization iteratively shapes the laser pulse with the deformable mirror and the obtained spectrum is measured with the CCD camera. A fitness measure  $F$  for each shaped laser pulse is derived from the HHG spectrum  $I_{HHG}(\omega)$ .  $F$  is thus written as a functional of the harmonic spectrum

$$F = f[I_{HHG}(\omega)]. \quad (5.3)$$

The definition of this functional, which is called the fitness functional or simply fitness function is crucial for the experiments. Achieving particular high-harmonic spectral shapes were the control goals under study. The fitness function therefore must be defined such that it becomes maximal for a certain spectral shape. In Fig. 5.4 the algorithm applied in the experiments is shown in principle. The fitness function shown in this example is the one used to optimize the relative harmonic yield of one harmonic order with respect to its spectral neighborhood. The harmonic spectrum is integrated over the range of the selected harmonic order and the remaining part to yield the integral values  $A$  and  $B$ , respectively. By defining the fitness function as the ratio  $F = A^2/B$  the relative yield  $A/B$  is favored. Also, for the same relative yield, a higher value of total signal in the selected harmonic is favored, by writing  $A^2$  in the denominator. The population size of each generation is fifty for any optimization presented below. The algorithm is repeated for a number of generations, until the fitness of the fittest individual has converged.

## 5.2 Closed-Loop Experimental Setup

### 5.2.1 Laser-Pulse Compression and Shaping

The setup used for the laser pulse-shaping experiments is shown in Fig. 5.5: The regeneratively amplified Ti:sapphire laser system (Section 1.1.1) delivers pulses of 80 fs duration, 800 nm center wavelength, 0.8 mJ energy at a 1 kHz repetition rate. These pulses are focused with a 0.8 m focal length lens into a 0.6 m long hollow fiber with an inner diameter of 250  $\mu\text{m}$ . In this argon-filled fiber the pulses are spectrally broadened and then compressed with a pair of prisms. The self-phase-modulated spectrum used for the experiments, recorded at the output of the argon filled hollow fiber at a gas pressure of  $\sim 0.8$  bar, is shown in Fig. 5.6 (solid line). The dotted line indicates the spectrum of the regeneratively amplified pulse prior to self-phase modulation. The spectrum is thus significantly broadened and shows the typical shape of a self-phase modulated pulse (compare Fig. 1.20).

The retroreflecting mirror in the prism compressor is the deformable membrane mirror, as described in Section 1.1.4. Applying voltages to the nineteen linearly arranged control electrodes placed behind the membrane results in slight deformations of the mirror surface. The spatial modulations translate into spectral phase modulations because the impinging laser pulses are spectrally dispersed. A computer is used to control the high voltage levels and thus the laser pulse shape.

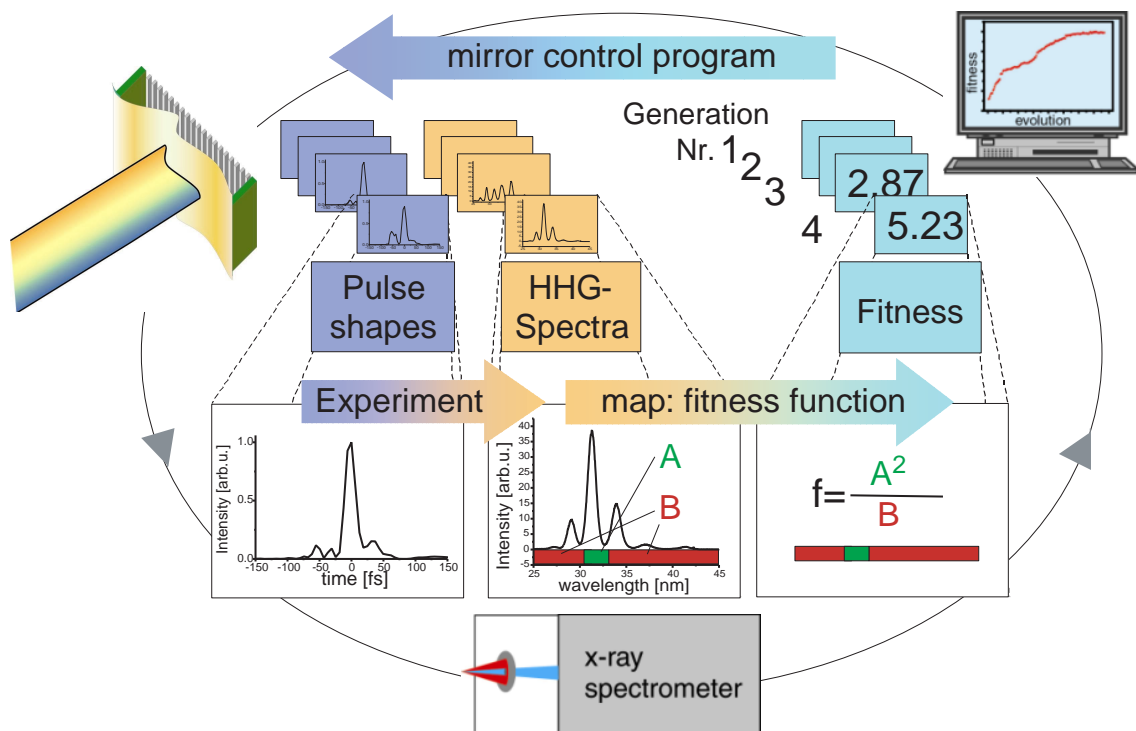


**Figure 5.4:** Specific algorithm used for the control of the harmonic spectral shape. The computer is connected to the deformable mirror and the x-ray spectrometer. It is therefore able to produce shaped laser pulses and also to acquire the high-harmonic spectrum produced by the application of these pulses in the experiment. A fitness function is defined that maps the spectrum onto a scalar quantity—the fitness  $F$ . In this case, as an example, it is calculated by integrating over different parts of the spectrum. The integrated yields  $A$  and  $B$  are used to define the fitness function as  $F = A^2/B$  in order to enhance a given harmonic order with respect to its neighbors. Shown is always the fittest individual of each generation comprising a total number of fifty individuals. From generation to generation the fitness increases by applying the evolutionary strategy, identifying the magnitude of controllability of the high-harmonic spectral shape.

## 5.2.2 Second-harmonic Maximization

In order to check the versatility of the pulse shaping apparatus, initial tests on the optimization of second-harmonic generation (SHG) in a nonlinear BBO crystal (Section 1.2.3) were performed, described in detail in [364]. The SHG signal generated by the laser pulses in the crystal was measured with a fast photodiode. A box-car signal averager was used in order to convert the fast signal to a DC voltage for each laser shot, which was read by the computer. The computer was thus able to control the pulse shape and to immediately record the effect on SHG light simultaneously. An evolutionary algorithm was now run on the computer to maximize the SHG signal. It can be easily shown from Eq. (1.100) that the second harmonic signal is maximized for a fixed pulse energy if the pulse duration is minimized. A more detailed analysis has been carried out in [178]. The value of  $F$  in the optimization problem discussed above in Eq. (5.1) was now experimentally given by the SHG yield. Fig. 5.7a (solid circles) shows an evolution of SHG

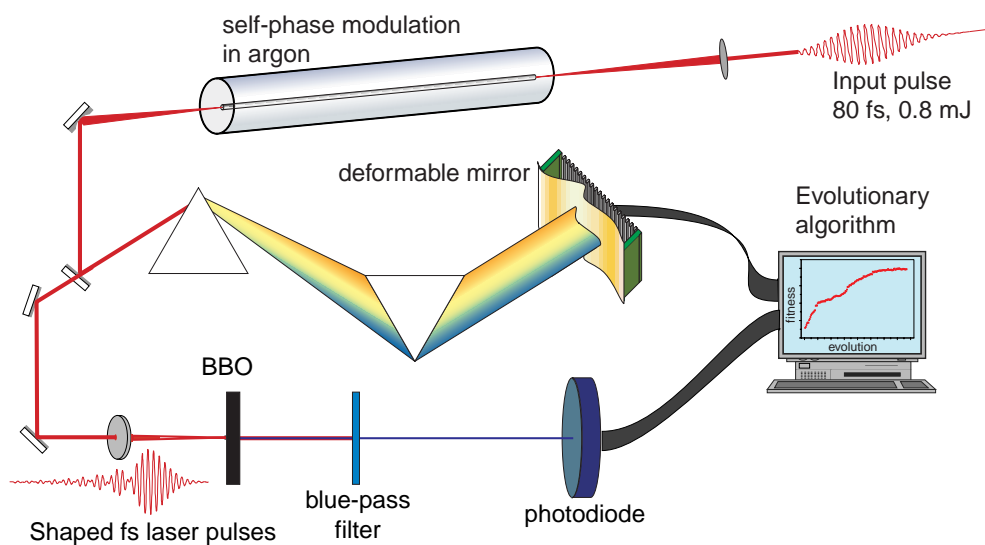


**Figure 5.5:** Experimental pulse-shaping setup used for adaptive femtosecond laser-pulse compression. The pulses are sent through an argon gas filled hollow core fiber in order to broaden the spectrum. The prism compressor is used to eliminate the second order phase, resulting in pulse compression. A deformable membrane mirror is used in order to minimize higher order spectral phase contributions of the laser pulses, resulting in further decrease of the pulse duration. The shortest pulses produce a maximum amount of second-harmonic emission by the focused laser pulse in a nonlinear crystal. An evolutionary algorithm is run on the computer to generate the laser pulse that maximizes the second-harmonic yield.

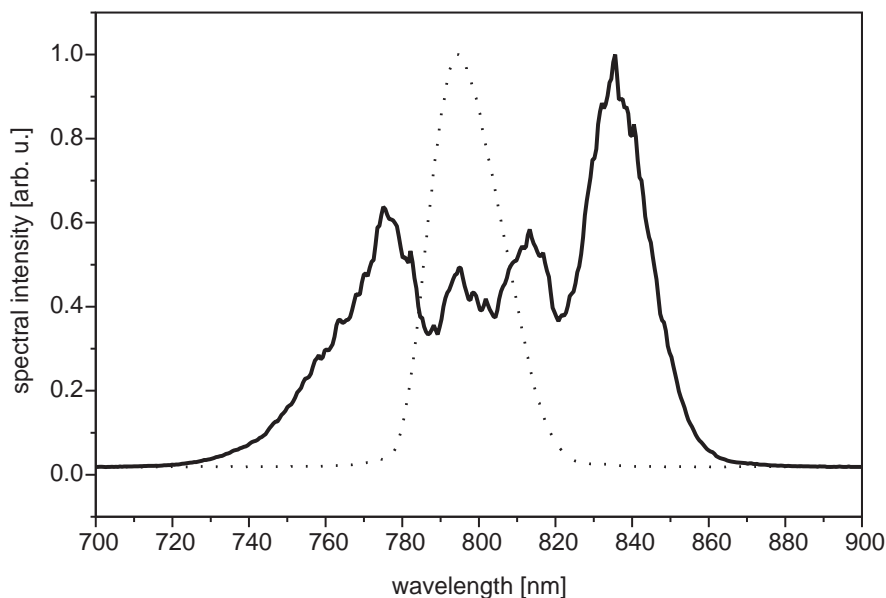


**Figure 5.6:** Spectrum after self-phase modulation of 80 fs laser pulses in a hollow-core fiber filled with argon gas (solid line). The dotted line shows the initial spectrum of the laser pulse at the entrance of the hollow fiber.

as a function of generation number where the prism insertion (closest distance between apex of prism and beam center inside prism) was chosen such that SHG was maximal for the relaxed mirror. The stability of the laser system during the optimization was continuously monitored by applying zero voltage to all mirror electrodes once per generation and recording the corresponding SHG signal which is shown in open diamonds in Fig. 5.7. After evolutionary optimization, the SHG yield increased by  $\sim 20\%$ . The evolution of an optimization where the prism insertion was larger than optimal is shown in Fig. 5.7b. As can be seen, the signal for the relaxed mirror (open diamonds) had dropped to  $\sim 60\%$  of the corresponding value in Fig. 5.7a. The SHG signal strength recovers the value of  $\sim 1.2$  after optimization which was the former result shown in Fig. 5.7a. Thus, the additional dispersion introduced by the larger prism insertion could be compensated. The actuator voltage settings applied to the mirror for the fittest individuals of each generation are shown in Fig. 5.8a and 5.8b, corresponding to the optimizations shown in Fig. 5.7a and 5.7b, respectively. The voltage value applied to the mirror electrodes is shown as a function of actuator number and generation number. In the evolutionary algorithm, the voltage values were initialized with random numbers, visible in the large fluctuations occurring at small generation numbers. For each optimization, both the SHG signal and the mirror actuator voltages finally converged to stationary values. As can be seen, the final sets of mirror control voltages are different for Figs. 5.8a and b indicating the difference in initial spectral phase of the laser pulses.

Optimal laser pulse shapes could not be measured at the time the experiments were performed as measurement devices available at that time were limited to pulses of smaller bandwidth ( $\text{FWHM} < 50 \text{ nm}$ ). For that reason a SPIDER (Section 1.1.5.3, Appendix B) setup was built which allowed the characterization of the produced spectrally broadened and temporally compressed laser pulses. The laser pulse shape—which can be regarded as typical unmodulated laser pulse (prior to optimization) for the experiments described below—is shown in Fig. 5.9.

### 5.3 Controlled Harmonic Generation in the Gas Jet

In the experiments on adaptive control of high-harmonic generation described in the following, both the free focusing and the waveguide geometry (see Section 2.2) were used. The same pulsed valve as described in Section 3.2 was employed to provide gas pulses at a 1 kHz repetition rate. All experiments were conducted in argon gas as conversion medium. The backing pressure of the valve was set to 2 bar. After passing through the compression fiber and the pulse shaping setup described above, the laser pulse was focused into the gas jet with a 0.3 m focal length lens (see Fig. 5.10). Careful alignment of the jet with respect to the laser focus along the optical axis and both transverse axes was carried out in order to manually optimize the high-harmonic output. The nozzle voltage was chosen such that the density in the interaction region was high enough to efficiently generate high-harmonics. In order not to overheat the nozzle, water cooling was necessary at all times during operation.

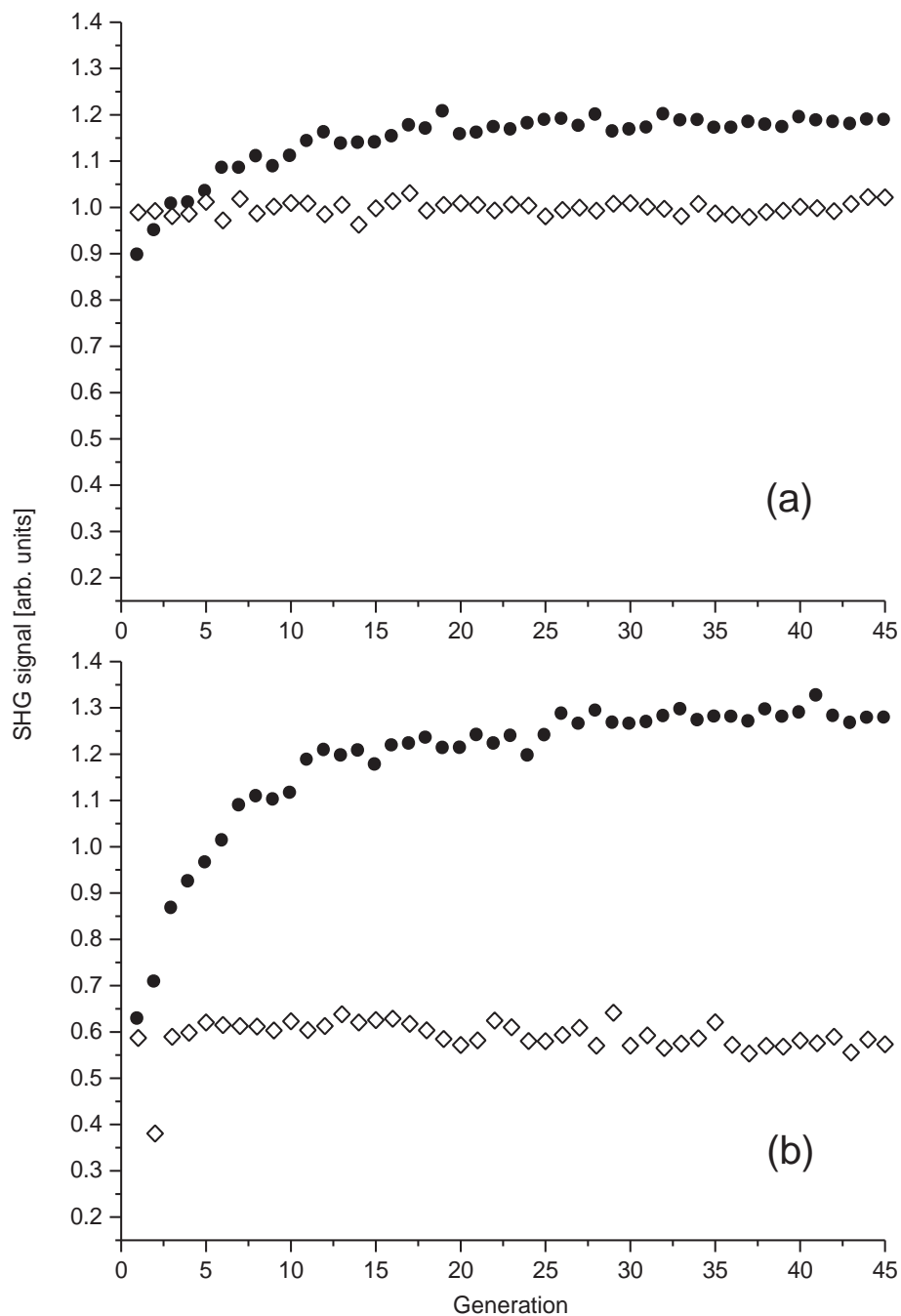


**Figure 5.7:** SHG optimization: (a): prism compressor optimized for maximum SHG signal, (b): more prism insertion than optimal. Shown are: full circles: fittest individual of each generation, open diamonds: relaxed mirror (zero voltage applied).

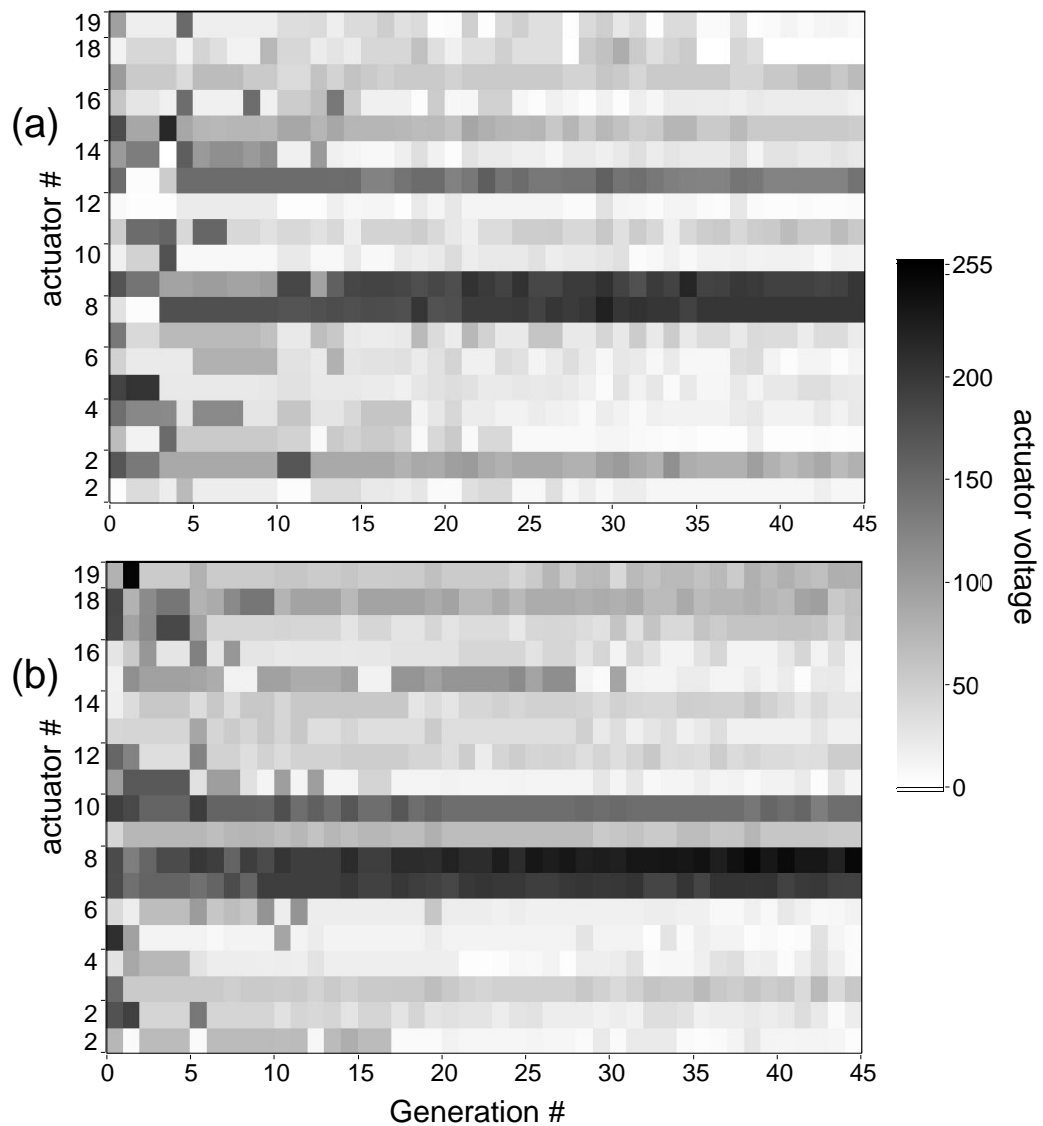


**Figure 5.8:** Mirror actuator settings of fittest individual versus generation for the optimizations shown in Fig. 5.7. The actuator voltage arrays in the first generation are randomly chosen. During the run of the optimization experiment, the voltage array of the fittest individuals converges as does the fitness value itself (compare Fig. 5.7). The difference in end results for (a) and (b) stems from the difference in the residual spectral phase of the laser pulses to be compensated.

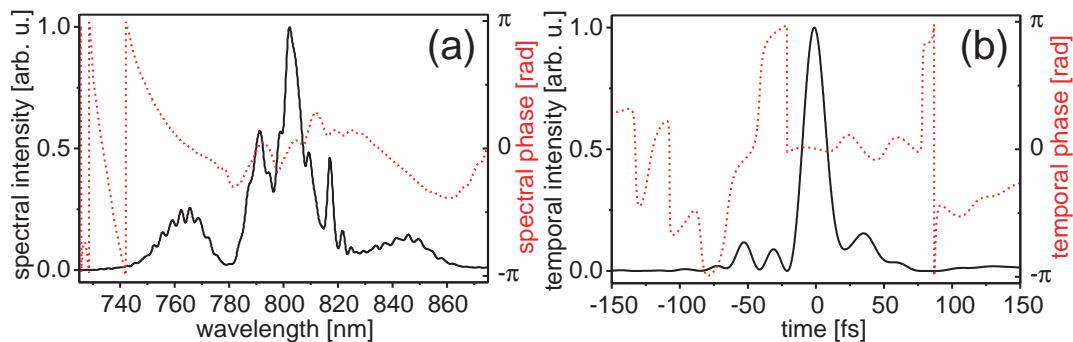


**Figure 5.9:** Typical laser pulse shape after self-phase modulation and prism compressor characterized by the SPIDER technique. Shown are (a) spectral and (b) temporal intensity (solid line) and phase (dotted line). The FWHM pulse duration is 20 fs.

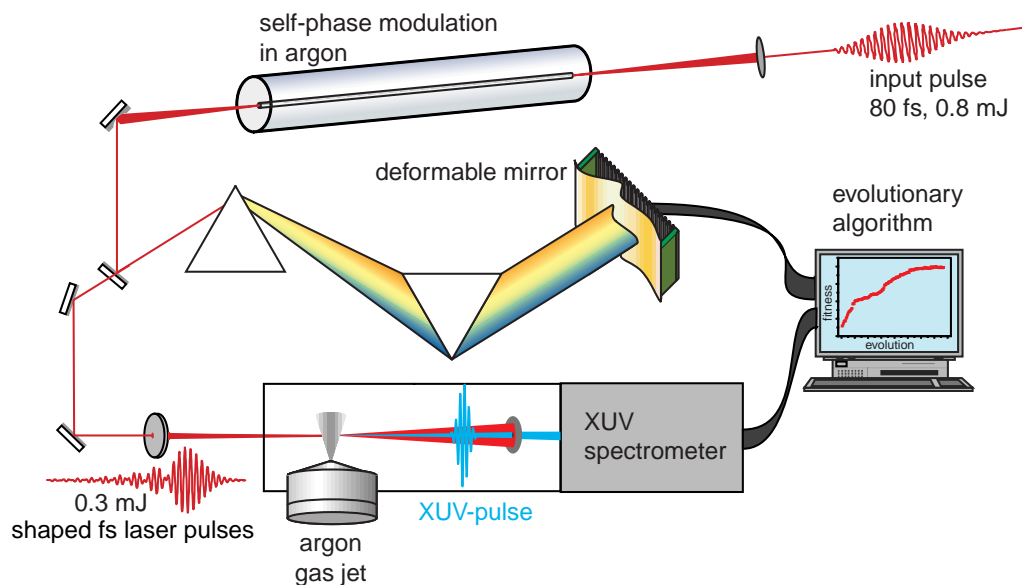


**Figure 5.10:** Setup for the experiments on control of high-harmonic generation produced in the gas jet. Self-phase modulated laser pulses are sent through the prism-compressor with the computer-controlled deformable mirror for compression and shaping. Afterwards, they are focused into a gas jet produced by a pulsed valve operating at the repetition rate of the pulsed laser (1 kHz). A monochromator equipped with a charge-coupled-device (CCD) camera is used to acquire the high-harmonic spectrum. The computer is used to run a closed-loop optimization with an evolutionary algorithm.



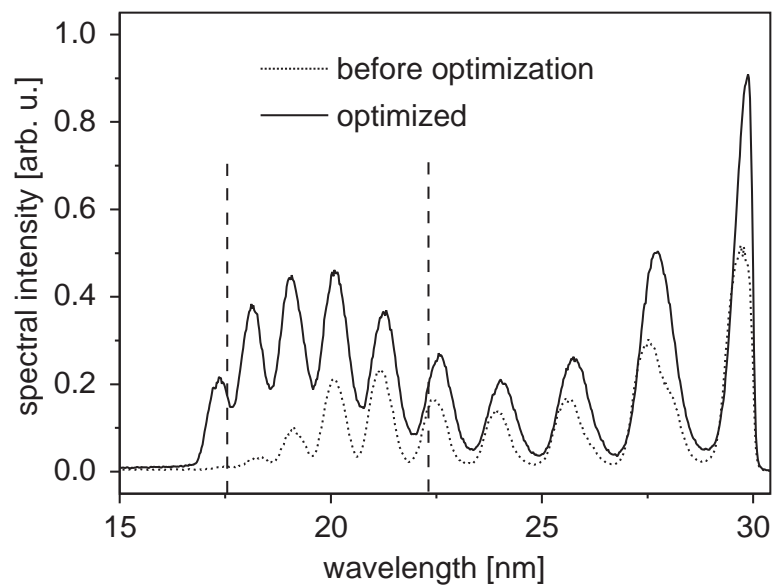


**Figure 5.11:** Optimization of the cut-off position of high-harmonic generation. Starting from a given spectrum and choosing the fitness function according to the integral over the cut-off region as indicated by the dashed lines, the evolutionary algorithm was able to shift the cut-off position by several orders. The emission of higher orders is in fact obscured by the aluminum absorption edge at 17 nm below which the light is absorbed.

### 5.3.1 Cut-off Extension

One major goal in high-harmonic generation is the generation of very high harmonic orders. In particular, generating harmonics in the water window [147,219] is a challenging endeavor. This is due to the fact that light in this wavelength region can be used to effectively image biological material. It is called water window because water (oxygen) is transparent at these frequencies whereas carbon, the building block of biomatter, is absorbing. It is thus an interesting question whether adaptive pulse shaping allows us to push the cut-off position to higher photon energies.

An aluminum filter of 0.8  $\mu\text{m}$  thickness was placed between the jet and the soft x-ray spectrometer in order to separate the high-harmonic radiation (which is transmitted through the filter) from the fundamental remainder. The spectrometer was aligned such that the high-harmonic beam illuminated the entrance slit. The laser pulse energy after the prism compressor was 0.28 mJ. The prism insertion (controlling quadratic phase, i.e. linear chirp) was chosen such that it maximized the high-harmonic output. Afterwards, the optimization program was started on the computer.

The high-harmonic soft x-ray spectra before and after optimization on the cutoff-region are shown in Fig. 5.11. The fitness function  $F$  was defined to be the integral harmonic emission in the cut-off region as indicated by the dashed lines in Fig. 5.11. The evolutionary algorithm on the computer was programmed to maximize this fitness value. It is clearly visible that not only the cut-off position shifted towards higher photon energies but also the efficiency of lower harmonic orders increased. However, the increase is lim-

ited to about a factor of two. These results can be immediately understood from the fact that the mirror clears up higher-order spectral phase distortions in the laser pulse, which the simple prism compressor (predominantly compensating linear chirp) cannot compensate. This results in higher peak intensity of the laser pulses, leading to a higher harmonic cut-off from formula Eq. (2.10). It is also well known that higher and higher intensity at the same pulse energy leads to higher conversion efficiency also for the plateau harmonics. Only recently was it shown that control and adaptive optimization of the spatial focal shape [365] also leads to an extended plateau with higher cut-off photon energy in high-harmonic generation.

### 5.3.2 Harmonic Selectivity?

A more interesting control objective is selective high-harmonic generation. Is it possible to enhance particular harmonic orders while at the same time suppressing (or at least decreasing the intensity of) the neighboring orders? As is known in literature, this selectivity is achievable in a waveguide geometry [299, 353], as will also be shown below in this work. This selective emission of single harmonic orders is important for the application of high-harmonics in spectroscopy applications, where a narrow-spectral-line source (e.g. only one harmonic) is highly favorable to achieve good spectral resolution.

Another question arises: is the waveguide geometry responsible for the observable selectivity in the generation process or can the same selectivity be achieved also in the free-focusing geometry? To answer the question, again a closed loop optimization experiment was performed. Prior to running the optimization algorithm, the harmonic spectrum was manually optimized by adjusting the experimental parameters for fixed settings of the deformable mirror pulse shaper. The fitness function was now chosen such that a selective excitation of a single harmonic order would increase it. The spectrum was divided into two parts,  $A$  and  $B$  as indicated in Fig. 5.12. The fitness function used was defined as  $F = A/(A + B)$ , the strength of the selected single harmonic relative to the intensity of the spectral region containing three harmonic orders: the selected one and its two nearest neighbors. After running the evolutionary algorithm on the computer, programmed to maximize the fitness  $F$ , the spectral shape changed only slightly. The relative spectral emission strengths of the three harmonics included in the optimization did not change qualitatively. The lowest harmonic order of the three decreased slightly more compared to the two higher orders. Obviously, the selected harmonic could not be enhanced beyond the intensity of its lower-order neighbor. The decrease of the overall spectral intensity is due to the fact that the total harmonic strength was not included in the fitness function. In order to achieve at least some improvement of the relative harmonic yield the search algorithm thus found a solution exhibiting very low harmonic conversion efficiency. These results demonstrate that the geometry of the waveguide is essential for the control of essential spectral features like selective harmonic generation and qualitative spectral control.

It should be added that there are some spectral features of harmonic generation in the focusing geometry which allow to be controlled by shaping the generating laser pulses. Very recently, Reitze *et al.* [218] published results on the selective shifting of the spectral position of the comb of harmonics produced in a gas jet. Again a closed-loop optimization

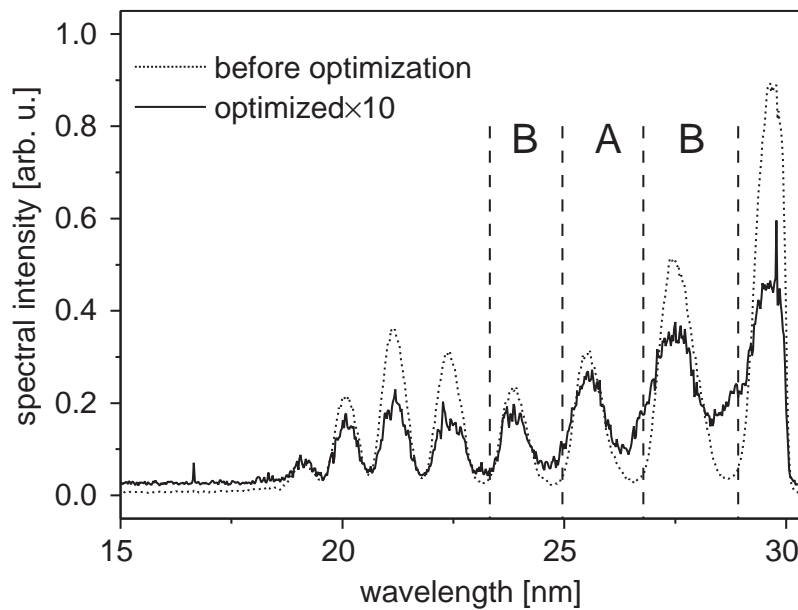


**Figure 5.12:** Is selective harmonic emission achievable in the free-focusing geometry? The harmonic in region A was selected and maximized with respect to the total region  $A + B$ . No significant enhancement over the neighborhood can be observed, in contrast to the waveguide geometry. The overall signal strength decreased as a consequence of not being included in the fitness function.

strategy was used. The fitness function was chosen such that it increased when a selected harmonic order came closer to a target wavelength, specified by the experimenter. It could be shown that a single harmonic was tunable over a wide range of wavelengths. This finding has been attributed to the control of the plasma generation process during high-harmonic generation. The fast buildup of a plasma created by the laser pulse can affect the spectral features of the laser pulse itself. The refractive index (modified by the plasma) thus changes on the time scale of the laser pulse. As has been discussed at the end of Section 1.2, a rapidly changing refractive index causes spectral shifting of the laser pulse. In the case of the plasma, the refractive index is steadily decreased (since recombination occurs on a much longer time scale), leading to a blueshift of the spectrum [366–368]. Since plasma buildup directly depends on the laser pulse shape, the spectral blue-shift also depends on the temporal shape of the laser pulse. This effect becomes visible in Fig. 5.11, where the plateau harmonics around 25 nm exhibit different central wavelengths.

## 5.4 Controlled Harmonic Generation in the Waveguide

For the experiments in the waveguide geometry, the shaped laser pulses from the prism compressor were focused onto the entrance of a second argon-filled hollow fiber with an inner diameter of  $140 \mu\text{m}$  and a length of 0.1 m, where the high harmonics are generated. Here, a focusing lens of 40 cm focal length was used, which explains the difference in harmonic cut-off positions due to a reduced intensity compared to the jet case. The complete setup is shown in Fig. 5.13. The fiber in which high-harmonic generation takes place

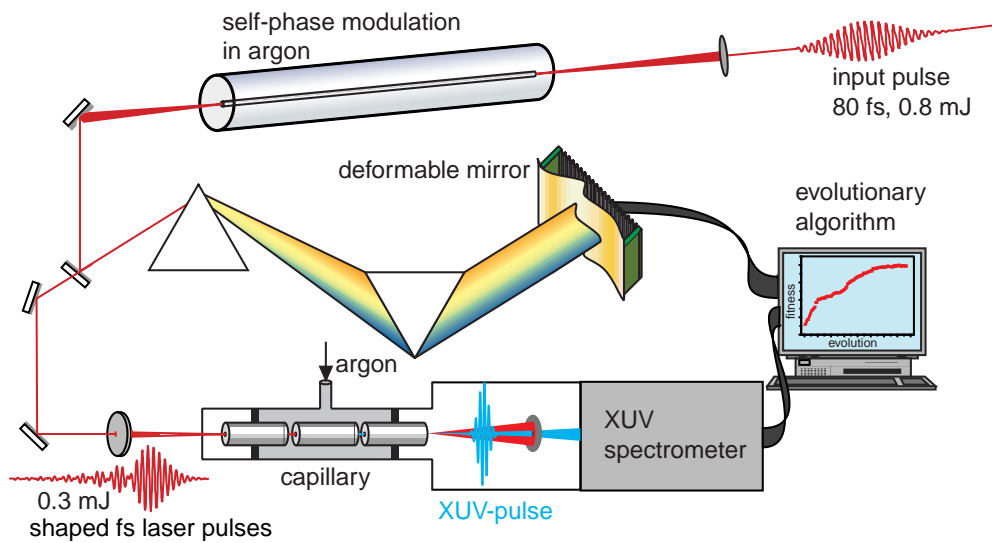


**Figure 5.13:** Experimental setup for the spectral shaping experiments. Self-phase modulation in an argon-filled hollow capillary and a prism compressor are used to shorten the laser pulses. Pulse shaping is accomplished by a deformable membrane mirror as the retroreflector in the compressor. The shaped pulses are focused into a second argon-filled capillary where high-harmonic generation takes place. The spectrum of the resulting radiation is analyzed by an extreme-ultraviolet (XUV) spectrometer equipped with an x-ray CCD camera. The computer is used to run a closed-loop evolutionary algorithm, optimizing the harmonic spectral shape.

actually consists of three pieces, produced by breaking a single capillary and rejoining the pieces on a v-shaped metal groove, ensuring line-up. A gap of  $\sim 0.2$  mm between the fiber pieces allows the gas to enter the capillary. Both end pieces (30 mm in length) are used to separate the center piece (in which the gas pressure of  $\sim 0.1$  bar is constant) from the vacuum prevailing at the entrance and exit of the fiber. After leaving the fiber, the visible laser pulse and the lower order harmonics are blocked by a  $0.3 \mu\text{m}$  thick aluminum filter. The transmitted soft x-ray radiation is then characterized with an extreme-ultraviolet (XUV) spectrometer equipped with a backside-illuminated charge-coupled-device (CCD) camera read out by the computer. A similar setup was used by Rundquist *et al.* [136] who demonstrated phase-matched generation of high-harmonic radiation in a hollow fiber for the first time.

The laser intensity in the hollow fiber is  $2 \times 10^{14} \text{ W/cm}^2$ . For this intensity the cut-off harmonic order  $q_c$  can be calculated from the simple scaling law  $q_c \hbar \omega = 3.17 U_p + I_p$  [105, 107] (see Section 2.1), where  $\omega$  is the fundamental laser frequency,  $U_p$  is the ponderomotive potential which is directly proportional to the intensity, and  $I_p$  is the ionization potential. For the estimated peak intensity and argon as the nonlinear medium ( $I_p = 15.8 \text{ eV}$ ) the harmonic cut-off is expected near the 29th order, which is in agreement with the experimental findings.

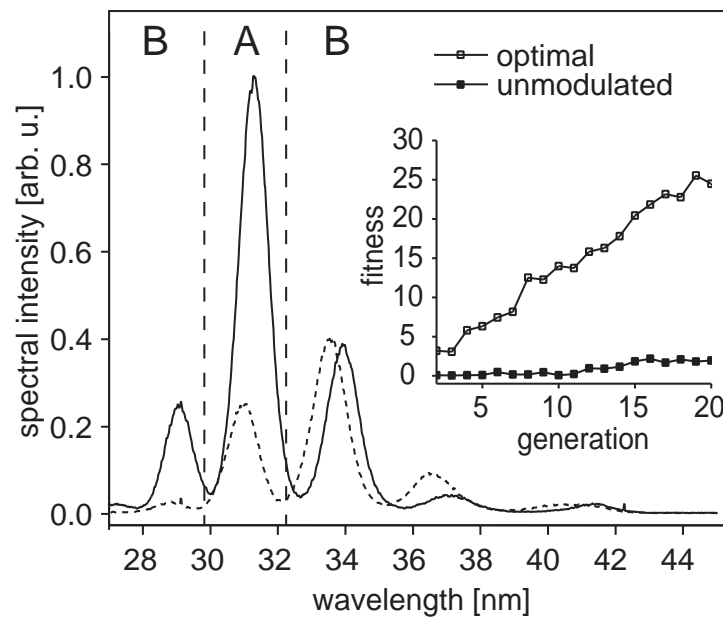


**Figure 5.14:** Optimization of a single harmonic. The graph shows results for the optimization of the 25th harmonic both absolute and relative to the neighboring orders (solid line: optimized result, dashed line: initial spectrum (unmodulated laser pulse)). The fitness function to be maximized by the evolutionary algorithm is defined as  $A^2/B$ . During the run of the optimization experiment the fitness increases (see inset). The soft x-ray spectra obtained for unmodulated (filled squares) and optimal (open squares) laser pulses are presented.

### 5.4.1 Single-Harmonic Generation

First of all, enhancement of a particular harmonic with respect to the neighboring orders is addressed in the experiment. A similar optimization strategy has already been implemented by Bartels et al. [299,353]. In contrast to these earlier studies it can be shown that several harmonics can be isolated. The results are summarized in Fig. 5.14 and Fig. 5.15. For this optimization the spectrum was divided into two parts. Part A contained the spectral range around the harmonic to be enhanced whereas part B consisted of the remaining part of the spectrum measured with the CCD camera. The fitness function  $F$  was then chosen to be  $F = A^2/B$  and implemented into the optimization algorithm, where  $A$  and  $B$  denote the integrated signal in parts A and B, respectively. This definition of the fitness favors both the relative yield of the selected harmonic with respect to the neighboring harmonic orders and also the absolute enhancement of the selected harmonic. Prior to running the optimization algorithm, the total harmonic yield was maximized by adjusting the prism compressor while applying the same voltage to all mirror electrodes. The fitness of this reference pulse was calculated and was used as a measure for the stability of the whole system. The course of the optimization experiment is depicted in the inset of Fig. 5.14. The fitness of the fittest pulse shape for each generation increases while the fitness of the reference laser pulse is nearly constant and stays at low levels. The harmonic spectrum obtained with the reference pulse along with the optimized spectrum obtained with the best laser pulse shape after 23 generations is presented in Fig. 5.14. The 25th

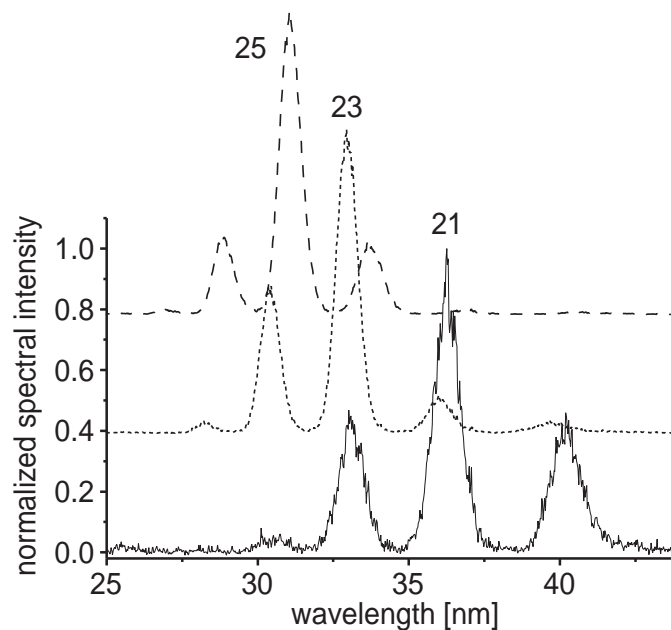


**Figure 5.15:** Optimization of the harmonic yield of different selected single harmonics relative to the adjacent orders for a range of harmonics. It is possible to achieve quasi-monochromatic tunable harmonic emission. This can be used as a unique tool for high-resolution femtosecond pump-probe photoelectron spectroscopy.

harmonic order has gained a factor of four in amplitude compared to the reference case. As intended only the 25th harmonic is selectively enhanced and the adjacent harmonics are less intense by a factor of three. To demonstrate that the same approach does not only work for a certain harmonic, selectively enhanced harmonics of the orders 21 to 25 are presented (Fig. 5.15). It is thus possible to create tunable narrow line emission in the soft x-ray spectral range. Since the duration of the high-harmonic pulses is always shorter than the generating laser pulse, this tunable radiation can for instance be applied for femtosecond time-resolved spectroscopy in the soft x-ray range.

### 5.4.2 Selective High-Harmonic Generation

The crucial question for coherent control in the soft x-ray region arises: Can we achieve a more comprehensive control over the coherent HHG spectrum, enabling us to engineer the spectral properties and possibly temporal evolution of the emerging sub-femtosecond pulses or pulse trains? It is now shown that this is indeed possible. As a next step selective enhancement of coherent soft x-ray radiation over a wide spectral range is demonstrated. The spectrum is divided into two parts containing three to four harmonic orders each. The optimization goal was the suppression of the signal in one part while maximizing it in the other part. The applied fitness functions in these cases were (a):  $F = B - A$  and (b):  $F = A - B$ , where  $A$  and  $B$  in this case denote the harmonic yield integrated over higher (H25-H31) and lower (H19, H23) harmonic orders, respectively. In Fig. 5.16

the corresponding results are shown. While selective generation of the lower-order part of the spectrum can be readily understood by considering reduced peak intensity in a chirped generating pulse, it is not clear yet what causes the enhancement of higher orders while simultaneously suppressing lower order harmonics almost completely.

Mairesse *et al.* [164] recently measured the sub-optical-cycle timing of the attosecond pulse with respect to the carrier wave of the femtosecond driver pulse in high-harmonic generation. The possibility to shift the harmonic spectral emission enables the production of sub-femtosecond pulses at defined times relative to the carrier wave with attosecond precision. This is particularly important for laser–soft-x-ray cross-correlation experiments. Moreover, the selective generation of a part of the harmonic spectrum is a possible solution to single out the spectral region, where the harmonics have a fixed relative phase, resulting in a train of identical attosecond pulses. In addition it is now feasible to easily tune the frequency of the attosecond pulses produced in high-harmonic generation. At the moment, this is not easily possible as the selection and isolation of certain spectral regions has to be done by multilayer mirrors [170, 171]. These mirrors exhibit a fixed spectrally narrow region, where the reflectivity is optimized.

Apart from these important technological implications of the spectral engineering technique, the following section will demonstrate the versatility of harmonic control going beyond spectral shifting and enhancement to produce unprecedented high harmonic spectra.

### 5.4.3 Suppression of Single Plateau Harmonics

The level of control over the process of harmonic generation becomes evident in spectra where one or two harmonics in the plateau region are suppressed as shown in Fig. 5.17. Fig. 5.17a shows the typical harmonic spectrum after adjusting the prism compressor and the pressure in the hollow fiber to maximize the total soft x-ray yield. Under this condition equally intense harmonics are observed implying that the displayed range lies in the plateau. Fig. 5.17b and c display the spectra after running the adaptive closed-loop optimization with the goal to suppress one and two adjacent harmonics, respectively. The selected harmonic orders were “switched off” while neighboring peaks are still present. This is the first demonstration of the suppression of a selected number of plateau harmonics.

Full control over the shape of the soft x-ray spectrum has a major impact on energy-resolved spectroscopy and can also pave the way to control electron dynamics. Suppressing one or two harmonics effectively produces a bimodal spectral distribution, with a mode spacing of approximately seven times the fundamental frequency. This results in a sub-half-cycle beating in the temporal response with a period of about one seventh of the optical period. This consideration only demonstrates the potential of this technique for extending pulse shaping into the attosecond regime.

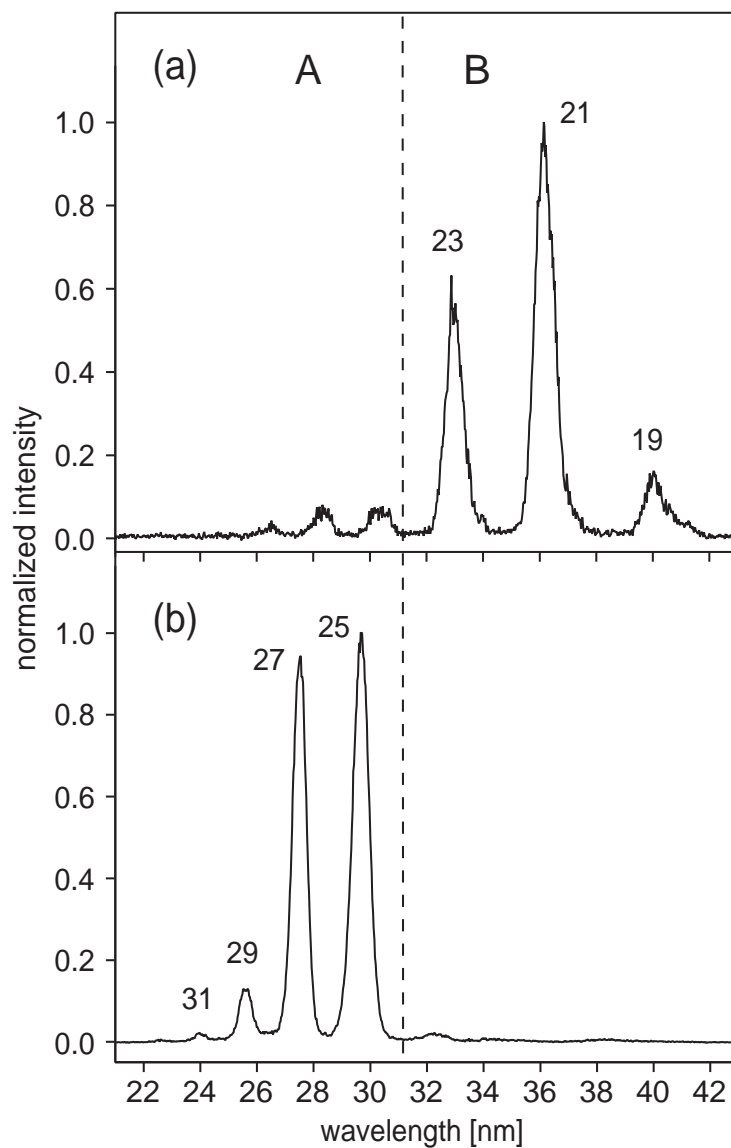


**Figure 5.16:** Selective enhancement of high-harmonic generation. (a) Optimization of the low frequency spectral part while simultaneously reducing the high frequency part and vice versa (b). The ability to control wide spectral ranges of harmonic emission allows for the generation of frequency-tunable attosecond pulses. In addition, selecting suitable spectral ranges allows for sub-optical-cycle timing of the attosecond pulse with respect to the carrier wave (see text).



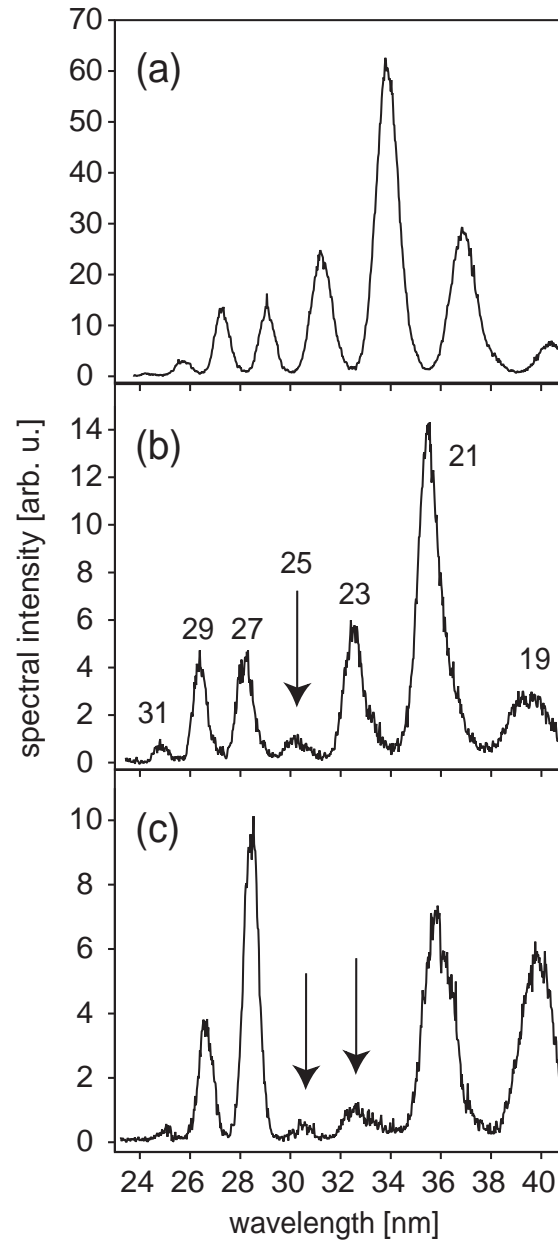


**Figure 5.17:** Suppression of harmonics while generating adjacent ones at about ten times higher efficiency. (a) Typical harmonic emission in the plateau region, (b) one suppressed harmonic order, (c) two suppressed harmonic orders. The high degree of controllability of soft-x-ray spectral shape over a large range of photon energies ( $\sim 10$  eV) implies major modifications of the corresponding temporal shape on a sub-femtosecond time scale.

#### 5.4.4 Simulation and Discussion

To shed light onto the physical processes responsible for the observed spectral modifications the experiments presented were repeated on the computer. The simulation was based on a numerical integration of the one-dimensional Schrödinger equation in an arbitrarily shaped laser field. The HHG spectra are obtained by Fourier transformation of the time-dependent expectation value of the electric dipole acceleration [131]. This simple model only describes the single atom response without considering propagation effects. It was implemented into the same evolutionary algorithm as the one used in the experiment. In analogy to the experimental setup, phase-shaped laser pulses were generated by defining the spectral phase at fourteen positions sampling the entire laser spectrum. The fitness functions were calculated in the same way as in the experiment. With this simulation both maximization and minimization of the 25th harmonic order relative to the neighboring harmonics could be demonstrated (Fig. 5.18). However, the relative enhancement or suppression with respect to the neighboring harmonics is not as significant as observed in the experiment. This is most clearly visible for the selective minimization of the 25th harmonic order (H25) shown in Fig. 5.18c and d. While it was experimentally possible to decrease the H25 yield to a ratio of about 1:5 compared to the yield of each nearest neighbor (H23, H27), the optimized single-atom-response result was only 1:2. This finding is consistent with other simulation results [123] and points to the importance of considering both the single-atom response *and* propagation effects for efficient control of high-harmonic generation. In the experiments on selective high-harmonic generation in the atomic jet it was not possible to control the soft x-ray spectral emission in the way described above. This provides additional evidence that the guided geometry of the waveguide is important to control also the spatial properties of the laser. Whereas in the gas jet any spatial modification of the laser focus is only present over a very small distance, the capillary waveguide allows to sustain and apply this change over an extended interaction length. In agreement with previous work, the simulation shows that fundamental pulse shapes are only slightly different for harmonic spectra that differ substantially. A comparison of the pulse shape obtained in our simulations with the experimental results was not carried out because the subtle structure of the spatial pulse shape at the entrance of the hollow fiber cannot be measured. Before and during the process of HHG the laser pulses experience a substantial spatial and temporal reshaping making a quantitative comparison with theoretical results meaningless.

### 5.5 Conclusion

Adaptive control of high-harmonic generation was presented for two scenarios, the free-space focusing and the waveguide geometry. For the case of focusing into a jet it was possible to enhance the high-harmonic yield in the cut-off region by about a factor of two. The cut-off could be shifted to higher photon energies. However, it was not possible to selectively enhance a single harmonic relative to its neighboring orders. In the waveguide geometry on the other hand, selective generation of single harmonics was feasible at high contrast ratios. Single harmonics at different photon energies in the plateau region could be selectively generated. In addition, extended parts of the harmonic spectrum comprising

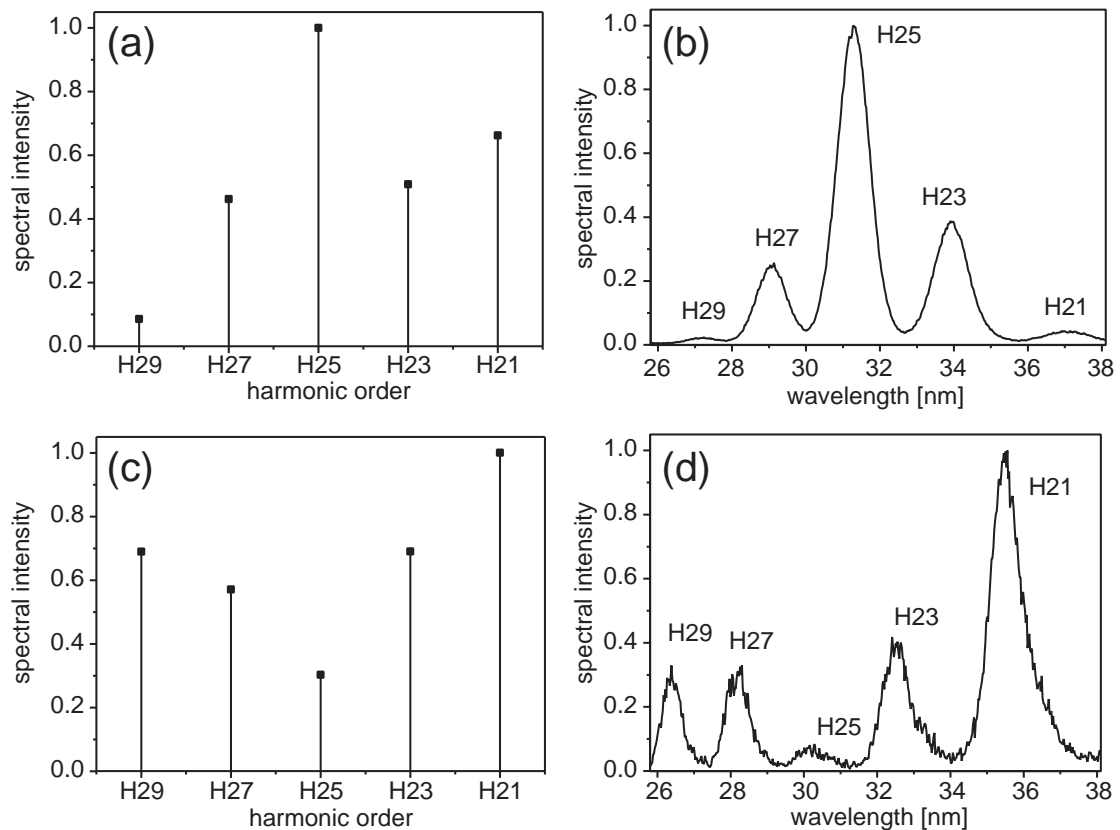


**Figure 5.18:** Comparison of simulation (a,c) and experimental (b,d) results for selective maximization (a,b) and minimization (c,d) of the yield  $A$  of the 25th harmonic order with respect to the total yield  $B$  of the surrounding harmonic orders. The fitness function was defined as  $A^2/B$  for the maximization and  $B^2/A$  for the minimization. The simulation based on the single-atom response alone was not able to reproduce the contrast ratio between optimized 25th order (H25) and neighboring harmonics (H21, H23, H27, and H29). The origin of the observed controllability thus goes beyond the single-atom response, indicating the importance of propagation effects. For better visibility, the simulated harmonic spectrum shows the harmonic spectral intensity integrated over equally large spectral regions centered at the indicated harmonic orders.

a defined number of multiple harmonic orders could be selected to contribute to the soft x-ray emission while at the same time impairing harmonic generation at adjacent orders. Moreover, harmonic orders in the harmonic plateau region could be “switched off”. It is thus possible to use femtosecond pulse shaping to generate user-defined coherent spectral emission in the soft x-ray region.

Two important conclusions can be drawn from the results presented in this chapter. The success of selective control in the waveguide geometry and failure in the focusing geometry indicates the importance of propagation effects for the control of the harmonic generation process. Secondly, the variety of coherent soft x-ray spectral shapes opens the door to a number of new scientific perspectives. In order to excite and manipulate electrons in tightly bound states of atoms and molecules we typically need to provide soft x-ray photons. Electronic dynamics in these states proceeds on the time-scale of attoseconds.

High-harmonic generation produces soft x-ray light that is emitted in attosecond bunches and is therefore ideally suited for the monitoring of electronic dynamics. It is now possible to control and engineer the high-harmonic spectrum of coherent soft x-rays spanning more than 10 eV bandwidth by shaping the driving laser pulses [303]. Controlling the high-harmonic generation process in the presented qualitative fashion supplies shaped coherent soft x-ray light fields that can be used not only to monitor but to actively control electronic dynamics. Another application is shaping of the attosecond pulses emerging from the process. These mentioned applications of the here presented method of coherent soft x-ray spectral shaping are addressed in the following part of this work.

# Part IV

## Adaptive Control in the Soft X-Ray Region

Having at hand the results of the previous part one could ask: What new insights did we gain from the experiments on the optimization of qualitative coherent soft x-ray spectral shape? It was not possible to identify a new control mechanism besides the ones that were already extensively discussed in the literature before: single-atom response and propagation control. However, even without further insight into the mechanism of control, the very possibility to perform spectral modifications as the ones presented opens the door to a variety of new applications and perspectives.

It is now possible to control the spectral characteristics of coherent soft x-ray radiation to generate almost arbitrary spectral modifications. The first experimental demonstration of soft x-ray spectral amplitude shaping over extended spectral regions has been demonstrated. By virtue of the dual representation of light in the frequency and time domain (see Section 1.1.2), this finding points towards the feasibility to perform attosecond pulse shaping, as will be discussed in detail in this part. The availability of tailored soft x-ray light has important consequences for the field of optimal control of quantum dynamics. It has become a common technique to shape femtosecond infrared to visible laser pulses in order to control molecular dynamics. The magnitude of attainable control is hereby always limited by the timescale dictated by the bandwidth of the laser pulse. For that reason, the motion of heavy nuclei in molecules or crystal lattices is a target of many control experiments. The much lighter electrons could so far only be controlled for slowly varying Rydberg superposition states of atoms. To control electronic dynamics in the ground state or even core states of atomic or molecular systems, shaped coherent soft x-ray light fields on the natural time and frequency scale of electronic dynamics have to be available. As will be shown here, the technique developed in the previous part can be employed for these kinds of applications.

This part contains two chapters that point out the two fundamentally new applications of the technique of soft x-ray spectral shaping. Chapter 6 shows how the newly introduced flexible soft x-ray source can be used in order to control branching ratios of a photodissociation reaction of molecules in the gas phase. Again, a closed-loop optimization experiment is carried out in order to demonstrate the feasibility of optimal control in this hitherto unexplored spectral region. Chapter 7 discusses the temporal aspects of spectral soft x-ray shaping for the control of the attosecond pulse shape.



## Chapter 6

# Selective Photochemistry with Shaped Soft X-Rays

The control of chemical reactions is a central topic of optimal quantum control. It has always been a dream of chemists and physicists to use laser light in order to steer chemical reactions towards desired targets. As has been discussed in the previous part of this work, in particular the idea of closed loop quantum control [300] has been a major breakthrough [301, 302] in the field. For these early experiments, shaped 800 nm laser pulses were used. Transfer of pulse shaping techniques into the visible [369], MIR [370] and UV [47] (down to 200 nm) wavelength range has already been achieved in the past and is available for control experiments.

With the technique of coherent soft x-ray engineering introduced in the last part of this work it becomes possible for the first time to do closed loop learning control experiments in the soft x-ray spectral range. The experimental setup presented in the previous chapter was modified to apply the shaped soft x-ray light to a molecular sample (Section 6.1). The branching ratios of a photodissociation reaction of sulfur hexafluoride ( $\text{SF}_6$ ) are controlled by adaptive soft x-ray spectral shaping (Section 6.2). This chapter is devoted to the demonstration of the principle technical versatility of the adaptive coherent soft x-ray source for this type of experiments, regardless of the physical process at work. The particular experiment presented here only serves as a prototype example. Many more applications that directly observe the electronic dynamics are expected to follow up on the herein developed technological advance in the future.

### 6.1 Experimental Setup

For the application of the variably shaped high-harmonic spectral emission to some target system, the gas jet produced with the 1 kHz pulsed nozzle (Section 3.2) was again employed. It was located after the capillary used for the generation of the harmonics (see Fig. 6.1), which was described in Chapter 5. A linear time-of-flight (TOF) mass spectrometer of the Wiley-McLaren type [371] was used in order to detect positively charged ions produced by the high-harmonic pulses. This mass spectrometer used for the exper-

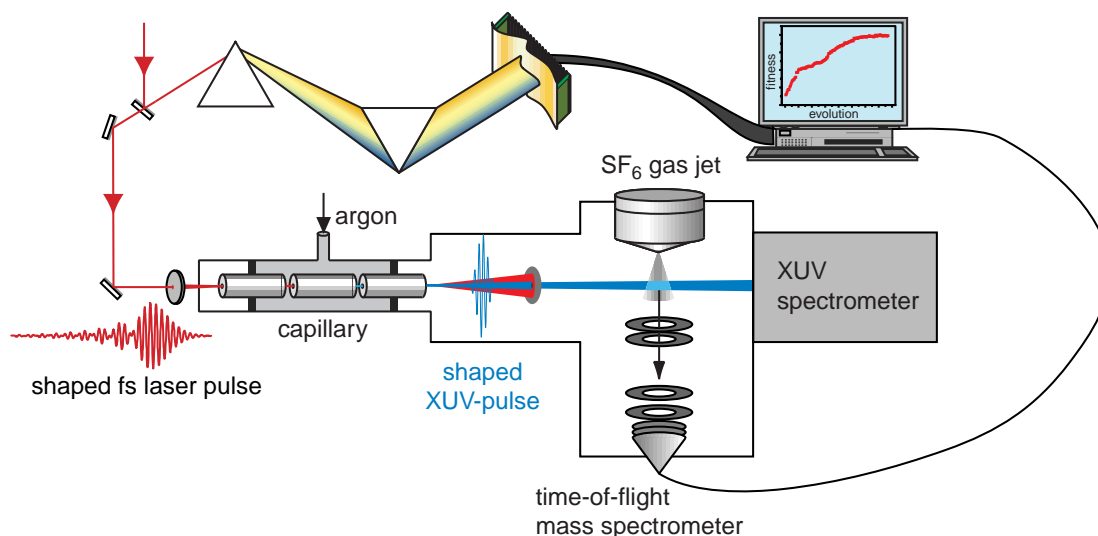


**Figure 6.1:** Setup for the experiments on adaptive control of photochemistry by high-harmonic spectral engineering. The high-harmonic radiation output from the capillary is used to induce dissociative ionization in  $\text{SF}_6$  gas. The fragments are detected with a linear time-of-flight mass spectrometer. The spectral shape of the soft x-ray pulses can be measured in parallel, since only a small fraction of the harmonic light is absorbed by the gas.

iments is described in detail elsewhere [372]. In brief, the mass of an ionic particle is deduced from the time it takes it—accelerated by constant electric fields—to reach the detector. This time of flight  $t$  can then be readily converted into the particle mass  $m$  by the quadratic relation

$$m = aZ(t - t_0)^2, \quad (6.1)$$

where  $Z$  is the charge of the ion,  $t_0$  is the time at which the laser pulse interacts with the target, and  $a$  is a factor containing the accelerating electric fields and the geometry of the spectrometer. All experiments presented here were conducted in sulfur hexafluoride ( $\text{SF}_6$ ). A backing pressure of 2 bar was used behind the nozzle. The high-voltage controlling the opening of the pulsed nozzle was chosen such that the pressure in the chamber was at  $2 \times 10^{-5}$  mbar. The pressure was limited to this order of magnitude by the maximum tolerable pressure of the microsphere-plate detector (MSP, manufacturer: El-Mul Technologies) installed in the TOF mass spectrometer. The nozzle was aligned relative to the harmonic beam in order to maximize the ion signal from the mass spectrometer.

The laser pulse energy was 0.29 mJ after the prism compressor. Again, the prism compressor was manually optimized for maximum high-harmonic efficiency, resulting in highest ion count rates. The pressure in the capillary used for high-harmonic generation was set to 0.1 bar. Due to the setup geometry (see Fig. 6.1), the harmonic-beam traversed the molecular  $\text{SF}_6$  cloud produced by the nozzle and could be analyzed by the soft-x-ray spectrometer. Since the beam is only negligibly absorbed in the jet due to the low gas density, this setup is capable of recording the ionic mass spectra and the photon-energy spectra at the same time. This gives the opportunity to compare qualitative changes in the mass spectra—e.g. the changing branching ratios—directly to changes in the soft-x-ray



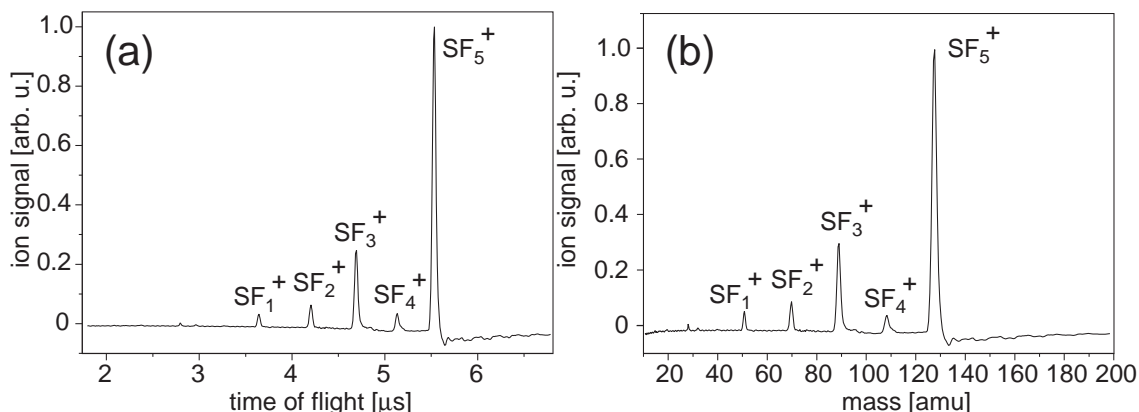


**Figure 6.2:** Time-of-flight (TOF) cation mass spectra of SF<sub>6</sub> after interaction with high-harmonic light from the capillary. (a): ion signal versus time of flight, (b): ion-signal versus fragment mass. The molecule undergoes fragmentation, where a number of F atoms are detached. The parent ion SF<sub>6</sub><sup>+</sup> at a mass of 146 amu is not observed. A characteristic distribution of peak heights for the fragments is recorded where SF<sub>5</sub><sup>+</sup> and SF<sub>3</sub><sup>+</sup> are the most abundant species. Other fragments are about equally abundant.

spectra of the light.

## 6.2 Optimal Control of Soft X-Ray Photofragmentation in SF<sub>6</sub>

The earliest experiments to demonstrate selectivity in chemical reactions by applying shaped light fields focused on photofragmentation [302, 334, 373]. This is because of the experimental simplicity to prepare the system and to detect the products. In gas-phase photochemistry, the detection of ionic fragments is particularly simple. A time-of-flight mass spectrometer as the one described above is ideally suited to serve as a detector for the product ions.

Sulfur hexafluoride (SF<sub>6</sub>) is an interesting, well-known system for the study of photofragmentation. When this molecule interacts with light in the soft x-ray spectral region (Ionization potential  $I_p = 15.32$  eV), different positively charged ionic fragments are produced. This can be explained by dissociative photoionization [374–377], which is the dominant fragmentation process in the soft x-ray range for many molecules. It means that electrons are transferred to high-lying excited states by the high-energy photons. The ionic potential energy curve versus internuclear distance can be repulsive for a particular bond, which leads to dissociation. One or more fluorine atoms can be detached. In Fig. 6.2 a typical time-of-flight mass-spectrum is shown for excitation with high-harmonic light. No aluminum filter was used for this recording to obtain a high count rate. This implies that both the fundamental and lower harmonic orders were present in the interaction region. However, it was verified that the spectrum vanished when the HHG-capillary was evacuated and therefore no harmonic radiation was produced. Thus, the fundamental laser alone could not be responsible for the fragmentation process. In order to rule out

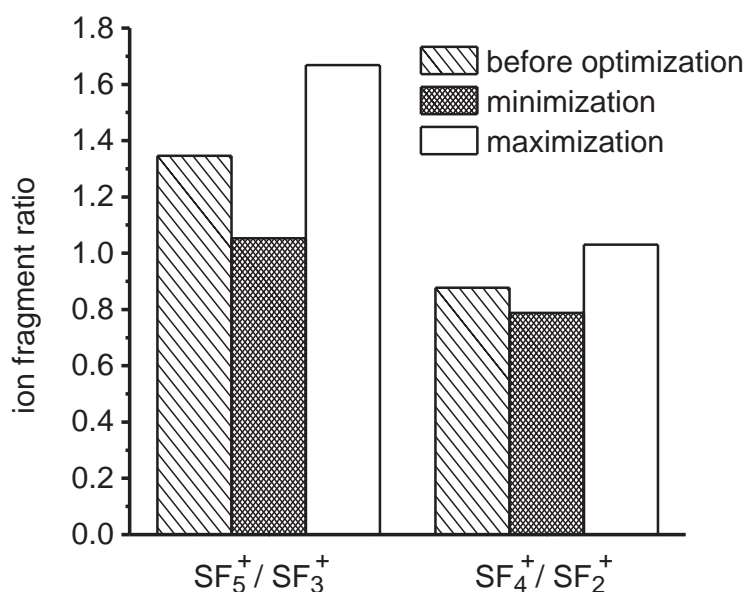


**Figure 6.3:** Control of the branching ratio of  $SF_6$  photofragmentation by shaped soft x-ray light. The two most dominant fragmentation channels  $SF_5^+$  and  $SF_3^+$  as well as the ratio of  $SF_4^+$  versus  $SF_2^+$  were optimized. Both minimization and maximization of product ratios as compared to an unmodulated reference harmonic emission were achieved.

modifications of the lower harmonic orders, the experiments on soft x-ray optimal control of photofragmentation described below were carried out with an aluminum filter between the capillary exit and the  $SF_6$  gas jet. The relative weights of the mass peaks were not much different in both cases (see below). The presented results concentrate on the two most dominant fragmentation channels,  $SF_5^+$  and  $SF_3^+$ . The relative yield of ions was used as fitness function

$$F = \frac{y(SF_5^+)}{y(SF_3^+)}, \quad (6.2)$$

where  $y(SF_n^+)$  is written for the ion yield of  $SF_n^+$  ions detected with the TOF mass spectrometer.

An aluminum filter of  $0.3 \mu\text{m}$  thickness was used between the HHG-capillary and the  $SF_6$  jet in order to ensure interaction of  $SF_6$  molecules only with the soft x-ray light transmitted through the filter (see Fig. 4.3). The branching ratio, i.e. the value of the fitness function  $F$  was recorded by the computer. The evolutionary algorithm was now programmed to perform a maximization and afterwards a minimization of the product ratio. The results of these experiments are summarized in Fig. 6.3. The relative product yields could be maximized and minimized by 25% with respect to the reference yield obtained for the unmodulated spectrum prior to optimization. The soft x-ray spectra recorded for the case of maximization and minimization of the ion yield, along with the spectrum before optimization are presented in Fig. 6.4. As the aluminum filter was used, the recorded spectra contain the full spectral intensity information about the light used in the experiment. The spectrum before optimization (unmodulated spectrum) is typical for phase-matched harmonic generation in a capillary. For the maximization case, a pronounced shift (of the

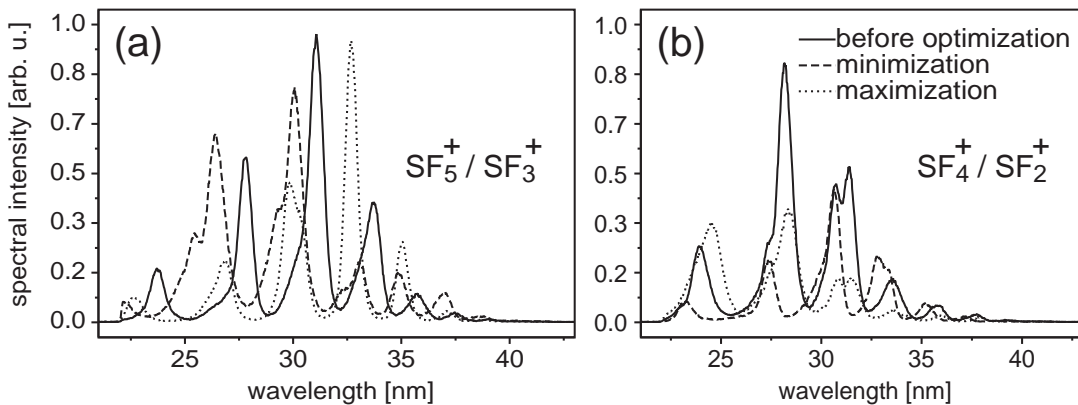


**Figure 6.4:** Soft x-ray spectra of shaped harmonic emission to optimize photofragmentation of SF<sub>6</sub>. Optimal harmonic spectra are shown that maximize (dotted lines) or minimize (dashed lines) the two branching ratios SF<sub>5</sub><sup>+</sup> versus SF<sub>3</sub><sup>+</sup> (a) and SF<sub>4</sub><sup>+</sup> versus SF<sub>2</sub><sup>+</sup> (b). The unmodulated reference harmonic spectrum before optimization is also given for comparison.

spectral mean) towards lower frequencies is visible. In contrast, the minimization leads to a spectral distribution which is shifted towards higher soft x-ray photon energies. Additionally, both optimized spectra exhibit the same amount of blueshift of the harmonic peaks with respect to the unmodulated spectrum. The substructure of some harmonic peaks is also modified in the results that correspond to different optimization goals.

The complete mass spectra acquired for the interaction with different soft x-ray spectra (the unmodulated and the optimized ones) are shown in Fig. 6.5 for the optimization results on SF<sub>5</sub><sup>+</sup> versus SF<sub>3</sub><sup>+</sup>. The spectra are normalized to the integral ion yield of the total SF<sub>3</sub><sup>+</sup> peak area, which makes it easier to observe the change in branching ratio by comparing the different yields of the SF<sub>5</sub><sup>+</sup> peak. The shifting of the peaks is indicative of a difference in fragmentation dynamics. In dissociative ionization, the fragments are produced at different kinetic energies, depending on the particular high-lying excited electronic states populated by the soft x-ray light. Not only the energy can be different but there can also be an angular dependence of ionization with respect to the polarization direction of the linearly polarized high-harmonic light. It is known from earlier studies [375, 376] that a pronounced anisotropy of the fragmentation process of SF<sub>6</sub> prevails for exciting photon energies in the range of interest here. Further investigations are necessary to fully understand the details of the photofragmentation process in the soft x-ray spectral region for the interaction with shaped coherent harmonic light.

The same experiment was repeated for the branching ratio between two different photofragment ions, namely SF<sub>4</sub><sup>+</sup> versus SF<sub>2</sub><sup>+</sup>. The fitness function used here was defined as

$$F = \frac{y(\text{SF}_4^+)}{y(\text{SF}_2^+)}. \quad (6.3)$$

The results of the maximization and minimization are also shown in Fig. 6.3. The branching ratio of SF<sub>4</sub><sup>+</sup> versus SF<sub>2</sub><sup>+</sup> ion yields turns out to be more rigid and cannot be changed to the same degree as the ratio of SF<sub>5</sub><sup>+</sup> versus SF<sub>3</sub><sup>+</sup> in this control experiment. Maximization resulted in an increase of the ratio by 15%, whereas minimization by 10% was achieved.

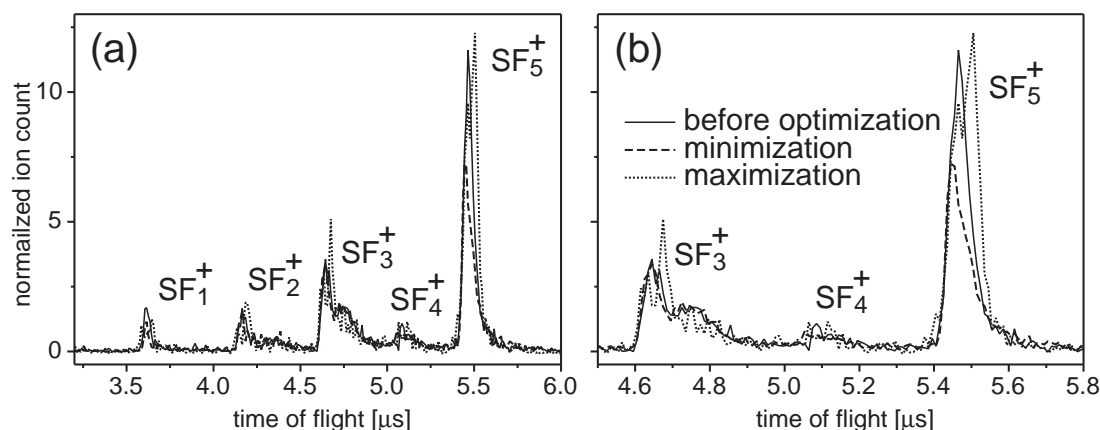


**Figure 6.5:** Time-of-flight mass spectra for the interaction of  $\text{SF}_6$  with tailored high-harmonic spectral emission for the case of maximization and minimization of the  $\text{SF}_5^+$  versus  $\text{SF}_3^+$  branching ratio. The two mass-spectra are normalized to the integral ion yield of the  $\text{SF}_3^+$  peak area to visualize the relative changes on the  $\text{SF}_5^+$  peak. The changing fine structure of the peaks indicates differences in the fragmentation dynamics. (b) is an enlarged view of (a) in the region of interest.

It is important to note that the short- and long-term stability of the shaped coherent soft-x-ray light from the high-harmonic generation process is high enough to allow the evolutionary algorithm to find an optimal set of control parameters even although the branching ratio can only be slightly changed. This demonstrates the technical versatility of the presented method to perform in principle any optimal control experiment in the soft-x-ray spectral region.

The soft-x-ray spectra for the closed-loop optimization experiment on the branching ratio of  $\text{SF}_4^+$  versus  $\text{SF}_2^+$  are shown in Fig. 6.4b. As in the case of  $\text{SF}_5^+/\text{SF}_3^+$  before, the optimal soft-x-ray spectra are different for maximization or minimization of the product branching ratios. Compared to the unmodulated spectrum (which is slightly different than in the previous optimization due to long term environmental drifts in the experiment), the spectrum corresponding to maximization of the branching ratio of  $\text{SF}_4^+/\text{SF}_2^+$  is now shifted to shorter wavelengths (regarding the spectral mean) while the spectrum recorded for the minimization case is centered at longer wavelengths of the soft x-ray light. The shift of the central frequencies of the harmonic peaks is less pronounced than in the previous optimization, however, both optimizations show a fine structure on the harmonic peaks. The following section on attosecond pulse shaping will discuss implications for the temporal shape of the soft-x-ray signals arising from these kinds of spectral modifications.

The origin of control of this photodissociation reaction cannot immediately be determined. The spectral amplitude changes significantly for the different control tasks. This could imply a soft-x-ray wavelength dependence of the branching ratio in photofragmentation of  $\text{SF}_6$ . In fact, it was shown in earlier studies [375]—although in a slightly different spectral regime (14–29 eV, i.e. 43–89 nm wavelength)—that the yields of photofragments of  $\text{SF}_6$  depend on the photon energy used. These studies were performed with spectrally incoherent soft x-rays from a synchrotron facility. It is unknown to date if and how the spectral coherence (short pulsed nature) of the soft x-rays in the optimal control experi-

ments above affect the process of dissociative ionization. The development of harmonic fine structure in the optimized spectra could be an indicator of these additional effects.

It is even possible to speculate about a new type of control mechanism based on coherently excited electronic states to control molecular dynamics. By using a sufficiently broad (multi-eV) coherent spectrum in the soft-x-ray region, one could imagine the creation of a coherent superposition of electronic excited states from a lower-lying bound state, resulting in a time-dependent electronic wavefunction that changes on a (possibly attosecond) ultrafast time scale. If the soft-x-ray intensity is high enough or a strong infrared/visible laser field is present, this dynamic wavefunction can be transferred to a dissociative molecular state depending on the instantaneous shape of the electronic wavefunction. The experiment shown here does not allow to verify or falsify this possibility. For a detailed analysis, a pump–probe experiment has to be set up and conducted in the future.

## 6.3 Conclusion

The first experiment on optimal control in the soft-x-ray spectral region was performed using the technique of high-harmonic spectral engineering. The photofragmentation reaction of the SF<sub>6</sub> molecule was controlled by the application of shaped coherent soft-x-ray light. In one case the branching ratio could only be slightly changed, which demonstrates sufficient stability of the shaped soft-x-ray light for this kind of optimal control experiments. The soft-x-ray spectral distribution changed significantly for different control objectives (maximization and minimization).

The spectral variability of the source allows for a variety of different coherent soft-x-ray spectral distributions. However, using more sophisticated laser systems (controlled carrier–envelope phase) or pulse-shaping devices (more degrees of freedom, phase-and-amplitude, spatiotemporal and/or polarization shaping) can be expected to lead to much larger spectral shaping capability.

The presented experiment is a first demonstration of the applicability of high-harmonic spectral engineering in optimal control of quantum dynamics with soft-x-ray light. In the future, quantum control will not only concentrate on the control of molecular motion and vibrational dynamics but will also include the control of electronic dynamics in tightly bound core levels of atoms and extended systems.



# Chapter 7

## Attosecond Pulse Shaping

A major breakthrough in the field of high-harmonic generation (HHG) was the experimental detection of pulses with duration of only a fraction of a femtosecond, opening the door to the attosecond realm (see also Section 2.3). These attosecond pulses had long been postulated to emerge in HHG [161, 165, 169] and schemes for experimental generation have been worked out, which were also proven to work in practice [163, 167, 171]. The best and easiest way to obtain single attosecond pulses in practice turned out to be the use of the shortest possible driver pulses [169, 171]. If long pulses are used in the generation process, in general not single attosecond pulses but trains of attosecond pulses are produced.

For future applications of these attosecond pulses to the study of electronic wavepacket dynamics on its natural time scale it would be highly desirable to have controllable attosecond laser pulse shapes. The same leap forward that occurred in quantum control of molecular dynamics by the application of adaptively shaped femtosecond light fields can be expected to take place when we are able to shape attosecond soft-x-ray pulses in an adaptive manner. It is then feasible to control the electronic dynamics.

Here it will be shown (Section 7.1) that the temporal shape of the attosecond pulses produced in the process of high-harmonic generation can be significantly altered by analyzing the controlled soft x-ray spectral shapes presented in Chapter 5. In addition, simulation results are used to illustrate the magnitude of achievable control (Section 7.2), proving that large temporal modifications on the attosecond time-scale are possible by very slight modifications in the driving laser pulse shape.

### 7.1 Experimental Indications

Any modification of the spectral shape of a signal, be it spectral amplitude or phase, results in a change in the time domain. This is a direct consequence from the dual nature of frequency and time expressed by the Fourier relation Eqs. (1.1) and (1.2). The better we are able to change the qualitative coherent spectral shape the more we are able to affect the temporal characteristics of the emerging pulses.

It is known that neighboring harmonics in a certain region of the spectrum have a fixed

phase relation [164], which is almost constant. This is the reason why attosecond pulses are produced at all, since the shortest pulses are generated when the spectral phase is flat. In our analysis, we made use of this fact and assumed a flat spectral phase just for the sake of clarity. The case of a non-flat spectral phase will also be addressed below.

The experimental results on high-harmonic plateau-hole production are analyzed in the following. The square root of the spectral intensity yields the electric field amplitude, which was Fourier transformed into the time domain, applying a flat spectral phase. The results are plotted in Fig. 7.1. The spectral intensity is shown on the left-hand side of the figure, while the temporal pulse shape is shown to the right. Clearly, the spectral modification alters the temporal response on the attosecond time scale. This can be understood by considering the large spectral bandwidth that is controlled, which is on the order of 10 eV in total. By virtue of the reciprocity of the dual variables time and frequency, large scale spectral modifications result in short- time-scale temporal changes.

In the time domain, reading the plots from top to bottom, a simple attosecond pulse train breaks up into sub-pulses. This beating behavior, which is most pronounced in the lowermost plot, can be understood from a simple consideration. The spectral emission in the cases where holes are present resembles a bimodal distribution. Thus, a beating pattern will arise in the time-domain created by the interference of two separate spectral emission centers.

This analysis shows clearly that even if we consider amplitude-only shaping of soft x-ray light—where the phase is assumed to be flat—the temporal structure of the attosecond pulses can be affected. If the phase is not flat, the beating pattern (envelope) will effectively shift with respect to the carrier wave, which does not affect the statement made about the possible shaping of the temporal attosecond features by generating amplitude-shaped soft-x-ray spectra.

One could argue that the spectral phase is changed along with the spectral amplitude in the spectra presented above. This is possible and would lead to even larger changes in the attosecond temporal structure of the soft x-ray pulses produced.

## 7.2 Numerical Modeling

A simulation was performed to gain more insight into the temporal changes of the attosecond pulses that are created in the optimization experiments. For that reason, selective enhancement and selective minimization of a single harmonic order with respect to the surrounding harmonic orders was reinvestigated. As described already in Section 5.4, shaped laser pulse electric fields were calculated by varying the spectral phase under a fixed spectral amplitude of the laser pulses. These pulses were the input of a computer simulation that calculated the high-harmonic radiative response of a single atom in a highly intense laser field. The simulation was based on a one-dimensional model of argon atoms, following the description in Chapter 3. The split-step-operator technique (Appendix C) was also used here to solve the time-dependent Schrödinger equation. The output was the nonlinear dipole acceleration, which was used to calculate the high-harmonic spectrum by Fourier transformation. Again, the same evolutionary algorithm as applied in the ex-



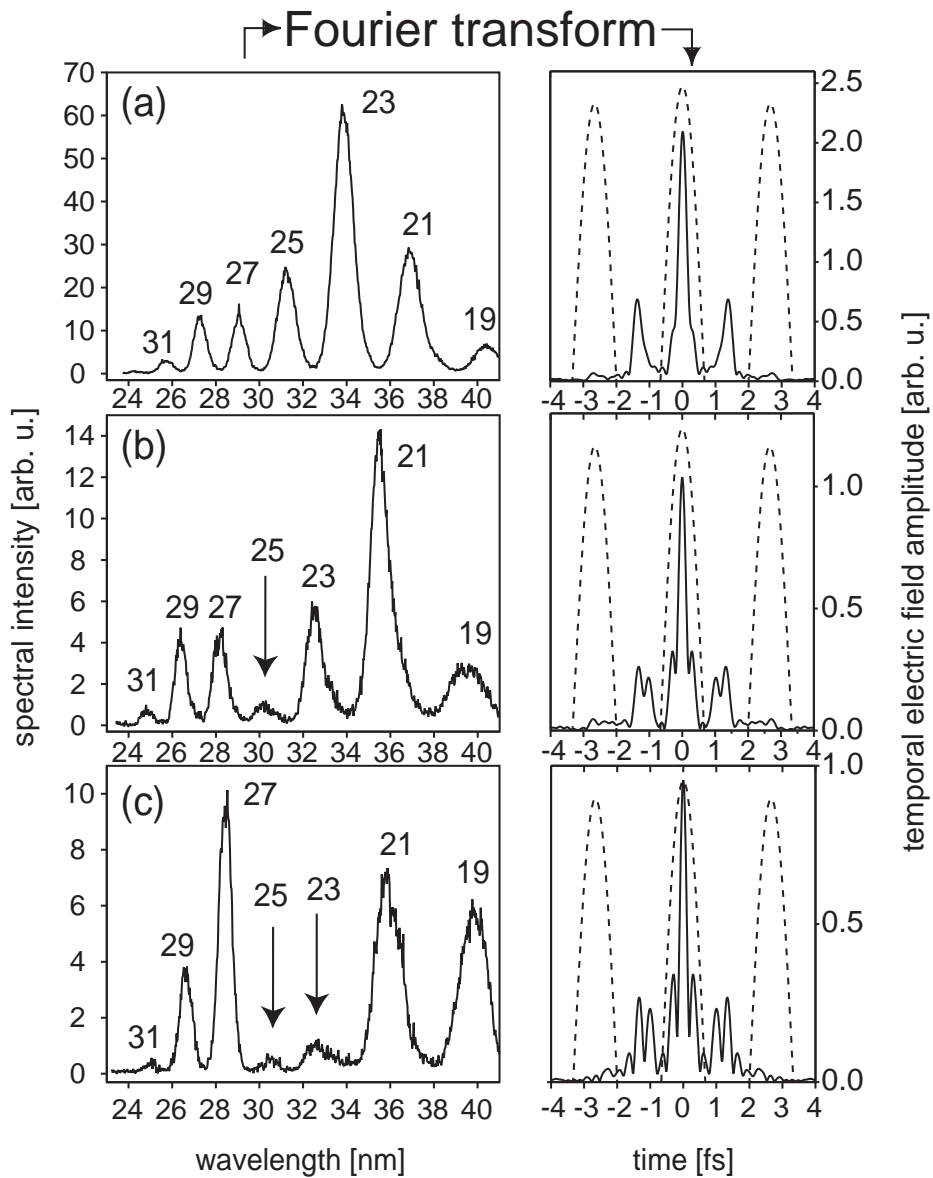


**Figure 7.1:** The experimentally obtained spectra shown in Fig. 5.17 along with the Fourier transforms of the spectral electric fields, assuming a constant phase. The corresponding trains of attosecond pulses are significantly modified. The spectra exhibiting holes can be interpreted as bimodal spectral distributions, giving rise to a beating pattern in the time domain. The contrast of the beating pattern is increased for two plateau holes.

periments was used. The spectrum was divided into part A, containing the 23rd harmonic order and part B containing the surrounding harmonic orders (H19, H21, H25, and H27). The fitness functions were defined as

$$F_1 = \frac{A^2}{B} \quad (7.1)$$

for selective maximization and

$$F_2 = \frac{B^2}{A} \quad (7.2)$$

for selective minimization of the 23rd harmonic yield relative to the total yield of the neighboring orders.  $A$  and  $B$  again denoted the integrated harmonic yield over parts A and B, respectively. In Fig. 7.2 the results of the simulation are shown. The left-hand side of the figure shows the high-harmonic spectrum. The temporal shape of the soft-x-ray radiative response is plotted right besides each of the spectra. For enhanced visibility, the presented spectra show the integrated harmonic signal over the region  $[2n\omega_f; 2(n+1)\omega_f]$  surrounding the harmonic order of interest  $2n+1\omega_f$ . The temporal response is calculated from the harmonics in the given interval, corresponding to the application of a band-pass filter transmitting the monitored frequency range, which is often employed in experiments [170, 171]. The electric fields of the shaped fundamental laser pulses are also depicted. Since the fundamental laser pulse duration is not in the few-cycle regime and the harmonics contained in the interval shown are not in the cut-off region of the harmonic spectrum, an attosecond pulse train is generated instead of a single attosecond pulse. Obviously, only a very slight change in the driving electric field is necessary to cause major modifications of the attosecond-time-scale temporal characteristics of the soft x-ray emission. This simulation provides additional confidence that we can use femtosecond pulse shaping in order to shape the temporal features of the attosecond pulses that are generated in the process of high-harmonic generation.

### 7.3 Conclusion

Both experimental and theoretical findings lead us to conclude that we are now able to change the attosecond temporal features of the subfemtosecond pulses or pulse trains produced in high-harmonic generation. Major spectral modifications like the ones observed in the experiment naturally cause significant changes also in the time domain. A simulation of the single-atom response reveals even more the ability to modify the attosecond pulse shape by using tailored femtosecond light fields to drive HHG.

These results have important consequences for the new field of ultrafast x-ray science. Adaptively shaped femtosecond laser pulses are nowadays used to control the dynamics of molecules or vibrational motion of atoms in general. The advent of attosecond pulse shaping provides an open road towards the control of electronic dynamics on its natural time scale. New insights about the inner workings of atoms and molecules are expected to be obtained by extending quantum control to core level electronic states.

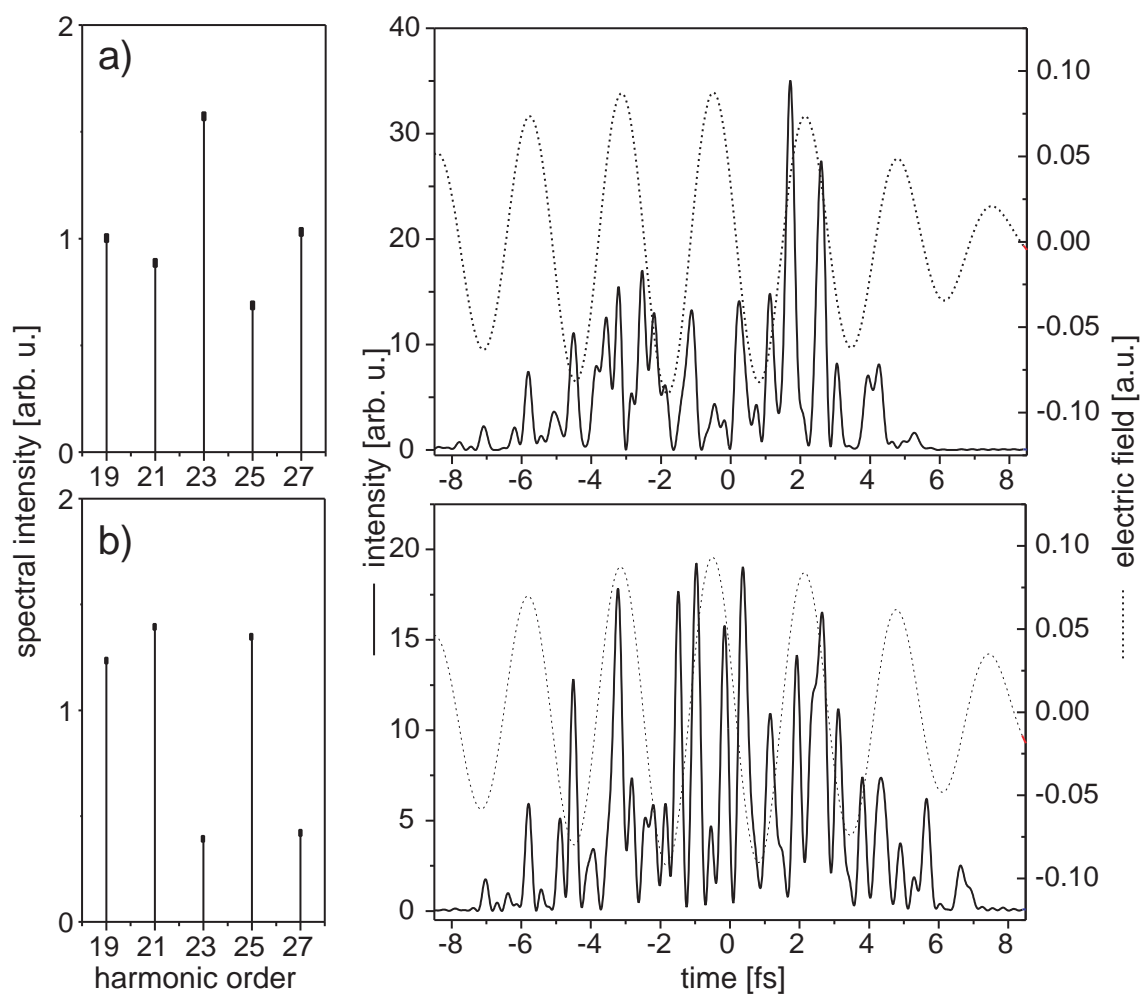


**Figure 7.2:** Simulation of the changes of the attosecond pulse's temporal shape by performing the same optimization operations as in the experiment. One harmonic order (the 23rd) is maximized and minimized with respect to its neighboring orders. A large difference in the attosecond soft x-ray radiative response is visible for only slight modifications in the electric field of the driving laser pulse.



# Part V

## Summary and Outlook

The availability of coherent soft x-rays through the nonlinear optical process of high-harmonic generation allows for the monitoring of the fastest events ever observed in the laboratory. The attosecond pulses produced are the fundamental tool for the time-resolved study of electron motion in atoms, molecules, clusters, liquids and solids in the future. However, in order to exploit the full potential of this new tool it is necessary to control the coherent soft x-ray spectra and to enhance the efficiency of conversion from laser light to the soft x-ray region in the harmonic-generation process.

This work developed a comprehensive approach towards the optimization of the harmonic generation process. As this process represents a fundamental example of *light-matter* interaction there are two ways of controlling it: Shaping the generating laser *light* and designing ideal states of *matter* for the conversion medium. Either of these approaches was closely examined. In addition, going far beyond simply enhancing the conversion process it could be shown that the qualitative spectral response of the process can be modified by shaping the driving laser pulse. This opens the door to a completely new field of research: Optimal quantum control in the attosecond soft x-ray region—the realm of electron dynamics. In the same way as it is possible to control molecular or lattice vibrational dynamics with adaptively shaped femtosecond laser pulses these days, it will now be feasible to perform real-time manipulation of tightly bound electron motion with adaptively shaped attosecond light fields. The last part of this work demonstrated the capability of the herein developed technique of coherent soft-x-ray spectral shaping, where a measured experimental feedback was used to perform a closed-loop optimization of the interaction of shaped soft x-ray light with a sulfur hexafluoride molecule to arrive at different control objectives.

For the optimization of the high-harmonic-generation process by engineering the conversion medium, both the gas phase and the liquid phase were explored both in experiment and theory. Molecular media were demonstrated to behave more efficiently than commonly used atomic targets when elliptically polarized driving laser pulses are applied. Theory predicted enhancement of harmonic generation for linearly polarized driving fields when the internuclear distance is increased. Reasons for this are identified as the increased overlap of the returning electron wavefunction due to molecular geometry and the control over the delocalization of the initial electronic state leading to less quantum-mechanical spreading of the electron wavepacket during continuum propagation. A new experimental scheme has been worked out, using the method of molecular wavepacket generation as a tool to enhance the harmonic conversion efficiency in ‘pump-drive’ schemes. The latter was then experimentally implemented in the study of high-harmonic generation from water microdroplets. A transition between the dominant laser-soft-x-ray conversion mechanisms could be observed, identifying plasma-breakdown as

the fundamental limit of high-density high-harmonic generation. Harmonics up to the 27th order were observed for optimally laser-prepared water droplets.

To control the high-harmonic generation process by the application of shaped laser light fields a laser-pulse shaper based on a deformable membrane mirror was built. Pulse-shape optimization resulted in increased high-harmonic generation efficiency — but more importantly the qualitative shape of the spectral response could be significantly modified for high-harmonic generation in waveguides. By adaptive optimization employing closed-loop strategies it was possible to selectively generate narrow (single harmonics) and broad bands of harmonic emission. Tunability could be demonstrated both for single harmonic orders and larger regions of several harmonics. Whereas any previous experiment reported to date always produced a plateau of equally intense harmonics, it has been possible to demonstrate “untypical” harmonic soft x-ray spectra exhibiting “switched-off” harmonic orders. The high degree of controllability paves the way for quantum control experiments in the soft x-ray spectral region.

It was also demonstrated that the degree of control over the soft x-ray shape depends on the high-harmonic generation geometry. Experiments performed in the gas jet could not change the relative emission strengths of neighboring harmonic orders. In the waveguide geometry, the relative harmonic yield of neighboring orders could be modified at high contrast ratios. A simulation based solely on the single atom response could not reproduce the experimentally observed contrast ratios, pointing to the importance of propagation (phase matching) effects as a reason for the high degree of controllability observed in capillaries, answering long-standing debates in the field.

A prototype experiment was presented demonstrating the versatility of the developed soft x-ray shaping technique for quantum control in this hitherto unexplored wavelength region. Shaped high-harmonic spectra were again used in an adaptive feedback loop experiment to control the gas-phase photodissociation reaction of  $\text{SF}_6$  molecules. A time-of-flight mass spectrometer was used for the detection of the ionic fragments. The branching ratios of particular fragmentation channels could be varied by optimally shaped soft x-ray light fields. Although in one case only slight changes of the branching ratio were possible, an optimal solution was found, proving the sufficient technical stability of this unique coherent soft-x-ray shaping method for future applications in optimal control.

Active shaping of the spectral amplitude in coherent spectral regions of  $\sim 10$  eV bandwidth was shown to directly correspond to shaping the temporal features of the emerging soft x-ray pulses on sub-femtosecond time scales. This can be understood by the dualism of frequency and time with the Fourier transformation acting as translator. A quantum-mechanical simulation was used to clarify the magnitude of temporal control over the shape of the attosecond pulses produced in the high-harmonic-generation process. In conjunction with the experimental results, the first attosecond time-scale pulse shaper could thus be demonstrated in this work.

The availability of femtosecond pulse shapers opened the field of adaptive femtosecond quantum control. The milestone idea of closed-loop feedback control to be implemented experimentally was expressed by Judson and Rabitz in their seminal work titled “Teaching lasers to control molecules”. This present work extends and turns around this statement. Two fundamentally new achievements can now be added, which are “Teaching

molecules to control laser light conversion” and “Teaching lasers to control coherent soft x-ray light”. The original idea thus enabled the leap from femtosecond control of molecular dynamics into the new field of attosecond control of electron motion to be explored in the future. The *closed*-loop approach could really *open* the door towards fascinating new perspectives in science.

Coming back to the introduction in order to close the loop, let us reconsider the analogy to the general chemical reaction. Photonic reaction control was presented by designing and engineering effective media (catalysts) and controlling the preparation of educt photons within the shaped laser pulses to selectively produce desired photonic target states in the soft x-ray spectral region. These newly synthesized target states in turn could be shown to be effective in the control of chemical reactions. The next step to be accomplished will be the control of sub-femtosecond time-scale electronic reactions with adaptively controlled coherent soft x-ray photon bunches. To that end a time-of-flight high-energy photoelectron spectrometer has recently been built, which will now allow to directly monitor electronic dynamics in atomic, molecular or solid state systems. Fundamentally new insights and applications of the nonlinear interaction of shaped attosecond soft x-ray pulses with matter can be expected from these experiments.





# **Part VI**

## **Appendix**



# Appendix A

## Adaptive Femtosecond Polarization Control

The process of high-harmonic generation depends on the polarization state of the driving laser light, as was discussed in Chapter 3. Elliptically polarized driving fields typically result in a reduction of harmonic conversion efficiency as the returning electron misses its parent ion. Therefore, controlling the polarization state of the driving laser light can be used to synthesize single attosecond pulses (Section 2.3): If the driving laser field is linearly polarized only for a short time within the laser pulse, high-harmonic generation is temporally confined to this short time and will not occur at earlier or later times in the laser pulse. If more complex conversion media are considered, the ability to temporally control the polarization state of the driving laser can also be expected to lead to additional attosecond pulse shaping capability. In order to demonstrate the versatility of the recently developed technique of femtosecond polarization shaping (Section 1.1.4), an adaptive control experiment in a small molecule ( $K_2$ ) was performed [43]. The goal was to enhance the first step of the high-harmonic generation process: ionization.

Apart from its relevance to high-harmonic generation, controlling molecular dynamics is at the heart of the field of quantum control. The time scale of molecular vibration is in the femtosecond regime, determined by the bond strength and the masses of the binding nuclei. This enables us to apply shaped femtosecond light fields in order to steer molecular wavepacket motion along specific user-defined pathways on the nuclear potential energy surfaces of the molecule (Section 5.1). The basic microscopic origin of this control is the nonlinear interaction of the shaped visible to near-infrared laser pulses with the electronic wavefunction in the system. Electronic excitation thus gives rise to the creation and the control of the molecular wavepacket. The electronic wavefunction  $\Psi(x, y, z)$  is a three-dimensional object. It is immediately clear that in order to fully control electronic transitions and thus molecular dynamics on a femtosecond time scale, a linearly polarized shaped electric field is not sufficient. Only a subgroup of electronic transitions can be addressed in this case, limiting the realm of attainable control. When the polarization state of the controlling light field can be varied on a femtosecond time scale, a much more comprehensive access to the variety of electronic transitions is possible, significantly enhancing the ability to control the dynamical properties of a molecule or any other quantum system.

To demonstrate the fundamental advantage of femtosecond polarization shaping, a closed-loop experiment on the well-known prototype system  $K_2$  is described in this part of the appendix. The ionization pathway of the  $K_2$  molecule proceeds via two intermediate potential energy curves, which are coupled by transition dipole matrix elements that are parallel and perpendicular to the molecular axis. A linearly polarized controlling laser field can thus only ionize molecules that are not aligned close to parallel or perpendicular to the laser field polarization direction, such that projections onto the transition dipole moment vectors are nonzero. A varying polarization state of the laser field can access the complete ensemble of molecules in the interaction region, which was expected to result in an enhancement of the ionization signal. Indeed, in the experiment described here, this enhancement becomes clearly evident by comparing the result of two closed-loop adaptive control experiments. In one of them, the laser polarization state was restricted to linear, in the other one, the polarization state of the laser light was included in the optimization. The optimal polarization-shaped laser pulse created a higher amount of  $K_2^+$  ions than the optimal linearly shaped laser pulse. This demonstration shows that even to control simple homonuclear diatomic molecules the time-dependent polarization state of the laser light is an important control parameter. In larger molecules—in particular in the presence of alignment—the time-dependent polarization of the controlling laser field can be considered to be an even more efficient control agent.

## Quantum Control by Ultrafast Polarization Shaping

T. Brixner, G. Krampert, T. Pfeifer, R. Selle, and G. Gerber\*

*Physikalisches Institut, Universität Würzburg, Am Hubland, 97074 Würzburg, Germany*

M. Wollenhaupt, O. Graefe, C. Horn, D. Liese, and T. Baumert

*Experimentalphysik III, Universität Kassel, Heinrich-Plett-Strasse 40, 34132 Kassel, Germany*

(Received 12 January 2004; published 20 May 2004)

We demonstrate that the use of time-dependent light polarization opens a new level of control over quantum systems. With potassium dimer molecules from a supersonic molecular beam, we show that a polarization-shaped laser pulse increases the ionization yield beyond that obtained with an optimally shaped linearly polarized laser pulse. This is due to the different multiphoton ionization pathways in  $K_2$  involving dipole transitions which favor different polarization directions of the exciting laser field. This experiment is a qualitative extension of quantum control mechanisms which opens up new directions giving access to the three-dimensional temporal response of molecular systems.

DOI: 10.1103/PhysRevLett.92.208301

PACS numbers: 82.50.Nd, 42.25.Ja, 42.79.Kr, 82.53.-k

Coherent control is a powerful method which allows one to “steer” quantum-mechanical processes toward a desired outcome by applying optimal light fields [1]. The main experimental tool for achieving this goal has been spectral phase shaping of femtosecond laser pulses [2]. Numerous implementations were reported in recent years, among others the control of chemical reactions [3–5], molecular population transfer [6–9], atomic multiphoton absorption [10], Rydberg wave packets [11], high-harmonic generation [12], crystal lattice vibrations [13], or single-pulse Raman spectroscopy [14]. In all of these experiments, the spectral-temporal intensity and phase characteristics of laser fields are manipulated and exploited in a sophisticated manner, in many cases employing automated learning loops based on experimental feedback [15–17]. “Conventional” pulse shaping [2], however, accesses only the scalar properties of ultrashort laser pulses, while the electric field is a vectorial quantity. Since quantum systems and their wave functions are three-dimensional objects, the use of polarization as an active agent could tremendously increase the degree of attainable control. The same is true for any type of nonlinear optical spectroscopy, where to date the polarization states of the employed light fields (continuous wave or pulsed) have always been constant in time.

We have developed femtosecond polarization pulse shaping techniques [18–20] by which the polarization state of light (i.e., degree of polarization ellipticity and orientation of elliptical principal axes) as well as the temporal intensity and the momentary oscillation frequency can be varied as functions of time within a single femtosecond laser pulse. Time-dependent polarization states have been suggested, for example, for the generation [21,22] and characterization [23] of attosecond light pulses, optical control of lattice vibrations [24], and the selective production of enantiomers [25,26]. Simple time-dependent polarization profiles (without using pulse shapers) had already been exploited in several experi-

ments on optical [27,28], atomic [29], and molecular systems [30]. In an optical demonstration experiment, we have recently implemented adaptive shaping of complex polarization profiles within a learning loop [20], and Oron *et al.* have used spectral modulation of phase and polarization direction in coherent anti-Stokes Raman spectroscopy [31].

However, the prospect for manipulating light-matter interactions in three dimensions using complex polarization-modulated laser pulses goes beyond these initial suggestions or demonstrations. While this interaction is governed by the scalar product  $\vec{\mu} \cdot \vec{E}(t)$ , in most experimental and theoretical studies on quantum control or nonlinear spectroscopy the vectorial character of  $\vec{E}(t)$  is ignored completely and only  $\mu E(t)$  is considered. However, if the momentary polarization of the applied electromagnetic field is varied,  $\vec{\mu} \cdot \vec{E}(t)$  can be optimized throughout the complete temporal evolution of a quantum system. This opens many experimental perspectives, e.g., controlling which dipole transitions are allowed at any particular time during a wave packet evolution. Thus, one can address and exploit the spatiotemporal properties of quantum wave functions.

In the work reported here, we carry out molecular quantum control making explicit use of polarization variation on an ultrashort time scale, i.e., the duration of the bandwidth-limited laser pulse [32]. In order to illustrate the novel features of such experiments, we maximize photoionization in a small prototype system, the potassium dimer  $K_2$ . Within the bandwidth of our laser system, the dominant transition pathway that contributes to the  $K_2^+$  yield [33] populates the  $2^1\Pi_g$  state as an intermediate before the final ionization step [Fig. 1(a)]. The  $2^1\Pi_g$  state can be reached from the  $X^1\Sigma_g^+$  ground state by a two-photon process with intermediate wave packet propagation in the  $A^1\Sigma_u^+$  state. This pathway is strongly polarization dependent because according to selection rules the two involved electronic transitions,

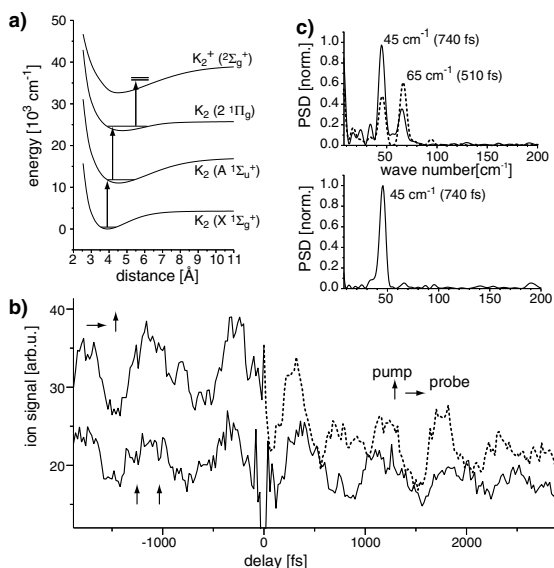


FIG. 1. (a) Calculated potential energy curves [33] of the potassium dimer system. Only those curves are shown which are relevant at the central excitation wavelength of  $\lambda = 785 \text{ nm}$  used in this experiment. (b) Section of pump-probe transients with mutually parallel (solid line) and crossed (dashed line) linear polarizations around delay time zero. (c) Fast-Fourier-transform (FFT) analysis of pump-probe transients with parallel (lower graph) and crossed (upper graph) mutual polarizations. The numbers in brackets indicate the vibrational period of the associated wave packet motion. The FFTs have been performed over time periods from  $-4 \text{ ps}$  to  $0 \text{ ps}$  for crossed polarizations (negative delays, solid line),  $0$  to  $+4 \text{ ps}$  for crossed polarizations (positive delays, dotted line), and  $0$  to  $+3 \text{ ps}$  (parallel polarizations, solid line, identical at negative delay times).

$A^1\Sigma_u^+ \leftarrow X^1\Sigma_g^+$  and  $2^1\Pi_g \leftarrow A^1\Sigma_u^+$ , require electromagnetic fields with polarizations parallel and perpendicular to the molecular axis, respectively. This means that for maximum population of the  $2^1\Pi_g$  state one needs a laser pulse sequence in which the correct direction of the electric field vector is provided at the appropriate Franck-Condon transition windows reached during vibrational wave packet motion. The enhancement factor for polarization-shaped laser pulses can be estimated in a simple model. Consider an isotropic ensemble of quantum systems in which two subsequent transitions require two electromagnetic fields with mutually perpendicular polarizations. If one employs two laser pulses with the same linear polarization, only the projections of the polarization vector onto the involved dipole moments of the randomly oriented systems contribute to the transition rates. The total transition rate is then given by averaging over the isotropic ensemble. For comparison, then, if the polarizations of the two laser pulses are perpendicular to each other the averaging procedure gives a yield that is enhanced by a factor of 2. Further advantages of polarization shaping arise if the quantum systems are aligned or

oriented with respect to the incoming light fields [34,35]. Optimal control of the multiphoton ionization process therefore requires both adjustment of the temporal intensity profile (to maximize the transition probability in the Franck-Condon regions) as well as variation of the polarization direction to fulfill the appropriate selection-rule requirements. Such a scheme cannot be achieved with shaped laser pulses of only one polarization component.

In order to illustrate these issues further, we performed a conventional pump-probe experiment in partially aligned  $K_2$  molecules where the alignment is due to suitable molecular-beam conditions [36,37]. The experimental setup consists of a supersonic molecular-beam apparatus with a linear time-of-flight (TOF) mass spectrometer. Both pump and probe laser pulses have an energy of  $150 \text{ nJ}$  and are focused with a  $500 \text{ mm}$  lens onto a molecular beam of potassium dimers, thus avoiding strong field effects.

First, we used equally intense pump and probe laser pulses both polarized parallel to the TOF axis. The amount of  $K_2^+$  as a function of pump-probe delay [Fig. 1(b), solid line] is symmetric and shows a minimum with respect to time zero. On the other hand, if the probe-pulse polarization is perpendicular to that of the pump pulse, the signal is asymmetric [Fig. 1(b), dashed line], and for negative time delays the  $K_2^+$  production is significantly enhanced. This result proves the polarization dependence of the  $K_2^+$  ionization pathways. It indicates that a certain final quantum state (in our case the  $K_2^+$  ion) can be more efficiently reached by a time-dependent polarization of the controlling laser field.

Fourier analysis of the pump-probe transients reveals that for mutually parallel pump and probe polarizations [Fig. 1(c), bottom graph] only the dynamics in the  $2^1\Pi_g$  state with a vibrational period of  $740 \text{ fs}$  [33] (corresponding to  $45 \text{ cm}^{-1}$ ) is visible. For mutually perpendicular pump and probe polarizations [Fig. 1(c), upper graph], an additional Fourier peak is found at  $65 \text{ cm}^{-1}$  (corresponding to  $510 \text{ fs}$ ), which can be attributed to vibrational dynamics in the  $A^1\Sigma_u^+$  state. This result proves that a time-dependent polarization of the controlling laser field gives access to the observation of additional dynamics on different electronic states. Note that all other experimental parameters in the two cases of Fig. 1 were identical (pulse intensities, etc.), so that the differences are entirely due to light-polarization properties. This type of polarization sensitivity can then be exploited even in much more generality in connection with femtosecond laser pulse shaping, providing a qualitatively novel mechanism for the control of quantum systems. In the following, we use flexible and automated polarization and phase shaping of femtosecond laser pulses in combination with an evolutionary algorithm to control molecular dynamics and, in this case, maximize ionization of  $K_2$ .

For this purpose, the experimental setup is complemented by a polarization pulse shaper and a computer with the optimization algorithm (Fig. 2). For polarization

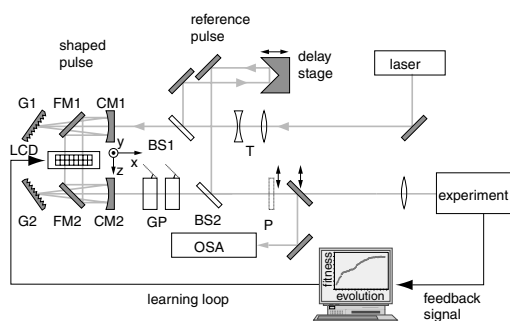


FIG. 2. Experimental setup. The pulse shaper that creates time-dependent polarization profiles consists of a telescope (T), cylindrical mirrors (CM), optical gratings (G), folding mirrors (FM), a two-layer liquid-crystal display (LCD), and a stack of glass plates at Brewster's angle (GP) to provide equal intensity and independently shaped polarization components at the output. Pulse characterization is carried out by experimentally calibrated Jones-matrix analysis [19] and dual-channel spectral interferometry with the help of a characterized and appropriately delayed reference pulse. For this purpose, shaped pulse and reference pulse are recombined collinearly along the beam path towards the experiment by a beam splitter (BS2), and the spectral interferences are recorded by an optical spectrum analyzer (OSA). A polarizer (P) selects the polarization component that is analyzed. During the actual experiment, the polarizer is removed and the reference pulse is blocked. Shaped pulses then interact with a seeded molecular beam of  $K_2$ . Ion yields are measured in a TOF mass spectrometer and used as feedback signal in an evolutionary learning algorithm.

shaping [1,18–20], the linearly polarized input pulses (30 fs, 785 nm) are dispersed onto a two-layer liquid-crystal display (LCD) within a  $4f$ -configuration zero-dispersion compressor. By applying specific voltages to the  $2 \times 128$  independent LCD pixels contained in the two layers, spectral phase modulation can be imposed independently onto two orthogonal polarization directions. The interference of the resulting elliptically polarized spectral components leads to complex evolutions of the polarization state in the time domain. If the same phase function is applied to both LCD layers, the linear input polarization is maintained and conventional phase-only pulse shaping can be realized. In the actual experiment, shaped 300 nJ laser pulses are used instead of the unshaped pump and probe laser pulses.

We performed two types of adaptive control experiments to maximize the  $K_2^+$  yield: spectral polarization- and-phase laser pulse shaping as well as phase-only shaping. In both cases, the same number of free parameters is optimized and the two strategies are run in a parallel implementation. This ensures identical experimental conditions allowing us to compare the results directly. The evolution of the  $K_2^+$  signal as a function of generation number within the evolutionary algorithm is shown in Fig. 3. The increase for phase-only pulse shaping (solid circles) is due to the adaptation of the laser pulse structure

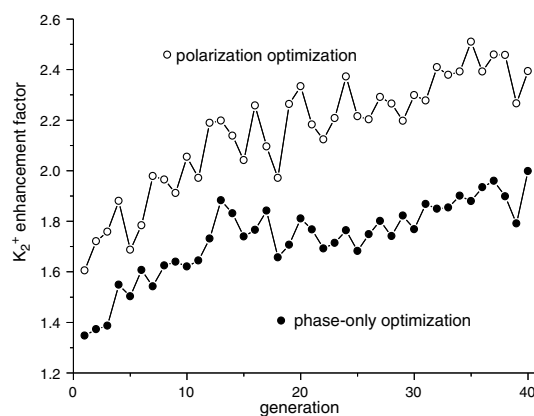


FIG. 3. Evolution curves show the  $K_2^+$  ion yield relative to that obtained with an unshaped laser pulse. The best individual of each generation for the polarization optimization (open circles) and phase-only optimization (solid circles) is shown.

to the vibrational dynamics of the potassium dimer, providing high laser intensities when the wave packet is in a suitable Franck-Condon region. This general type of mechanism is what had been exploited and discussed in the theoretical and experimental literature on quantum control to date.

However, when the additional mechanism of light-polarization control is used (open circles), one can go beyond the limitations set by linearly polarized fields, and achieve significantly higher product yields. This demonstrates not just a quantitative improvement but rather a qualitative extension of quantum control mechanisms, because it goes beyond one-dimensional addressing of transition dipoles and rather makes use of their directional properties by shaping the polarization state of the controlling laser pulse.

Figure 4 shows a representation of the best laser pulse shape reached in the final generation of the polarization optimization. The momentary frequency and the polarization state of the optimized pulse changes substantially in a complex fashion as a function of time. Some reasons for this complexity are briefly discussed now. First, the detection step in this experiment (i.e., the ionization) needs to be considered in more detail. Observation of  $2^1\Pi_g$  state dynamics in our pump-probe measurement (Fig. 1) proves that ionization from the  $2^1\Pi_g$  is dependent on the internuclear distance and occurs predominantly at the outer turning point [33]. Ionization, for example, can occur via doubly excited, autoionizing states [38]. Excitations of these doubly excited states via the outer turning point in the  $2^1\Pi_g$  state as well as transitions involving the  $4^1\Sigma_g^+$  state have not been considered. Another reason for the complicated pulse structure is the broad spectrum of the ultrashort laser pulse. The vibrational dynamics of the potassium dimer are known to depend strongly on the center frequency of the excitation laser pulse [33]. In our case, this means that the optimized polarization needs to

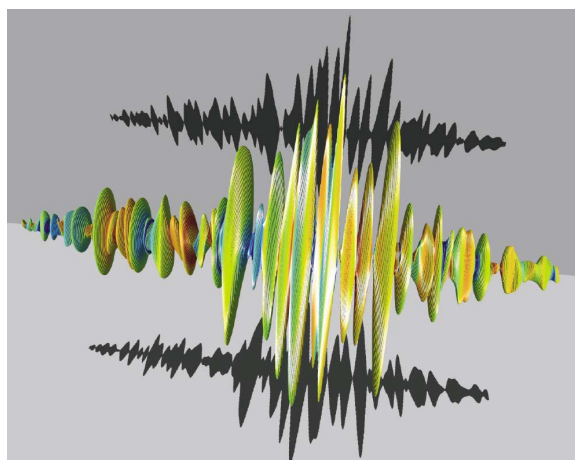


FIG. 4 (color online). Quasi-three-dimensional representation of the optimal polarization-shaped laser pulse. Time evolves from  $-1.5$  ps (left) to  $+1.5$  ps (right), and electric field amplitudes are indicated by the sizes of the corresponding ellipses. The momentary frequencies are indicated by colors or gray shading, and the shadows represent the amplitude envelopes of the two orthogonal components.

be provided for a wide distribution of frequencies and timings. While all these factors complicate the analysis and interpretation efforts of the optimal pulse shape, the important point is that despite the complexity an optimized electric field with time-varying polarization indeed has been exploited by the evolutionary learning algorithm as a novel control agent.

In conclusion, we have demonstrated that time-dependent shaping of femtosecond light polarization can give access to a further level of control of quantum systems. Comparative optimizations of  $K_2^+$  yield show that polarization laser pulse shaping is superior to phase-only shaping, because the vectorial electric field can adapt to the time evolution of the polarization-dependent transition dipole moments. We have, hence, exploited the vectorial properties of light-matter interaction to achieve quantum control in a molecular model system. This opens the door to a number of new experimental schemes exploiting the full vectorial temporal response of systems, allowing one to address stereochemical aspects in quantum control such as chiral selectivity. The optical control of lattice vibrations [13] and the generation of attosecond light pulses [21,22] are further examples of numerous new perspectives.

The Würzburg group acknowledges financial support from the European Coherent Control Network (COCOMO) (HPRN-CT-1999-0129) and the German-Israeli Cooperation in Ultrafast Laser Technologies (GILCULT) (FKZ-13N7966). The Kassel group acknowledges financial support from the NRC/Helmholtz program and the Deutsche Forschungsgemeinschaft.

\*Electronic address: gerber@physik.uni-wuerzburg.de

- [1] T. Brixner and G. Gerber, *Chem. Phys. Chem.* **4**, 418 (2003).
- [2] A. M. Weiner, *Rev. Sci. Instrum.* **71**, 1929 (2000).
- [3] A. Assion *et al.*, *Science* **282**, 919 (1998).
- [4] R. J. Levis, G. M. Menkir, and H. Rabitz, *Science* **292**, 709 (2001).
- [5] C. Daniel *et al.*, *Science* **299**, 536 (2003).
- [6] C. J. Bardeen *et al.*, *Chem. Phys. Lett.* **280**, 151 (1997).
- [7] T. C. Weinacht, J. L. White, and P. H. Bucksbaum, *J. Phys. Chem. A* **103**, 10166 (1999).
- [8] T. Brixner, N. H. Damrauer, P. Niklaus, and G. Gerber, *Nature (London)* **414**, 57 (2001).
- [9] J. L. Herek *et al.*, *Nature (London)* **417**, 533 (2002).
- [10] D. Meshulach and Y. Silberberg, *Nature (London)* **396**, 239 (1998).
- [11] T. C. Weinacht, J. Ahn, and P. H. Bucksbaum, *Nature (London)* **397**, 233 (1999).
- [12] R. Bartels *et al.*, *Nature (London)* **406**, 164 (2000).
- [13] T. Feurer, J. C. Vaughan, and K. A. Nelson, *Science* **299**, 374 (2003).
- [14] N. Dudovich, D. Oron, and Y. Silberberg, *Nature (London)* **418**, 512 (2002).
- [15] R. S. Judson and H. Rabitz, *Phys. Rev. Lett.* **68**, 1500 (1992).
- [16] D. Yelin, D. Meshulach, and Y. Silberberg, *Opt. Lett.* **22**, 1793 (1997).
- [17] T. Baumert *et al.*, *Appl. Phys. B* **65**, 779 (1997).
- [18] T. Brixner and G. Gerber, *Opt. Lett.* **26**, 557 (2001).
- [19] T. Brixner, G. Krampert, P. Niklaus, and G. Gerber, *Appl. Phys. B* **74**, S133 (2002).
- [20] T. Brixner *et al.*, *J. Opt. Soc. Am. B* **20**, 878 (2003).
- [21] P. B. Corkum, N. H. Burnett, and M. Y. Ivanov, *Opt. Lett.* **19**, 1870 (1994).
- [22] M. Y. Ivanov, P. B. Corkum, T. Zuo, and A. D. Bandrauk, *Phys. Rev. Lett.* **74**, 2933 (1995).
- [23] E. Constant, V. D. Taranukhin, A. Stolow, and P. B. Corkum, *Phys. Rev. A* **56**, 3870 (1997).
- [24] M. M. Wefers, H. Kawashima, and K. A. Nelson, *J. Chem. Phys.* **108**, 10248 (1998).
- [25] Y. Fujimura *et al.*, *Chem. Phys. Lett.* **306**, 1 (1999).
- [26] M. Shapiro, E. Frishman, and P. Brumer, *Phys. Rev. Lett.* **84**, 1669 (2000).
- [27] W. J. Walecki, D. N. Fittinghoff, A. L. Smirl, and R. Trebino, *Opt. Lett.* **22**, 81 (1997).
- [28] C. Altucci *et al.*, *Phys. Rev. A* **58**, 3934 (1998).
- [29] M. Kakehata *et al.*, *Appl. Phys. B* **70**, S207 (2000).
- [30] D. N. Villeneuve *et al.*, *Phys. Rev. Lett.* **85**, 542 (2000).
- [31] D. Oron, N. Dudovich, and Y. Silberberg, *Phys. Rev. Lett.* **90**, 213902 (2003).
- [32] T. Brixner, *Appl. Phys. B* **76**, 531 (2003).
- [33] C. Nicole *et al.*, *J. Chem. Phys.* **111**, 7857 (1999).
- [34] H. Stapelfeldt and T. Seideman, *Rev. Mod. Phys.* **75**, 543 (2003).
- [35] A. Ulman, *Chem. Rev.* **96**, 1533 (1996).
- [36] U. Hefter *et al.*, *J. Chem. Phys.* **85**, 286 (1986).
- [37] H. Hulsman and J. Korving, *J. Chem. Phys.* **95**, 5719 (1991).
- [38] T. Baumert, M. GROSSER, R. Thalweiser, and G. Gerber, *Phys. Rev. Lett.* **67**, 3753 (1991).



# Appendix B

## SPIDER Details

As explained above, the SPIDER technique (spectral interferometry for direct electric-field reconstruction) is able to reconstruct the phase of some unknown laser pulse. Since the spectrum of the laser pulse is readily available in practice, the technique allows to measure the full information about the laser pulse shape (except for the carrier-envelope phase). SPIDER employs the method of spectral interferometry, which is often used in the laboratory to measure the difference in spectral phase of a laser pulse with respect to a known reference pulse. Spectral interferometry alone is not capable of retrieving phases of unknown pulses. The idea introduced by Iaconis and Walmsley was that the laser pulse itself can be made to be its own reference in such a way that the spectral phase can be extracted. This is sometimes described as ‘self-referencing’. In contrast to spectral interferometry it is based on a nonlinear optical process.

This appendix section is devoted to a more detailed description of the SPIDER technique by first explaining the principles of spectral interferometry in Section B.1. Section B.2 describes the self-referencing approach. The final Section B.3 deals with possible ways how to extract the spectral phase of an unknown pulse from the SPIDER signal (Fig. 1.13).

### B.1 Spectral Interferometry

Spectral interferometry is a pulse characterization technique which allows the retrieval of the spectral phase of a pulse if a fully characterized reference pulse is available. A useful property of the spectral-interferometry technique is that it does not rely on a nonlinear process. This makes it particularly useful for the analysis of very weak light signals.

The setup is very simple: the reference pulse  $\tilde{E}_0^+(\omega) = \tilde{A}_0(\omega)e^{i\tilde{\Phi}_0(\omega)}$  and the pulse to be measured  $\tilde{E}^+(\omega) = \tilde{A}(\omega)e^{i\tilde{\Phi}(\omega)}$  are combined on a beamsplitter. For simplicity in our discussion, let us assume the reference pulse to arrive earlier than the unknown pulse. The positive delay of the latter be  $\tau$ . We analyze the combined electric field of the two pulses

with a spectrometer

$$\begin{aligned}
\tilde{I}_{\text{SI}}(\omega) &= |\tilde{E}_0^+(\omega) + \tilde{E}^+(\omega)e^{-i\omega\tau}|^2 \\
&= \tilde{I}_0(\omega) + \tilde{I}(\omega) + \tilde{E}_0^{+*}(\omega)\tilde{E}^+(\omega)e^{-i\omega\tau} + \tilde{E}_0^+(\omega)\tilde{E}^{+*}(\omega)e^{i\omega\tau} \\
&= \tilde{I}_0(\omega) + \tilde{I}(\omega) + 2\sqrt{\tilde{I}_0(\omega)\tilde{I}(\omega)}\cos(\tilde{\Phi}(\omega) - \tilde{\Phi}_0(\omega) - \omega\tau) \quad (\text{B.1})
\end{aligned}$$

The asterisk denotes complex conjugation. If the two pulse spectra overlap (we always have to provide frequencies in the same range as those in the unknown pulse), we obtain a spectrum which is spectrally modulated with an average fringe spacing of  $2\pi/\tau$ . The difference in spectral phase of the two pulses is contained in the fringe pattern in its deviations from a perfectly periodic modulation. It is also obvious at this point that in order for spectral interferometry to work properly, a very precise spectrometer wavelength calibration is required [378]. If this is not ensured, the correct modulation of the spectral intensity is distorted by the imperfect calibration, leading to wrong results.

For further analysis of the spectral interferometry signal, we now define the function  $S(\omega)$  as the difference of the spectrometer signal of the combined fields minus the spectra of each of the two signals alone (by blocking the other)

$$\tilde{S}(\omega) = \tilde{I}_{\text{SI}}(\omega) - \tilde{I}(\omega) - \tilde{I}_0(\omega) \quad (\text{B.2})$$

$$= 2\sqrt{\tilde{I}_0(\omega)\tilde{I}(\omega)}\cos(\tilde{\Phi}(\omega) - \tilde{\Phi}_0(\omega) - \omega\tau). \quad (\text{B.3})$$

All that remains to be done is to extract the phase difference from this measurable signal. Since the spectral intensities of each pulse are known, we could simply perform an inversion of the cosine function to obtain the argument. Due to experimental noise, this way to determine the phase difference leads to a large error. A simple argument is that values larger than 1 would appear in the argument of an arccos function when noise is present, leading to undefined results. Another more reliable way to extract the argument of the cosine is provided by the Fourier transform. By transforming Eq. (B.3) into the time domain, we obtain

$$\begin{aligned}
S(t) &= \frac{1}{\sqrt{2\pi}} \int_{-\infty}^{\infty} \tilde{S}(\omega)e^{i\omega t} d\omega \\
&= \frac{1}{\sqrt{2\pi}} \int_{-\infty}^{\infty} \tilde{E}_0^{+*}(\omega)\tilde{E}^+(\omega)e^{i\omega(t-\tau)} d\omega \\
&\quad + \left( \frac{1}{\sqrt{2\pi}} \int_{-\infty}^{\infty} \tilde{E}_0^{+*}(\omega)\tilde{E}^+(\omega)e^{i\omega(-t-\tau)} d\omega \right)^* \\
&= \bar{S}(t - \tau) + \bar{S}^*(-t - \tau). \quad (\text{B.4})
\end{aligned}$$

$\bar{S}(t - \tau)$  does not overlap with  $\bar{S}(-t - \tau)$  if the temporal pulses corresponding to  $E_0(\omega)$  and  $E(\omega)$  do not overlap in the time domain. We can therefore filter out one contribution  $\bar{S}(t - \tau)$  and transform it back into the frequency domain to arrive at

$$\begin{aligned}
\tilde{S}^+(\omega) &= \frac{1}{\sqrt{2\pi}} \int_{-\infty}^{\infty} \bar{S}(t - \tau)e^{-i\omega t} dt \\
&= \tilde{E}_0^{+*}(\omega)\tilde{E}^+(\omega)e^{-i\omega\tau} \\
&= \sqrt{\tilde{I}_0(\omega)\tilde{I}(\omega)}e^{i(\tilde{\Phi}(\omega) - \tilde{\Phi}_0(\omega) - \omega\tau)}. \quad (\text{B.5})
\end{aligned}$$

We thus generated the argument of the cosine function in  $\tilde{S}(\omega)$  as the complex argument of the function  $\tilde{S}^+(\omega)$ . The evaluation of this argument is now decoupled from the spectral intensity which may fluctuate due to experimental noise. The phase of the unknown pulse to be measured can now straightforwardly be calculated:

$$\tilde{\Phi}(\omega) = \tilde{\Phi}_0(\omega) + \arg \tilde{S}^+(\omega) + \omega\tau. \quad (\text{B.6})$$

Generally, for spectral interferometry the linear phase  $\omega\tau$  in  $\tilde{\Phi}(\omega)$  is not important, since it corresponds to a translation of the pulse in time. In most cases, we are only interested in the nonlinear phase contributions, since they are responsible for the amplitude shape of the pulse. In the SPIDER technique described below, however, a careful determination of this linear phase, meaning the exact temporal pulse delay is crucial to retrieve the pulse shape. In order to use spectral interferometry in the experiment we measure the spectrum at discrete spectral positions. The Fourier transformation is thus realized by a discrete algorithm (fast Fourier transform (FFT) [379] for example). In that case, we need to make sure that the fringe pattern of the spectral signal  $\tilde{I}_{\text{SI}}(\omega)$  is well resolved, requiring a minimum of two sample points per oscillation. This condition is also known as the Nyquist limit of sampling. The spectrometer resolution for a given pulse delay  $\tau$  has thus to be better than

$$\delta\omega = \frac{\pi}{\tau}. \quad (\text{B.7})$$

Once more it should be noted that  $\tau$  has to be large enough such that we can still separate the two functions  $\tilde{S}(t - \tau)$  and  $\tilde{S}^*(-t - \tau)$ . For application in the experiment, it is sometimes helpful not only to be able to separate these two functions, but in addition to be able to separate them from remaining DC-offset which results from imperfect subtraction of the single pulse spectra in Eq. (B.2). In particular, for the SPIDER technique described in the following, we may not be able to perform this subtraction at all since the single-pulse spectra can sometimes not be measured.

## B.2 Self-Referencing

Spectral interferometry gives us information about a phase difference. However, it is only able to compare the spectral phase at *the same frequency*  $\omega$ :  $\tilde{\Phi}(\omega) - \tilde{\Phi}_0(\omega)$  of *two different laser pulses*  $\tilde{E}^+(\omega)$  and  $\tilde{E}_0^+(\omega)$ . What we would need in order to reconstruct the spectral phase  $\Phi(\omega)$  of an unknown laser pulse is to measure the phase difference at *two different frequencies* for *the same laser pulse*. The idea to do this [52] is to use two identical replica of the same pulse and to shift one in frequency with respect to the other. As we know from Section 1.2, nonlinear optics allows for converting the frequency for example by sum-frequency mixing. It is possible to shift one pulse replica with respect to the other by a small frequency  $\Omega$ , thus producing the new “reference” pulse

$$\tilde{E}_0^+(\omega) = \tilde{E}^+(\omega + \Omega) \quad (\text{B.8})$$

which is the same as the unknown pulse except that it is slightly red-shifted along the frequency axis. In the SPIDER setup, this frequency shift is accomplished by sum-frequency mixing of two delayed replica with a long chirped pulse. It is crucial that the delay between the replica and the duration of the chirped pulse is much larger than the duration of

these pulses. Only then is mixing with a constant frequency for each of the pulses realized. At a given time delay  $\tau$  between the replica, the magnitude of  $\Omega$  can be controlled by the amount of linear chirp introduced in the long chirped pulse.

After recording the spectrum produced by these two pulses and doing the same analysis as above, we can now reformulate Eq. (B.6) as

$$\tilde{\Phi}(\omega) - \tilde{\Phi}_0(\omega) = \tilde{\Phi}(\omega) - \tilde{\Phi}(\omega + \Omega) \quad (\text{B.9})$$

$$= \arg \tilde{S}^+(\omega) + \omega\tau. \quad (\text{B.10})$$

We only need to precisely measure the temporal delay  $\tau$ , which can be done using spectral interferometry on the pair of identical pulses before shifting one of them in frequency. The difference phase extracted from this spectral interferometry measurement is exactly given by  $\tilde{\Phi}(\omega) - \tilde{\Phi}_0(\omega) = \omega\tau$ , since the two pulses are identical. After the temporal delay has been determined, the spectral phase of the unknown pulse can be reconstructed up to an additive constant. For example, we only have to assume a certain phase  $\tilde{\Phi}(\omega_0)$  at some frequency  $\omega_0$  and find the complete function  $\tilde{\Phi}(\omega)$  sampled at frequencies spaced by  $\Omega$  by application of Eq. (B.10). There are a variety of ways how to extract the phase function from the SPIDER signal. The two most commonly used in practice will now be outlined.

### B.3 Phase-Function Retrieval

Let us define the function

$$\Delta(\omega) = \tilde{\Phi}(\omega) - \tilde{\Phi}(\omega + \Omega) \quad (\text{B.11})$$

$$= \arg \tilde{S}^+(\omega) + \omega\tau, \quad (\text{B.12})$$

as the result directly obtained from the experimental SPIDER measurement.

#### B.3.1 Concatenation

The apparently most straightforward but also the least precise way is to define

$$\tilde{\Phi}(\omega_0) = \Phi_0 \quad (\text{B.13})$$

and to reconstruct the phase by iterative addition of  $-\Delta(\omega)$

$$\tilde{\Phi}(\omega_0 + n\Omega) = \Phi_0 - \sum_{j=1}^n \Delta(\omega_0 + (j-1)\Omega) \quad (\text{B.14})$$

for  $n > 0$ . This reconstruction method is thus not using the complete data set  $\Delta(\omega)$  which is experimentally sampled at positions spaced by  $\delta\omega$  but only the subset at positions spaced by  $\Omega$  that is typically larger than  $\delta\omega$ . In principle, one could choose the frequency shift (also called ‘shear’) such that the spectral resolution matches  $\Omega$ . This is in general not recommended since  $\delta\omega$  is a very small quantity. Remember that it had to be small enough to sample the spectral fringes produced by the interference of the two pulses and

is typically smaller than a hundredth of the bandwidth. If  $\Omega$  is chosen to be of the same size, the summation in Eq. (B.14) covers more than a hundred summands and is very sensitive to a small error in the determination of  $\tau$ . This is because  $\tau$  is present in every summand  $\Delta(\omega)$  by Eq. (B.12). In practice a good choice for the size of  $\Omega$  is one twentieth of the pulse's FWHM bandwidth in order to keep the error at an acceptable level. Then four out of five data points of  $\Delta(\omega)$  are wasted with the above method. If we choose  $\Omega$  much larger, we reconstruct the spectral phase  $\tilde{\Phi}(\omega_0 + n\Omega)$  at too few points which directly results in lower resolution of the phase function in frequency space.

### B.3.2 Integration Method

Another method to reconstruct the phase takes all data points into account and is in general more reliable than the concatenation technique described above [380]. By integrating  $\Delta(\omega)$  we obtain the integral over the spectral phase in an interval of length  $\Omega$

$$\begin{aligned}\Theta(\omega) &= \int_{-\infty}^{\omega} \Delta(\omega') d\omega' \\ &= \int_{-\infty}^{\omega} \tilde{\Phi}(\omega') d\omega - \int_{-\infty}^{\omega} \tilde{\Phi}(\omega' + \Omega) d\omega \\ &= \int_{\omega-\Omega}^{\omega} \tilde{\Phi}(\omega') d\omega\end{aligned}\tag{B.15}$$

This integral can now approximately be written employing the midpoint rule of integration:

$$\int_{\omega-\Omega}^{\omega} \tilde{\Phi}(\omega') d\omega \simeq \Omega \tilde{\Phi}\left(\omega - \frac{\Omega}{2}\right)\tag{B.16}$$

From this, we can then straightforwardly extract the spectral phase

$$\tilde{\Phi}(\omega) = \frac{1}{\Omega} \Theta\left(\omega + \frac{\Omega}{2}\right).\tag{B.17}$$

It can be noticed that the spectral phase  $\tilde{\Phi}(\omega)$  depends quadratically on  $\omega$  as  $\Delta(\omega)$  depends linearly on  $\omega$  in Eq. (B.12). As in the case in the concatenation approach (section B.3.1), this has important consequences for the reconstruction of the pulse shape. One has to make absolutely sure that the pulse delay between the two replica is precisely known. For smaller and smaller values of the shear  $\Omega$ , the precision in the determination of the pulse delay must increase in order to keep the error at an acceptable level. Again, in practice, a twentieth of the FWHM of the pulse's spectrum is a good choice for  $\Omega$ .



# Appendix C

## Numerical Solution of the Schrödinger-Equation

### C.1 Laser–Atom-Interaction Hamiltonian Operator

In the dipole approximation [76, 381], the Hamilton operator for an electron in a static potential plus the potential created by the laser field  $E(t)$  (atomic units are used throughout this section):

$$\hat{H} = \frac{1}{2}\vec{p}^2 + V(\vec{r}) + \vec{r}\vec{E}(t) \quad (\text{C.1})$$

can also be written in the form

$$\hat{H} = \frac{1}{2}(\vec{p} - \vec{A}(t))^2 + V(\vec{r}) \quad (\text{C.2})$$

$$= \frac{1}{2}\vec{p}^2 - \vec{p}\vec{A}(t) + \frac{1}{2}A^2(t) + V(\vec{r}) \quad (\text{C.3})$$

Here,  $\vec{A}(t) = -\int_{-\infty}^t E(t')dt'$  is the vector potential of the laser. A gauge transformation [76] mediates between  $\hat{H}$  and  $\hat{H}$ , which means that any physically meaningful observables extracted from them are equivalent. The operators  $\vec{p}$  and  $\vec{r}$  can be written either in position space

$$\vec{p} = \frac{1}{i}\vec{\nabla}_x \quad (\text{C.4})$$

$$\vec{r} = \vec{r} \quad (\text{C.5})$$

or in momentum space

$$\vec{p} = \vec{p} \quad (\text{C.6})$$

$$\vec{r} = i\vec{\nabla}_p \quad (\text{C.7})$$

The wavefunctions in position and momentum space depend on each other by means of the Fourier transformation

$$\tilde{\Psi}(\vec{p}, t) = \mathcal{F} \Psi(\vec{r}, t) \quad (\text{C.8})$$

$$\Psi(\vec{r}, t) = \mathcal{F}^{-1} \tilde{\Psi}(\vec{p}, t). \quad (\text{C.9})$$

with the Fourier transformation operator  $\mathcal{F}$  and its inverse  $\mathcal{F}^{-1}$  defined as

$$\begin{aligned} g(\vec{p}) &= \mathcal{F} f(\vec{r}) = \frac{1}{\sqrt{2\pi\hbar}} \int_{-\infty}^{\infty} f(\vec{x}) e^{-\frac{i}{\hbar}\vec{p}\vec{r}} d^3r \\ f(\vec{r}) &= \mathcal{F}^{-1} g(\vec{p}) = \frac{1}{\sqrt{2\pi\hbar}} \int_{-\infty}^{\infty} g(\vec{p}) e^{\frac{i}{\hbar}\vec{p}\vec{r}} d^3p. \end{aligned} \quad (\text{C.10})$$

It should be pointed out that both operators do not *physically* change the wavefunction, but only switch the *mathematical* representation from the position into the momentum space and vice versa.

How can we solve the time dependent Schrödinger equation

$$i \frac{\partial}{\partial t} \Psi(\vec{r}, t) = \hat{H} \Psi(\vec{r}, t) \quad (\text{C.11})$$

by numerical computation? The general solution to this differential equation can be written in the form

$$\Psi(\vec{r}, t) = e^{-i \int_{t'}^t \hat{H} dt} \Psi(\vec{r}, t'). \quad (\text{C.12})$$

It can be seen from this expression that the term  $A^2(t)$  is a function only dependent on time and can thus be left out. It only introduces a phase in the total electronic wavefunction, which is of no physical relevance here. Of course we could have written the general solution in momentum space representation, where the  $\Psi(\vec{r}, t)$  would simply be replaced by the  $\tilde{\Psi}(\vec{p}, t)$ . Obviously, inserting any representation of the Hamilton operator in either position or momentum space introduces the differential operator  $\vec{\nabla}$  in the exponent. Numerical evaluation is therefore hard to be done in either representation. What we would like to do is to work in a mixed representation, where we evaluate the position operator  $\vec{r}$  in position space and the momentum operator  $\vec{p}$  in momentum space. This is exactly what is done in the split-step-operator computation method [279, 280].

## C.2 Split-Step-Operator Method

We can split the full Hamiltonian operator  $\hat{H}$  into two parts

$$\hat{H} = \hat{H}_p + \hat{H}_r, \quad (\text{C.13})$$

where  $H_p$  contains only the part depending on the momentum operator  $\vec{p}$  and  $H_r$  the part depending solely on the position operator  $\vec{r}$

$$\hat{H}_p = \frac{1}{2} \vec{p}^2 - \vec{p} \vec{A}(t) \quad (\text{C.14})$$

$$\hat{H}_r = V(\vec{r}). \quad (\text{C.15})$$

We could now evolve the quantum-mechanical system in time for either of the Hamiltonian parts by writing the partial time-evolution operators

$$\begin{aligned} \Psi(\vec{r}, t) &= e^{-i \int_{t'}^t \hat{H}_r dt} \Psi(\vec{r}, t') \\ &= e^{-i \int_{t'}^t V(r) dt} \Psi(\vec{r}, t') \\ &= e^{-i(t-t')V(r)} \Psi(\vec{r}, t'), \end{aligned} \quad (\text{C.16})$$



and

$$\begin{aligned}
\tilde{\Psi}(\vec{p}, t) &= e^{-i \int_{t'}^t \hat{H}_p dt} \tilde{\Psi}(\vec{p}, t') \\
&= e^{-i \int_{t'}^t \frac{1}{2} \vec{p}^2 - \vec{p} \vec{A}(t) dt} \tilde{\Psi}(\vec{p}, t') \\
&= e^{-i \frac{1}{2} (t-t') \vec{p}^2 + \vec{p} \int_{t'}^t -\vec{A}(t) dt} \tilde{\Psi}(\vec{p}, t').
\end{aligned} \tag{C.17}$$

We must keep in mind that evolution over an extended period of time ( $t - t'$ ) of any partial operator is not physical, since either the kinetic part is neglected for evolution in position space with Eq. (C.16) or the potential for evolution in momentum space with Eq. (C.17). We can, however, evolve only a small period of time in either representation and then, after switching the representation of the wavefunction by means of a Fourier transformation, evolve the same time in the other representation:

$$\begin{aligned}
\Psi(\vec{r}, t = t' + dt) &= e^{-i \int_{t'+dt/2}^{t'+dt} \hat{H}_r dt} \mathcal{F}^{-1} e^{-i \int_{t'}^{t'+dt} \hat{H}_p dt} \mathcal{F} e^{-i \int_{t'}^{t'+dt/2} \hat{H}_r dt} \Psi(\vec{r}, t') \\
&= e^{-\frac{idt}{2} V(r)} \mathcal{F}^{-1} e^{-idt \frac{1}{2} \vec{p}^2 + \vec{p} \int_{t'}^{t'+dt} -\vec{A}(t) dt} \mathcal{F} e^{-\frac{idt}{2} V(r)} \Psi(\vec{r}, t'),
\end{aligned} \tag{C.18}$$

By choosing a sufficiently small time step  $dt$ , the computational error becomes very small. The split-step algorithm used for the numerical solution of the time-dependent Schrödinger equation from time  $t_0$  to  $t_n$  can thus be summarized as follows:

1. Start with an initial wavefunction in position space  $\Psi(\vec{r}, t_{j=0})$ .
2. Multiply  $\Psi(\vec{r}, t_j)$  with  $e^{-\frac{idt}{2} V(r)}$  to obtain  $\Psi(\vec{r}, t_j + dt/2)$ .
3. Perform a Fourier transformation  $\mathcal{F}$  on  $\Psi(\vec{r}, t_j + dt/2)$  to obtain the wavefunction in momentum space  $\tilde{\Psi}(\vec{p}, t_j)$ .
4. Multiply  $\tilde{\Psi}(\vec{p}, t_j)$  with  $e^{-idt \frac{1}{2} \vec{p}^2 + \vec{p} \int_{t'}^{t'+dt} -\vec{A}(t) dt}$  to obtain  $\tilde{\Psi}(\vec{p}, t_j + dt)$ .
5. Perform an inverse Fourier transformation  $\mathcal{F}^{-1}$  on  $\tilde{\Psi}(\vec{p}, t_j + dt)$  to obtain the wavefunction again in position space  $\tilde{\Psi}(\vec{r}, t_j + dt/2)$ .
6. Multiply  $\tilde{\Psi}(\vec{r}, t_j + dt/2)$  with  $e^{-\frac{idt}{2} V(r)}$  to obtain  $\Psi(\vec{r}, t_j + dt) = \Psi(\vec{r}, t_{j+1})$ .
7. Repeat from the second step until time  $t_n$  is reached.

By defining the wave-function on a grid and using the Fast Fourier transform algorithm (FFT) [379] the approach can be readily implemented on a computer.



# Bibliography

- [1] U. Morgner, F. X. Kärtner, S. H. Cho, Y. Chen, H. A. Haus, J. Fujimoto, E. P. Ippen, V. Scheuer, G. Angelow, and T. Tschudi.  
*Sub-two-cycle pulses from a Kerr-lens mode-locked Ti:sapphire laser.*  
Opt. Lett. **24**, 411–413 (1999).
- [2] B. Schenkel, J. Biegert, U. Keller, C. Vozzi, M. Nisoli, G. Sansone, S. Stagira, S. DeSilvestri, and O. Svelto.  
*Generation of 3.8-fs pulses from adaptive compression of a cascaded hollow fiber supercontinuum.*  
Opt. Lett. **28**, 1987–1989 (2003).
- [3] K. Yamane, Z. G. Zhang, K. Oka, R. Morita, M. Yamashita, and A. Suguro.  
*Optical pulse compression to 3.4 fs in the monocycle region by feedback phase compensation.*  
Opt. Lett. **28**, 2258–2260 (2003).
- [4] D. M. Pennington, C. G. Brown, T. E. Cowan, S. P. Hatchett, E. Henry, S. Herman, M. Kartz, M. Key, J. Koch, A. J. MacKinnon, M. D. Perry, T. W. Phillips, M. Roth, T. C. Sangster, M. Singh, R. A. Snavely, M. Stoyer, B. C. Stuart, and S. C. Wilks.  
*Petawatt laser system and experiments.*  
IEEE J. Sel. Top. Quantum Electr. **6**, 676–688 (2000).
- [5] Y. Nabekawa, Y. Kuramoto, T. Togashi, T. Sekikawa, and S. Watanabe.  
*Generation of 0.66-TW pulses at 1 kHz by a Ti:sapphire laser.*  
Opt. Lett. **23**, 1384–1386 (1998).
- [6] S. V. Bulanov, T. Esirkepov, and T. Tajima.  
*Light intensification towards the Schwinger limit.*  
Phys. Rev. Lett. **91**, 085001 (2003).
- [7] A. E. Siegman.  
*Lasers.*  
First edition. University Science Books, Sausalito (1986).
- [8] P. W. Milonni and J. H. Eberly.  
*Lasers.*  
Wiley, New York (1988).
- [9] J.-C. Diels and W. Rudolph.  
*Ultrashort Laser Pulse Phenomena.*  
Academic Press, London (1996).
- [10] C. Rullière (Ed.).  
*Femtosecond Laser Pulses.*  
Springer, Berlin (1998).
- [11] C. Spielmann, P. F. Curley, T. Brabec, and F. Krausz.  
*Ultrabroadband Femtosecond Lasers.*  
IEEE J. Quantum Electron. **30**, 1100–1114 (1994).
- [12] R. Szipocs, K. Ferencz, C. Spielmann, and F. Krausz.  
*Chirped Multilayer Coatings for Broad-Band Dispersion Control in Femtosecond Lasers.*  
Opt. Lett. **19**, 201–203 (1994).

- [13] A. Stingl, M. Lenzner, C. Spielmann, F. Krausz, and R. Szipocs.  
*Sub-10-Fs Mirror-Dispersion-Controlled Ti-Sapphire Laser.*  
Opt. Lett. **20**, 602–604 (1995).
- [14] F. X. Kartner, N. Matuschek, T. Schibli, U. Keller, H. A. Haus, C. Heine, R. Morf, V. Scheuer, M. Tilsch, and T. Tschudi.  
*Design and fabrication of double-chirped mirrors.*  
Opt. Lett. **22**, 831–833 (1997).
- [15] D. Strickland and G. Mourou.  
*Compression of Amplified Chirped Optical Pulses.*  
Opt. Commun. **56**, 219–221 (1985).
- [16] E. B. Treacy.  
*Optical Pulse Compression with Diffraction Gratings.*  
IEEE J. Quantum Electron. **QE 5**, 454 (1969).
- [17] O. E. Martinez.  
*Grating and Prism Compressors in the Case of Finite Beam Size.*  
J. Opt. Soc. Am. B **3**, 929–934 (1986).
- [18] S. D. Brorson and H. A. Haus.  
*Diffraction Gratings and Geometrical-Optics.*  
J. Opt. Soc. Am. B **5**, 247–248 (1988).
- [19] C. Lemell, X. M. Tong, F. Krausz, and J. Burgdörfer.  
*Electron emission from metal surfaces by ultrashort pulses: Determination of the carrier-envelope phase.*  
Phys. Rev. Lett. **90**, 076403 (2003).
- [20] G. G. Paulus, F. Lindner, H. Walther, A. Baltuska, E. Goulielmakis, M. Lezius, and F. Krausz.  
*Measurement of the phase of few-cycle laser pulses.*  
Phys. Rev. Lett. **91**, 253004 (2003).
- [21] D. J. Jones, S. A. Diddams, J. K. Ranka, A. Stentz, R. S. Windeler, J. L. Hall, and S. T. Cundiff.  
*Carrier-envelope phase control of femtosecond mode-locked lasers and direct optical frequency synthesis.*  
Science **288**, 635–639 (2000).
- [22] A. Baltuška, T. Fuji, and T. Kobayashi.  
*Controlling the carrier-envelope phase of ultrashort light pulses with optical parametric amplifiers.*  
Phys. Rev. Lett. **88**, 133901 (2002).
- [23] C. J. Bardeen, Q. Wang, and C. V. Shank.  
*Selective excitation of vibrational wave-packet motion using chirped pulses.*  
Phys. Rev. Lett. **75**, 3410–3413 (1995).
- [24] B. Kohler, V. V. Yakovlev, J. Che, J. L. Krause, M. Messina, K. R. Wilson, N. Schwentner, R. M. Whitnell, and Y. J. Yan.  
*Quantum control of wave-packet evolution with tailored femtosecond pulses.*  
Phys. Rev. Lett. **74**, 3360–3363 (1995).
- [25] A. Assion, T. Baumert, J. Helbing, V. Seyfried, and G. Gerber.  
*Coherent control by a single phase shaped femtosecond laser pulse.*  
Chem. Phys. Lett. **259**, 488–494 (1996).
- [26] G. Cerullo, C. J. Bardeen, Q. Wang, and C. V. Shank.  
*High-power chirped pulse excitation of molecules in solution.*  
Chem. Phys. Lett. **262**, 362–368 (1996).

- [27] C. J. Bardeen, Q. Wang, and C. V. Shank.  
*Femtosecond chirped pulse excitation of vibrational wave packets in LD690 and bacteriorhodopsin.*  
J. Phys. Chem. A **102**, 2759–2766 (1998).
- [28] C. J. Bardeen, V. V. Yakovlev, J. A. Squier, and K. R. Wilson.  
*Quantum control of population transfer in green fluorescent protein by using chirped femtosecond pulses.*  
J. Am. Chem. Soc. **120**, 13027 (1998).
- [29] T. Baumert, T. Brixner, V. Seyfried, M. Strehle, and G. Gerber.  
*Femtosecond pulse shaping by an evolutionary algorithm with feedback.*  
Appl. Phys. B **65**, 779–782 (1997).
- [30] D. Yelin, D. Meshulach, and Y. Silberberg.  
*Adaptive femtosecond pulse compression.*  
Opt. Lett. **22**, 1793–1795 (1997).
- [31] J. Desbois, F. Gires, and P. Tournois.  
*New Approach to Picosecond Laser Pulse Analysis Shaping and Coding.*  
IEEE J. Quantum Electron. **QE 9**, 213–218 (1973).
- [32] J. Agostinelli, G. Harvey, T. Stone, and C. Gabel.  
*Optical Pulse Shaping with A Grating Pair.*  
Appl. Opt. **18**, 2500–2504 (1979).
- [33] R. N. Thurston, J. P. Heritage, A. M. Weiner, and W. J. Tomlinson.  
*Analysis of Picosecond Pulse Shape Synthesis by Spectral Masking in A Grating Pulse Compressor.*  
IEEE J. Quantum Electron. **22**, 682–696 (1986).
- [34] A. M. Weiner, J. P. Heritage, and E. M. Kirschner.  
*High-Resolution Femtosecond Pulse Shaping.*  
J. Opt. Soc. Am. B **5**, 1563–1572 (1988).
- [35] T. Brixner and G. Gerber.  
*Femtosecond polarization pulse shaping.*  
Opt. Lett. **26**, 557–559 (2001).
- [36] T. Brixner, G. Krampert, P. Niklaus, and G. Gerber.  
*Generation and characterization of polarization-shaped femtosecond laser pulses.*  
Appl. Phys. B **74**, S133–S144 (2002).
- [37] T. Brixner, N. H. Damrauer, G. Krampert, P. Niklaus, and G. Gerber.  
*Adaptive shaping of femtosecond polarization profiles.*  
J. Opt. Soc. Am. B **20**, 878–881 (2003).
- [38] T. Brixner.  
*Poincaré representation of polarization-shaped femtosecond laser pulses.*  
Appl. Phys. B **76**, 531–540 (2003).
- [39] A. M. Weiner, D. E. Leaird, J. S. Patel, and J. R. Wullert II.  
*Programmable femtosecond pulse shaping by use of a multielement liquid-crystal phase modulator.*  
Opt. Lett. **15**, 326–328 (1990).
- [40] E. Zeek, K. Maginnis, S. Backus, U. Russek, M. Murnane, G. Mourou, H. Kapteyn, and G. Vdovin.  
*Pulse compression by use of deformable mirrors.*  
Opt. Lett. **24**, 493–495 (1999).
- [41] M. E. Fermann, V. da Silva, D. A. Smith, Y. Silberberg, and A. M. Weiner.  
*Shaping of ultrashort optical pulses by using an integrated acousto-optic tunable filter.*  
Opt. Lett. **18**, 1505–1507 (1993).

- [42] D. Oron, N. Dudovich, and Y. Silberberg.  
*Femtosecond phase-and-polarization control for background-free coherent anti-Stokes Raman spectroscopy.*  
Phys. Rev. Lett. **90**, 213902 (2003).
- [43] T. Brixner, G. Krampert, T. Pfeifer, R. Selle, G. Gerber, M. Wollenhaupt, O. Graefe, C. Horn, D. Liese, and T. Baumert.  
*Quantum control by ultrafast polarization shaping.*  
Phys. Rev. Lett. **92**, 208301 (2004).
- [44] A. Prakelt, M. Wollenhaupt, A. Assion, C. Horn, C. Sarpe-Tudoran, M. Winter, and T. Baumert.  
*Compact, robust, and flexible setup for femtosecond pulse shaping.*  
Rev. Sci. Instrum. **74**, 4950–4953 (2003).
- [45] T. Feurer, J. C. Vaughan, R. M. Koehl, and K. A. Nelson.  
*Multidimensional control of femtosecond pulses by use of a programmable liquid-crystal matrix.*  
Opt. Lett. **27**, 652–654 (2002).
- [46] T. Feurer, J. C. Vaughan, and K. A. Nelson.  
*Spatiotemporal coherent control of lattice vibrational waves.*  
Science **299**, 374–377 (2003).
- [47] M. Hacker, G. Stobrawa, R. Sauerbrey, T. Buckup, M. Motzkus, M. Wildenhain, and A. Gehner.  
*Micromirror SLM for femtosecond pulse shaping in the ultraviolet.*  
Appl. Phys. B **76**, 711–714 (2003).
- [48] T. Pfeifer, U. Weichmann, S. Zipfel, and G. Gerber.  
*Compression and shaping of a self-phase-modulated laser pulse with a deformable mirror device.*  
J. Mod. Opt. **50**, 705–710 (2003).
- [49] E. Zeek, R. Bartels, M. M. Murnane, H. C. Kapteyn, S. Backus, and G. Vdovin.  
*Adaptive pulse compression for transform-limited 15-fs high-energy pulse generation.*  
Opt. Lett. **25**, 587–589 (2000).
- [50] T. Feurer, M. Hacker, B. Schmidt, and G. Stobrawa.  
*lab2 – A Virtual Femtosecond-Laser Laboratory.*  
Webpage <http://www.lab2.de> (2002).
- [51] D. J. Kane and R. Trebino.  
*Single-shot measurement of the intensity and phase of an arbitrary ultrashort pulse by using frequency-resolved optical gating.*  
Opt. Lett. **18**, 823–825 (1993).
- [52] C. Iaconis and I. A. Walmsley.  
*Spectral phase interferometry for direct electric-field reconstruction of ultrashort optical pulses.*  
Opt. Lett. **23**, 792–794 (1998).
- [53] R. Trebino and D. J. Kane.  
*Using phase retrieval to measure the intensity and phase of ultrashort pulses: Frequency-resolved optical gating.*  
J. Opt. Soc. Am. A **10**, 1101–1111 (1993).
- [54] R. Trebino, K. W. DeLong, D. N. Fittinghoff, J. N. Sweetser, M. A. Krumbgel, B. A. Richman, and D. J. Kane.  
*Measuring ultrashort laser pulses in the time-frequency domain using frequency-resolved optical gating.*  
Rev. Sci. Instrum. **68**, 3277–3295 (1997).
- [55] R. Trebino.  
*Frequency-Resolved Optical Gating: The Measurement of Ultrashort Laser Pulses.*  
Kluwer Academic Publishers, Boston (2002).

- [56] D. J. Kane.  
*Recent progress toward real-time measurement of ultrashort laser pulses.*  
IEEE J. Quantum Electron. **35**, 421–431 (1999).
- [57] D. J. Kane, J. Weston, and K. C. J. Chu.  
*Real-time inversion of polarization gate frequency-resolved optical gating spectrograms.*  
Appl. Opt. **42**, 1140–1144 (2003).
- [58] Z. Y. Wang, E. Zeek, R. Trebino, and P. Kvam.  
*Determining error bars in measurements of ultrashort laser pulses.*  
J. Opt. Soc. Am. B **20**, 2400–2405 (2003).
- [59] A. Baltuška, M. S. Pshenichnikov, and D. A. Wiersma.  
*Amplitude and phase characterization of 4.5-fs pulses by frequency-resolved optical gating.*  
Opt. Lett. **23**, 1474–1476 (1998).
- [60] Q. Cao, X. Gu, E. Zeek, M. Kimmel, R. Trebino, J. Dudley, and R. S. Windeler.  
*Measurement of the intensity and phase of supercontinuum from an 8-mm-long microstructure fiber.*  
Appl. Phys. B **77**, 239–244 (2003).
- [61] S. Linden, H. Giessen, and J. Kuhl.  
*XFROG - A new method for amplitude and phase characterization of weak ultrashort pulses.*  
Phys. Status Solidi B **206**, 119–124 (1998).
- [62] J. Y. Zhang, A. P. Shreenath, M. Kimmel, E. Zeek, R. Trebino, and S. Link.  
*Measurement of the intensity and phase of attojoule femtosecond light pulses using optical-parametric-amplification cross-correlation frequency-resolved optical gating.*  
Opt. Express **11**, 601–609 (2003).
- [63] D. T. Reid, P. Loza-Alvarez, C. T. A. Brown, T. Beddard, and W. Sibbett.  
*Amplitude and phase measurement of mid-infrared femtosecond pulses by using cross-correlation frequency-resolved optical gating.*  
Opt. Lett. **25**, 1478–1480 (2000).
- [64] S. Linden, J. Kuhl, and H. Giessen.  
*Amplitude and phase characterization of weak blue ultrashort pulses by downconversion.*  
Opt. Lett. **24**, 569–571 (1999).
- [65] S. Akturk, M. Kimmel, P. O’Shea, and R. Trebino.  
*Measuring spatial chirp in ultrashort pulses using single-shot Frequency-Resolved Optical Gating.*  
Opt. Express **11**, 68–78 (2003).
- [66] P. Baum, S. Lochbrunner, and E. Riedle.  
*Zero-additional-phase SPIDER: full characterization of visible and sub-20-fs ultraviolet pulses.*  
Opt. Lett. **29**, 210–212 (2004).
- [67] T. M. Shuman, M. E. Anderson, J. Bromage, C. Iaconis, L. Waxer, and I. A. Walmsley.  
*Real-time SPIDER: ultrashort pulse characterization at 20 Hz.*  
Opt. Express **5**, 134–143 (1999).
- [68] C. Dorrer, E. M. Kosik, and I. A. Walmsley.  
*Spatio-temporal characterization of the electric field of ultrashort optical pulses using two-dimensional shearing interferometry.*  
Appl. Phys. B **74**, S209–S217 (2002).
- [69] R. Morita, M. Hirasawa, N. Karasawa, S. Kusaka, N. Nakagawa, K. Yamane, L. M. Li, A. Suguro, and M. Yamashita.  
*Sub-5 fs optical pulse characterization.*  
Measurement Science & Technology **13**, 1710–1720 (2002).

- [70] L. Gallmann, D. H. Sutter, N. Matuschek, G. Steinmeyer, U. Keller, C. Iaconis, and I. A. Walmsley. *Characterization of sub-6-fs optical pulses with spectral phase interferometry for direct electric-field reconstruction*. *Opt. Lett.* **24**, 1314–1316 (1999).
- [71] M. Hirasawa, N. Nakagawa, K. Yamamoto, R. Morita, H. Shigekawa, and M. Yamashita. *Sensitivity improvement of spectral phase interferometry for direct electric-field reconstruction for the characterization of low-intensity femtosecond pulses*. *Appl. Phys. B* **74**, S225–S229 (2002).
- [72] L. Gallmann, D. H. Sutter, N. Matuschek, G. Steinmeyer, and U. Keller. *Techniques for the characterization of sub-10-fs optical pulses: a comparison*. *Appl. Phys. B* **70**, S67–S75 (2000).
- [73] Y. R. Shen. *The Principles of Nonlinear Optics*. John Wiley & Sons, New York (1984).
- [74] R. W. Boyd. *Nonlinear Optics*. Academic Press, San Diego (1992).
- [75] M. O. Scully and M. S. Zubairy. *Quantum Optics*. Cambridge University Press, Cambridge (1995).
- [76] W. P. Schleich. *Quantum Optics in Phase Space*. Wiley–VCH, Weinheim (2001).
- [77] J. D. Jackson. *Classical Electrodynamics*. Third edition. Wiley, New York (1998).
- [78] P. N. Butcher and D. Cotter. *The Elements of Nonlinear Optics*, volume 9 of *Cambridge Studies in Modern Optics*. Cambridge University Press, Cambridge (1990).
- [79] L. D. Landau and E. M. Lifshitz. *Quantum Mechanics*, volume 3 of *Course of theoretical physics*. Third edition. Pergamon Press, Oxford (1977).
- [80] J. J. Sakurai. *Modern Quantum Mechanics*. Second edition. Addison Wesley, Reading (1994).
- [81] P. L. Shkolnikov, A. Lago, and A. E. Kaplan. *Optimal Quasi-Phase-Matching for High-Order Harmonic-Generation in Gases and Plasma*. *Phys. Rev. A* **50**, R4461–R4464 (1994).
- [82] I. P. Christov, H. C. Kapteyn, and M. M. Murnane. *Quasi-phase matching of high-harmonics and attosecond pulses in modulated waveguides*. *Opt. Express* **7**, 362–367 (2000).
- [83] I. P. Christov. *Control of high harmonic and attosecond pulse generation in aperiodic modulated waveguides*. *J. Opt. Soc. Am. B* **18**, 1877–1881 (2001).
- [84] A. Paul, R. A. Bartels, R. Tobey, H. Green, S. Weiman, I. P. Christov, M. M. Murnane, H. C. Kapteyn, and S. Backus. *Quasi-phase-matched generation of coherent extreme-ultraviolet light*. *Nature* **421**, 51–54 (2003).



- [85] E. A. Gibson, A. Paul, N. Wagner, R. Tobey, D. Gaudiosi, S. Backus, I. P. Christov, A. Aquila, E. M. Gullikson, D. T. Attwood, M. M. Murnane, and H. C. Kapteyn.  
*Coherent Soft X-ray Generation in the Water Window with Quasi-Phase Matching.*  
Science **302**, 95–98 (2003).
- [86] G. A. Magel, M. M. Fejer, and R. L. Byer.  
*Quasi-phase-matched second-harmonic generation of blue light in periodically poled LiNbO<sub>3</sub>.*  
Appl. Phys. Lett. **56**, 108–110 (1990).
- [87] J. A. Armstrong, N. Bloembergen, J. Ducuing, and P. S. Pershan.  
*Interactions between Light Waves in a Nonlinear Dielectric.*  
Phys. Rev. **127**, 1918–1938 (1962).
- [88] A. L’Huillier, L.-A. Lompré, G. Mainfray, and C. Manus.  
*High-order harmonic generation in rare gases*, pp. 139–206.  
New York Academic (1992).
- [89] M. Protopapas, C. H. Keitel, and P. L. Knight.  
*Atomic physics with super-high intensity lasers.*  
Rep. Prog. Phys. **60**, 389–486 (1997).
- [90] A. L’Huillier, K. J. Schafer, and K. C. Kulander.  
*High-Order Harmonic Generation in Xenon at 1064 nm: The Role of Phase Matching.*  
Phys. Rev. Lett. **66**, 2200–2203 (1991).
- [91] V. G. Dmitriev, G. G. Gurzadyan, and D. N. Nikogosyan.  
*Handbook of Nonlinear Optical Crystals.*  
Springer (1991).
- [92] D. Eimerl, L. Davis, S. Velsko, E. K. Graham, and A. Zalkin.  
*Optical, Mechanical, and Thermal-Properties of Barium Borate.*  
J. Appl. Phys. **62**, 1968–1983 (1987).
- [93] T. J. Driscoll, G. M. Gale, and F. Hache.  
*Ti:Sapphire 2nd-Harmonic-Pumped Visible Range Femtosecond Optical Parametric Oscillator.*  
Opt. Commun. **110**, 638–644 (1994).
- [94] A. Baltuška, T. Fuji, and T. Kobayashi.  
*Visible pulse compression to 4 fs by optical parametric amplification and programmable dispersion control.*  
Opt. Lett. **27**, 306–308 (2002).
- [95] T. Wilhelm, J. Piel, and E. Riedle.  
*Sub-20-fs pulses tunable across the visible from a blue-pumped single-pass noncollinear parametric converter.*  
Opt. Lett. **22**, 1494–1496 (1997).
- [96] J. König.  
*Frequenzkonversion infraroter FemtosekundenLaserpulse in das sichtbare Spektrum und in den Bereich weicher Röntgenstrahlen.*  
Diplomarbeit, Universität Würzburg (2001).
- [97] C. Treml.  
*Polarisationspulsformung im sichtbaren Spektralbereich.*  
Diplomarbeit, Universität Würzburg (2003).
- [98] M. Nisoli and S. De Silvestri und O. Svelto.  
*Generation of high energy 10 fs pulses by a new pulse compression technique.*  
Appl.Phys.Lett. **68**, 2793–2795 (1996).
- [99] M. Nisoli, S. D. Silvestri, O. Svelto, R. Szipöcs, K. Ferencz, C. Spielmann, S. Sartania, and F. Krausz.  
*Compression of high-energy laser pulses below 5 fs.*  
Opt. Lett. **22**, 522–524 (1997).

- [100] M. Nisoli, G. Sansone, S. Stagira, C. Vozzi, S. DeSilvestri, and O. Svelto.  
*Ultra-broadband continuum generation by hollow-fiber cascading.*  
Appl. Phys. B **75**, 601–604 (2002).
- [101] S. A. Kovalenko, A. L. Dobryakov, J. Ruthmann, and N. P. Ernsting.  
*Femtosecond spectroscopy of condensed phases with chirped supercontinuum probing.*  
Phys. Rev. A **59**, 2369–2384 (1999).
- [102] R. R. Alfano (Ed.).  
*The Supercontinuum Laser Source.*  
Springer Verlag, New York (1989).
- [103] A. McPherson, G. Gibson, H. Jara, U. Johann, T. S. Luk, I. A. McIntyre, K. Boyer, and C. K. Rhodes.  
*Studies of multiphoton production of vacuum-ultraviolet radiation in the rare gases.*  
J. Opt. Soc. Am. B **4**, 595–600 (1987).
- [104] M. Ferray, A. L’Huillier, X. F. Li, L. A. Lompré, G. Mainfray, and C. Manus.  
*Multiple-harmonic conversion of 1064 nm radiation in rare gases.*  
J. Phys. B **21**, L31–L35 (1988).
- [105] P. B. Corkum.  
*Plasma Perspective on Strong-Field Multiphoton Ionization.*  
Phys. Rev. Lett. **71**, 1994–1997 (1993).
- [106] K. C. Kulander, K. J. Schafer, and J. L. Krause.  
*Dynamics of short-pulse excitation and ionization and harmonic generation*, pp. 95–110.  
Plenum Press, New York (1993).
- [107] M. Lewenstein, P. Balcou, M. Y. Ivanov, A. L’Huillier, and P. B. Corkum.  
*Theory of high-harmonic generation by low-frequency laser fields.*  
Phys. Rev. A **49**, 2117–2132 (1994).
- [108] P. Antoine, A. L’Huillier, M. Lewenstein, P. Salières, and B. Carré.  
*Theory of high-order harmonic generation by an elliptically polarized laser field.*  
Phys. Rev. A **53**, 1725–1754 (1996).
- [109] U. Weichmann.  
*Erzeugung hoher Harmonischer von Femtosekunden-Laserpulsen.*  
Dissertation, Universität Würzburg (2001).
- [110] T. Brabec and F. Krausz.  
*Intense few-cycle laser fields: Frontiers of nonlinear optics.*  
Rev. Mod. Phys. **72**, 545–591 (2000).
- [111] L. V. Keldysh.  
*Ionization in the field of a strong electromagnetic wave.*  
Soviet Physics JETP **20**, 1307–1314 (1965).
- [112] M. V. Ammosov, N. B. Delone, and V. P. Krainov.  
*Tunnel ionization of complex atoms and of atomic ions in an alternating electromagnetic field.*  
Sov. Phys. JETP **64**, 1191–1194 (1986).
- [113] S. Augst, D. D. Meyerhofer, D. Strickland, and S. L. Chin.  
*Laser ionization of noble gases by Coulomb-barrier suppression.*  
J. Opt. Soc. Am. B **8**, 858–867 (1991).
- [114] J. L. Krause, K. J. Schafer, and K. C. Kulander.  
*High-Order Harmonic Generation from Atoms and Ions in the High Intensity Regime.*  
Phys. Rev. Lett. **68**, 3535–3538 (1992).
- [115] S. Y. Chen, A. Maksimchuk, and D. Umstadter.  
*Experimental observation of relativistic nonlinear Thomson scattering.*  
Nature **396**, 653–655 (1998).

- [116] D. N. Fittinghoff, P. R. Bolton, B. Chang, and K. C. Kulander.  
*Observation of Nonsequential Double Ionization of Helium with Optical Tunneling.*  
Phys. Rev. Lett. **69**, 2642–2645 (1992).
- [117] B. Walker, B. Sheehy, L. F. DiMauro, P. Agostini, K. J. Schafer, and K. C. Kulander.  
*Precision-Measurement of Strong-Field Double-Ionization of Helium.*  
Phys. Rev. Lett. **73**, 1227–1230 (1994).
- [118] P. Agostini, F. Fabre, G. Mainfray, G. Petite, and N. K. Rahman.  
*Free-Free Transitions Following Six-Photon Ionization of Xenon Atoms.*  
Phys. Rev. Lett. **42**, 1127–1130 (1979).
- [119] G. G. Paulus, W. Nicklich, H. L. Xu, P. Lambropoulos, and H. Walther.  
*Plateau in Above-Threshold Ionization Spectra.*  
Phys. Rev. Lett. **72**, 2851–2854 (1994).
- [120] K. J. Schafer, B. Yang, L. F. DiMauro, and K. C. Kulander.  
*Above Threshold Ionization Beyond the High Harmonic Cutoff.*  
Phys. Rev. Lett. **70**, 1599–1602 (1993).
- [121] P. Salières, B. Carré, L. L. Déroff, F. Grasbon, G. G. Paulus, H. Walther, R. Kopold, W. Becker, D. B. Milošević, A. Sanpera, and M. Lewenstein.  
*Feynman's Path-Integral Approach for Intense-Laser-Atom Interactions.*  
Science **292**, 902–905 (2001).
- [122] R. Bartels, S. Backus, E. Zeek, L. Misoguti, G. Vdovin, I. P. Christov, M. M. Murnane, and H. C. Kapteyn.  
*Shaped-pulse optimization of coherent emission of high-harmonic soft-X-rays.*  
Nature **406**, 164–166 (2000).
- [123] I. P. Christov, R. Bartels, H. C. Kapteyn, and M. M. Murnane.  
*Attosecond Time-Scale Intra-atomic Phase Matching of High Harmonic Generation.*  
Phys. Rev. Lett. **86**, 5458–5461 (2001).
- [124] M. B. Gaarde, F. Salin, E. Constant, P. Balcou, K. J. Schafer, K. C. Kulander, and A. L'Huillier.  
*Spatiotemporal separation of high harmonic radiation into two quantum path components.*  
Phys. Rev. A **59**, 1367–1373 (1999).
- [125] P. Balcou, A. S. Dederichs, M. B. Gaarde, and A. L'Huillier.  
*Quantum-path analysis and phase matching of high-order harmonic generation and high-order frequency mixing processes in strong laser fields.*  
J. Phys. B **32**, 2973–2989 (1999).
- [126] M. Lewenstein, P. Salières, and A. L'Huillier.  
*Phase of the atomic polarization in high-order harmonic generation.*  
Phys. Rev. A **52**, 4747–4753 (1995).
- [127] M. Bellini, C. Lyngå, A. Tozzi, M. Gaarde, T. Hänsch, A. L'Huillier, and C.-G. Wahlström.  
*Temporal Coherence of Ultrashort High-Order Harmonic Pulses.*  
Phys. Rev. Lett. **81**, 297–300 (1998).
- [128] D. G. Lee, J. H. Kim, K. H. Hong, and C. H. Nam.  
*Coherent control of high-order harmonics with chirped femtosecond laser pulses.*  
Phys. Rev. Lett. **87**, 243902 (2001).
- [129] H. T. Kim, D. G. Lee, K. H. Hong, J. H. Kim, I. W. Choi, and C. H. Nam.  
*Continuously tunable high-order harmonics from atoms in an intense femtosecond laser field.*  
Phys. Rev. A **67**, 051801 (2003).
- [130] M. Wollenhaupt, A. Assion, D. Liese, C. Sarpe-Tudoran, T. Baumert, S. Zamith, M. A. Bouchene, B. Girard, A. Flettner, U. Weichmann, and G. Gerber.  
*Interferences of ultrashort free electron wave packets.*  
Phys. Rev. Lett. **89**, 173001 (2002).

- [131] K. Burnett, V. C. Reed, J. Cooper, and P. L. Knight.  
*Calculation of the background emitted during high-harmonic generation.*  
Phys. Rev. A **45**, 3347–3349 (1992).
- [132] A. D. Bandrauk and H. Yu.  
*High-order harmonic generation by one- and two-electron molecular ions with intense laser pulses.*  
Phys. Rev. A **59**, 539–548 (1999).
- [133] J. Prager, S. X. Hu, and C. H. Keitel.  
*High-order regime of harmonic generation with two active electrons.*  
Phys. Rev. A **6404**, 045402 (2001).
- [134] S. P. Tewari and G. S. Agarwal.  
*Control of Phase Matching and Nonlinear Generation in Dense Media by Resonant Fields.*  
Phys. Rev. Lett. **56**, 1811–1814 (1986).
- [135] K. J. Boller, A. Imamoglu, and S. E. Harris.  
*Observation of Electromagnetically Induced Transparency.*  
Phys. Rev. Lett. **66**, 2593–2596 (1991).
- [136] A. Rundquist, C. G. Durfee III, Z. Chang, C. Herne, S. Backus, M. M. Murnane, and H. C. Kapteyn.  
*Phase-Matched Generation of Coherent Soft X-rays.*  
Science **280**, 1412–1415 (1998).
- [137] M. Schnürer, Z. Cheng, S. Sartania, M. Hentschel, G. Tempea, T. Brabec, and F. Krausz.  
*Guiding and high-harmonic generation of sub-10-fs pulses in hollow-core fibers at  $10^{15}$  W/cm<sup>2</sup>.*  
Appl. Phys. B **67**, 263–266 (1998).
- [138] C. G. Durfee III, A. R. Rundquist, S. Backus, C. Herne, M. M. Murnane, and H. C. Kapteyn.  
*Phase Matching of High-Order Harmonics in Hollow Waveguides.*  
Phys. Rev. Lett. **83**, 2187–2190 (1999).
- [139] Y. Tamaki, Y. Nagata, M. Obara, and K. Midorikawa.  
*Phase-matched high-order-harmonic generation in a gas-filled hollow fiber.*  
Phys. Rev. A **59**, 4041–4044 (1999).
- [140] E. A. J. Marcatili and R. A. Schmeltzer.  
*Hollow Metallic and Dielectric Waveguides for Long Distance Optical Transmission and Lasers.*  
The Bell System Techn. J. pp. 1783–1809 (1964).
- [141] P. Salières, A. L’Huillier, and M. Lewenstein.  
*Coherence Control of High-Order Harmonics.*  
Phys. Rev. Lett. **74**, 3776–3779 (1995).
- [142] M. Nisoli, E. Priori, G. Sansone, S. Stagira, G. Cerullo, S. DeSilvestri, C. Altucci, R. Bruzzese, C. de Lisio, P. Villoresi, L. Poletto, M. Pascolini, and G. Tondello.  
*High-brightness high-order harmonic generation by truncated Bessel beams in the sub-10-fs regime.*  
Phys. Rev. Lett. **88**, 033902 (2002).
- [143] Lawrence Berkeley Laboratory.  
*Atomic Scattering Factors.*  
Webpage <http://www-cxro.lbl.gov/opticalconstants> (2001).
- [144] R. A. Bartels, A. Paul, H. Green, H. C. Kapteyn, M. M. Murnane, S. Backus, I. P. Christov, Y. W. Liu, D. Attwood, and C. Jacobsen.  
*Generation of spatially coherent light at extreme ultraviolet wavelengths.*  
Science **297**, 376–378 (2002).
- [145] J. Zhou, J. Peatross, M. M. Murnane, H. C. Kapteyn, and I. P. Christov.  
*Enhanced High-Harmonic Generation Using 25 fs Laser Pulses.*  
Phys. Rev. Lett. **76**, 752–755 (1996).

- [146] I. P. Christov, J. Zhou, A. Rundquist, M. M. Murnane, and H. C. Kapteyn.  
*Nonadiabatic Effects in High-Harmonic Generation with Ultrashort Pulses.*  
Phys. Rev. Lett. **77**, 1743–1746 (1996).
- [147] C. Spielmann, N. H. Burnett, S. Sartania, R. Koppitsch, M. Schnürer, C. Kan, M. Lenzner, P. Wobrauschek, and F. Krausz.  
*Generation of Coherent X-rays in the Water Window Using 5-Femosecond Laser Pulses.*  
Science **278**, 661–664 (1997).
- [148] C. Kan, N. H. Burnett, C. E. Capjack, and R. Rankin.  
*Coherent XUV generation from Gases Ionized by Several Cycle Optical Pulses.*  
Phys. Rev. Lett. **79**, 2971–2974 (1997).
- [149] M. Kakehata, H. Takada, K. Miyazaki, H. Kono, I. Kawata, and Y. Fujimura.  
*Effects of laser pulsewidth on higher-order harmonic generation in the barrier-suppression-ionization regime.*  
Appl. Phys. B **70**, 219–224 (2000).
- [150] M. Nisoli, S. Stagira, G. Cerullo, S. D. Silvestri, O. Svelto, P. Ceccherini, L. Poletto, G. Tondello, C. A. P. Villaresi, R. Bruzzese, and C. Lisio.  
*Spectral analysis of high-order harmonics generated by 30-fs and sub-10-fs laser pulses.*  
Appl. Phys. B **70**, 215–220 (2000).
- [151] P. Chessa, E. D. Wispelaere, F. Dorchies, V. Malka, J. R. Marques, G. Hamoniaux, P. Mora, and F. Amiranoff.  
*Temporal and angular resolution of the ionization-induced refraction of a short laser pulse in helium gas.*  
Phys. Rev. Lett. **82**, 552–555 (1999).
- [152] Y. Tamaki, J. Itatani, Y. Nagata, M. Obara, and K. Midorikawa.  
*Highly efficient, phase-matched high-harmonic generation by a self-guided laser beam.*  
Phys. Rev. Lett. **82**, 1422–1425 (1999).
- [153] V. Tosa, E. Takahashi, Y. Nabekawa, and K. Midorikawa.  
*Generation of high-order harmonics in a self-guided beam.*  
Phys. Rev. A **67**, 063817 (2003).
- [154] E. Constant, D. Garzella, P. Breger, E. Mevel, C. Dorrer, C. LeBlanc, F. Salin, and P. Agostini.  
*Optimizing High Harmonic Generation in Absorbing Gases: Model and Experiment.*  
Phys. Rev. Lett. **82**, 1668–1671 (1999).
- [155] M. Schnürer, Z. Cheng, M. Hentschel, G. Tempea, P. Kálmán, T. Brabec, and F. Krausz.  
*Absorption-Limited Generation of Coherent Ultrashort Soft-X-Ray Pulses.*  
Phys. Rev. Lett. **83**, 722–725 (1999).
- [156] M. Schnürer, Z. Cheng, M. Hentschel, F. Krausz, T. Wilhein, D. Hambach, G. Schmahl, M. Drescher, Y. Lim, and U. Heinzmann.  
*Few-cycle-driven XUV laser harmonics: generation and focusing.*  
Appl. Phys. B **70**, S227–S232 (2000).
- [157] N. Zhavoronkov and G. Korn.  
*Generation of single intense short optical pulses by ultrafast molecular phase modulation.*  
Phys. Rev. Lett. **88**, 203901 (2002).
- [158] D. D. Yavuz, D. R. Walker, M. Y. Shverdin, G. Y. Yin, and S. E. Harris.  
*Quasiperiodic Raman technique for ultrashort pulse generation.*  
Phys. Rev. Lett. **91**, 233602 (2003).
- [159] V. Kalosha, M. Spanner, J. Herrmann, and M. Ivanov.  
*Generation of single dispersion precompensated 1-fs pulses by shaped-pulse optimized high-order stimulated Raman scattering.*  
Phys. Rev. Lett. **88**, 103901 (2002).

- [160] K. J. Schafer and K. C. Kulander.  
*High Harmonic Generation from Ultrafast Pump Lasers.*  
Phys. Rev. Lett. **78**, 638–641 (1997).
- [161] P. Antoine, A. L’Huillier, and M. Lewenstein.  
*Attosecond Pulse Trains Using High-Order Harmonics.*  
Phys. Rev. Lett. **77**, 1234–1237 (1996).
- [162] N. A. Papadogiannis, B. Witzel, C. Kalpouzos, and D. Charalambidis.  
*Observation of Attosecond Light Localization in Higher Order Harmonic Generation.*  
Phys. Rev. Lett. **83**, 4289–4292 (1999).
- [163] P. M. Paul, E. S. Toma, P. Breger, G. Mullot, F. Augé, P. Balcou, H. G. Muller, and P. Agostini.  
*Observation of a Train of Attosecond Pulses from High Harmonic Generation.*  
Science **292**, 1689–1692 (2001).
- [164] Y. Mairesse, A. de Bohan, L. J. Frasinski, H. Merdji, L. C. Dinu, P. Monchicourt, P. Breger, M. Kovačev, R. Taïeb, B. Carré, H. G. Muller, P. Agostini, and P. Salières.  
*Attosecond synchronization of high-harmonic soft x-rays.*  
Science **302**, 1540–1543 (2003).
- [165] P. B. Corkum, N. H. Burnett, and M. Y. Ivanov.  
*Subfemtosecond pulses.*  
Opt. Lett. **19**, 1870–1872 (1994).
- [166] K. Budil, P. Salières, A. L’Huillier, T. Ditmire, and M. Perry.  
*Influence of ellipticity on harmonic generation.*  
Phys. Rev. A **48**, R3437–R3440 (1993).
- [167] O. Tcherbakoff, E. Mevel, D. Descamps, J. Plumridge, and E. Constant.  
*Time-gated high-order harmonic generation.*  
Phys. Rev. A **68** (2003).
- [168] M. Ivanov, P. B. Corkum, T. Zuo, and A. Bandrauk.  
*Routes to Control of Intense-Field Atomic Polarizability.*  
Phys. Rev. Lett. **74**, 2933–2936 (1995).
- [169] I. P. Christov, M. M. Murnane, and H. C. Kapteyn.  
*High-harmonic generation of attosecond pulses in the "single-cycle" regime.*  
Phys. Rev. Lett. **78**, 1251–1254 (1997).
- [170] M. Drescher, M. Hentschel, R. Kienberger, G. Tempea, C. Spielmann, G. A. Reider, P. B. Corkum, and F. Krausz.  
*X-ray Pulses Approaching the Attosecond Frontier.*  
Science **291**, 1923–1927 (2001).
- [171] M. Hentschel, R. Kienberger, C. Spielmann, G. A. Reider, N. Milosevic, T. Brabec, P. Corkum, U. Heinzmann, M. Drescher, and F. Krausz.  
*Attosecond metrology.*  
Nature **414**, 509–513 (2001).
- [172] J. A. R. Samson.  
*Techniques of Vacuum Ultraviolet Spectroscopy.*  
John Wiley & Sons, Inc., New York - London - Sydney (1967).
- [173] D. T. Attwood.  
*Soft X-Rays and Extreme Ultraviolet Radiation: Principles and Applications.*  
Cambridge University Press, Cambridge (1999).
- [174] F. L. Kien, K. Midorikawa, and A. Suda.  
*Attosecond pulse generation using high harmonics in the multicycle regime of the driver pulse.*  
Phys. Rev. A **58**, 3311–3319 (1998).

- [175] A. Pukhov, S. Gordienko, and T. Baeva.  
*Temporal structure of attosecond pulses from intense laser-atom interactions.*  
Phys. Rev. Lett. **91**, 173002 (2003).
- [176] G. Tempea, M. Geissler, and T. Brabec.  
*Phase sensitivity of high-order harmonic generation with few-cycle laser pulses.*  
J. Opt. Soc. Am. B **16**, 669–673 (1999).
- [177] V. S. Yakovlev and A. Scrinzi.  
*High harmonic imaging of few-cycle laser pulses.*  
Phys. Rev. Lett. **91**, 153901 (2003).
- [178] T. Brixner.  
*Adaptive Femtosecond Quantum Control.*  
Dissertation, Universität Würzburg (2001).
- [179] P. Tzallas, D. Charalambidis, N. A. Papadogiannis, K. Witte, and G. D. Tsakiris.  
*Direct observation of attosecond light bunching.*  
Nature **426**, 267–271 (2003).
- [180] M. Y. Schelev, M. C. Richards, and A. J. Alcock.  
*Image-Converter Streak Camera with Picosecond Resolution.*  
Appl. Phys. Lett. **18**, 354 (1971).
- [181] D. J. Bradley, B. Liddy, and W. E. Sleat.  
*Direct linear measurement of ultrashort light pulses with a picosecond streak camera.*  
Opt. Comm. **2**, 391–395 (1971).
- [182] E. Constant, V. D. Taranukhin, A. Stolow, and P. B. Corkum.  
*Methods for the measurement of the duration of high-harmonic pulses.*  
Phys. Rev. A **56**, 3870–3878 (1997).
- [183] R. Kienberger, M. Hentschel, C. Spielmann, G. A. Reider, N. Milosevic, U. Heinzmann, M. Drescher, and F. Krausz.  
*Sub-femtosecond X-ray pulse generation and measurement.*  
Appl. Phys. B **74**, S3–S9 (2002).
- [184] J. Itatani, F. Quéré, G. L. Yudin, M. Y. Ivanov, F. Krausz, and P. B. Corkum.  
*Attosecond streak camera.*  
Phys. Rev. Lett. **88**, 173903 (2002).
- [185] M. Kitzler, N. Milosevic, A. Scrinzi, F. Krausz, and T. Brabec.  
*Quantum theory of attosecond XUV pulse measurement by laser dressed photoionization.*  
Phys. Rev. Lett. **88**, 173904 (2002).
- [186] J. Norin, J. Mauritsson, A. Johansson, M. K. Raarup, S. Buil, A. Persson, O. Dühr, M. B. Gaarde, K. J. Schafer, U. Keller, C. G. Wahlström, and A. L’Huillier.  
*Time-frequency characterization of femtosecond extreme ultraviolet pulses.*  
Phys. Rev. Lett. **88**, 193901 (2002).
- [187] F. Quéré, J. Itatani, G. L. Yudin, and P. B. Corkum.  
*Attosecond spectral shearing interferometry.*  
Phys. Rev. Lett. **90**, 073902 (2003).
- [188] T. Sekikawa, T. Kanai, and S. Watanabe.  
*Frequency-resolved optical gating of femtosecond pulses in the extreme ultraviolet.*  
Phys. Rev. Lett. **91**, 103902 (2003).
- [189] T. Sekikawa, T. Katsura, S. Miura, and S. Watanabe.  
*Measurement of the intensity-dependent atomic dipole phase of a high harmonic by frequency-resolved optical gating.*  
Phys. Rev. Lett. **88**, 193902 (2002).

- [190] A. D. Bandrauk, S. Chelkowski, and N. H. Shon.  
*How to measure the duration of subfemtosecond XUV laser pulses using asymmetric photoionization.*  
Phys. Rev. A **68**, 041802 (2003).
- [191] E. Goulielmakis, G. Nersisyan, N. A. Papadogiannis, D. Charalambidis, G. D. Tsakiris, and K. Witte.  
*A dispersionless Michelson interferometer for the characterization of attosecond pulses.*  
Appl. Phys. B **74**, 197–206 (2002).
- [192] L. H. Yu, M. Babzien, I. B. Zvi, L. F. DiMauro, A. Doyuran, W. Graves, E. Johnson, S. Krinsky, R. Malone, I. Pogorelsky, J. Skaritka, G. Rakowsky, L. Solomon, X. J. Wang, M. Woodle, V. Yakimenko, S. G. Biedron, J. N. Galayda, E. Gluskin, J. Jagger, V. Sajaev, and I. Vasserman.  
*High-gain harmonic-generation free-electron laser.*  
Science **289**, 932–934 (2000).
- [193] L. H. Yu, L. DiMauro, A. Doyuran, W. S. Graves, E. D. Johnson, R. Heese, S. Krinsky, H. Loos, J. B. Murphy, G. Rakowsky, J. Rose, T. Shaftan, B. Sheehy, J. Skaritka, X. J. Wang, and Z. Wu.  
*First ultraviolet high-gain harmonic-generation free-electron laser.*  
Phys. Rev. Lett. **91**, 074801 (2003).
- [194] M. M. Murnane, H. C. Kapteyn, M. D. Rosen, and R. W. Falcone.  
*Ultrafast X-Ray Pulses from Laser-Produced Plasmas.*  
Science **251**, 531–536 (1991).
- [195] R. Kienberger, E. Goulielmakis, M. Uiberacker, A. Baltuška, V. Yakovlev, F. Bammer, A. Scrinzi, T. Westerwalbesloh, U. Kleineberg, U. Heinzmann, M. Drescher, and F. Krausz.  
*Atomic transient recorder.*  
Nature **427**, 817–821 (2004).
- [196] A. D. Bandrauk, S. Chelkowski, and N. H. Shon.  
*Measuring the electric field of few-cycle laser pulses by attosecond cross correlation.*  
Phys. Rev. Lett. **89**, 283903 (2002).
- [197] R. Kienberger, M. Hentschel, M. Uiberacker, C. Spielmann, M. Kitzler, A. Scrinzi, M. Wieland, T. Westerwalbesloh, U. Kleineberg, U. Heinzmann, M. Drescher, and F. Krausz.  
*Steering attosecond electron wave packets with light.*  
Science **297**, 1144–1148 (2002).
- [198] M. Drescher, M. Hentschel, R. Kienberger, M. Uiberacker, V. Yakovlev, A. Scrinzi, T. Westerwalbesloh, U. Kleineberg, U. Heinzmann, and F. Krausz.  
*Time-resolved atomic inner-shell spectroscopy.*  
Nature **419**, 803–807 (2002).
- [199] T. Shimizu, T. Sekikawa, T. Kanai, S. Watanabe, and M. Itoh.  
*Time-resolved Auger decay in CsBr using high harmonics.*  
Phys. Rev. Lett. **91**, 017401 (2003).
- [200] L. Nugent-Glandorf, M. Scheer, D. A. Samuels, A. M. Mulhisen, E. R. Grant, X. M. Yang, V. M. Bierbaum, and S. R. Leone.  
*Ultrafast time-resolved soft x-ray photoelectron spectroscopy of dissociating Br<sub>2</sub>.*  
Phys. Rev. Lett. **8719**, 193002 (2001).
- [201] L. Nugent-Glandorf, M. Scheer, D. A. Samuels, V. M. Bierbaum, and S. R. Leone.  
*Ultrafast photodissociation of Br<sub>2</sub>: Laser-generated high-harmonic soft x-ray probing of the transient photoelectron spectra and ionization cross sections.*  
J. Chem. Phys. **117**, 6108–6116 (2002).
- [202] S. Cavalieri, R. Eramo, M. Materazzi, C. Corsi, and M. Bellini.  
*Ramsey-type spectroscopy with high-order harmonics.*  
Phys. Rev. Lett. **89**, 133002 (2002).



- [203] T. Sekikawa, T. Yamazaki, Y. Nabekawa, and S. Watanabe.  
*Femtosecond lattice relaxation induced by inner-shell excitation.*  
J. Opt. Soc. Am. B **19**, 1941–1945 (2002).
- [204] J. F. Hergott, T. Auguste, P. Salières, L. L. Déroff, P. Monot, P. d’Oliveira, D. Campo, H. Merdji, and B. Carré.  
*Application of frequency-domain interferometry in the extreme-ultraviolet range by use of high-order harmonics.*  
J. Opt. Soc. Am. B **20**, 171–181 (2003).
- [205] M. Schnürer, C. Strelly, P. Wobaruschek, M. Hentschel, R. Kienberger, C. Spielmann, and F. Krausz.  
*Femtosecond X-Ray Fluorescence.*  
Phys. Rev. Lett. **85**, 3392–3395 (2000).
- [206] T. Sekikawa, T. Ohno, Y. Nabekawa, and S. Watanabe.  
*Auger-free luminescence excited by high-order harmonics of a femtosecond Ti:sapphire laser.*  
J. Luminesc **87-89**, 827–829 (2000).
- [207] G. Tsilimis, C. Benesch, J. Kutzner, and H. Zacharias.  
*Laser based soft-x-ray pulses for photoelectron spectroscopy of surfaces.*  
J. Opt. Soc. Am. B **20**, 246–253 (2003).
- [208] G. Tsilimis, J. Kutzner, and H. Zacharias.  
*Photoemission study of clean and c(4 x 2)-2CO-covered Pt (111) using high-harmonic radiation.*  
Applied Physics A-Materials Science & Processing **76**, 743–749 (2003).
- [209] M. Wieland, R. Frueke, T. Wilhein, C. Spielmann, M. Pohl, and U. Kleineberg.  
*Submicron extreme ultraviolet imaging using high-harmonic radiation.*  
Appl. Phys. Lett. **81**, 2520–2522 (2002).
- [210] M. Wieland, T. Wilhein, C. Spielmann, and U. Kleineberg.  
*Zone-plate interferometry at 13 nm wavelength.*  
Appl. Phys. B **76**, 885–889 (2003).
- [211] C. Valentin, D. Douillet, S. Kazamias, T. Lefrou, G. Grillon, F. Augé, G. Mullot, P. Balcou, P. Mercère, and P. Zeitoun.  
*Imaging and quality assessment of high-harmonic focal spots.*  
Opt. Lett. **28**, 1049–1051 (2003).
- [212] N. A. Papadogiannis, L. A. A. Nikolopoulos, D. Charalambidis, G. D. Tsakiris, P. Tzallas, and K. Witte.  
*Two-photon ionization of He through a superposition of higher harmonics.*  
Phys. Rev. Lett. **90**, 133902 (2003).
- [213] E. Takahashi, Y. Nabekawa, T. Otsuka, M. Obara, and K. Midorikawa.  
*Generation of highly coherent submicrojoule soft x rays by high-order harmonics.*  
Phys. Rev. A **66**, 021802 (2002).
- [214] J.-F. Hergott, M. Kovacev, H. Merdji, C. Hubert, Y. Mairesse, E. Jean, P. Breger, P. Agostini, B. Carré, and P. Salières.  
*Extreme-ultraviolet high-order harmonic pulses in the microjoule range.*  
Phys. Rev. A **66**, 021801(R) (2002).
- [215] E. Takahashi, Y. Nabekawa, M. Nurhuda, and K. Midorikawa.  
*Generation of high-energy high-order harmonics by use of a long interaction medium.*  
J. Opt. Soc. Am. B **20**, 158–165 (2003).
- [216] F. Lindner, W. Stremme, M. G. Schätzel, F. Grasbon, G. G. Paulus, H. Walther, R. Hartmann, and L. Strüder.  
*High-order harmonic generation at a repetition rate of 100 kHz.*  
Phys. Rev. A **68**, 013814 (2003).

- [217] B. Shan, A. Cavalieri, and Z. Chang.  
*Tunable high harmonic generation with an optical parametric amplifier.*  
Appl. Phys. B **74**, S23–S26 (2002).
- [218] D. H. Reitze, S. Kazamias, F. Weihe, G. Mullot, D. Douillet, F. Augé, O. Albert, V. Ramanathan, J. P. Chambaret, D. Hulin, and P. Balcou.  
*Enhancement of high-order harmonic generation at tuned wavelengths through adaptive control.*  
Opt. Lett. **29**, 86–88 (2004).
- [219] Z. Chang, A. Rundquist, H. Wang, M. M. Murnane, and H. C. Kapteyn.  
*Generation of Coherent Soft X Rays at 2.7 nm Using High Harmonics.*  
Phys. Rev. Lett. **79**, 2967–2970 (1997).
- [220] L. X. Chen, W. J. H. Jäger, G. Jennings, D. J. Gosztola, A. Munkholm, and J. P. Hessler.  
*Capturing a photoexcited molecular structure through time-domain X-ray absorption fine structure.*  
Science **292**, 262–264 (2001).
- [221] M. Saes, C. Bressler, R. Abela, D. Grolimund, S. L. Johnson, P. A. Heimann, and M. Chergui.  
*Observing photochemical transients by ultrafast x-ray absorption spectroscopy.*  
Phys. Rev. Lett. **90**, 047403 (2003).
- [222] T. E. Glover, G. D. Ackerman, A. Belkacem, P. A. Heimann, Z. Hussain, R. W. Lee, H. A. Padmore, C. Ray, R. W. Schoenlein, W. F. Steele, and D. A. Young.  
*Metal-insulator transitions in an expanding metallic fluid: Particle formation kinetics.*  
Phys. Rev. Lett. **90**, 236102 (2003).
- [223] S. L. Johnson, P. A. Heimann, A. M. Lindenberg, H. O. Jeschke, M. E. Garcia, Z. Chang, R. W. Lee, J. J. Rehr, and R. W. Falcone.  
*Properties of liquid silicon observed by time-resolved x-ray absorption spectroscopy.*  
Phys. Rev. Lett. **91**, 157403 (2003).
- [224] F. Schotte, M. H. Lim, T. A. Jackson, A. V. Smirnov, J. Soman, J. S. Olson, G. N. Phillips, M. Wulff, and P. A. Anfinrud.  
*Watching a protein as it functions with 150-ps time-resolved X-ray crystallography.*  
Science **300**, 1944–1947 (2003).
- [225] A. H. Chin, R. W. Schoenlein, T. E. Glover, P. Balling, W. P. Leemans, and C. V. Shank.  
*Ultrafast structural dynamics in InSb probed by time-resolved x-ray diffraction.*  
Phys. Rev. Lett. **83**, 336–339 (1999).
- [226] R. W. Schoenlein, S. Chattopadhyay, H. H. W. Chong, T. E. Glover, P. A. Heimann, C. V. Shank, A. A. Zholents, and M. S. Zolotarev.  
*Generation of femtosecond pulses of synchrotron radiation.*  
Science **287**, 2237–2240 (2000).
- [227] M. F. Decamp, D. A. Reis, P. H. Bucksbaum, B. Adams, J. M. Caraher, R. Clarke, C. W. S. Conover, E. M. Dufresne, R. Merlin, V. Stoica, and J. K. Wahlstrand.  
*Coherent control of pulsed X-ray beams.*  
Nature **413**, 825–828 (2001).
- [228] J. Andruszkow *et al.*  
*First observation of self-amplified spontaneous emission in a free-electron laser at 109 nm wavelength.*  
Phys. Rev. Lett. **85**, 3825–3829 (2000).
- [229] H. Wabnitz, L. Bittner, A. R. B. de Castro, R. Dohrmann, P. Gurtler, T. Laarmann, W. Laasch, J. Schulz, A. Swiderski, K. von Haefen, T. Moller, B. Faatz, A. Fateev, J. Feldhaus, C. Gerth, U. Hahn, E. Saldin, E. Schneidmiller, K. Sytchev, K. Tiedtke, R. Treusch, and M. Yurkov.  
*Multiple ionization of atom clusters by intense soft X-rays from a free-electron laser.*  
Nature **420**, 482–485 (2002).

- [230] R. Santra and C. H. Greene.  
*Xenon clusters in intense VUV laser fields.*  
Phys. Rev. Lett. **91**, 233401 (2003).
- [231] A. Rousse, P. Audebert, J. P. Geindre, F. Fallies, J. C. Gauthier, A. Mysyrowicz, G. Grillon, and A. Antonetti.  
*Efficient K-Alpha-X-Ray Source from Femtosecond Laser-Produced Plasmas.*  
Phys. Rev. E **50**, 2200–2207 (1994).
- [232] Y. Jiang, T. Lee, and C. G. Rose-Petruck.  
*Structure of solvated Fe(CO)<sub>5</sub>: FTIR measurements and density functional theory calculations.*  
J. Phys. Chem. A **107**, 7524–7538 (2003).
- [233] C. Rose-Petruck, R. Jimenez, T. Guo, A. Cavalleri, C. W. Siders, F. Ráksi, B. J. A. Squier, K. R. Wilson, and C. P. J. Barty.  
*Picosecond-milliångström lattice dynamics by ultrafast X-ray diffraction.*  
Nature **398**, 310–312 (1999).
- [234] K. Sokolowski-Tinten, C. Blome, J. Blums, A. Cavalleri, C. Dietrich, A. Tarasevitch, I. Uschmann, E. Förster, M. Kammler, M. H. von Hoegen, and D. der Linde.  
*Femtosecond X-ray measurement of coherent lattice vibrations near the Lindemann stability limit.*  
Nature **422**, 287–289 (2003).
- [235] C. W. Siders, A. Cavalleri, K. Sokolowski-Tinten, C. Tóth, T. Guo, M. Kammler, M. H. von Hoegen, K. R. Wilson, D. der Linde, and C. P. J. Barty.  
*Detection of nonthermal melting by ultrafast X-ray diffraction.*  
Science **286**, 1340–1342 (1999).
- [236] K. Sokolowski-Tinten, C. Blome, C. Dietrich, A. Tarasevitch, M. H. von Hoegen, D. der Linde, A. Cavalleri, J. Squier, and M. Kammler.  
*Femtosecond x-ray measurement of ultrafast melting and large acoustic transients.*  
Phys. Rev. Lett. **8722**, 225701 (2001).
- [237] C. Rischel, A. Rousse, I. Uschmann, P. A. Albouy, J. P. Geindre, P. Audebert, J. C. Gauthier, E. Förster, J. L. Martin, and A. Antonetti.  
*Femtosecond time-resolved X-ray diffraction from laser-heated organic films.*  
Nature **390**, 490–492 (1997).
- [238] F. Ráksi, K. R. Wilson, Z. M. Jiang, A. Ikhlef, C. Y. Côté, and J. C. Kieffer.  
*Ultrafast x-ray absorption probing of a chemical reaction.*  
J. Chem. Phys. **104**, 6066–6069 (1996).
- [239] J. Y. Liu, J. Wang, B. Shan, C. Wang, and Z. H. Chang.  
*An accumulative x-ray streak camera with sub-600-fs temporal resolution and 50-fs timing jitter.*  
Appl. Phys. Lett. **82**, 3553–3555 (2003).
- [240] S. Kazamias, D. Douillet, F. Weihe, C. Valentin, A. Rousse, S. Sebban, Grillon, F. Augé, D. Hulin, and P. Balcou.  
*Global Optimization of High Harmonic Generation.*  
Phys. Rev. Lett. **90**, 193901 (2003).
- [241] D. von der Linde, T. Engers, G. Jenke, P. Agostini, E. N. G. Grillon, A. Mysyrowicz, and A. Antonetti.  
*Generation of high-order harmonics from solid surfaces by intense femtosecond laser pulses.*  
Phys. Rev. A **52**, R25–R27 (1995).
- [242] P. A. Norreys, M. Zepf, S. Moustazis, A. P. Fews, P. L. J. Zhang, M. Bakarezos, C. N. Danson, A. Dyson, P. L. P. Gibbon, D. Neely, F. N. Walsh, J. S. Wark, and A. E. Dangor.  
*Efficient Extreme UV Harmonics Generated from Picosecond Laser Pulse Interactions with Solid Targets.*  
Phys. Rev. Lett. **76**, 1832–1835 (1996).

- [243] K. Z. Hatsagortsyan and C. H. Keitel.  
*Phase-matched high-harmonic generation from laser-driven crystals.*  
J. Phys. B **35**, L175–L180 (2002).
- [244] T. D. Donnelly, T. Ditmire, K. Neuman, M. D. Perry, and R. W. Falcone.  
*High-Order Harmonic Generation in Atom Clusters.*  
Phys. Rev. Lett. **76**, 2472–2475 (1996).
- [245] J. W. G. Tisch, T. Ditmire, D. J. Fraser, N. Hay, M. B. Mason, J. P. M. E. Springate, and M. H. R. Hutchinson.  
*Investigation of high-harmonic generation from xenon atom clusters.*  
J. Phys. B **30**, L709–L714 (1997).
- [246] J. W. G. Tisch.  
*Phase-matched high-order harmonic generation in an ionized medium using a buffer gas of exploding atomic clusters.*  
Phys. Rev. A **62**, 041802(R) (2000).
- [247] V. Vénier, R. Taïeb, and A. Maquet.  
*Simple model for harmonic generation from atomic clusters.*  
Phys. Rev. A **60**, 3952–3959 (1999).
- [248] H. Stapelfeldt and T. Seideman.  
*Colloquium: Aligning molecules with strong laser pulses.*  
Rev. Mod. Phys. **75**, 543–557 (2003).
- [249] R. Velotta, N. Hay, M. B. Mason, M. Castillejo, and J. P. Marangos.  
*High-Order Harmonic Generation in Aligned Molecules.*  
Phys. Rev. Lett. **87**, 183901 (2001).
- [250] M. Lein, N. Hay, R. Velotta, J. P. Marangos, and P. L. Knight.  
*Role of the intramolecular phase in high-harmonic generation.*  
Phys. Rev. Lett. **88**, 183903 (2002).
- [251] R. Kopold, W. Becker, and M. Kleber.  
*Model calculations of high-harmonic generation in molecular ions.*  
Phys. Rev. A **58**, 4022–4038 (1998).
- [252] R. Numico, P. Moreno, L. Plaja, and L. Roso.  
*High-order harmonic generation after photodissociation.*  
J. Phys. B **31**, 4163–4171 (1998).
- [253] T. Zuo, S. Chelkowski, and A. D. Bandrauk.  
*Harmonic generation by the  $H_2^+$  molecular ion in intense laser fields.*  
Phys. Rev. A **48**, 3837–3844 (1993).
- [254] M. Y. Ivanov and P. B. Corkum.  
*Generation of high-order harmonics from inertially confined molecular ions.*  
Phys. Rev. A **48**, 580–590 (1993).
- [255] A. D. Bandrauk, S. Chelkowski, and H. S. Nguyen.  
*Controlling continuum harmonic generation with attosecond pulses.*  
Appl. Phys. B **77**, 337–342 (2003).
- [256] T. Kreibich, M. Lein, V. Engel, and E. K. U. Gross.  
*Even-Harmonic Generation due to Beyond-Born-Oppenheimer Dynamics.*  
Phys. Rev. Lett. **87**, 103901 (2001).
- [257] O. E. Alon, V. Averbukh, and N. Moiseyev.  
*Selection Rules for the High Harmonic Generation Spectra.*  
Phys. Rev. Lett. **80**, 3743–3746 (1998).

- [258] Y. Liang, S. Augst, S. L. Chin, Y. Beaudoin, and M. Chaker.  
*High harmonic-generation in atomic and diatomic molecular gases using intense picosecond laser pulses – a comparison.*  
J. Phys. B: At. Mol. Opt. Phys. **27**, 5119–5130 (1994).
- [259] H. Sakai and K. Miyazaki.  
*High-order harmonic generation in nitrogen molecules with subpicosecond visible dye-laser pulses.*  
Appl. Phys. B **61**, 493–498 (1995).
- [260] D. J. Fraser, M. H. R. Hutchinson, Y. L. Shao, J. W. G. Tisch, and M. Castillejo.  
*High harmonic generation in butane and butadiene.*  
J. Phys. B: At. Mol. Opt. Phys. **28**, L739–L745 (1995).
- [261] C. Lyngå, A. L’Huillier, and C.-G. Wahlström.  
*High-order harmonic generation in molecular gases.*  
J. Phys. B **29**, 3293–3302 (1996).
- [262] N. Hay, R. de Nalda, T. Halfmann, K. J. Mendham, M. B. Mason, M. Castillejo, and J. P. Marangos.  
*Pulse-length dependence of high-order harmonic generation in dissociating cyclic organic molecules.*  
Phys. Rev. A **62**, 041803(R) (2000).
- [263] Y. Liang, M. V. Ammosov, and S. L. Chin.  
*High-order harmonic generation in argon by elliptically polarized picosecond dye laser pulses.*  
J. Phys. B **27**, 1269–1276 (1994).
- [264] P. Antoine, B. Carré, A. L’Huillier, and M. Lewenstein.  
*Polarization of high-order harmonics.*  
Phys. Rev. A **55**, 1314–1324 (1997).
- [265] N. Hay, R. de Nalda, T. Halfmann, K. J. Mendham, M. B. Mason, M. Castillejo, and J. P. Marangos.  
*High-order harmonic generation from organic molecules in ultra-short pulses.*  
Europ. Phys. J. D **14**, 231–240 (2001).
- [266] N. Hay, M. Castillejo, R. de Nalda, E. Springate, K. J. Mendham, and J. P. Marangos.  
*High-order harmonic generation in cyclic organic molecules.*  
Phys. Rev. A **61**, 053810 (2000).
- [267] N. H. Burnett, C. Kan, and P. B. Corkum.  
*Ellipticity and polarization effects in harmonic generation in ionizing neon.*  
Phys. Rev. A **51**, R3418–R3421 (1995).
- [268] P. Dietrich, N. H. Burnett, M. Ivanov, and P. B. Corkum.  
*High-harmonic generation and correlated two-electron multiphoton ionization with elliptically polarized light.*  
Phys. Rev. A **50**, R3585–R3588 (1994).
- [269] H. J. Lehmeier, W. Leupacher, and A. Penzkofer.  
*Nonresonant third order hyperpolarizability of rare gases and N<sub>2</sub> determined by third harmonic generation.*  
Opt. Comm. **56**, 67–72 (1985).
- [270] F. A. Weihe and P. H. Bucksbaum.  
*Measurement of the polarization state of high harmonics generated in gases.*  
J. Opt. Soc. Am. B **13**, 157–161 (1996).
- [271] D. Proch and T. Trickl.  
*A high-intensity multi-purpose piezoelectric pulsed molecular beam source.*  
Rev. Sci. Instrum. **60**, 713–716 (1989).

- [272] C. Reusch.  
*Erzeugung hoher Harmonischer an Atomen und Molekülen in intensiven Femtosekunden-Laserfeldern.*  
Diplomarbeit, Universität Würzburg (1999).
- [273] K. Miyazaki and H. Takada.  
*High-order harmonic generation in the tunneling regime.*  
Phys. Rev. A **52**, 3007–3021 (1995).
- [274] M. Y. Ivanov, T. Brabec, and N. Burnett.  
*Coulomb corrections and polarization effects in high-intensity high-harmonic emission.*  
Phys. Rev. A **54**, 742–745 (1996).
- [275] N. Hay, R. Velotta, M. B. Mason, M. Castillejo, and J. P. Marangos.  
*High-order harmonic generation efficiency increased by controlled dissociation of molecular iodine.*  
J. Phys. B **35**, 1051–1060 (2002).
- [276] A. D. Bandrauk and N. H. Shon.  
*Attosecond control of ionization and high-order harmonic generation in molecules.*  
Phys. Rev. A **66**, 031401(R) (2002).
- [277] Q. Su, B. A. Smetanko, and R. Grobe.  
*Relativistic suppression of wave packet spreading.*  
Opt. Express **2**, 277–281 (1998).
- [278] A. Giusti-Suzor, F. H. Mies, L. F. DiMauro, E. Charron, and B. Yang.  
*Dynamics of  $H_2^+$  in Intense Laser Fields.*  
J. Phys. B **28**, 309–339 (1995).
- [279] J. A. Fleck, Jr., J. R. Morris, and M. D. Feit.  
*Time-Dependent Propagation of High-Energy Laser-Beams Through Atmosphere.*  
Appl. Phys. **10**, 129–160 (1976).
- [280] M. D. Feit, J. A. Fleck, Jr., and A. Steiger.  
*Solution of the Schrödinger equation by a spectral method.*  
J. Comput. Phys. **47**, 412–433 (1982).
- [281] M. Y. Emelin, M. Y. Ryabikin, A. M. Sergeev, M. D. Chernobrovtsseva, T. Pfeifer, D. Walter, and G. Gerber.  
*Attosecond Burst and High-Harmonic Generation in Molecular Ionization by Ultrashort Laser Pulses.*  
JETP Lett. **77**, 212–216 (2003).
- [282] A. Flettner, J. König, M. B. Mason, T. Pfeifer, U. Weichmann, R. Düren, and G. Gerber.  
*Ellipticity dependence of atomic and molecular high harmonic generation.*  
Europ. Phys. J. D **21**, 115–119 (2002).
- [283] A. Flettner, J. König, M. B. Mason, T. Pfeifer, U. Weichmann, and G. Gerber.  
*Atomic and molecular high-harmonic generation: A comparison of ellipticity dependence based on the three-step model.*  
J. Mod. Opt. **50**, 529–537 (2003).
- [284] T. Pfeifer, D. Walter, G. Gerber, M. Y. Emelin, M. Y. Ryabikin, M. D. Chernobrovtsseva, and A. M. Sergeev.  
*Transient Enhancement of High-Harmonic Generation in Expanding Molecules.*  
Manuscript in Preparation (2004).
- [285] S. Düsterer, H. Schwoerer, W. Ziegler, C. Ziener, and R. Sauerbrey.  
*Optimization of EUV radiation yield from laser-produced plasma.*  
Appl. Phys. B **73**, 693–698 (2001).

- [286] S. J. McNaught, J. Fan, E. Parra, and H. M. Milchberg.  
*A pump-probe investigation of laser-droplet plasma dynamics.*  
Appl. Phys. Lett. **79**, 4100–4102 (2001).
- [287] F. Courvoisier, V. Boutou, C. Favre, S. C. Hill, and J. P. Wolf.  
*Plasma formation dynamics within a water microdroplet on femtosecond time scales.*  
Opt. Lett. **28**, 206–208 (2003).
- [288] T. Ditmire, T. Donnelly, R. W. Falcone, and M. D. Perry.  
*Strong X-Ray Emission from High-Temperature Plasmas Produced by Intense Irradiation of Clusters.*  
Phys. Rev. Lett. **75**, 3122–3125 (1995).
- [289] T. Ditmire, T. Donnelly, A. M. Rubenchik, R. W. Falcone, and M. D. Perry.  
*Interaction of intense laser pulses with atomic clusters.*  
Phys. Rev. A **53**, 3379–3402 (1996).
- [290] R. Zürl and H. Graener.  
*High-harmonic generation of mid-IR pulses in simple liquids.*  
Appl. Phys. B **66**, 213–216 (1998).
- [291] A. Flettner.  
*Erzeugung von XUV Strahlung an Mikrotröpfchen und Interferenzen von freien Elektronen-Wellenpaketen.*  
Diplomarbeit, Universität Würzburg (2002).
- [292] C. Favre, V. Boutou, S. C. Hill, W. Zimmer, M. Krenz, H. Lambrecht, J. Yu, R. K. Chang, L. Woeste, and J. P. Wolf.  
*White-Light Nanosource with Directional Emission.*  
Phys. Rev. Lett. **89**, 035002 (2002).
- [293] J. H. Eickmans, W.-F. Hsieh, and R. K. Chang.  
*Laser-induced explosion of H<sub>2</sub>O droplets: spatially resolved spectra.*  
Opt. Lett. **12**, 22–24 (1987).
- [294] A. N. Zaidel', V. K. Prokof'ev, S. M. Raiskii, V. A. Slavnyi, and E. Y. Shreider.  
*Tables of Spectral Lines.*  
IFI/Plenum, New York-London (1970).
- [295] NIST, *Atomic Spectra Database (2003)*  
[http://physics.nist.gov/cgi-bin/AtData/main\\_asd](http://physics.nist.gov/cgi-bin/AtData/main_asd).
- [296] J. D. Kmetec, C. L. Gordon III, J. J. Macklin, B. E. Lemoff, G. S. Brown, and S. E. Harris.  
*MeV X-Ray Generation with a Femtosecond Laser.*  
Phys. Rev. Lett. **68**, 1527–1530 (1992).
- [297] A. Flettner, T. Pfeifer, D. Walter, C. Winterfeldt, C. Spielmann, and G. Gerber.  
*High-harmonic generation and plasma radiation from water microdroplets.*  
Appl. Phys. B **77**, 747–751 (2003).
- [298] V. Kumarappan, M. Krishnamurthy, and D. Mathur.  
*Explosions of water clusters in intense laser fields.*  
Phys. Rev. A **67**, 063207 (2003).
- [299] R. Bartels, S. Backus, E. Zeek, L. Misoguti, G. Vdovin, I. Christov, M. M. Murnane, and H. C. Kapteyn.  
*Shaped-pulse optimization of coherent emission of high-harmonic soft X-rays.*  
Nature **406**, 164–166 (2000).
- [300] R. S. Judson and H. Rabitz.  
*Teaching lasers to control molecules.*  
Phys. Rev. Lett. **68**, 1500–1503 (1992).

- [301] C. J. Bardeen, V. V. Yakovlev, K. R. Wilson, S. D. Carpenter, P. M. Weber, and W. S. Warren. *Feedback quantum control of molecular electronic population transfer*. Chem. Phys. Lett. **280**, 151–158 (1997).
- [302] A. Assion, T. Baumert, M. Bergt, T. Brixner, B. Kiefer, V. Seyfried, M. Strehle, and G. Gerber. *Control of chemical reactions by feedback-optimized phase-shaped femtosecond laser pulses*. Science **282**, 919–922 (1998).
- [303] T. Pfeifer, D. Walter, C. Winterfeldt, C. Spielmann, and G. Gerber. *Adaptive engineering of coherent soft x-rays*. manuscript in preparation (2004).
- [304] F. Verluise, V. Laude, Z. Cheng, C. Spielmann, and P. Tournois. *Amplitude and phase control of ultrashort pulses by use of an acousto-optic programmable dispersive filter: pulse compression and shaping*. Opt. Lett. **25**, 575–577 (2000).
- [305] R. J. Gordon and S. A. Rice. *Active control of the dynamics of atoms and molecules*. Annu. Rev. Phys. Chem. **48**, 601–641 (1997).
- [306] H. Rabitz, R. de Vivie-Riedle, M. Motzkus, and K. Kompa. *Chemistry - Whither the future of controlling quantum phenomena?* Science **288**, 824–828 (2000).
- [307] S. A. Rice and M. Zhao. *Optical Control of Molecular Dynamics*, volume 403. Wiley, New York (2000).
- [308] T. Brixner, N. H. Damrauer, and G. Gerber. *Femtosecond quantum control*. In B. Bederson and H. Walther (Eds.), *Advances in Atomic, Molecular, and Optical Physics*, volume 46 of *Advances in Atomic, Molecular, and Optical Physics Series*, pp. 1–54. Academic Press, London (2001).
- [309] M. Shapiro and P. Brumer. *Principles of the Quantum Control of Molecular Processes*. John Wiley & Sons, Inc., Hoboken (2003).
- [310] P. Hannaford (Ed.). *Femtosecond Laser Spectroscopy*. Kluwer Series on Progress in Lasers. Kluwer Academic Publishers, in press (2004).
- [311] R. V. Ambartsumian and V. S. Letokhov. In C. B. Moore (Ed.), *Chemical and biochemical applications of lasers*, volume 3. Academic Press, New York (1977).
- [312] V. S. Letokhov. *Photophysics and photochemistry*. Phys. Today pp. 23–32 (1977).
- [313] N. Bloembergen and E. Yablonovitch. *Infrared-laser-induced unimolecular reactions*. Phys. Today pp. 23–30 (1978).
- [314] A. H. Zewail. *Laser chemistry—Is it possible?* Phys. Today **33**, 27–33 (1980).
- [315] J. Jortner, R. D. Levine, and S. A. Rice (Eds.). *Photoselective Chemistry*, volume 47 of *Advances in Chemical Physics*. Wiley, New York (1981).



- [316] N. Bloembergen and A. H. Zewail.  
*Energy redistribution in isolated molecules and the question of mode-selective laser chemistry revisited.*  
J. Phys. Chem. **88**, 5459–5465 (1984).
- [317] T. Elsaesser and W. Kaiser.  
*Vibrational and vibronic relaxation of large polyatomic molecules in liquids.*  
Annu. Rev. Phys. Chem. **42**, 83–107 (1991).
- [318] D. J. Nesbitt and R. W. Field.  
*Vibrational energy flow in highly excited molecules: Role of intramolecular vibrational redistribution.*  
J. Phys. Chem. **100**, 12735–12756 (1996).
- [319] M. Gruebele and R. Bigwood.  
*Molecular vibrational energy flow: Beyond the golden rule.*  
Int. Rev. Phys. Chem. **17**, 91–145 (1998).
- [320] V. Wong and M. Gruebele.  
*How does vibrational energy flow fill the molecular state space?*  
J. Phys. Chem. A **103**, 10083–10092 (1999).
- [321] P. Brumer and M. Shapiro.  
*Control of unimolecular reactions using coherent light.*  
Chem. Phys. Lett. **126**, 541–546 (1986).
- [322] M. Shapiro, J. W. Hepburn, and P. Brumer.  
*Simplified laser control of unimolecular reactions: Simultaneous ( $\omega_1$ ,  $\omega_3$ ) excitation.*  
Chem. Phys. Lett. **149**, 451–454 (1988).
- [323] D. J. Tannor and S. A. Rice.  
*Control of selectivity of chemical reaction via control of wavepacket evolution.*  
J. Chem. Phys. **83**, 5013–5018 (1985).
- [324] D. J. Tannor, R. Kosloff, and S. A. Rice.  
*Coherent pulse sequence induced control of selectivity of reactions: Exact quantum mechanical calculations.*  
J. Chem. Phys. **85**, 5805–8520 (1986).
- [325] M. Shapiro and P. Brumer.  
*On the origin of pulse shaping control of molecular dynamics.*  
J. Phys. Chem. A **105**, 2897–2902 (2001).
- [326] U. Gaubatz, P. Rudecki, M. Becker, S. Schiemann, M. Külz, and K. Bergmann.  
*Population switching between vibrational levels in molecular beams.*  
Chem. Phys. Lett. **149**, 463–468 (1988).
- [327] U. Gaubatz, P. Rudecki, S. Schiemann, and K. Bergmann.  
*Population transfer between molecular vibrational levels by stimulated Raman scattering with partially overlapping laser fields: A new concept and experimental results.*  
J. Chem. Phys. **92**, 5363–5376 (1990).
- [328] K. Bergmann, H. Theuer, and B. W. Shore.  
*Coherent population transfer among quantum states of atoms and molecules.*  
Rev. Mod. Phys. **70**, 1003–1025 (1998).
- [329] A. Shi, A. Woody, and H. Rabitz.  
*Optimal control of selective vibrational excitation in harmonic linear chain molecules.*  
J. Chem. Phys. **88**, 6870–6883 (1988).
- [330] A. P. Peirce, M. Dahleh, and H. Rabitz.  
*Optimal control of quantum-mechanical systems: Existence, numerical approximation, and applications.*  
Phys. Rev. A **37**, 4950–4964 (1988).

- [331] R. Kosloff, S. A. Rice, P. Gaspard, S. Tersigni, and D. J. Tannor.  
*Wavepacket dancing: Achieving chemical selectivity by shaping light pulses.*  
Chem. Phys. **139**, 201–220 (1989).
- [332] D. Meshulach and Y. Silberberg.  
*Coherent quantum control of two-photon transitions by a femtosecond laser pulse.*  
Nature **396**, 239–242 (1998).
- [333] N. Dudovich, B. Dayan, S. M. G. Faeder, and Y. Silberberg.  
*Transform-limited pulses are not optimal for resonant multiphoton transitions.*  
Phys. Rev. Lett. **86**, 47–50 (2001).
- [334] R. J. Levis, G. M. Menkir, and H. Rabitz.  
*Selective bond dissociation and rearrangement with optimally tailored, strong-field laser pulses.*  
Science **292**, 709–713 (2001).
- [335] N. H. Damrauer, C. Dietl, G. Krampert, S. H. Lee, K. H. Jung, and G. Gerber.  
*Control of bond-selective photochemistry in CH<sub>2</sub>BrCl using adaptive femtosecond pulse shaping.*  
Eur. Phys. J. D **20**, 71–76 (2002).
- [336] T. C. Weinacht, J. Ahn, and P. H. Bucksbaum.  
*Controlling the shape of a quantum wavefunction.*  
Nature **397**, 233–235 (1999).
- [337] T. Hornung, R. Meier, D. Zeidler, K. L. Kompa, D. Proch, and M. Motzkus.  
*Optimal control of one- and two-photon transitions with shaped femtosecond pulses and feedback.*  
Appl. Phys. B **71**, 277–284 (2000).
- [338] T. Brixner, N. H. Damrauer, P. Niklaus, and G. Gerber.  
*Photoselective adaptive femtosecond quantum control in the liquid phase.*  
Nature **414**, 57–60 (2001).
- [339] J. Kunde, B. Baumann, S. Arlt, F. Morier-Genoud, U. Siegner, and U. Keller.  
*Adaptive feedback control of ultrafast semiconductor nonlinearities.*  
Appl. Phys. Lett. **77**, 924–926 (2000).
- [340] J. L. Herek, W. Wohlleben, R. J. Cogdell, D. Zeidler, and M. Motzkus.  
*Quantum control of energy flow in light harvesting.*  
Nature **417**, 533–535 (2002).
- [341] C. Daniel, J. Full, L. González, C. Lupulescu, J. Manz, A. Merli, S. Vajda, and L. Wöste.  
*Deciphering the reaction dynamics underlying optimal control laser fields.*  
Science **299**, 536–539 (2003).
- [342] A. Efimov, M. D. Moores, N. M. Beach, J. L. Krause, and D. H. Reitze.  
*Adaptive control of pulse phase in a chirped-pulse amplifier.*  
Opt. Lett. **23**, 1915–1917 (1998).
- [343] T. Brixner, M. Strehle, and G. Gerber.  
*Feedback-controlled optimization of amplified femtosecond laser pulses.*  
Appl. Phys. B **68**, 281–284 (1999).
- [344] A. Efimov, M. D. Moores, B. Mei, J. L. Krause, C. W. Siders, and D. H. Reitze.  
*Minimization of dispersion in an ultrafast chirped pulse amplifier using adaptive learning.*  
Appl. Phys. B **70**, S133–S141 (2000).
- [345] D. Zeidler, T. Hornung, D. Proch, and M. Motzkus.  
*Adaptive compression of tunable pulses from a non-collinear-type OPA to below 16 fs by feedback-controlled pulse shaping.*  
Appl. Phys. B **70**, S125–S131 (2000).
- [346] D. Meshulach, D. Yelin, and Y. Silberberg.  
*Adaptive real-time femtosecond pulse shaping.*  
J. Opt. Soc. Am. B **15**, 1615–1619 (1998).

- [347] P. Gross, H. Singh, H. Rabitz, K. Mease, and G. M. Huang.  
*Inverse quantum-mechanical control: A means for design and a test of intuition.*  
Phys. Rev. A **47**, 4593–4604 (1993).
- [348] Z. M. Lu and H. Rabitz.  
*Unified formulation for control and inversion of molecular-dynamics.*  
J. Phys. Chem. **99**, 13731–13735 (1995).
- [349] H. Rabitz and W. S. Zhu.  
*Optimal control of molecular motion: Design, implementation, and inversion.*  
Acc. Chem. Res. **33**, 572–578 (2000).
- [350] T. Brixner, B. Kiefer, and G. Gerber.  
*Problem complexity in femtosecond quantum control.*  
Chem. Phys. **267**, 241–246 (2001).
- [351] J. M. Geremia and H. Rabitz.  
*Optimal identification of Hamiltonian information by closed-loop laser control of quantum systems.*  
Phys. Rev. Lett. **89**, 263902 (2002).
- [352] A. Mitra and H. Rabitz.  
*Identifying mechanisms in the control of quantum dynamics through Hamiltonian encoding.*  
Phys. Rev. A **67**, 033407 (2003).
- [353] R. Bartels, S. Backus, I. Christov, H. Kapteyn, and M. Murnane.  
*Attosecond time-scale feedback control of coherent X-ray generation.*  
Chem. Phys. **267**, 277–289 (2001).
- [354] L. Roos, M. B. Gaarde, and A. L’Huillier.  
*Tailoring harmonic radiation to different applications using a genetic algorithm.*  
J. Phys. B **34**, 5041–5054 (2001).
- [355] E. A. Nersesov, S. V. Popruzhenko, D. F. Zaretsky, and W. Becker.  
*The gain of high harmonics in an atomic jet and in a hollow-core fiber.*  
Opt. Commun. **183**, 289–297 (2000).
- [356] E. A. Nersesov, S. V. Popruzhenko, D. F. Zaretsky, W. Becker, and P. Agostini.  
*Amplification of high-order harmonics in a short laser pulse by stimulated interaction.*  
Phys. Rev. A **6402**, 023419 (2001).
- [357] G. Tempea and T. Brabec.  
*Optimization of high-harmonic generation.*  
Appl. Phys. B **70**, S197–S202 (2000).
- [358] K. Ishikawa.  
*Photoemission and ionization of  $\text{He}^+$  under simultaneous irradiation of fundamental laser and high-order harmonic pulses.*  
Phys. Rev. Lett. **91**, 043002 (2003).
- [359] S. L. Voronov, I. Kohl, J. B. Madsen, J. Simmons, N. Terry, J. Titensor, Q. Wang, and J. Peatross.  
*Control of laser high-harmonic generation with counterpropagating light.*  
Phys. Rev. Lett. **8713**, 133902 (2001).
- [360] F. Brandi, D. Neshev, and W. Ubachs.  
*High-order harmonic generation yielding tunable extreme-ultraviolet radiation of high spectral purity.*  
Phys. Rev. Lett. **91**, 163901 (2003).
- [361] D. E. Goldberg.  
*Genetic Algorithms in Search, Optimization, and Machine Learning.*  
Addison-Wesley, Reading (1993).

- [362] H.-P. Schwefel.  
*Evolution and Optimum Seeking*.  
Wiley, New York (1995).
- [363] F. Hoffmeister and T. Bäck.  
*Genetic algorithms and evolution strategies: Similarities and differences*.  
Technical Report SYS-1/92, Institut für Informatik (1992).
- [364] S. Zipfel.  
*Erzeugung und Anwendung von Femtosekunden-Laserpulsen*.  
Diplomarbeit, Universität Würzburg (2002).
- [365] P. Villoresi, S. Bonora, M. Pascolini, L. Poletto, G. Tondello, C. Vozzi, M. Nisoli, G. Sansone, S. Stagira, and S. DeSilvestri.  
*Optimization of high-order harmonic generation by adaptive control of a sub-10-fs pulse wave front*.  
Opt. Lett. **29**, 207–209 (2004).
- [366] E. Yablonov.  
*Self-Phase Modulation and Short-Pulse Generation from Laser-Breakdown Plasmas*.  
Phys. Rev. A **10**, 1888–1895 (1974).
- [367] W. M. Wood, G. Focht, and M. C. Downer.  
*Tight Focusing and Blue Shifting of Millijoule Femtosecond Pulses from A Conical Axicon Amplifier*.  
Opt. Lett. **13**, 984–986 (1988).
- [368] T. Pfeifer.  
*Propagation of high intensity light through gas-filled hollow-core capillaries*.  
Master thesis, University of Texas at Austin, Austin (2000).
- [369] D. Zeidler, T. Hornung, D. Proch, and M. Motzkus.  
*Adaptive compression of tunable pulses from a non-collinear-type OPA to below 16 fs by feedback-controlled pulse shaping*.  
Appl. Phys. B **70**, S125–S131 (2000).
- [370] F. Eickemeyer, R. A. Kaindl, M. Woerner, T. Elsaesser, and A. M. Weiner.  
*Controlled shaping of ultrafast electric field transients in the mid-infrared spectral range*.  
Opt. Lett. **25**, 1472–1474 (2000).
- [371] W. C. Wiley and I. H. McLaren.  
*Time-of-Flight Mass Spectrometer with Improved Resolution*.  
Rev. Sci. Instr. **26**, 1150–1157 (1955).
- [372] J. Günther.  
*Femtosekunden-Laserpulse im Vakuum-Ultraviolett*.  
Diplomarbeit, Universität Würzburg (2000).
- [373] S. Vajda, A. Bartelt, E. C. Kaposta, T. Leisner, C. Lupulescu, S. Minemoto, P. Rosendo-Francisco, and L. Wöste.  
*Feedback optimization of shaped femtosecond laser pulses for controlling the wavepacket dynamics and reactivity of mixed alkaline clusters*.  
Chem. Phys. **267**, 231–239 (2001).
- [374] K. Mochiji, K. Lee, C. I. Ma, D. Y. Kim, M. Mahalingam, and D. M. Hanson.  
*Photodissociation of SF<sub>6</sub> Near the F 1s Absorption-Edge*.  
J. Vac. Sci. Technol. A **12**, 216–218 (1994).
- [375] D. S. Peterka, M. Ahmed, C. Y. Ng, and A. G. Suits.  
*Dissociative photoionization dynamics of SF<sub>6</sub> by ion imaging with synchrotron undulator radiation*.  
Chem. Phys. Lett. **312**, 108–114 (1999).

- [376] M. Ono and K. Mitsuke.  
*Anisotropy of fragment ions from SF<sub>6</sub> by photoexcitation between 23 and 210 eV.*  
Chem. Phys. Lett. **366**, 595–600 (2002).
- [377] M. Ono and K. Mitsuke.  
*Kinetic energy distribution and anisotropy of fragment ions from SF<sub>6</sub> by photoexcitation of a sulfur 2p-electron.*  
Chem. Phys. Lett. **379**, 248–254 (2003).
- [378] C. Dorrer.  
*Influence of the calibration of the detector on spectral interferometry.*  
J. Opt. Soc. Am. B **16**, 1160–1168 (1999).
- [379] W. H. Press (Ed.).  
*Numerical Recipes.*  
Cambridge Univ. Press, Cambridge (1996).
- [380] C. Dorrer and I. A. Walmsley.  
*Accuracy criterion for ultrashort pulse characterization techniques: application to spectral phase interferometry for direct electric field reconstruction.*  
J. Opt. Soc. Am. B **19**, 1019–1029 (2002).
- [381] B. H. Bransden and C. J. Joachain.  
*Physics of atoms and molecules.*  
Second edition. Prentice Hall, Harlow (2003).



# Acknowledgments

This work has been possible only through the interaction of many people. These two pages give a by no means complete list of persons that made substantial contributions. My thanks go to all of you listed or not who helped me and/or taught me important things.

Thank you all very much.

Special thanks are given to the following people:

- Prof. Dr. Gustav Gerber, for much more than his greatly generous support and advice over all the years and the unique opportunity he gave me when I started to work in his group. He has been the one both to close and to open my personal loop of physics at the University of Würzburg, as he was the one to give the introductory lecture I attended as a first year physics student.
- Prof. Dr. Christian Spielmann, for much more than his devotion to any project and help with any problem by his outstanding competence. A lot of this work has been accomplished by equipment available through his grant money.
- Prof. Dr. Alexander Mikhail Sergeev for much more than being an ideal advisor of theoretical physics. Many of the simulations shown in this work would not have been possible without his help with the computer code and conceptual expertise.
- Dr. Ulrich Weichmann for much more than preparing an excellent experimental working environment by the construction of the vacuum apparatus and for the first important steps within the ellipticity experiments that he initiated.
- Dr. Tobias Brixner for much more than being the first person to give me a comprehensive interactive introduction into the femtosecond world and thus getting me interested in the subject.
- Dominik Walter for much more than his motivation, collaboration and patience as a coworker in any respect throughout the longest period of this work.
- Carsten Winterfeldt for much more than his opinion, knowledge of the English language and collaboration on various parts of the work since he joined as a coworker in the final year.
- Robert Spitzenpfeil for much more than his devotion to the projects and the prospect of interesting experiments to come.

- The diploma students for much more than making important contributions in many ways: Axel Flettner (droplet generation and measurements), Jens König (NOPA setup and characterization), Steffen Zipfel (hollow-fiber pulse compression and shaping), Claudia Treml (visible-laser-pulse polarization shaping), Alexander Paulus (soft x-ray photoelectron spectrometer construction and operation), Frank Dimler (mid-IR generation by intrapulse difference-frequency mixing), Thomas Sokollik (visible-NIR crosscorrelation studies), and Ron Kemmer (two-dimensional spatio-temporal laser pulse shaping).
- The advanced lab (Fortgeschrittenenpraktikum) students for much more than their interest and work in many different areas: Jan Pfannes (SPIDER characterization), Markus Müller and Thomas Sokollik (both: Water-microdroplet studies in experiment and simulation), Daniel Kurfeß (CPA design), Philipp Mertsch (high-harmonic generation in heteronuclear molecules), Andreas Wörle (high-energy photoelectron spectroscopy), Dimitri Ebel (spatial laser-pulse shaping), Stefan Eyring (soft-x-ray beamline design), Melanie Kögler (x-ray spectrometer characterization), Alexander Heinz (programmable spatial wavefront analysis), and Daniel Höhne (flat-field x-ray spectroscopy).
- Dr. Walter Pfeiffer for much more than his helpful advice on various problems and issues. He was a great source of help in particular when there were questions related to teaching lab and exercise classes.
- Helga Schwark, Monika Seifer, and Diep Krafft for much more than fighting off the perils and hassle of administrative issues. They were always there to keep things up and running.
- Michael Hafner for much more than his help by designing and supervising the construction of a substantial part of the vacuum apparatus used in the experiments.
- The computer team Christian Dietl, Patrick Niklaus, Dominik Walter and Sandra Dantscher, for much more than fulfilling the vital and consuming job of maintaining the informational technology network in our group.
- Everybody of the EP1 group for much more than being great friends and colleagues.
- The people of the machine and electronics shop of the physics department for much more than building hardware and taking care of the important hidden details.
- Prof. Dr. Volker Engel and Marco Erdmann for much more than the calculation of the  $\text{Na}_2^+$  wave-packet dynamics.
- The reviewers of earlier versions of this manuscript Dominik Walter, Carsten Winterfeldt, and Gerhard Krampert for much more than their helpful suggestions on style and meaning.

Particular thanks go to Ilka Bischofs, in words, phrases, books and libraries that could never adequately describe why.

Extraordinary thanks are given to all my family and friends for so much more than their continuing loving support in all these years.



# Lebenslauf

## Persönliche Daten

Name: Thomas Pfeifer  
Wohnort: Händelstr. 27a, 97074 Würzburg  
geboren am: 5. April 1977 in Miltenberg  
Staatsangehörigkeit: deutsch  
Familienstand: ledig

## Schulbildung

09/1983 – 07/1987 Grundsschule Großheubach  
09/1987 – 06/1996 Johannes-Butzbach-Gymnasium Miltenberg  
Juni 1996 Allgemeine Hochschulreife

## Studium der Physik

10/1996 – 06/1999 Bayerische Julius-Maximilians-Universität Würzburg  
08/1999 – 12/2000 University of Texas at Austin (USA)  
Master-Arbeit bei Prof. Dr. M. C. Downer  
Dezember 2000 Abschluss: Master of Arts  
seit 01/2001 Bayerische Julius-Maximilians-Universität Würzburg  
Promotion bei Prof. Dr. G. Gerber

## Berufsweg

seit 01/2001 wissenschaftlicher Mitarbeiter der Universität Würzburg

Würzburg, den 4. Juni 2004

---

Thomas Pfeifer